

# **Atomistic and Continuum Scale Models for Flexoelectric Nanostructures and Composites**

Von der Fakultät für Mathematik und Physik  
der Gottfried Wilhelm Leibniz Universität Hannover

zur Erlangung des Grades  
Doktor der Naturwissenschaften

Dr. rer. nat.

genehmigte Dissertation von

**M. Sc. Bo He**

2023

Referentin: Prof. Dr. Xiaoying Zhuang

Korreferent: Prof. Dr. Ludovic Chamoin

Korreferent: Prof. Shengping Shen

Tag der Promotion: 12.01.2023





---

Unity of knowledge and action.

---

## Zusammenfassung

In dieser Arbeit wird das Phänomen der Flexoelektrizität in Nanomaterialien und Nanostrukturen mittels Molekulardynamikmodellen und Kontinuumsmodellen untersucht. Flexoelektrizität ist ein elektromechanisches Phänomen, das die Kopplung zwischen elektrischer Polarisierung und Dehnungsgradient in einem Material beschreibt. Dank des Dehnungsgradienten-Terms weist die Flexoelektrizität eine universelle Existenz und ein größenabhängiges Verhalten auf, was eine starke elektromechanische Kopplung auf der Mikro- und Nanoskala ermöglicht, was zu einer idealen Anwendung in Mikro- und Nanogeräten, wie z. B. Nanogenerator, führt. Es ist jedoch schwierig, die intrinsischen flexoelektrischen Koeffizienten eines Materials zu messen oder abzuschätzen, da sie durch den piezoelektrischen Effekt gestört werden, der die Kopplung zwischen elektrischer Polarisierung und Dehnung darstellt. Darüber hinaus kann das Standard-Kontinuumsmodell, wie z. B. das Finite-Elemente-Modell, die Flexoelektrizität aufgrund der Kontinuitätsanforderung höherer Ordnung ( $C^1$ -Kontinuität), die durch den Dehnungsgradiententerm auferlegt wird, nicht berücksichtigen, was die Entwicklung spezieller Kontinuumsansätze für die Designführung von flexoelektrischen Bauteilen erfordert. Diese Schwierigkeiten begrenzen unser Verständnis und die mögliche technische Nutzung der Flexoelektrizität.

Im Rahmen der Molekulardynamik entwickelt diese Arbeit ein Kern-Schale- und Ladungs-Dipol-Modell zur Extraktion der flexoelektrischen Koeffizienten eines traditionellen elektromechanischen Materials ( $\text{BaTiO}_3$ ) bzw. neu entstandener zweidimensionaler (2D) Materialien (insgesamt 21 Materialien). Speziell entwickelte mechanische Belastungsschemata werden innerhalb des Kern-Schale- und des Ladungs-Dipol-Modells eingesetzt, um die Störung durch die Piezoelektrizität zu eliminieren, was eine direkte Messung der flexoelektrischen Reaktion der Materialien ermöglicht. Die Ergebnisse der Kern-Schale-Modelle zeigen, dass der Größen-/Oberflächeneffekt den longitudinalen und scherbezogenen flexoelektrischen Koeffizienten der  $\text{BaTiO}_3$ -Nanostrukturen signifikant beeinflusst. Für zweidimensionale Materialien extrahierte das Ladungs-Dipol-Modell ihre Biege-Flexoelektrizitätskoeffizienten und identifizierte ihre Einflussfaktoren. Es wird beobachtet, dass Übergangsmetall-Dichalcogenid-Monolagen die höchsten flexoelektrischen Koeffizienten unter den untersuchten 2D-Materialien besitzen.

In dieser Arbeit werden auch Kontinuumsmodelle zur Charakterisierung der Flexoelektrizität in Kontinuums-Festkörperstrukturen, wie z. B. flexoelektrischen Verbundwerkstoffen, entwickelt. Ein 2D Meshless-Modell und ein 3D nichtlineares gemischtes Finite-Elemente-Modell verwenden Formfunktionen höherer Ordnung und zusätzliche Freiheitsgrade, um die  $C^1$ -Kontinuitätsanforderung der Flexoelektrizität zu erfüllen. Beide Modelle zeigen, dass Strukturkonfigurationen und Materialeigenschaften das elektromechanische Verhalten der flexoelektrischen Verbundwerkstoffe beeinflussen. Das 3D-nichtlineare gemischte Finite-Elemente-Modell zeigte zusätzlich die Wesentlichkeit der geometrischen Nichtlinearität für eine präzise Darstellung der Flexoelektrizität durch Kontinuumsmodelle.

Stichworte: Flexoelektrizität, Molekulardynamik, Core-shell-Modell, Charge-dipole-Modell, Meshless-Methode, Gemischte Formulierung, Bariumtitanat, 2D-Materialien, Komposite





## Abstract

This work explores the phenomenon of flexoelectricity in nanomaterials and nanostructures by molecular dynamics models and continuum models. Flexoelectricity is an electromechanical phenomenon describing the coupling between electric polarization and strain gradient in a material. Thanks to the strain gradient term, flexoelectricity exhibits an universal existence and size-dependent behavior, enabling strong electromechanical coupling at micro/nano-scale, leading to ideal application in micro/nano-devices, such as Nanogenerator. However, it is difficult to measure or estimate the intrinsic flexoelectric coefficients of a material due to the interference from the piezoelectric effect, representing the coupling between electric polarization and strain. Additionally, the standard continuum model, such as the finite element model, cannot accommodate flexoelectricity due to the higher-order continuity requirement ( $C^1$  continuity) imposed by the strain gradient term, requiring the development of novel continuum approaches for the design guidance of flexoelectric devices. These difficulties limit our understanding and potential engineering utilization of flexoelectricity.

In the framework of molecular dynamics, this work develops a core-shell and charge-dipole model for extracting flexoelectric coefficients of a traditional electromechanical material ( $\text{BaTiO}_3$ ) and newly emerged two-dimensional (2D) materials (in total 21 materials), respectively. Specially designed mechanical loading schemes are employed within the core-shell and charge-dipole model to eliminate the interference from piezoelectricity, enabling direct measurement of the materials' flexoelectric response. The core-shell models' results show that the size/surface effect significantly influences the longitudinal and shear flexoelectric coefficient of the  $\text{BaTiO}_3$  nanostructures. For two-dimensional materials, the charge-dipole model extracted their bending flexoelectric coefficients and identified their contributors. It observes that transition metal dichalcogenide monolayers possess the highest flexoelectric coefficients among the studied 2D materials.

This work also develops continuum models to characterize flexoelectricity in continuum solid structures, such as flexoelectric composite. A 2D Meshless model and a 3D nonlinear mixed finite element model employ higher-order shape function and extra degrees of freedom to fulfill the  $C^1$  continuity requirement of flexoelectricity. Both models show that structure configurations and material properties influence the electromechanical behavior of flexoelectric composites. Besides, the 3D nonlinear mixed finite element model demonstrated the essentialness of the geometrical nonlinearity for an accurate representation of flexoelectricity by continuum models.

**Keywords:** Flexoelectricity, Molecular dynamics, Core-shell model, Charge-dipole model, Meshless method, Mixed formulation, Barium Titanate, 2D materials, Composite.



## Acknowledgements

This thesis presents the author's research work under Prof. Xiaoying Zhuang's supervision at the Institute of Photonics (IOP) and Institute of Continuum Mechanics (IKM), Leibniz Universität Hannover. The Alexander von Humboldt Foundation and ERC Starting Grant (No. 802205) funded this project.

I want to express my sincere thanks to my supervisor and principal referee, Prof. Xiaoying Zhuang, for the chance she gave me and her support during my study. Prof. Zhuang has provided me sound advice whenever I needed it. Moreover, I am thankful for her pioneer vision and profound knowledge, which has expanded my horizon.

I would also like to thank the reviewers, Prof. Ludovic Chamoin and Prof. Shengping Shen, and the committee's chairman, Prof. Clemens Walther.

I am very grateful that Prof. Harold Park from Boston University provided insightful inputs about flexoelectricity in 2D materials.

Furthermore, I would like to thank my colleagues at the institute for the countless discussions during my research, which helped me solve the problems I encountered during my study. I have also benefited from the knowledge of all the institute members through weekly seminars. I am thankful to Dr. Javvaji for the joint development of the charge-dipole model for studying flexoelectricity in 2D materials. Moreover, I appreciate Dr. Hudobivnik's guidance in AceGen and support in developing the nonlinear mixed finite element model. Thanks also go to Mr. Nguyen, Mr. Thai, and Mr. Guo, with whom I shared an office, for the enjoyable working atmosphere. I appreciate the technical support, especially from Mr. Bsdok, who has helped with computer-related problems.

I am very grateful for my family's support, particularly my parents and sister, who always supported me with my decisions and encouraged me to follow my idea. My life would be a lot difficult without their support.

Finally, I want to thank my wife, Evelyn, for her patience and support. More importantly, bringing our son Benedikt into the world, which enriches our life.



# Contents

<b>1</b>	<b>Introduction</b>	<b>5</b>
1.1	Motivation . . . . .	5
1.2	Background and the state of the art . . . . .	6
1.2.1	Mechanism and material candidates of flexoelectricity . . . . .	6
1.2.2	Continuum modeling of flexoelectricity . . . . .	7
1.3	How this work approaches the identified issues . . . . .	8
1.4	Structure of this work . . . . .	9
<b>2</b>	<b>Size Effect of Flexoelectricity</b>	<b>11</b>
2.1	Core-Shell Model . . . . .	12
2.2	Validation of the Core-shell model . . . . .	13
2.3	Flexoelectrical and mechanical properties of Barium titanate oxide . . . . .	18
2.3.1	Flexoelectrical property . . . . .	18
2.3.2	Mechanical property . . . . .	21
2.4	Conclusion . . . . .	24
<b>3</b>	<b>Flexoelectricity in two-dimensional materials</b>	<b>25</b>
3.1	Charge-dipole model . . . . .	26
3.1.1	Charge-dipole formulation . . . . .	26
3.1.2	Estimation of charge-dipole potential parameter $R$ . . . . .	29
3.1.3	Validation of the charge-dipole model . . . . .	30
3.2	Simulation method for extracting flexoelectric coefficients of 2D materials . . . . .	34
3.2.1	Deformation pattern . . . . .	34
3.2.2	Validation the assumption in the deformation pattern . . . . .	35
3.3	Flexoelectric coefficient of 2D materials . . . . .	36
3.3.1	Mechanisms of inducing polarization in 2D materials . . . . .	37
3.3.2	Flat 2D Monolayers . . . . .	39
3.3.3	Buckled 2D Monolayers . . . . .	40
3.3.4	Transition metal dichalcogenide monolayers . . . . .	42
3.3.5	Janus transition metal dichalcogenide monolayers . . . . .	44
3.3.6	In-plane flexoelectric polarization . . . . .	49
3.4	Conclusion . . . . .	52

---

<b>4</b>	<b>Continuum Modeling of Flexoelectric Composites</b>	<b>55</b>
4.1	Meshless model for flexoelectric composites . . . . .	56
4.1.1	Theory of linear flexoelectricity . . . . .	56
4.1.2	Moving least square approximation . . . . .	58
4.1.3	Numerical results and discussion . . . . .	60
4.2	Mixed finite element model for flexoelectric composites . . . . .	67
4.2.1	Mixed finite element formulation for the nonlinear flexoelectricity .	68
4.2.2	Numerical results and discussion . . . . .	72
4.3	Conclusion . . . . .	91
<b>5</b>	<b>Conclusions and Future Perspectives</b>	<b>93</b>
<b>A</b>	<b>Derivatives of potential function</b>	<b>95</b>
<b>B</b>	<b>Mathematical expression for the elements in equation (4.27)</b>	<b>97</b>
<b>C</b>	<b>Matrix form of the components in equation (4.62)</b>	<b>99</b>
	<b>Bibliography</b>	<b>104</b>
	<b>List of Figures</b>	<b>121</b>
	<b>List of Tables</b>	<b>127</b>
	<b>CURRICULUM VITAE</b>	<b>128</b>
	<b>PUBLICATIONS</b>	<b>129</b>



# List of symbols

$A$	constant used in Buckingham potential
$\mathbf{A}$	moment matrix
$\bar{\mathbf{A}}$	Matrix $\bar{\mathbf{A}}$
$\alpha, \beta, \gamma$ and $\delta$	direction components
$\bar{\alpha}$	polarizability
$B_{ij}$	components of matrix $\bar{\mathbf{A}}^{-1}$
$C$	constant used in Buckingham potential
$\mathbf{C}$	cubic
$\mathbb{C}$	the fourth-order elastic moduli
$\mathbf{C}$	matrix for dynamic effect
$\chi$	electron affinity of atom
$\bar{\chi}$	electric susceptibility
$d_s$	search radius
$\mathbf{d}, d_{ijk}$	third-order piezoelectric coefficient tensor and its component
$\bar{\mathbf{d}}, \bar{d}_{ijkl}$	fourth-order converse flexoelectric coefficient tensor and its component
$\mathbf{D}, D_i$	first-order electric displacement vector and its component
$\bar{\mathbf{D}}, \bar{D}_{ij}$	second-order flexoelectric electric displacement vector and its component
$\hat{\mathbf{D}}, \hat{D}_i$	first-order piezoelectric electric displacement vector and its component
$e$	positive elementary charge
$e$	element
$\epsilon$	dielectric constant
$\epsilon_0$	dielectric permittivity of vacuum
$\boldsymbol{\varepsilon}, \varepsilon_{ij}$	strain tensor and its component
$\tilde{\boldsymbol{\eta}}$	the gradient of the Green Lagrange strain tensor
$\bar{\boldsymbol{\eta}}$	the gradient of the Green Lagrange strain tensor at a given point
$\mathbf{E}, E_i$	electric field and its component
$\bar{\mathbf{E}}$	electric field at a given point
$E$	potential
$E^{\text{Buckingham}}$	Buckingham potential
$E^{\text{Coulombic}}$	Coulombic potential
$E^{\text{Spring}}$	spring interaction
$E_{\text{els}}$	Young's modulus
$\mathbf{f}, \bar{f}_{ijkl}$	fourth-order direct flexoelectric coefficient tensor and its component
$\mathbf{F}, f$	force
$\mathbf{g}$	tangent non-local elastic tensor



$G$	second order Green Lagrange strain tensor
$\bar{G}$	second order Green Lagrange strain tensor at a given point
$\Gamma$	boundary
$h$	height
$\mathcal{H}$	enthalpy density of dielectric solid
$H$	total electrical enthalpy
$I$	identity matrix
$\boldsymbol{\kappa}, \kappa_{ij}$	second-order dielectric tensor and its component
$\bar{k}_{eff}$	effective electromechanical coupling factor
$K$	inverse of curvature for 2D material
$K_2, K_4$	constant used in bond spring potential
$\mathbf{K}, K_{ij}$	Stiffness matrix and its component
$L, l$	length
$L$	linearization operator
$\lambda$	Lagrange multiplier
$\bar{\lambda}$	Lagrange multiplier at a given point
$m$	mass
$M$	mass matrix
$\mu$	flexoelectric coefficient
$N$	number of item
$\mathbf{N}, N_i$	shape function and its component
$O$	Orthorhombic
$\Omega$	domain
$\mathbf{P}, P_i$	polarization and its component
$\mathbf{p}, p_i$	dipole moment and its component
$\bar{p}$	a polynomial of certain order
$\pi$	Pi
$\Pi$	total potential energy
$\bar{\psi}$	sign distance function
$\bar{\Psi}$	absolute sign distance function
$\boldsymbol{\psi}$	gradient of displacement
$\bar{\boldsymbol{\psi}}$	gradient of displacement at a given point
$q$	charge
$\bar{\rho}$	constant used in Buckingham potential
$\rho$	density
$R$	Rhombohedral
$R$	width of Gaussian distribution
$r_{ij}$	distance between particle i and j
$\mathbf{S}$	second Piola-Kirchhoff tensor
$\bar{\mathbf{S}}$	second Piola-Kirchhoff tensor at a given point
$\boldsymbol{\sigma}, \sigma_{ij}$	second-order stress tensor and its component
$\bar{\boldsymbol{\sigma}}, \bar{\sigma}_{ijk}$	third-order stress tensor from flexoelectricity and its component
$\hat{\boldsymbol{\sigma}}, \hat{\sigma}_{ij}$	second-order stress tensor from piezoelectricity and its component
$t$	time
$\mathbf{t}, \bar{\mathbf{t}}$	traction force and applied traction force

<b>T</b>	Tetragonal
$T^{q-q}$	charge-charge interaction coefficients
$\mathbf{T}^{q-p}$	charge-dipole interaction coefficients
$\mathbf{T}^{p-p}$	dipole-dipole interaction coefficients
$\theta$	electric potential
$\tilde{\tau}$	third order double stress tensor
$\bar{\tau}$	third order double stress tensor at a given point
$\mathbf{u}, u_i$	displacement vector and its component
$\bar{\mathbf{u}}$	displacement vector at a given point
$U_{flexo}$	internal strain energy density
$\bar{v}$	velocity
$V, v$	volume
$w$	surface charge density
$\bar{w}$	weight function
$W$	relative distance between core and shell
$\mathbf{W}_{ext}$	external work
$\mathbf{x}, \mathbf{X}$	location vector
$Y$	shell charge
$Z$	core charge



# Chapter 1

## Introduction

### 1.1 Motivation

A surgeon attaches paper-like nanofilms onto a patient's heart, and these nanofilms generate enough electrical energy from the patient's cardiac motion to power the patient's cardiac pacemaker. Sounds like science fiction? Not really. Researchers have successfully implemented this type of self-powered biomedical implants in animal trials, see AZIMI ET AL. (2021); LI ET AL. (2010). The "magic" behind these self-powered biomedical implants is a physical phenomenon called electromechanical coupling. It describes the conversion between electrical energy and mechanical energy that enables electrically controlled mechanical actuation or electrical generation by applying a mechanical load. Along with the biomedical applications, electromechanical coupling is also widely applied in energy harvester, see LIN ET AL. (2008); WANG ET AL. (2007); WANG & SONG (2006); PARK ET AL. (2014), nanoelectronics, see WASER ET AL. (2003); LU & LIEBER (2010); COMPANO ET AL. (2000), nanosensors, see HUANG ET AL. (2008); MEGRICHE ET AL. (1999); IHN & CHANG (2004) and nanorobots, see MALLOUK & SEN (2009); REQUICHA (2003); SANCHEZ & PUMERA (2009). Most of these applications utilizing electromechanical coupling rely on an electromechanical interaction called piezoelectricity, which describes the coupling between electric polarization and strain. For instance, ZnO piezoelectric nanowires generate over 1 Volt open-circuit voltage from the mechanical strain induced by compressing the nanowires, see HU ET AL. (2011). However, piezoelectricity exists only in materials with a non-center symmetric crystal structure like ZnO, see IKEDA (1996). A recently discovered electromechanical interaction called flexoelectricity describes the relationship between the electric polarization and strain gradient, which exists theoretically in all material groups, see YUDIN & TAGANTSEV (2013b). Furthermore, the involvement of strain gradient in flexoelectricity suggests a size-dependent behavior of the flexoelectricity, enabling a strong electromechanical coupling from a high strain gradient at a small-length scale, see MAJDOUB ET AL. (2008). Preliminary studies demonstrated that the energy conversion from flexoelectricity is much higher than that of piezoelectricity at a small-length scale, see HU ET AL. (2014); ABDOLLAHI ET AL. (2019). These advantages of flexoelectricity are desirable for small-scale electromechanical applications, such as nanogenerators or nanosensors. Researchers mainly focus on three approaches to induce a strong electromechanical cou-

pling from flexoelectricity in small-scale applications: utilizing size-effect, using materials with high flexoelectric coefficient, and engineering high strain gradient by structure patterning/composition. For instance, an experimental study uses scanning probe microscopy (SPM) to apply  $1 \mu\text{N}$  force onto ultrathin Barium titanate oxide ( $\text{BaTiO}_3$ ) films inducing a highly irregular stress field over several nanometers resulting in a strong flexoelectric response, see LU ET AL. (2012). Various studies measure and estimate the flexoelectric coefficients of the traditional ferroelectric materials: ceramics, single crystal, and polycrystal, to find a suitable candidate for flexoelectric applications, see HUANG ET AL. (2011); KWON ET AL. (2014); SHU ET AL. (2017b); ZUBKO ET AL. (2007). Engineering high strain gradient through structure pattern/composition have also shown significant enhancement of flexoelectric response, see ZHANG ET AL. (2014); KARTHIK ET AL. (2013). However, many questions/difficulties around flexoelectricity remain unsolved, such as the underlying mechanism of the size-dependent behavior of flexoelectricity is unexplored due to the difficulties in the experimental setup and simulation size limitation, see MAJDOUB ET AL. (2008); MARANGANTI & SHARMA (2009). Meanwhile, the newly emerged 2D nanomaterials have also shown great potential in flexoelectric application due to their flexibility and high polarizability, but their flexoelectric coefficients and contributing factors are still unknown, see JIANG ET AL. (2013c). Furthermore, the lack of a continuum model for characterizing flexoelectric composite hinders the optimization of flexoelectric devices through structure patterning/composition. Addressing these open issues will help advance the development of flexoelectric devices in engineering applications. The motivation of this work is to solve the stated open issues. The following section discusses the existing studies on flexoelectricity and the origins of the open issues.

## 1.2 Background and the state of the art

This section presents a compact literature study on flexoelectricity regarding its underlying mechanism, material candidate, and continuum model. The main focus here is on the aforementioned aspects of flexoelectricity in traditional electromechanical materials and newly emerged 2D materials, presenting a fraction of research on flexoelectricity. For a comprehensive overview of flexoelectricity, please refer to the review papers, see WANG ET AL. (2019); YUDIN & TAGANTSEV (2013a); JIANG ET AL. (2013c).

### 1.2.1 Mechanism and material candidates of flexoelectricity

Early studies on flexoelectricity exploring its underlying mechanism or searching for suitable material candidates mainly focus on the traditional electromechanical materials, such as  $\text{BaTiO}_3$  or periclase ( $\text{MgO}$ ), which possess high electric polarizability due to the active oxygen atoms. For example, study shows unexpected large bending flexoelectric coefficients of  $\text{BaTiO}_3$  and  $\text{Pb}(\text{Mg}_{1/3}\text{Nb}_{2/3})\text{O}_3$ , where their magnitudes of electromechanical response from flexoelectricity surpass that of the piezoelectric effect, see MA & CROSS (2001, 2006); FU ET AL. (2006). Meanwhile, a study found that the flexoelectric coefficients of oxide materials linearly scale with their relative electric permittivity, see YUDIN & TAGANTSEV (2013a), which depends on the temperature, see MARANGANTI & SHARMA (2009). This

temperature dependency is further confirmed in a charge transfer molecular dynamics (MD) model studying Barium and Strontium titanate (BST), see MBARKI ET AL. (2014). Studies also show that oxide materials doped with extrinsic elements improve their flexoelectric coefficients significantly, see LI ET AL. (2014); HUANG ET AL. (2017); JIN ET AL. (2021). Comprehensive Density Functional Theory (DFT) simulations report the flexoelectric coefficients of various oxide and semiconductor materials, see MARANGANTI & SHARMA (2009). Although researchers have conducted various studies on flexoelectricity in oxide materials, the size-dependent behavior of flexoelectricity in oxide materials such as  $\text{BaTiO}_3$  remains unresolved due to the limited simulation size of DFT and difficulties in an experimental setup, see JIANG ET AL. (2013c). Meanwhile, the size-dependent behavior of flexoelectricity is the key aspect that makes flexoelectricity extremely attractive for small-length scale devices, so understanding its mechanism is essential.

In recent years, the number of studies on flexoelectricity in 2D materials has increased with the rising interest in the newly emerged 2D materials due to the desire to miniaturize sensors and actuators to the micro and nanoscales. The majority of these studies employed mechanically induced curvatures in 2D materials to activate flexoelectricity. For instance, a study shows a linear relationship between the induced electric dipole moment and bending curvature in graphene using DFT calculations, see KALININ & MEUNIER (2008). A theoretical analysis of flexoelectricity in carbon nanostructures (nanotubes, fullerenes, and nanocones) further proves the dependency of the flexoelectric dipole moments on local curvature, see KVASHNIN ET AL. (2015). Researchers have also successfully induced flexoelectric response in Boron Nitride and transition metal dichalcogenide monolayers (TMDCs) by indentation and bending, see AHMADPOOR & SHARMA (2015a); ROY ET AL. (2021); DOU ET AL. (2020). Besides, a study provided evidence that monolayer  $\text{MoS}_2$  exhibits an out-of-plane bending flexoelectric response using the piezoresponse force microscopy, see BRENNAN ET AL. (2017). An alternative to activate flexoelectricity in 2D materials is structural modification. For example, studies introduced defects into graphene sheets to generate strain gradients under a tensile load, thus induces flexoelectric response and electric polarization, see CHANDRATRE & SHARMA (2012); KUNDALWAL ET AL. (2017); JAVVAJI ET AL. (2018). The presented studies primarily focused on the overall electromechanical response of the studied 2D materials and left the flexoelectric coefficients of these 2D materials unresolved. They suggested that the main issue in calculating or measuring the flexoelectric coefficients of 2D materials is that it has been challenging to isolate the relative contributions of piezoelectricity and flexoelectricity to the resulting polarization, see JIANG ET AL. (2013c). As a result, most 2D materials' intrinsic flexoelectric properties remain unresolved, and the mechanisms controlling the intrinsic flexoelectric properties of different 2D materials are also unresolved.

### 1.2.2 Continuum modeling of flexoelectricity

The difficulty in developing a continuum model for flexoelectricity lies in the existing higher-order strain gradient term in the governing equation of flexoelectricity. The strain gradient term requires  $C^1$  continuity, which the traditional finite element method does not provide. Researchers proposed two approaches to overcome this obstacle: (a) utilizing meth-

ods equipped with a global higher-order shape function. For instance, a Meshfree model equipped with a smooth shape function studies the flexoelectric responses of a dielectric cantilever beam and truncated pyramid, see ABDOLLAHI ET AL. (2014, 2015). This model further suggested that the simplified analytical model is unable to accurately characterize flexoelectricity in multi-dimensional geometries. Another Meshfree model investigates the influence of the surface flexoelectric effect and finite deformation on a flexoelectric device's overall electromechanical response, see ZHUANG ET AL. (2019b). Similar to the Meshless model, Isogeometric Analysis (IGA) employs the NURBS or B-splines basis function to handle the  $C^1$  continuity requirement. For instance, a study developed an IGA model and applied the level-set technique to optimize the topology of a flexoelectric structure to enhance its electromechanical response, see GHASEMI ET AL. (2017). Another IGA model considering the material nonlinearity investigated the influence of the electric field acting on a droplet on its deformation pattern., see THAI ET AL. (2018); (b) utilizing extra degrees of freedom to enforce the  $C^1$  continuity. For example, a 2D mixed finite element model equipped with the Lagrange multiplier achieved the  $C^1$  continuity and characterized a flexoelectric device's electromechanical behavior, see MAO ET AL. (2016). Another study extends this mixed finite element model to 3D, see DENG ET AL. (2017) and develops a topology optimization scheme for flexoelectric structures within the mixed finite element framework, see NANTHAKUMAR ET AL. (2017). However, the continuum models presented here primarily focus on single-phase flexoelectric structures. Meanwhile, several studies suggest that flexoelectric composites can induce a stronger electromechanical response through flexoelectricity than a single-phase flexoelectric structure, see ZHANG ET AL. (2016); WAN ET AL. (2017); RAY (2018), and this enhancement requires further investigation by extending the existing continuum models.

### 1.3 How this work approaches the identified issues

To address the identified issues on flexoelectricity, this work undertakes the following tasks

- To understand the mechanism of the size-dependent behavior of flexoelectricity in  $\text{BaTiO}_3$ ;
- To estimate the flexoelectric coefficients of 2D materials and identify their contributing factors;
- To develop continuum models of flexoelectricity for the design guidance of flexoelectric composites.

The author has chosen the atomistic modeling approach for addressing the first two tasks. More specifically, this work develops molecular dynamics models to explore the size-dependent behavior of flexoelectricity in  $\text{BaTiO}_3$ , and to extract the flexoelectric coefficients of the newly emerged 2D materials (graphene allotropes, nitrides, graphene analog group-IV elements, and transition metal dichalcogenide monolayers (TMDCs)). Atomistic approaches, such as the molecular dynamics model, describe a system with discrete atoms or particles governed by Newton's second law of motion, and they have

demonstrated extensive accuracy and correctness in studying piezoelectricity with respect to experimental results, see BRISCOE ET AL. (2013); ZHANG ET AL. (2019); MOMENI ET AL. (2012). Several studies have also obtained accurate results for flexoelectricity in oxide materials using the same MD models for piezoelectricity, see MBARKI ET AL. (2014); MAJDOUB ET AL. (2008). Meanwhile, the atomistic approach enables the researcher to apply controlled complex boundary conditions to the nanostructures, which is advantageous for studying flexoelectricity since it requires a deformation-induced strain gradient field. Compare to another atomistic approach called DFT based on quantum mechanics, the molecular dynamics is advantageous in simulation size. DFT allows less than 1000 atoms in a simulation, limiting the study of the size/surface effect of flexoelectricity, see HONG ET AL. (2010). Furthermore, experimental studies on flexoelectricity in 2D materials suggested that it has been challenging to isolate the relative contributions of piezoelectricity and flexoelectricity to the resulting polarization. The MD approach can efficiently eliminate the contribution of piezoelectricity by specially designed deformation schemes. It worth noting here that the accuracy of the MD models highly relies on the chosen interatomic potentials. This work develops two continuum models to address the third task. A 2D linear Meshless model coupled with the level-set technique explores flexoelectricity in flexoelectric composites. Besides, a 3D nonlinear mixed finite element model incorporated the geometric nonlinearity and strain gradient elasticity investigates flexoelectricity in 3D composite structures under static and dynamic loading conditions. The following section presents the structure of this work.

## 1.4 Structure of this work

The structure of this work: chapter 2 investigates the size effect of flexoelectricity in  $\text{BaTiO}_3$ , followed by chapter 3 examines the flexoelectric effect in newly emerged 2D materials and extracts their bending flexoelectric coefficients. Subsequently, in chapter 4, a 2D Meshless model and a 3D nonlinear mixed finite element model are developed to investigate flexoelectricity in composite structures considering the geometric nonlinearity and dynamic effect. Finally, chapter 5 presents the conclusions and outlook.





# Chapter 2

## Size Effect of Flexoelectricity

This chapter investigates the size-dependent behavior of flexoelectricity in Barium titanate oxide ( $\text{BaTiO}_3$ ) and its mechanical property.  $\text{BaTiO}_3$  is a ferroelectric material with numerous industrial applications due to its outstanding piezoelectric, flexoelectric and electrical hysteresis properties, see SETTER ET AL. (2006). For instance, studies found that it retains electric polarization without the presence of an electric field, see MA & CROSS (2001); BERLINCOURT & JAFFE (1958). It is also possible to control the strain in  $\text{BaTiO}_3$  by applying an external electric field, see WU ET AL. (2014b). Besides, the polarization in  $\text{BaTiO}_3$  can be altered by a sufficiently strong electric field, see SANG ET AL. (2008). These advantageous electromechanical properties enable  $\text{BaTiO}_3$  to be a potential candidate as the next generation advanced material.

Flexoelectricity is an electromechanical phenomenon describing the linear relationship between the electric polarization and strain gradient, see YUDIN & TAGANTSEV (2013a). During the past decade, flexoelectricity received wide attention due to its strong electromechanical effects at the micro-and nanoscale, see JIANG ET AL. (2013c); YUDIN & TAGANTSEV (2013a); ZUBKO ET AL. (2013a). However, the questions about the range of the flexoelectric coefficient of a material, contributors to a materials' flexoelectric response, and size dependence behavior of flexoelectricity are open to solve. Several studies attempted to answer the first two open questions. For example, experimental findings show an unexpected large bending flexoelectric response of  $\text{BaTiO}_3$  and  $\text{Pb}(\text{Mg}_{1/3}\text{Nb}_{2/3})\text{O}_3$  comparing to the theoretical studies by density functional theory (DFT), see MA & CROSS (2001, 2006); FU ET AL. (2006). This difference between the experiment measurement and theoretical estimation by DFT correlates with the operational temperature of the experiment (ambient temperature condition) and DFT (absolute zero temperature), see MARANGANTI & SHARMA (2009); XU ET AL. (2013). Meanwhile, various studies measure or estimate the flexoelectric coefficients of ceramics, single crystals, and polycrystals to find a suitable candidate for flexoelectric applications, see HUANG ET AL. (2011); KWON ET AL. (2014); SHU ET AL. (2017b); ZUBKO ET AL. (2007). It worth noting here that the existing studies on the range of the flexoelectric coefficients of these materials show a significant discrepancy among each other, see WANG ET AL. (2019) Other findings suggest that the flexoelectric response of a material signifi-

---

The content of this chapter is partially published in author's paper (DOI: 10.1016/j.physb.2018.01.031)

cantly influenced by temperature, see MARANGANTI & SHARMA (2009); MBARKI ET AL. (2014), and loading frequency, see SHU ET AL. (2017a). However, the size-dependency of flexoelectricity remains unexplored and unsolved due to the difficulty in modeling by DFT and experimental setup, see HONG ET AL. (2010).

In this chapter, a core-shell molecular dynamics model explores the size-dependent behavior of flexoelectricity in  $\text{BaTiO}_3$ , the parameters used in the core-shell model are from quantum mechanics approaches, such as DFT, see COHEN & KRAKAUER (1992); ZHONG ET AL. (1994); VIELMA & SCHNEIDER (2013); PILANIA & RAMPRASAD (2010), so that the core-shell model inherits the high level of accuracy as the quantum mechanics approach. Meanwhile, the core-shell model allows a large atomic structure that can not be achieved using a quantum mechanics approach, see HONG ET AL. (2010). In the literature, the core-shell model has been successfully applied for Periclase to investigate its spontaneous polarization, see CHATZOPOULOS ET AL. (2016) and numerous oxide materials to study their electrical, mechanical properties, see MACHADO ET AL. (2010); MATSUI (1998); TILOCCA ET AL. (2006); TINTE ET AL. (2004). Another model called the reactive force field (ReaxFF) potential model depending on the self-consistent charge optimization also investigated the phase transition and polarization of  $\text{BaTiO}_3$ , see GODDARD III ET AL. (2002). Comparing to the ReaxFF potential model, the core-shell model is advantageous in terms of computational efficiency and accurate estimation of the phase transition of  $\text{BaTiO}_3$ , which will be demonstrated in the section 2.2

This chapter is structured as follows: section 2.1 presents the details of the core-shell model for  $\text{BaTiO}_3$ , and the validation of the core-shell model in terms of the phase transition temperatures of  $\text{BaTiO}_3$  is shown in section 2.2. Following by the studies on the size-dependent behavior of flexoelectricity in  $\text{BaTiO}_3$  and its mechanical properties in section 2.3.

## 2.1 Core-Shell Model

The adiabatic core-shell model is first proposed in MITCHELL & FINCHAM (1993) to study the melting process of  $\text{NaCl}$ , see WANG ET AL. (2008), superionic conduction in  $\text{CaF}_2$ , see LINDAN & GILLAN (1993), and the properties of  $\text{MgO}$  under the condition of high temperature (above 1500 K) and high pressure (100 GPa), see FINCHAM ET AL. (1994). The core-shell model is also extensively used for ferroelectric oxide materials thanks to its competency in estimating the dipolar polarization, see TINTE ET AL. (2004); CHEN ET AL. (2009); TINTE & STACHIOTTI (2001). These studies demonstrate that the applied core-shell models are advantageous in considering the dynamics of oxygen atoms in ferroelectric oxide materials.

In the core-shell model, each atom consists of a positively charged core and a negatively charged shell. The splitting of an atom into a core and a shell will induce polarization under perturbations. The total inter-atomic potential energy of a system represented by the core-shell model has three contributors. Namely, the long-range Coulombic potential ( $E^{\text{Coulombic}}$ ) to describe the electrostatic interaction among cores and shells of different atoms; Short-range Buckingham potential ( $E^{\text{Buckingham}}$ ) to describe the interactions between shells; Anharmonic bond spring potential ( $E^{\text{Spring}}$ ) to define the interactions between the core and shell of the same atom. Figure 2.1 shows a schematic illustration of the interactions between two

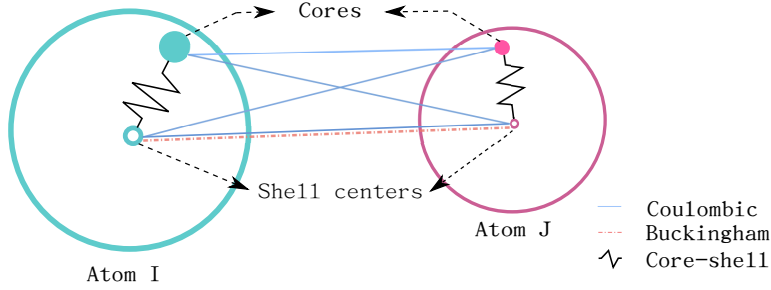


**Figure 2.1.** Schematic illustration of the interactions between particles.

atoms  $i$  and  $j$ .

The Coulombic energy between atoms  $i$  and  $j$  is

$$E_{ij}^{\text{Coulombic}} = \frac{q_i q_j}{4\pi\epsilon r_{ij}}, \quad (2.1)$$

where  $i, j$  are the indices of any two particles (either a core or a shell),  $q$  is the charge carried by the particle,  $r_{ij}$  is the distance between the particle  $i$  and  $j$ .  $\epsilon$  is the dielectric constant. The long-range Coulombic interactions between the shell and core of the same atom are excluded to avoid the divergence in the equation (2.1). The mathematical form of the short-range Buckingham potential is

$$E_{ij}^{\text{Buckingham}} = A e^{-r_{ij}/\bar{\rho}} - \frac{C}{r_{ij}^6}, \quad (2.2)$$

where  $A$ ,  $\bar{\rho}$  and  $C$  are numerical constants. The bond spring potential has the form

$$E_{ij}^{\text{Spring}} = \frac{1}{2} K_2 r_{ij}^2 + \frac{1}{24} K_4 r_{ij}^4, \quad (2.3)$$

where  $K_2$  and  $K_4$  are constants. The numerical parameters for  $\text{BaTiO}_3$  used in equation (2.1) to (2.3) are listed in the table 2.1. The studies on the size-dependent flexoelectricity and mechanical properties of  $\text{BaTiO}_3$  were performed with an open-source MD code called Large scale Atomic/Molecular Massive Parallel Simulator (LAMMPS) developed in PLIMPTON (1995a). In the following section 2.2, the adopted core-shell model and the chosen parameters in the table 2.1 validate with the experimental and numerical studies in terms of the phase transition temperatures and spontaneous polarizations of  $\text{BaTiO}_3$ .

## 2.2 Validation of the Core-shell model

It found that  $\text{BaTiO}_3$  undergoes phase transition: Rhombohedral (R)  $\rightarrow$  Orthorhombic (O)  $\rightarrow$  Tetragonal (T)  $\rightarrow$  Cubic (C), as the temperature increases, and the spontaneous polarizations of  $\text{BaTiO}_3$  correlates with the phase transition process, see LEMANOV ET AL. (1996). Here validates the core-shell model by reproducing this phase transition process and the correlated spontaneous polarizations of  $\text{BaTiO}_3$ . The phase transition process can be quantified by the varying lattice parameters of  $\text{BaTiO}_3$  with the changing temperature and the calculation of

**Table 2.1.** Core-Shell model parameters from VIELMA & SCHNEIDER (2013). Charges are in unit of electrons, energies in unit of eV, and length in unit of Å.

Atom	Core charge	Shell charge	$K_2$	$K_4$
Ba	5.042	-2.870	298.51	0.0
Ti	4.616	-1.544	306.14	500.0
O	0.970	-2.718	36.93	5000.0
Short-range	A	$\bar{\rho}$	C	
Ba-O	7149.81	0.3019	0.0	
Ti-O	7200.27	0.2303	0.0	
O-O	3719.60	0.3408	597.17	

the spontaneous polarization in a given direction  $\alpha$  follows the equation (2.4) as proposed in CHEN & CALLAWAY (1992):

$$P_\alpha = \frac{e}{\Omega} \sum_k [Z_k u_k^\alpha + Y_k W_k^\alpha], \quad (2.4)$$

where  $P_\alpha$  is the polarization in  $\alpha$  direction,  $e$  represents the positive elementary charge,  $\Omega$  is the unit cell volume,  $k$  is the total number of atoms in a unit cell,  $Z$  is core charge,  $u$  is the core displacement,  $Y$  is the shell charge,  $W$  is the relative displacement between core and shell. As polarization only makes sense when defined as a neutral stoichiometric unit, so for the BaO-terminated unit cell, the sum of Ba ions and O ions is divided by 8 and 2, respectively, as suggested in ZHONG ET AL. (1994).

The validation study carries out in LAMMPS and simulation details as following, the initial configuration of the BaTiO<sub>3</sub> system has  $N \times N \times N$  unit cells.  $N$  is the number of primitive cells in one direction of the Cartesian coordinate system. The unit cell is a BaO-terminated primitive cell constructed in the rhombohedral phase. The system first equilibrates for 10000 steps at 80 K, followed by a simulation run of 450000 steps. During the simulation run, the system is heated from 80 K to 450 K at a constant rate. The atmospheric pressure of 1 bar applies on the system. The relaxation time for the thermostat and barostat is 0.1 ps. The shells have a mass of 2 atomic units, which ensures the natural vibrational frequency of an an-harmonic spring well above the whole domain's frequency. This enables the shells to react with the electrostatic environment. The time step is set to 0.4 fs to record the atom trajectories. The interaction cut-off distance is 16 Å. Ewald summation sets the accuracy of  $1 \times 10^{-6}$  for calculating the long-range Coulombic interaction in the K-space. Periodic boundary conditions are imposed in all directions (unless otherwise stated) to remove surface effect while studying the phase transition of BaTiO<sub>3</sub>. The primitive cell's lattice constants are obtained by analyzing the simulation box size and shape during the heating period. Figure 2.2 presents the temperature-dependent lattice parameters of primitive cells extracted from the systems with different size. Systems with  $7 \times 7 \times 7$ ,  $10 \times 10 \times 10$ ,  $13 \times 13 \times 13$  and  $15 \times 15 \times 15$  primitive cells have 3430, 10000, 21970 and 33750 atoms, respectively.

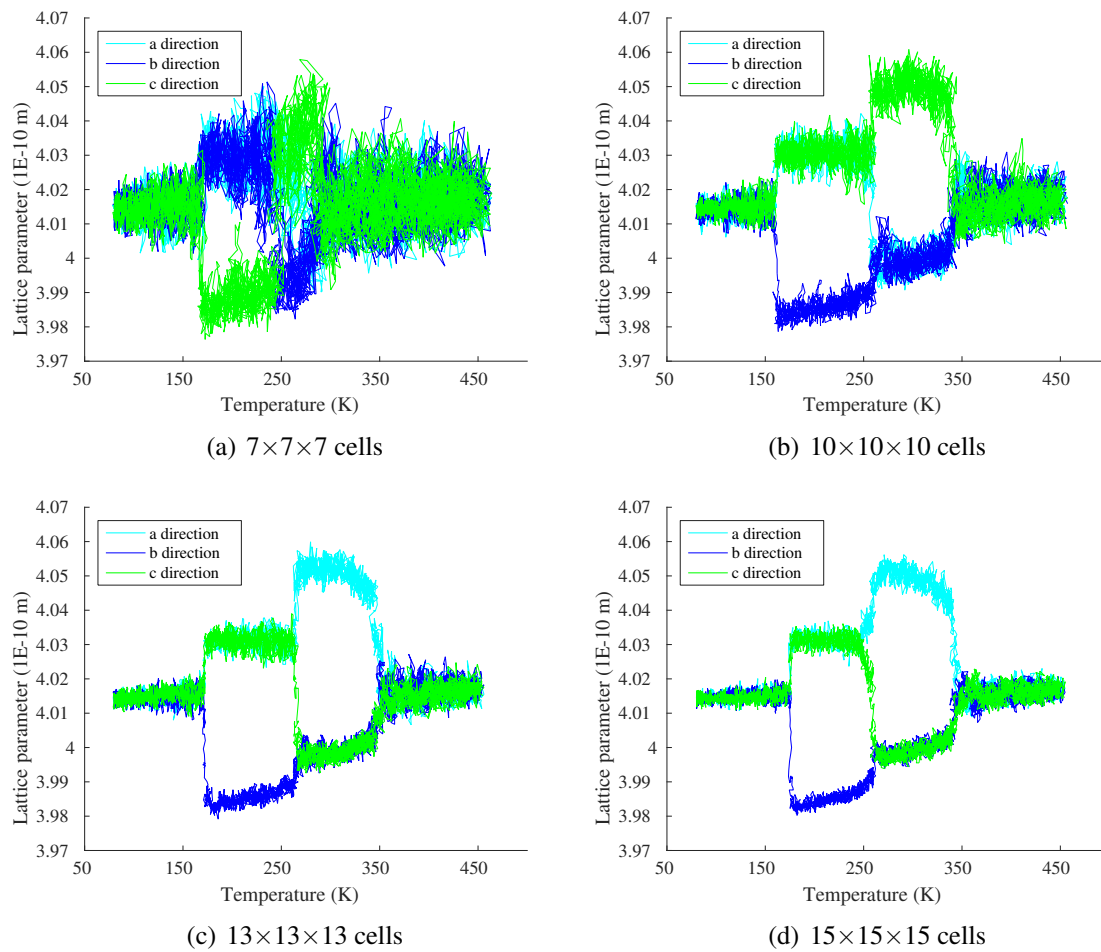


**Figure 2.2.** Temperature versus lattice parameters ( $\text{\AA}$ ) of different size  $\text{BaTiO}_3$  systems.

Figure 2.2 shows the variation of the lattice parameters with temperature for systems of different sizes. The increase in temperature changes the lattice parameters, which corresponds to the changes in the crystal structure. From the simulation results (figure 2.2), the phase transition sequence of Rhombohedral (R)  $\rightarrow$  Orthorhombic (O)  $\rightarrow$  Tetragonal (T)  $\rightarrow$  Cubic (C) is correctly captured. The numerical value of lattice parameters shows significant perturbations for the system consist of  $7 \times 7 \times 7$  cells. These perturbations originate from the unstable oscillations of atoms under the thermal and pressure constraints. The variation of lattice parameters shown in figure 2.2(b)  $\sim$  (d) demonstrates that the thermal and pressure-induced perturbations can be sufficiently relaxed with the increase in system size. The transition temperatures with respect to the system size is shown in figure 2.3 and suggests that a system with a total number of atoms larger than 10000 is required to achieve a stable and correct estimation of the phase transition of  $\text{BaTiO}_3$ . The transition temperatures obtained from the MD simulations compared with DFT and experimental results are shown in the table 2.2. The prediction from the core-shell model with parameters from the table 2.1 produces the transition temperatures in agreement with the experimental data for R  $\rightarrow$  O

**Table 2.2.** BaTiO<sub>3</sub> transition temperature (K) comparison by different methods. Rhombohedral (R) → Orthorhombic (O) → Tetragonal (T) → Cubic (C).

Study	R → O	O → T	T → C
This study (parameters from table 2.1.)	180	267	353
This study (parameters from SEPLIARSKY ET AL. (2005))	190	225	346
Anisotropic (see, TINTE ET AL. (1999))	80	120	180
ReaxFF (see, GODDARD III ET AL. (2002))	197	237	290
Experiment (see, LEMANOV ET AL. (1996))	183	279	393

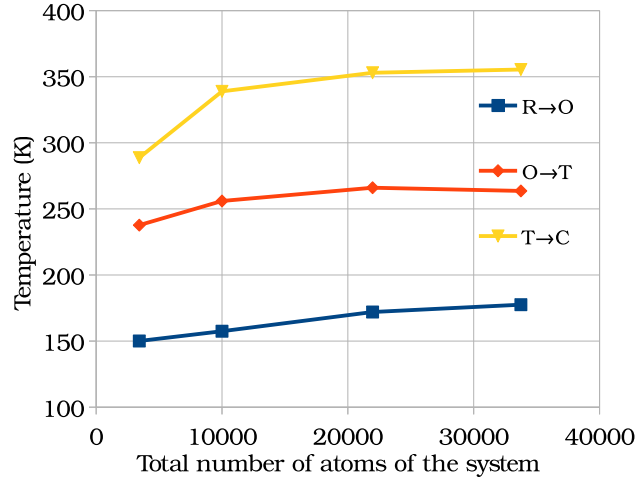


**Figure 2.3.** Size-dependent phase transition temperatures (K) of BaTiO<sub>3</sub> systems.

and O → T phase changes. A difference of 40 K is found for the transition temperature of T → C between the MD and the experiment result. Nevertheless, the present study's predictions have a better agreement with experiment values compared to other MD or DFT studies, which validates the effectiveness of the developed MD approach. As the lattice parameters vary with the temperature (shown in figure 2.2), it also alters the barycenter of all positively and all negatively charged particles, which results in a non-zero relative distance between the average center of the positively and negatively charged particles thus induces a non-zero dipole moment in the system. Additionally, for ferroelectric material, the electronic polarizability contributes to the overall polarization. The total spontaneous polarization  $P_\alpha$  in the direction  $\alpha$  is calculated with the equation (2.4) and the obtained results are shown in the figure 2.4 with respect to temperature.

Figure 2.4 presents the three components of the absolute averaged spontaneous polarization. As expected, the spontaneous polarizations show a temperature-dependent behavior, which is explained by the calculation procedure. As demonstrated by the equation (2.4), the polarization is calculated with the location of each particle and its charge. The lattice parameters dominate the location of each particle. Meanwhile, figure 2.2 clearly shown that the lattice

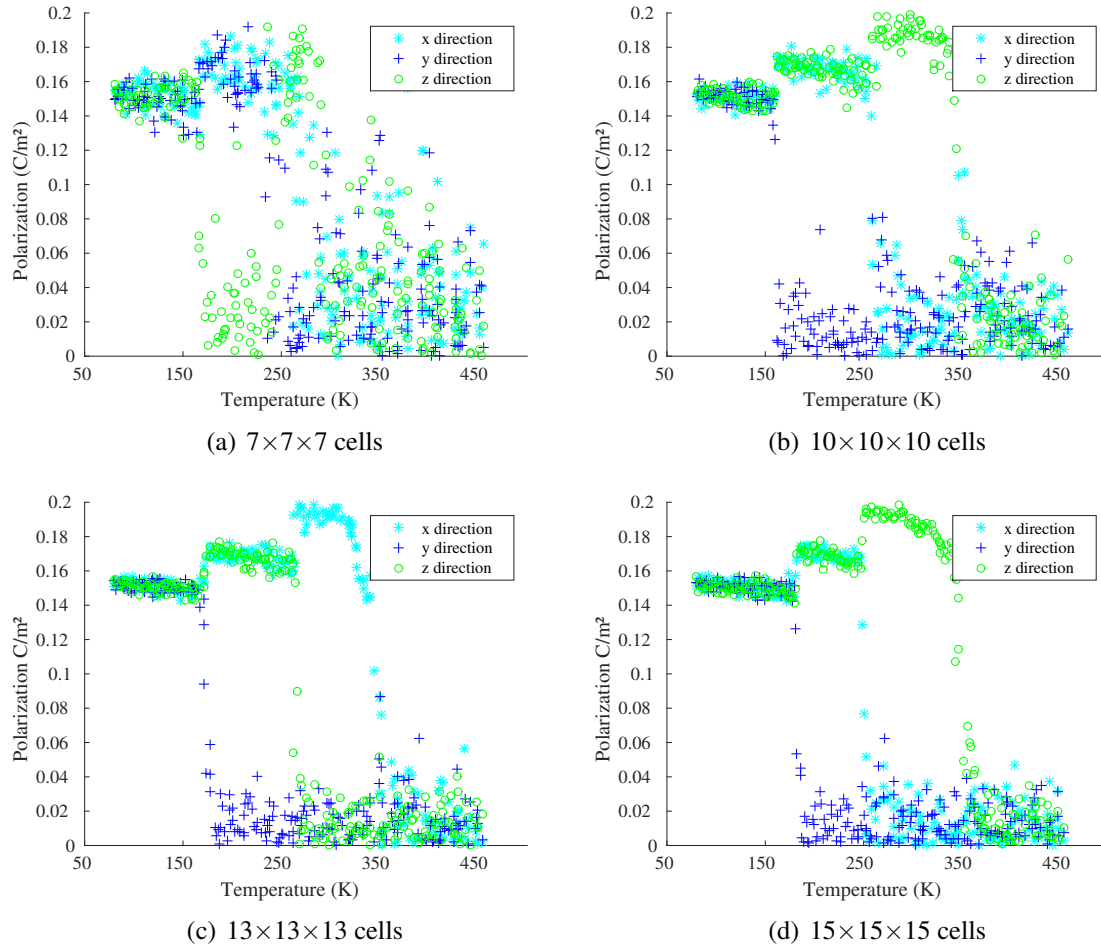


**Figure 2.4.** Temperature versus averaged absolute spontaneous polarization ( $C/m^2$ ) of different size  $BaTiO_3$  systems.

parameters are influenced by the temperature, suggesting that the system's spontaneous polarization also subjects to the temperature. The calculated absolute spontaneous polarization for phase R, O and T are 0.155, 0.176 and 0.195  $C/M^2$ , respectively. These values fall within the ranges of experimental measurements 0.13 to 0.19, 0.14 to 0.25 and 0.17 to 0.27  $C/M^2$  for R, O and T phase, respectively, see KWEI ET AL. (1993); SHIRANE & TAKEDA (1952), which further proves the effectiveness of the developed MD model. In the following section 2.3, the flexoelectric and mechanical properties of  $BaTiO_3$  are further examined by the developed MD model.



## 2.3 Flexoelectrical and mechanical properties of Barium titanate oxide

### 2.3.1 Flexoelectrical property

The induced polarization in a dielectric material (such as BaTiO<sub>3</sub>) by an inhomogeneous strain is

$$P_\alpha = d_{\alpha\beta\gamma}\varepsilon_{\beta\gamma} + \mu_{\alpha\beta\gamma\delta}\frac{\partial\varepsilon_{\beta\gamma}}{\partial x_\delta}, \quad (2.5)$$

where  $d_{\alpha\beta\gamma}$  is the piezoelectric coefficient,  $\varepsilon_{\beta\gamma}$  is the strain,  $\mu_{\alpha\beta\gamma\delta}$  is the flexoelectric coefficient and  $\frac{\partial\varepsilon_{\beta\gamma}}{\partial x_\delta}$  is the strain gradient, see YUDIN & TAGANTSEV (2013a). Indices  $\alpha, \beta, \gamma$  and  $\delta$  represent the directional components of the coordinate system. To extract the flexoelectric coefficient from the equation (2.5), one should eliminate the interference from the piezoelectric effect. Deformation schemes are developed within the developed MD model to fulfill this criterion for extracting the flexoelectric coefficient independently from the piezoelectric effect. Further details are given in the following subsections. Based on the crystal symmetry, only three flexoelectric coefficients exist for cubic perovskites, see SHU ET AL. (2011a). For isotropic materials, such as BaTiO<sub>3</sub>, these three coefficients further reduce to two coefficients (longitudinal and shear). To extract these two flexoelectric coefficients of BaTiO<sub>3</sub> with the consideration of size dependency, BaTiO<sub>3</sub> systems with  $N \times N \times 14$  unit cells are constructed,  $N \times N$  represents the total number of unit cells in the cross-section (X-Y plane). The geometrical details of the BaO-terminated unit cell are from KWEI ET AL. (1993). The values of  $N$  are 1, 3, 5, 9, 10, 12 and 16, which correspond 140, 812, 4942, 6188, 7574, 10766 and 18830 total number of atoms in the BaTiO<sub>3</sub> systems, respectively. All BaTiO<sub>3</sub> systems are set continuously periodic in the Z-direction and set free of movement in X and Y directions. Under the given boundary conditions, the atoms on the system surface have different energy state comparing to the internal atoms. It will result a surface effect that is strongly dependent on the number of exterior atoms available on the surface. By varying the cross-section size  $N \times N$ , the free surface atom ratios changes. Additionally, a fully periodic system is also constructed to simulate the bulk flexoelectric effect of BaTiO<sub>3</sub>.

#### Longitudinal flexoelectricity

To extract the longitudinal flexoelectric coefficient, a sinusoidal deformation applies to the BaTiO<sub>3</sub> systems, see HONG ET AL. (2010). The deformation function gives as

$$u^{long}(z) = \frac{\varepsilon_{max}h}{2\pi}\sin\left(\frac{2\pi z}{h}\right), \quad (2.6)$$

with  $\varepsilon_{max}$  is the given maximum strain,  $h$  is the height of the BaTiO<sub>3</sub> system in the longitudinal direction.

The corresponding strain and strain gradient in the longitudinal direction of the BaTiO<sub>3</sub> system are

$$\varepsilon_{zz}(z) = \varepsilon_{max}\cos\left(\frac{2\pi z}{h}\right) \quad \text{and} \quad \frac{\partial\varepsilon_{zz}(z)}{\partial z} = -\frac{2\pi}{h}\varepsilon_{max}\sin\left(\frac{2\pi z}{h}\right). \quad (2.7)$$

To eliminate the interference of the piezoelectric effect, the cells at position  $z = h/4$  of the BaTiO<sub>3</sub> system are selected for extracting longitudinal flexoelectric coefficient. At this position, the strain in the BaTiO<sub>3</sub> system is zero ( $\varepsilon_{zz}(z = h/4) = 0$ ) and the strain gradient is maximum. This is clearly visualized in figure 2.5. With the elimination of the piezoelectric effect at this location, the longitudinal flexoelectric coefficient ( $\mu_{zzzz}$ ) is

$$\mu_{zzzz} = \frac{P_z}{\left. \frac{\partial \varepsilon_{zz}(z)}{\partial z} \right|_{z=h/4}}, \quad (2.8)$$

where  $P_z$  is the Z direction (longitudinal direction) polarization at position  $z = h/4$ . To maintain the imposed deformation, the position of all Barium atom cores are fixed at the location according to the equation (2.6) during the relaxation and energy minimization step. After minimization, the total polarization of the selected cells (position  $z = h/4$ ) derives from the equation (2.4). The given  $\varepsilon_{max}$  varies between 0 to  $0.02 \text{ \AA}^{-1}$ . Figure 2.6(a) shows the polarization versus  $\varepsilon_{max}$  of all BaTiO<sub>3</sub> systems. It shows a linear relationship between the polarization and strain  $\varepsilon_{max}$ , which indicates a linear relationship between the polarization and strain gradient  $\frac{2\pi}{h}\varepsilon_{max}$  in the BaTiO<sub>3</sub> systems, since  $\frac{2\pi}{h}$  is a constant. The obtained polarizations are then averaged and substituted with the given strain gradient  $\frac{2\pi}{h}\varepsilon_{max}$  into the equation (2.8), the size-dependent longitudinal flexoelectric coefficients are calculated and presented in the figure 2.6(b). Clearly, the longitudinal flexoelectric coefficient shows a strong dependency on the system size. It can be explained by the ratio between the number of surface atoms and the total number of atoms in a system. The higher surface atom ratio results in more substantial atom mobility and a larger relative displacement between the positive charge center and negative charge center of the surface unit cells, which leads to a stronger polarization of the surface cells. Figure 2.7 shows the cell by cell polarization of the systems with  $N = 3, 5, 8$ , and it indicates a higher polarizations of surface cells (especially the corner cells) compared to the inner cells. It also found that the bulk longitudinal flexoelectric coefficient calculated from the MD model agrees well with the DFT calculations in MARANGANTI & SHARMA (2009); HONG ET AL. (2010), which further validates the effectiveness of the applied simulation scheme.

### Shear flexoelectricity

To extract the shear flexoelectric coefficient, a similar deformation pattern (figure 2.5(c)) is chosen

$$u^{shear}(x) = -\varepsilon_{max} \cos\left(\frac{2\pi z}{h}\right), \quad (2.9)$$

with  $\varepsilon_{max}$  is the given maximum strain.

The corresponding strain and strain gradient in the system:

$$\varepsilon_{xz}(z) = \frac{2\pi}{h}\varepsilon_{max} \sin\left(\frac{2\pi z}{h}\right) \quad \text{and} \quad \frac{\partial \varepsilon_{xz}(z)}{\partial z} = \varepsilon_{max} \left(\frac{2\pi}{h}\right)^2 \cos\left(\frac{2\pi z}{h}\right). \quad (2.10)$$

As demonstrated by the figure 2.5(d), the strain is zero at the location of  $z = h/2$ , which eliminates the piezoelectric effect and the flexoelectric effect is maximum. The calculation

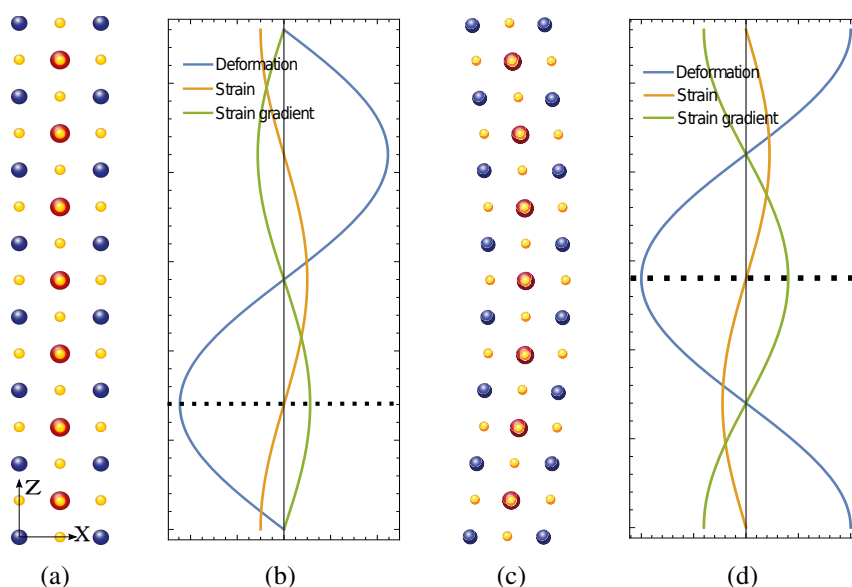


**Figure 2.5.** Schematic illustration of (a) deformed supercell structure according to the equation (2.6); (b) Deformation (equation (2.6)), strain and strain gradient (equation (2.7)) profile,  $h/4$  position indicated by the dash line; (c) deformed supercell structure according to the equation (2.9); (d) Deformation (equation (2.9)), strain and strain gradient (equation (2.10)) profile,  $h/2$  position indicated by the dash line.

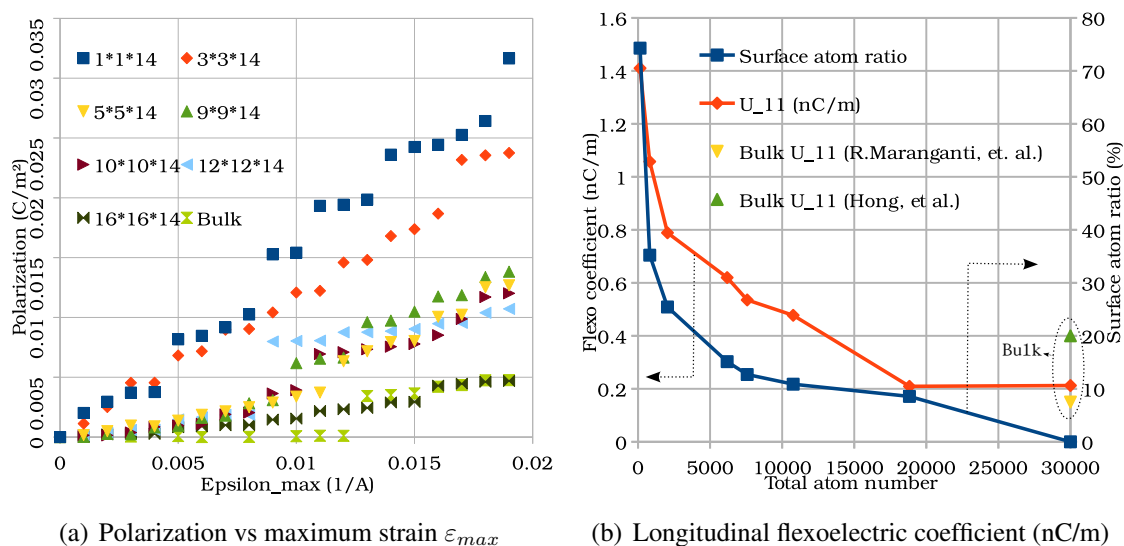


**Figure 2.6.** Plot of (a) polarization vs applied maximum strain  $\epsilon_{max}$  (b) size-dependent longitudinal flexoelectric coefficient. The bulk flexoelectric coefficients are from systems with total atom number equals 30000, the yellow and green triangle shows the DFT calculation result of MARANGANTI & SHARMA (2009) (0.15 nC/m) and HONG ET AL. (2010) (0.36 nC/m), respectively. The MD calculated bulk longitudinal flexoelectric coefficient is 0.201 nC/m.

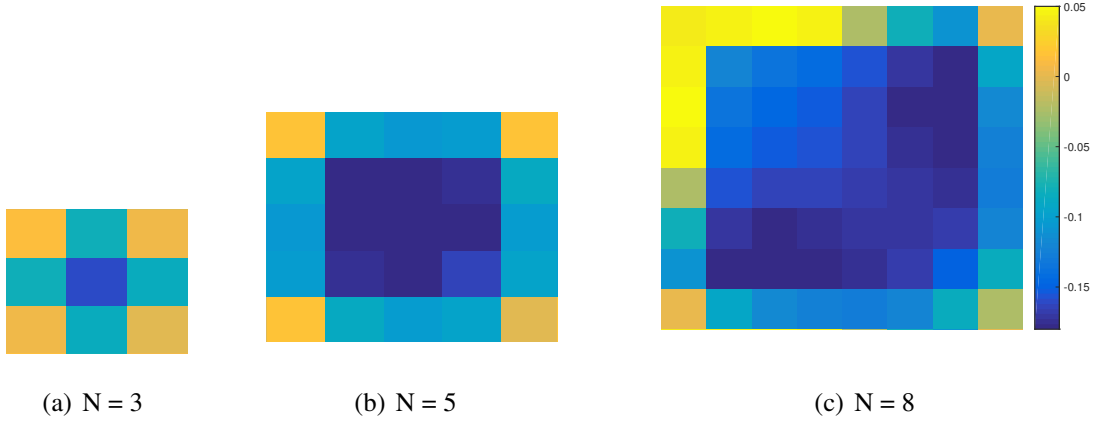


**Figure 2.7.** Cell by cell (at  $z = h/4$  section) polarization (calculated by the equation (2.8)) of different system sizes demonstrate the surface cells have higher polarization compare to the inner cells due to the higher mobility of surface atoms.

of the shear flexoelectric coefficient follows

$$\mu_{xzxz} = \frac{P_x}{\left. \frac{\partial \varepsilon_{xz}(z)}{\partial z} \right|_{z=h/2}}. \quad (2.11)$$

The identical approach applied for extracting the longitudinal flexoelectric coefficient has been employed to calculate the shear flexoelectric coefficient. Figure 2.8(a) shows a linear relationship between the polarization and the adopted  $\varepsilon_{max}$ , which indicates a linear relationship between the polarization and strain gradient  $\varepsilon_{max} \left(\frac{2\pi}{h}\right)^2$ , since  $\left(\frac{2\pi}{h}\right)^2$  is a constant. The size-dependent shear flexoelectric coefficient is shown in the figure 2.8. Contrast to the longitudinal flexoelectric coefficient (figure 2.6(b)), the shear flexoelectric coefficient increases with the cross-section size and converges to the bulk shear flexoelectric coefficient, see XU ET AL. (2013). The explanation of this behavior: in contrast to the calculation of the longitudinal flexoelectric coefficient (the Z-direction polarization  $P_z$  is required by equation (2.8)), the calculation of the shear flexoelectric coefficient requires the polarization  $P_x$  of X-direction by equation (2.11). Due to the applied vacuum boundary condition in the X and Y directions, the atoms have more freedom of movement in the X-direction compared to the Z-direction (periodic boundary condition applied). During minimization, for system with a smaller cross-section (in the X-Y plane), the surface atoms in the system can easily find a lower energy state in the transverse (X-Y) directions, which returns a lower transverse polarization of the surface cells. As the cross-section of the system increases, the transverse inter-atomic force strengthens, which forces the surface atoms to stay in a higher energy state, hence a higher transverse polarization ( $P_x$ ) of the surface unit cells.

### 2.3.2 Mechanical property

This subsection investigates the influence of the surface effect on the mechanical property of BaTiO<sub>3</sub>. For this propose, BaTiO<sub>3</sub> nanostructure (see figure 2.9(a)) with size of  $N \times N \times 35$

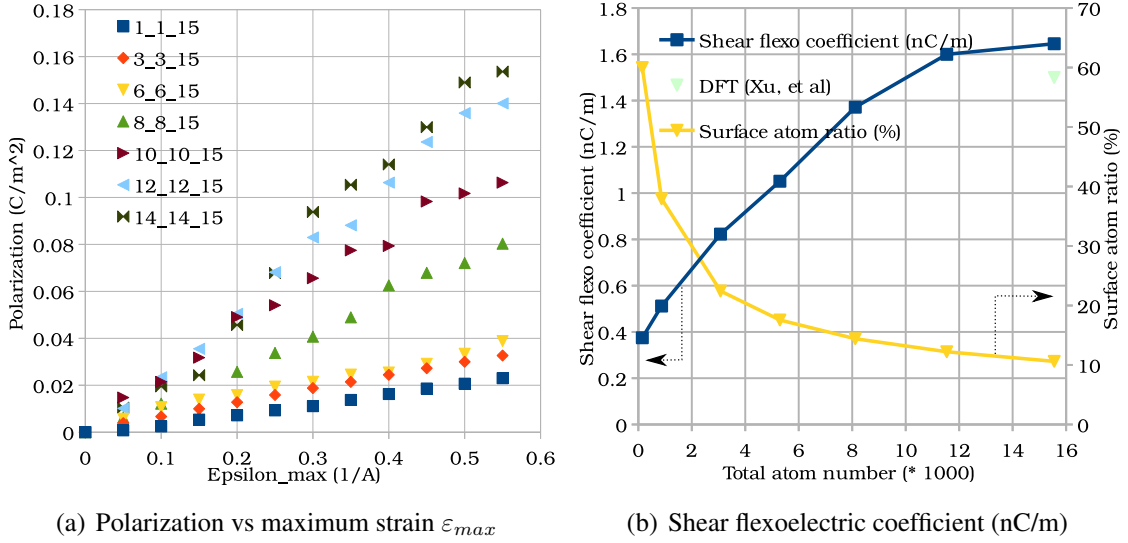


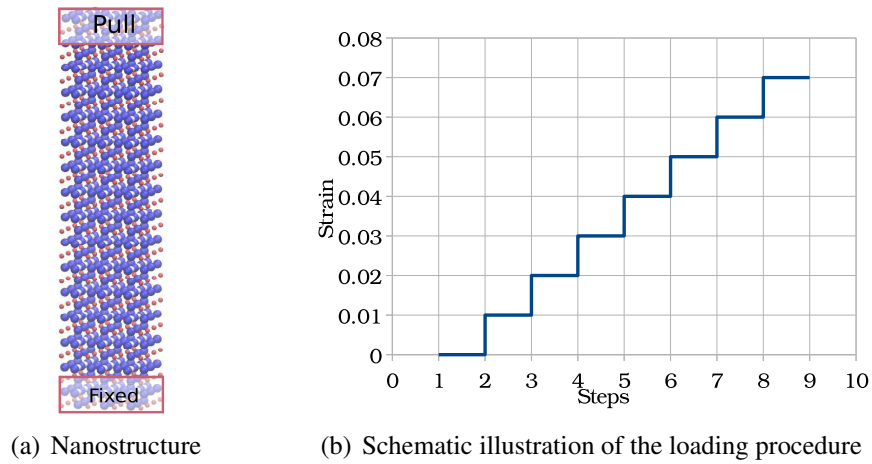
**Figure 2.8.** Plot of (a) polarization vs applied strain  $\varepsilon_{max}$  (b) size-dependent shear flexoelectric coefficient. The bulk flexoelectric coefficient indicated by the light green triangle shows the DFT calculation result (1.5 nC/m) of XU ET AL. (2013).

unit cells are constructed. The  $N \times N$  represents the total number of unit cells of the cross-section in the X-Y plane. The value of  $N$  ranges from 3, 4, 6, 8, 12 to 16, which yields different surface atom ratios of the BaTiO<sub>3</sub> systems. The BaTiO<sub>3</sub> unit cell is a BaO-terminated cubic cell, the lattice length of the unit cell is 4.01 Å. For each BaTiO<sub>3</sub> system, it initially equilibrates at 415 K for 10 ps with traction free boundary condition. Hereafter, the quasi-static tensile load applies to the system in two steps: first a ramped displacement applies to the top boundary atoms and follows by the energy minimization and equilibration procedures of the entire structure. Loop these two steps until the desired strain is achieved (schematic illustration of the loading procedure see figure 2.9(b)). At each loading step, the resulted stress is calculated from the equation (2.12) as suggested in ZHOU (2003). During the simulation, vacuum boundary condition applies in the transverse directions (X-Y plane), and the bottom atoms remain fixed.

$$\sigma_{\alpha\beta} = \frac{1}{\Omega} \left[ \frac{1}{2} \sum_i \sum_{ij} f_{ij}^{\alpha} r_{ij}^{\beta} - \sum_i m_i \bar{v}_i^{\alpha} \bar{v}_i^{\beta} \right], \quad (2.12)$$

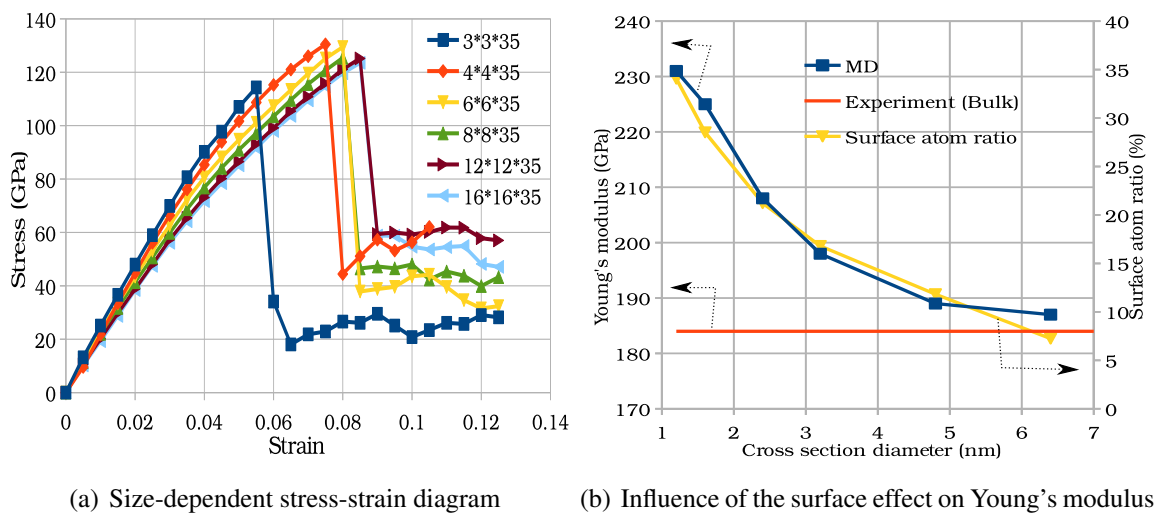
where  $\Omega$  is the system volume,  $m_i$  is the mass of the  $i^{\text{th}}$  particle,  $\bar{v}_i^{\alpha}$  is the velocity of the  $i^{\text{th}}$  particle in  $\alpha$  direction,  $f_{ij}$  is the inter-particle force between particle  $i$  and  $j$ .

Figure 2.10 presents the size-dependent stress-strain diagram for the BaTiO<sub>3</sub> systems and the comparison of their Young's modulus with the experimental result. The Young's modulus calculates from the tangent of the stress-strain diagrams. As shown in figure 2.10(b), the derived Young's modulus of BaTiO<sub>3</sub> systems strongly correlate to the surface atom ratio. It is explained by the different mobility between the surface and inner atoms. The surface atoms are less constrained compare to the inner atoms. A higher surface atom ratio results



**Figure 2.9.** Schematic illustration of (a) BaTiO<sub>3</sub> nanostructure and (b) loading procedure for extracting Young’s modulus of BaTiO<sub>3</sub> nanostructure.

in higher surface energy, thus higher stress. This enhanced stress contribution from the surface atoms leads to an overall enhancement of the Young’s modulus. It is also found that the surface effect diminishes, when the BaTiO<sub>3</sub> system has a transverse diameter larger than 6.4 nm, which agrees with the reported value, see SHAHRAKI ET AL. (2014), and the Young’s modulus of BaTiO<sub>3</sub> nanostructures converge to an experimental result shown in CHENG ET AL. (1996).



**Figure 2.10.** Illustration of (a) size-dependent stress-strain diagram and (b) influence of the surface effect on Young’s modulus of BaTiO<sub>3</sub> nanostructures.

## 2.4 Conclusion

This chapter presented a core-shell molecular dynamics model to study the size-dependent behavior of flexoelectricity in  $\text{BaTiO}_3$  nanostructures. The core-shell model reproduced the phase transition of  $\text{BaTiO}_3$  validating its correctness. Specially designed deformation patterns apply to the  $\text{BaTiO}_3$  nanostructures inducing flexoelectric effect without the interference of the piezoelectric effect enabling direct estimation of the flexoelectric coefficients of the  $\text{BaTiO}_3$  nanostructures. The results show that the surface effect significantly influences the longitudinal and shear flexoelectric coefficient of the  $\text{BaTiO}_3$  nanostructures. Namely, the longitudinal flexoelectric coefficients decrease with the surface atom ratios of the  $\text{BaTiO}_3$  nanostructures, while the shear flexoelectric coefficients show an opposite trend. The following chapter studies flexoelectricity in the newly emerged 2D materials.

## Chapter 3

# Flexoelectricity in two-dimensional materials

Atomically thin two-dimensional (2D) materials have a variety of unique physical properties that made them attractive for many different applications (sensor, actuator, energy harvester), see POP ET AL. (2012); GHOSH ET AL. (2010); FEI & YANG (2014); YU ET AL. (2017); WANG ET AL. (2012); HANAKATA ET AL. (2016); ANDREW ET AL. (2012); JAVVAJI ET AL. (2016); KIM ET AL. (2015); SUN ET AL. (2016); MAS-BALLESTÉ ET AL. (2011). An emerging area of interest for 2D materials is the electromechanical coupling due to the desire to miniaturize sensors and actuators to the micro and nanoscales. The most widely studied electromechanical coupling mechanism is piezoelectricity, which has also investigated for 2D materials, including graphene, hexagonal boron nitride (h-BN), transition metal dichalcogenides (TMDCs), and many others, see WANG ET AL. (2015); SONG ET AL. (2017); ZHENG ET AL. (2017); ZELISKO ET AL. (2014); BLONSKY ET AL. (2015); KUNDALWAL ET AL. (2017); CHANDRATRE & SHARMA (2012); DUERLOO & REED (2013); ZHANG (2017); ZHOU ET AL. (2016); JAVVAJI ET AL. (2018); WU ET AL. (2014a); DUERLOO ET AL. (2012). The majority of these works have focused on the in-plane electromechanical properties.

In contrast to the extensive studies on piezoelectricity in 2D materials, only a few preliminary studies on flexoelectricity in 2D materials have recently been carried out using the density functional theory (DFT) calculation, see KALININ & MEUNIER (2008), theoretical analyses, see KVASHNIN ET AL. (2015); CHANDRATRE & SHARMA (2012); KUNDALWAL ET AL. (2017) or experiment, see BRENNAN ET AL. (2017). However, one key issue in calculating or measuring the flexoelectric coefficients of 2D materials is that it has been difficult to isolate the relative contributions of piezoelectricity and flexoelectricity to the resulting polarization, see BRENNAN ET AL. (2017). As a result, the intrinsic flexoelectric properties of 2D materials remain unresolved, and the mechanisms controlling the intrinsic flexoelectric properties of different 2D materials are also unresolved. In this chapter, a charge-dipole (CD) molecular dynamics model is developed to calculate the intrinsic bend-

---

The content of this chapter is partially published in author's paper (DOI: 10.1103/PhysRevB.99.054105; 10.1103/PhysRevMaterials.3.125402)



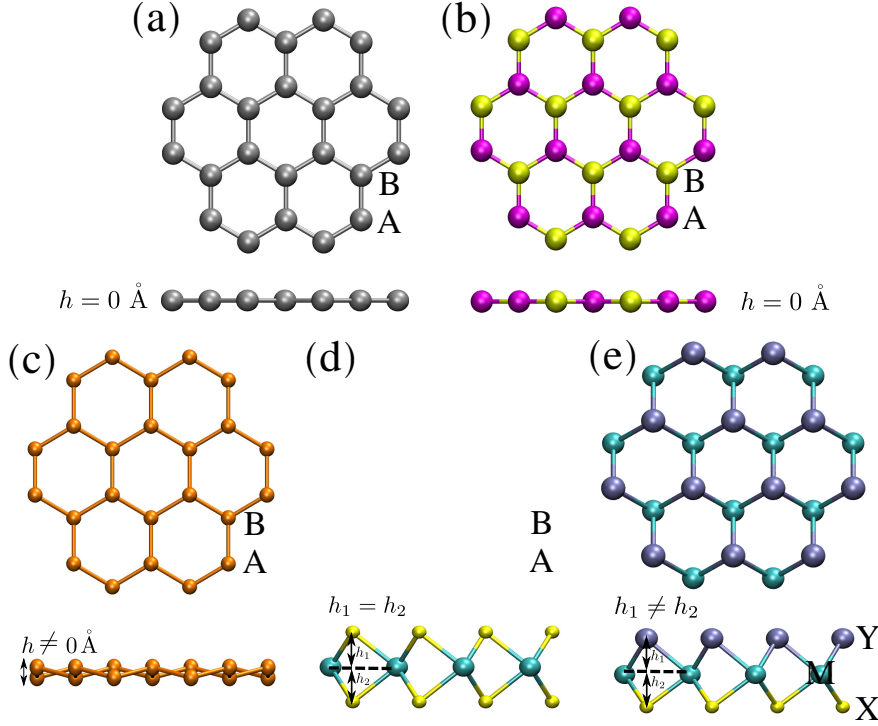


**Figure 3.1.** Top and side view of the studied materials: (a) Graphene allotropes AB, A = B = Carbon; (b) Nitrides AB, A = Nitrogen, B = Boron, Aluminium or Gallium; (c) graphene analogues of group-IV elements AB, A = B = Silicon, Germanium, Tin; (d) transition metal dichalcogenides  $AB_2$ , A = Molybdenum, Tungsten or Chromium, B = Sulfur; (e) Janus transition metal dichalcogenides MXY, M = Molybdenum or Tungsten; X = Sulfur or Selenium, Y = Selenium or Tellurium. For (a)-(c),  $h$  refers to the buckling height, while in (d)-(e)  $h_1$  and  $h_2$  refer to intralayer distances.

ing flexoelectric coefficients of the five different 2D material groups shown in figure 3.1: graphene allotropes (C1, C2, C3), nitrides (BN, AlN, GaN), graphene analogues of group-IV elements (Si, Ge, Sn), transition metal dichalcogenides (TMDCs) ( $MoS_2$ ,  $WS_2$ ,  $CrS_2$ ) and Janus TMDCs ( $MoSSe$ ,  $MoSTe$ ,  $MoSeTe$ ,  $WSSe$ ,  $WSTe$ ,  $WSeTe$ ). The calculation method, procedure and result are presented in the following sections 3.1 to 3.3.

## 3.1 Charge-dipole model

### 3.1.1 Charge-dipole formulation

The charge-dipole potential model was first proposed in OLSON & SUNDBERG (1978). It assumes that atom  $i$  in a system associates with a net point charge  $q_i$  and a dipole moment  $\mathbf{p}_i$ . And it further develops to overcome the numerical divergence under point charge approximation, see MAYER (2007, 2005). Following the work of MAYER (2007, 2005), the total electrostatic energy ( $E^{CD}$ ) for a  $N$  atoms system is

$$E^{CD} = E^{\text{short-range}} + E^{q-q} + E^{q-p} + E^{p-p} + E^{\text{ext}}, \quad (3.1)$$

where  $E^{\text{short-range}}$  represents the short range potential; the charge-to-charge ( $E^{q-q}$ ), charge-to-dipole ( $E^{q-p}$ ) and dipole-to-dipole ( $E^{p-p}$ ) potential functions complete the long range interactions. Along with internal interactions, there may exist an external energy, which represents as  $E^{\text{ext}}$ .  $E^{q-q}$  consists of (i) energy required to create a charge  $q_i$  on atom  $i$  in position  $\mathbf{r}_i$  with an assumption that other atoms are at infinite distance, (ii) energy required to bring atom  $i$  in the neighborhood of other atoms and (iii) energy contribution that accounts the interaction between its nucleus and electrons (electron affinity).  $E^{q-q}$  expresses as

$$E^{q-q} = \frac{1}{2} \sum_{i=1}^N q_i T_{ii}^{q-q} q_i + \frac{1}{2} \sum_{i=1}^N \sum_{j=1, i \neq j}^N q_i T_{ij}^{q-q} q_j + \sum_{i=1}^N q_i \chi_i, \quad (3.2)$$

where  $q_i$  is the net charge on atom  $i$ ,  $T^{q-q}$  is the charge-charge interaction coefficient.  $\chi_i$  is the electron affinity of atom  $i$ .  $E^{q-p}$  is the interaction between the dipole of each atom and charge associated with each other atom, including the self-interactions, which is

$$E^{q-p} = - \sum_{i=1}^N q_i \mathbf{T}_{ii}^{q-p} \mathbf{p}_i - \sum_{i=1}^N \sum_{j=1, i \neq j}^N q_i \mathbf{T}_{ij}^{q-p} \mathbf{p}_j, \quad (3.3)$$

where  $\mathbf{T}^{q-p}$  defines as the negative spatial gradient over  $T^{q-q}$  ( $\mathbf{T}_{ij}^{q-p} = -\nabla T_{ij}^{q-q}$ ). The product  $\mathbf{T}_{ij}^{q-p} \mathbf{p}_j$  is the electric potential produced at location  $\mathbf{r}_i$  by dipole  $\mathbf{p}_j$ . The energy for dipole-to-dipole interaction consists of self interaction and interactions with other dipoles.  $E^{p-p}$  expresses as

$$E^{p-p} = -\frac{1}{2} \sum_{i=1}^N \mathbf{p}_i \mathbf{T}_{ii}^{p-p} \mathbf{p}_i - \frac{1}{2} \sum_{i=1}^N \sum_{j=1, i \neq j}^N \mathbf{p}_i \mathbf{T}_{ij}^{p-p} \mathbf{p}_j, \quad (3.4)$$

where  $\mathbf{T}_{ij}^{p-p} = -\nabla \otimes \nabla T_{ij}^{q-q}$ . Product of  $\mathbf{T}_{ij}^{p-p}$  and  $\mathbf{p}_j$  is the electric field induced by the dipole  $j$  on dipole  $i$ .

$T_{ij}^{q-q}$  is the Coulombic interaction between atomic charges  $q_i$  and  $q_j$  separated by a distance  $r_{ij}$ , which is

$$T_{ij}^{q-q} = \frac{1}{4\pi\epsilon_0} \frac{1}{r_{ij}}, \quad (3.5)$$

where  $\epsilon_0$  is the dielectric permittivity of vacuum. From the equation (3.5),  $T^{q-q}$  involves the  $1/r_{ij}$  term, which diverges for a point charge approximation when  $r_{ij}$  tends to zero. In order to overcome this,  $r_{ij}$  is normalized with  $\text{erf}(r_{ij}/(\sqrt{2}R))$ .  $T_{ij}^{q-q}$  modifies as

$$T_{ij}^{q-q} = \frac{1}{4\pi\epsilon_0} \frac{\text{erf}\left(\frac{r_{ij}}{\sqrt{2}R}\right)}{r_{ij}}, \quad (3.6)$$

where  $R$  is equal to  $\sqrt{R_{A,i}^2 + R_{B,j}^2}/\sqrt{2}$ , where  $R_{A,i}$  represents the width of Gaussian distribution for atom index  $i$  with type  $A$ .  $R_{B,j}$  represents the Gaussian distributed charge width for atom type  $B$  and with index  $j$ . When  $r$  tends to zero (energy term belongs to the same

atom), neglecting the higher order terms in the expansion of the error function, the equation (3.6) reduces to

$$T_{ii}^{q-q} = \frac{1}{4\pi\epsilon_0} \sqrt{\frac{2}{\pi}} \frac{1}{R}. \quad (3.7)$$

The normalization approximates the interaction between two point charges as an interaction between two Gaussian distributed charges. It is identical to the electrostatic interactions between the electronic clouds of any two atoms. For a detailed mathematical understanding of  $T^{q-p}$ ,  $T^{p-p}$  and charge-dipole potential, the reader is referred to MAYER (2005, 2007), and references therein.

With the interatomic potential, the equation of motion for atom  $i$  derives from the Lagrangian approach. The equation of motion for atom  $i$  is

$$m_i \ddot{\mathbf{r}}_i = - \frac{\partial E^{\text{short-range}}}{\partial \mathbf{r}_i} - \frac{\partial E^{q-q}}{\partial \mathbf{r}_i} - \frac{\partial E^{q-p}}{\partial \mathbf{r}_i} - \frac{\partial E^{p-p}}{\partial \mathbf{r}_i}, \quad (3.8)$$

where the first-order derivatives of the short-range term were derived and implemented in recent versions of the open-source MD code called Large scale Atomic/Molecular Massively Parallel Simulator (LAMMPS), see PLIMPTON (1995b). The charge and dipole related force contributions are derived and incorporated as additional forces to the atoms. The present study utilizes the ‘addforce’ command in the LAMMPS package to include the additional force. The mathematical expressions for the potential energy derivatives are presented in Appendix A.

The charge and dipole moment of each atom estimated from the governing equations obtained in the Lagrangian approach. The governing equation for the atomic charge  $q_i$  is

$$\sum_{j=1, i \neq j}^N T_{ij}^{q-q} q_j - \sum_{j=1, i \neq j}^N \mathbf{T}_{ij}^{q-p} \mathbf{p}_j + T_{ii}^{q-q} q_i - \mathbf{T}_{ii}^{q-p} \mathbf{p}_i + \chi_i = 0. \quad (3.9)$$

The governing equation for the atomic dipole moment  $\mathbf{p}_i$  is

$$\sum_{j=1, i \neq j}^N \mathbf{T}_{ij}^{q-p} q_j + \sum_{j=1, i \neq j}^N \mathbf{T}_{ij}^{p-p} \mathbf{p}_j + \mathbf{T}_{ii}^{q-p} q_i + \mathbf{T}_{ii}^{p-p} \mathbf{p}_i = 0. \quad (3.10)$$

Equation (3.8) defines each atom’s dynamics under various forces that originated from the interatomic potential. The unknown charge and dipole moment of each atom obtained by solving the equation (3.9) and (3.10). Rearranging these equations into a matrix-vector form

$$\begin{bmatrix} T^{q-q} & T^{q-p} \\ T^{q-p} & T^{p-p} \end{bmatrix} \begin{bmatrix} q \\ \mathbf{p} \end{bmatrix} = \begin{bmatrix} -\chi \\ 0 \end{bmatrix}. \quad (3.11)$$

From the equation (3.11), the charge and dipole moment are known for the given atomic configuration. Using the charge and dipole moment data, force terms  $\frac{\partial E^{q-q}}{\partial \mathbf{r}_i}$ ,  $\frac{\partial E^{q-p}}{\partial \mathbf{r}_i}$  and  $\frac{\partial E^{p-p}}{\partial \mathbf{r}_i}$  in the equation (3.8) are calculated using the expressions given in the Appendix A. Equation (3.8) is time integrated using the Velocity-Verlet algorithm, see SWOPE ET AL. (1982). The time integration of the equation (3.8) updates the atomic configuration at one time instant, and for

the updated configuration the charge-dipole matrix-vector system is solved. For the atomic configuration at time instant  $t$ , the charge and dipole moment data of time step  $t - \Delta t$  is used.  $\Delta t$  represent the time interval between two successive time instances.

Based on the known dipole moment of each atom, the polarization for the unit cell is defined as the sum of dipole moments of atoms present in that unit cell divided by the unit cell volume. The polarization of the  $m^{\text{th}}$  unit cell ( $\mathbf{P}_m$ ) is

$$\mathbf{P}_m = \frac{1}{V_m} \left( \sum_{i=1}^n \mathbf{p}_i \right), \quad (3.12)$$

where  $n$  is the number of basis atoms present in unit cell  $m$ ,  $V_m$  is the unit cell volume, and the total polarization is the average among all unit cells in the system.

### 3.1.2 Estimation of charge-dipole potential parameter $R$

In the previous subsection 3.1.1, a parameter  $R$  is introduced to avoid the divergence of the equation (3.6). The estimation procedure of  $R$  as following

Consider the equation (3.10) for dipole moments, which rewrites as

$$\mathbf{T}_{ii}^{\text{p-p}} \mathbf{p}_i - \sum_{j, i \neq j}^N \mathbf{T}_{ij}^{\text{p-p}} \mathbf{p}_j = \sum_{j, i \neq j}^N \mathbf{T}_{ij}^{\text{q-p}} q_j + \mathbf{E}^{\text{ext}}(\mathbf{r}_i). \quad (3.13)$$

This represents that the dipole moment of an atom are defined by three different parts: electric field at position  $\mathbf{r}_i$  due to neighboring (i) dipoles  $\mathbf{p}_j$  (left hand side second term in the equation (3.13)); (ii) charges  $q_j$  (right hand side first term in equation (3.13)) and (iii) from the externally applied electric fields. The diagonal coefficient  $\mathbf{T}_{ii}^{\text{p-p}}$  is known as the inverse of atomic polarizability ( $\bar{\alpha}$ ). The mathematical expression for  $\mathbf{T}_{ii}^{\text{p-p}}$  is given under the CD potential approximations, see MAYER (2007, 2005):

$$\mathbf{T}_{ii}^{\text{p-p}} = \frac{1}{4\pi\epsilon_0} \frac{\sqrt{2}}{3\sqrt{\pi}R^3} = \frac{1}{\bar{\alpha}_i}, \quad (3.14)$$

where  $\epsilon_0$  is the dielectric permittivity of vacuum. The CD parameter  $R$  is related to the polarizability  $\bar{\alpha}$ . For an  $N$  atoms system, the equation (3.13) modifies into a matrix-vector system, which is

$$\bar{\mathbf{A}} \mathbf{p} = \mathbf{E}, \quad (3.15)$$

where

$$\bar{\mathbf{A}} = \begin{bmatrix} \bar{\alpha}_1^{-1} & \mathbf{T}_{12}^{\text{p-p}} & \cdots & \mathbf{T}_{1N}^{\text{p-p}} \\ \mathbf{T}_{21}^{\text{p-p}} & \bar{\alpha}_2^{-1} & \cdots & \mathbf{T}_{2N}^{\text{p-p}} \\ \cdot & \cdot & \cdots & \cdot \\ \mathbf{T}_{N1}^{\text{p-p}} & \mathbf{T}_{N2}^{\text{p-p}} & \cdots & \bar{\alpha}_N^{-1} \end{bmatrix}, \quad (3.16)$$

and  $\mathbf{p}$ ,  $\mathbf{E}$  represent the vector of dipole moments and the associated external electric field of each atom, respectively. In order to estimate the atom polarizability  $\bar{\alpha}$  thus the parameter  $R$ ,

one assumes that the dipoles are experiencing a uniform electric field ( $\mathbf{E}$ ) (which includes both external fields and charge related fields), see SILBERSTEIN (1917); THOLE (1981). Additionally, the total dipole moment ( $\mathbf{p}_{\text{total}}$ ) of the atomic system is

$$\mathbf{p}_{\text{total}} = \bar{\alpha}_{\text{total}} \mathbf{E}, \quad (3.17)$$

where  $\bar{\alpha}_{\text{total}}$  is the total polarizability of the atomic system, which expresses as

$$\bar{\alpha}_{\text{total}} = \sum_i^N \sum_j^N B_{ij}, \quad (3.18)$$

where  $B_{ij}$  is the components of the matrix  $\mathbf{A}^{-1}$ . Equation (3.18) represents that, in order to estimate  $R$ ,  $\bar{\alpha}_{\text{total}}$  has to be known. The total polarizability  $\bar{\alpha}_{\text{total}}$  is calculated from the changes in electronic wave functions in DFT. We used the function *polar* in Gaussian software, developed in FRISCH ET AL. (2016), to estimate  $\bar{\alpha}_{\text{total}}$ , where details about computing polarizability in DFT calculations elaborated in OLSEN & JØRGENSEN (1985); SEKINO & BARTLETT (1986).

To estimate the  $R$  values for all 2D material systems: graphene allotropes, nitrides, graphene analogues of group-IV elements, transition metal dichalcogenides (TMDCs) and Janus TMDCs, DFT simulations are performed for different sized samples of each material system. The isotropic polarizability values from DFT ( $\bar{\alpha}_{\text{total}}^{DFT}$ ) for these systems are noted. With the given atomic configuration of each sample and a variational range of  $R$  (less than the given bond length), the total polarizability is calculated ( $\bar{\alpha}_{\text{total}}^{CAL}$ ) from the equation (3.18). The  $R$  values are estimated, when  $\bar{\alpha}_{\text{total}}^{CAL} = \bar{\alpha}_{\text{total}}^{DFT}$  for different sized samples and these  $R$  values are averaged as the overall  $R$  value for a given material system. The calculated total polarizability ( $\bar{\alpha}_{\text{total}}^{DFT}$ ) from DFT, the estimated ( $\bar{\alpha}_{\text{total}}^{CAL}$ ) from the equation (3.18), the parameter  $R$  and lattice parameters of each material system are tabulated in the table 3.1 and table 3.2.

### 3.1.3 Validation of the charge-dipole model

In this section, the CD model and the derived material parameters in the section 3.1.2 are validated by calculating the piezoelectric coefficients of BN, MoS<sub>2</sub> and Janus TMDCs and comparing them with the results in literature, see DROTH ET AL. (2016); BLONSKY ET AL. (2015); DONG ET AL. (2017). The piezoelectric coefficients of these materials are estimated by subjecting the material samples with dimensions 80 Å × 80 Å to a tensile loading in the X-direction as shown in the figure 3.2. The lattice parameters of these materials are listed in the table 3.1 and table 3.2. The initial configurations are flat for all material samples, hereafter the samples are subjected to a relaxation process through energy minimization to stabilize material structures. For BN and MoS<sub>2</sub>, the samples remain flat (see figure 3.2(a)), whereas the structures of Janus TMDCs are bent (see figure 3.2(b)), which is due to the spontaneous curling effect, see XIONG ET AL. (2018); WANG ET AL. (2018a). This spontaneous curling effect arises from the structural asymmetry between the M-X and M-Y layers, resulting in stretching in the Y layer and compression in the X layer. The minimized samples then subject to tensile load and the samples are deformed until the desired in-plane strain  $\varepsilon_{xx}$  is achieved. During this loading procedure, the atomic charge  $q_i$  and dipole moments  $\mathbf{p}_i$

**Table 3.1.** Calculation details for each material. The unit cell dimensions  $a, b, c$  and  $h$  are given in Å. The bonding interactions are modeled using different types of 'short-range potentials'.  $\alpha_{\text{total}}^{\text{DFT}}$  is the polarizability estimates from DFT and  $\alpha_{\text{total}}^{\text{CAL}}$  is calculated using the equation (3.18) in Å<sup>3</sup>. The  $R_A$  and  $R_B$  (in Å units) are the CD potential parameters for atom types  $A$  and  $B$  in the given unit cell.

Material	a	b	c	h	short-range potential	$\alpha_{\text{total}}^{\text{DFT}}$	$\alpha_{\text{total}}^{\text{CAL}}$	$R_A$	$R_B$
C1	2.46 <sup>a</sup>	4.26 <sup>a</sup>	3.5 <sup>b</sup>	0.0	AIREBO <sup>c</sup>	2.49	2.78	0.64	0.64
C2	4.87 <sup>a</sup>	8.84 <sup>a</sup>	3.5	0.0	AIREBO <sup>c</sup>	2.46	2.72	0.64	0.64
C3	5.70 <sup>a</sup>	7.56 <sup>a</sup>	3.5	0.0	AIREBO <sup>c</sup>	2.45	2.77	0.64	0.64
BN	2.50 <sup>d</sup>	2.50 <sup>d</sup>	3.33 <sup>d</sup>	0.0	Tersoff <sup>e</sup>	2.85	2.84	0.76	0.35
AlN	3.13 <sup>f</sup>	3.13 <sup>f</sup>	3.39 <sup>f</sup>	0.0	Tersoff <sup>f</sup>	19.79	19.97	1.04	0.48
GaN	3.21 <sup>g</sup>	3.21 <sup>g</sup>	3.63 <sup>g</sup>	0.0	Tersoff <sup>h</sup>	15.80	16.38	1.05	0.48
Si	3.82 <sup>i</sup>	6.62 <sup>i</sup>	2.41 <sup>j</sup>	0.44 <sup>i</sup>	Tersoff <sup>k</sup>	20.62	20.92	1.37	1.37
Ge	3.97 <sup>i</sup>	6.87 <sup>i</sup>	3.20 <sup>l</sup>	0.65 <sup>i</sup>	Tersoff <sup>m</sup>	13.43	13.14	1.27	1.27
Sn	4.67 <sup>n</sup>	8.09 <sup>n</sup>	3.30 <sup>o</sup>	0.89 <sup>n</sup>	Tersoff <sup>o</sup>	15.25	15.86	1.52	1.52
MoS <sub>2</sub>	3.16 <sup>p</sup>	3.16 <sup>p</sup>	12.29 <sup>q</sup>	1.58	SW <sup>r</sup>	12.32	12.35	0.69	1.04
WS <sub>2</sub>	3.18 <sup>s</sup>	3.18 <sup>s</sup>	12.16 <sup>s</sup>	1.56	SW <sup>t</sup>	15.36	15.38	0.70	1.09
CrS <sub>2</sub>	3.04 <sup>q</sup>	3.04 <sup>q</sup>	14.41 <sup>q</sup>	1.45	SW <sup>t</sup>	10.86	10.87	0.75	1.00

<sup>a</sup>Reference ENYASHIN & IVANOVSKII (2011)

<sup>b</sup>Reference ISHIGAMI ET AL. (2007)

<sup>c</sup>Reference BRENNER ET AL. (2002)

<sup>d</sup>Reference VERMA ET AL. (2007)

<sup>e</sup>Reference ABADI ET AL. (2018)

<sup>f</sup>Reference ZHAO ET AL. (2016)

<sup>g</sup>Reference ONEN ET AL. (2016)

<sup>h</sup>Reference NORD ET AL. (2003)

<sup>i</sup>Reference DIMOULAS (2015)

<sup>j</sup>Reference PADILHA & PONTES (2015)

<sup>k</sup>Reference STILLINGER & WEBER (1985)

<sup>l</sup>Reference DÁVILA & LE LAY (2016)

<sup>m</sup>Reference MAHDIZADEH & AKHLAMADI (2017)

<sup>n</sup>Reference CHEN ET AL. (2016)

<sup>o</sup>Reference SAXENA ET AL. (2016)

<sup>p</sup>Reference STEWART & SPEAROT (2013)

<sup>q</sup>Reference JIANG ET AL. (2016)

<sup>r</sup>Reference JIANG ET AL. (2013a)

<sup>s</sup>Reference WANG ET AL. (2018b)

<sup>t</sup>Reference JIANG & ZHOU (2017)

**Table 3.2.** Total polarizability estimated by DFT ( $\alpha_{\text{DFT}}$  in  $\text{\AA}^3$ ) and the estimation from the present CD model ( $\alpha_{\text{Cal}}$  in  $\text{\AA}^3$ ), see ZHUANG ET AL. (2019a). Atomic polarizability ( $R_i$  in  $\text{\AA}$ ) and lattice parameters (a,b are the lattice constants,  $l_1$  and  $l_2$  are the bond lengths for M-X and M-Y in  $\text{\AA}$ , respectively) for the Janus TMDCs. For simplicity, in this study the Janus TMDCs are denoted as MXY with M = Mo and W; X, Y = S, Se and Te; X represents the chalcogenide atom with a smaller atomic number while Y represents the chalcogenide atom with a larger atomic number.

Material	a,b	$l_1$	$l_2$	short-range potential	$\alpha_{\text{total}}^{\text{DFT}}$	$\alpha_{\text{total}}^{\text{CAL}}$	$R_M$	$R_X$	$R_Y$
MoS <sub>2</sub>	3.160 <sup>a</sup>	2.420 <sup>b</sup>	2.420 <sup>b</sup>	SW <sup>b</sup>	12.320	12.350	0.69	1.04	1.04
MoSSe	3.288 <sup>a</sup>	2.416 <sup>a</sup>	2.530 <sup>a</sup>	SW <sup>b</sup>	13.456	13.450	0.84	1.14	1.06
MoSTe	3.343 <sup>a</sup>	2.432 <sup>a</sup>	2.715 <sup>a</sup>	SW <sup>b</sup>	15.590	15.593	1.0	1.16	1.02
MoSeTe	3.412 <sup>a</sup>	2.552 <sup>a</sup>	2.717 <sup>a</sup>	SW <sup>b</sup>	16.768	16.769	1.04	1.12	1.05
WSSe	3.232 <sup>a</sup>	2.421 <sup>a</sup>	2.538 <sup>a</sup>	SW <sup>b</sup>	16.824	16.822	0.94	1.18	1.08
WSTe	3.344 <sup>a</sup>	2.438 <sup>a</sup>	2.720 <sup>a</sup>	SW <sup>b</sup>	19.489	19.489	1.08	1.18	1.08
WSeTe	3.413 <sup>a</sup>	2.559 <sup>a</sup>	2.722 <sup>a</sup>	SW <sup>b</sup>	21.225	21.224	1.08	1.24	1.08

<sup>a</sup>Reference HU ET AL. (2018)

<sup>b</sup>Reference JIANG (2019)

are derived and noted from the CD model for each atom in each sample. Accordingly, the total polarizations  $\mathbf{P}$  of the samples are calculated by the equation (3.12) and the in-plane strains  $\varepsilon_{xx}$  are calculated by  $\varepsilon_{xx} = \frac{l_x - l_{x_{\min}}}{l_{x_{\min}}}$ , where  $l_x$  and  $l_{x_{\min}}$  are the deformed length and minimized length of the samples in the X-direction. The polarization ( $P_x$ ) - strain ( $\varepsilon_{xx}$ ) diagrams of all samples are shown in the figure 3.3 and the diagrams of Janus TMDCs are shifted to have zero initial polarization by subtracting the polarization caused by the initial spontaneous curling effect, see XIONG ET AL. (2018); WANG ET AL. (2018a). Linear relations are observed between the polarization  $P_x$  and given strain  $\varepsilon_{xx}$  in figure 3.3. The slope of the linear relation yields the in-plane piezoelectric coefficient ( $d_{xxx}$  or  $d_{11}$ ) of the samples. Table 3.3 indicates that the calculated piezoelectric coefficients are in good agreement with the reported DFT and experimental values from DROTH ET AL. (2016); BLONSKY ET AL. (2015); DONG ET AL. (2017), which validates the effectiveness of the CD model and the derived material parameters in the section 3.1.2.

**Table 3.3.** Piezoelectric coefficients ( $\times 10^{-10}$  C/m) from the CD model estimation and literature.

Material	BN	MoS <sub>2</sub>	MoSSe	MoSeTe	MoSTe	WSSe	WSeTe	WSTe
Calculated	0.986	3.95	4.099	4.676	4.733	3.144	3.209	3.327
Reported	1.35 <sup>a</sup>	3.56 <sup>b</sup>	3.74 <sup>a</sup>	4.35 <sup>a</sup>	4.53 <sup>a</sup>	2.57 <sup>a</sup>	3.34 <sup>a</sup>	3.48 <sup>a</sup>

<sup>a</sup>Reference DROTH ET AL. (2016)

<sup>b</sup>Reference BLONSKY ET AL. (2015)

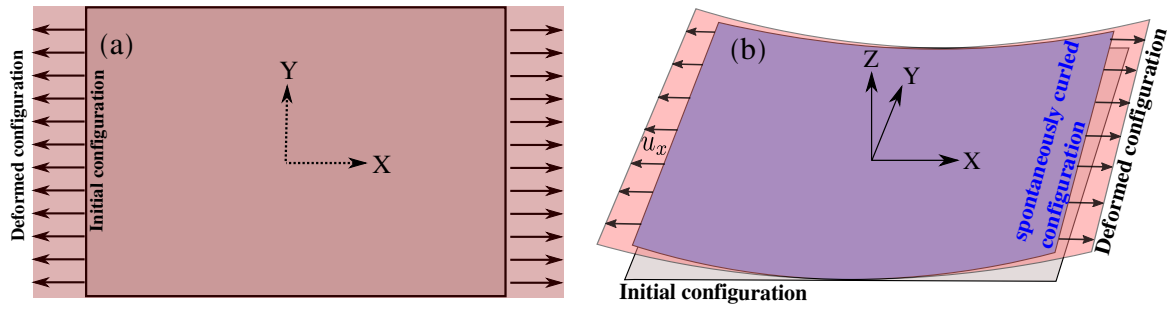


**Figure 3.2.** Loading scheme for estimating piezoelectric coefficient.

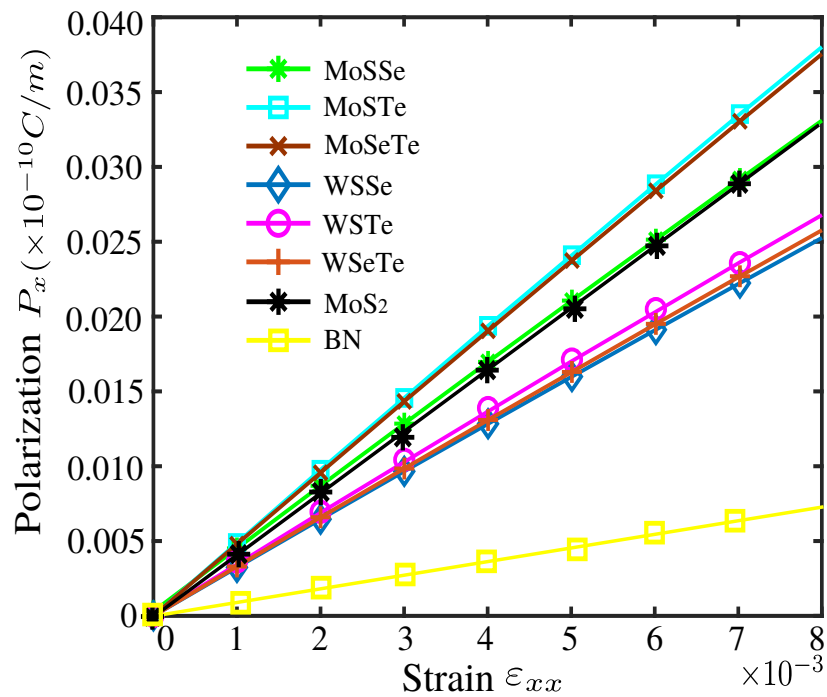


**Figure 3.3.** Polarization  $P_x$  vs strain  $\epsilon_{xx}$  for BN and MoS<sub>2</sub> and Janus TMDCs material systems.



## 3.2 Simulation method for extracting flexoelectric coefficients of 2D materials

In this section, a simulation method is proposed for extracting the flexoelectric coefficient of the interested 2D materials. As demonstrated in the equation (2.5), the measurement of the flexoelectric coefficient of a material is under the influence of the piezoelectric effect. Here the proposed simulation method employs a designed mechanical deformation pattern to eliminate the piezoelectric effect's contribution to the overall polarization, thus allowing a direct measurement of the flexoelectric coefficients.

### 3.2.1 Deformation pattern

The designed mechanical deformation pattern has the form

$$u_z = K \frac{x^2}{2}, \quad (3.19)$$

where  $x$  represents the atom coordinate in the X-direction,  $K$  represents the inverse of curvature (strain gradient) of the bending plane, and the prescribed mechanical deformation shown in the figure 3.4. In the MD models, the designed deformation pattern is applied to the material systems, which have identical dimension of  $80 \times 80 \text{ \AA}$  and the employed lattice parameters, short-range potentials are listed in the table 3.1 and table 3.2. Once the bending deformation is prescribed, the edge region atoms are held fixed while the interior atoms are allowed to relax to energy minimizing positions using the conjugate-gradient algorithm, after which the point charge  $q_i$  and dipole moments  $\mathbf{p}_i$  are found from the CD model for each atom.

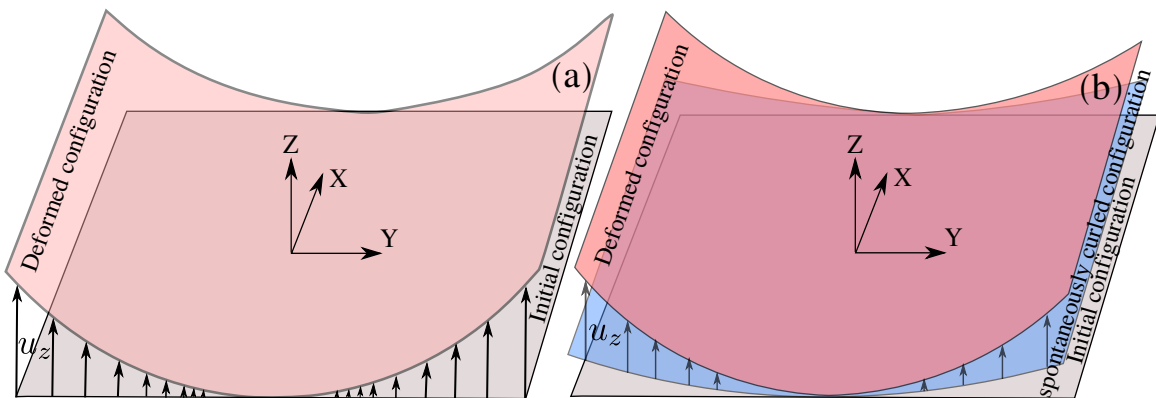


**Figure 3.4.** Schematic illustration of the geometry and loading condition for 2D material system. (a) flat system (graphene allotropes, nitrides, graphene analogues of group-IV elements and TMDC monolayers); (b) curled system (Janus TMDCs).

From the MD simulations, here establishes the relationship between polarization and strain gradient as follows. The strain gradient from the equation (3.19) is

$$\frac{\partial \varepsilon_{xz}}{\partial x} = \frac{1}{2} \frac{\partial^2 u_z}{\partial x^2} = \frac{1}{2} K, \quad (3.20)$$

where  $\varepsilon_{xz}$  is the strain in the X-direction from the applied deformation in the Z-direction. Substituting the equation (3.20) into the equation (2.4) and assuming that the imposed mechanical deformation in the equation (3.19) removes the piezoelectric contribution, thus obtains

$$P_z = \frac{1}{2} \mu_{zxzx} K, \quad (3.21)$$

where  $\mu_{zxzx}$  is the out-of-plane or bending flexoelectric coefficient and  $P_z$  is the out-of-plane polarization. The next subsection verifies the assumption of the removal of the piezoelectric contribution through the prescribed mechanical deformation pattern.

### 3.2.2 Validation the assumption in the deformation pattern

This subsection validates the assumption that the proposed bending scheme in the section 3.2.1 eliminates the piezoelectric contribution to the total polarization, enabling direct measurement of the intrinsic flexoelectric coefficients of the different 2D material groups. The applied deformation (using the equation (3.19)) results in strain ( $\varepsilon_{xz}$ ) and strain gradient ( $\frac{\partial \varepsilon_{xz}}{\partial x}$ ) along the XZ-direction, and a polarization along the Z-direction, where the MoS<sub>2</sub> is used here as a representative example for the validation process. The local atomic strain calculation for each atom  $i$  using the local deformation gradient  $\mathbf{F}$  which involves the initial and deformed atomic coordinates, see BELYTSCHKO ET AL. (2013). The local atomic strain tensor for the atom  $i$  ( $\varepsilon_i$ ) is

$$\varepsilon_i = \frac{1}{2} \left[ (\mathbf{F}_i)^T \mathbf{F}_i - \mathbf{I} \right], \quad (3.22)$$

where  $\mathbf{I}$  is the identity matrix.

Figure 3.5(a) represents the atomic configuration of MoS<sub>2</sub> system colored with the XZ component of strain  $\varepsilon_{xz}$ , which is calculated from the equation (3.22) at a given curvature ( $K = 0.1 \text{ nm}^{-1}$ ). The variation of strain  $\varepsilon_{xz}$  along the X-direction is plotted in the figure 3.5(b), where the strain was found by dividing the atomic system into several equal width bins and averaging the strain in each bin. A linear variation in  $\varepsilon_{xz}$  is observed from the figure 3.5(b). It demonstrates that the induced deformation is symmetric, and the resulting polarization due to strain cancels out. Therefore, the total strain  $\varepsilon_{xz}$  is zero (sum over all the bins), which eliminates the piezoelectric contribution to the polarization in the equation (2.4) and supports the assumption made in obtaining the equation (3.21), i.e., that for the prescribed bending deformation, the out-of-plane polarization is only dependent on the strain gradient. Furthermore, symmetry analysis on the piezoelectric tensor shows that  $d_{zxz}$  is zero for a point group symmetry associated with the 2D material sets, see DE JONG ET AL. (2015). The mechanical bending deformation leads strictly to zero out the out-of-plane piezoelectric contribution to the total polarization. However, it is important to note that an in-plane polarization is generated due to the out-of-plane bending. Furthermore, the in-plane polarization from the out-of-plane bending may receive a contribution from the

in-plane piezoelectricity. The further discussions of the in-plane polarization are in the section 3.3.4 and section 3.3.6.

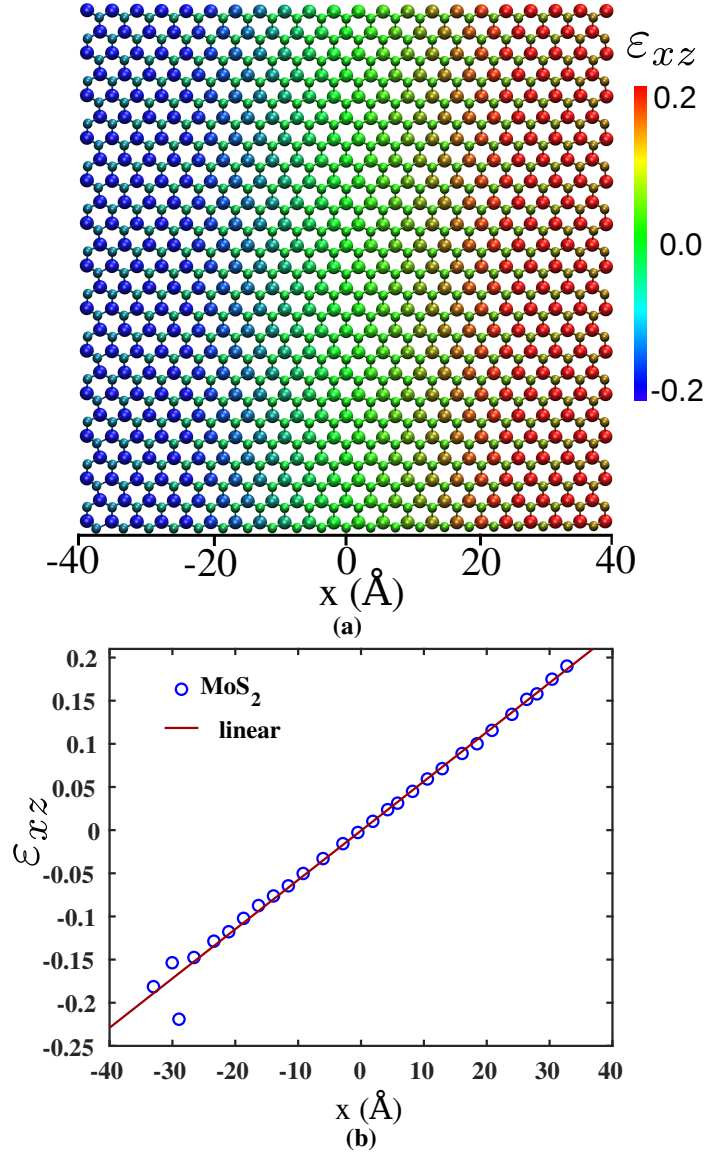


**Figure 3.5.** (a) Atomic configuration colored with strain  $\epsilon_{xz}$  in X-direction for MoS<sub>2</sub> sheet when strain gradient  $K = 0.01 \text{ \AA}^{-1}$ ; the large spheres represent Mo atoms and small spheres represent S atoms. (b) Bin-wise distribution of strain  $\epsilon_{xz}$  along X axis, circles represent the calculated average strain  $\epsilon_{xz}$  at location  $x$  and the solid line is linear fitting to the calculated data.

### 3.3 Flexoelectric coefficient of 2D materials

The simulation procedure described previously in the section 3.2 is applied here to extract the flexoelectric coefficients of four groups of 2D materials: graphene allotropes (C1, C2,

and C3), nitrides (BN, AlN, and GaN), graphene analogs of group-IV elements (Si, Ge, and Sn) and TMDC monolayers (MoS<sub>2</sub>, WS<sub>2</sub> and CrS<sub>2</sub>). C1 corresponds to pristine graphene, while C2 and C3 represent graphene with Stone-Wales defects, which replace some hexagons with pentagons and heptagons with different periodicity, respectively, see ENYASHIN & IVANOVSKII (2011). BN, AlN, and GaN are nitrogen-based hexagonal monolayers with boron, aluminum, and gallium. Silicene (Si), Germanene (Ge), and Stanene (Sn) are the group-IV 2D graphene analogs. However, the vertical distance between the atoms or buckling height ( $h$ ) in the unit cell is non-zero when compared to the graphene allotropes and nitride material groups (see figure 3.1(a) and (c)). The TMDCs possess three sub-layers or intra-layers where element 'X' (center layer) forms bonds with two S atoms in the top and bottom layers. The layers are vertically separated by the intralayer heights  $h_1$  and  $h_2$ , as shown in the figure 3.1(d). The figure 3.1(e) shows the geometrical configuration of Janus TMDCs, an uneven bond length ( $h_1 \neq h_2$ ) exist between the upper 'M-Y' and lower bond 'M-X'.

Here the applied inverse of curvature  $K$  has the range from 0 to 0.1 nm<sup>-1</sup> and the induced total polarizations of the material system at each  $K$  is calculated from the equation (3.12). The polarization- $K$  diagrams of several material systems are shown in the figure 3.6. For the case of Janus TMDCs (figure 3.6(b)), a effective strain gradient  $K_{eff} = \partial\varepsilon_{xz}/\partial x$  derived from the slope of the bin-wise strain distribution of the Janus TMDCs (similar as in the figure 3.5(b)) between  $\varepsilon_{xz}$  and the X-coordinate of each bin is used. The current value of  $K_{eff}$  differs from  $\frac{1}{2}K$  (from the equation (3.19)) by about 15%. Theoretically, the numerical value of  $K_{eff}$  should be equal to  $\frac{1}{2}K$  under the imposed bending deformation. For example, in the case of conventional TMDCs (MoS<sub>2</sub>, WS<sub>2</sub> and CrS<sub>2</sub>), the effective strain gradient is equal to half of the given value of  $K$  under the same bending deformation, see ZHUANG ET AL. (2019a). However, the observed difference in Janus TMDCs is due to the spontaneous curling effect, see XIONG ET AL. (2018); WANG ET AL. (2018a), which arises from the structural asymmetry between the M-X and M-Y layers, resulting in stretching in the Y layer and compression in the X layer. To account for the spontaneous deformation, the effective strain gradient  $K_{eff}$  is used to calculate the flexoelectric coefficient of Janus TMDCs. The flexoelectric coefficients of the 2D materials without Janus TMDCs are derived from the equation (3.21) and the equation  $P_z = \mu_{zxzx}K_{eff}$  is used for extracting flexoelectric coefficients of the Janus TMDCs. Figure 3.7 presents the flexoelectric coefficients of the interested 2D materials. The comparison is divided into two sub-figures due to the significant range difference between the value of Janus TMDCs and the remained 2D materials. The following sections 3.3.1 to 3.3.5 explain the underlying mechanism of the induced flexoelectricity in each 2D material group.

### 3.3.1 Mechanisms of inducing polarization in 2D materials

As shown in the figure 3.7 that 2D materials exhibit different flexoelectric constants. This subsection analysis the mechanisms governing the flexoelectric constants for the 2D materials. The analysis depends on understanding, within the framework of the utilized CD model, the various contributions to the dipole moments induced from the prescribed bending deformation. Specifically, the dipole moment  $\mathbf{p}_i$  on atom  $i$  depends on its polarizability and the

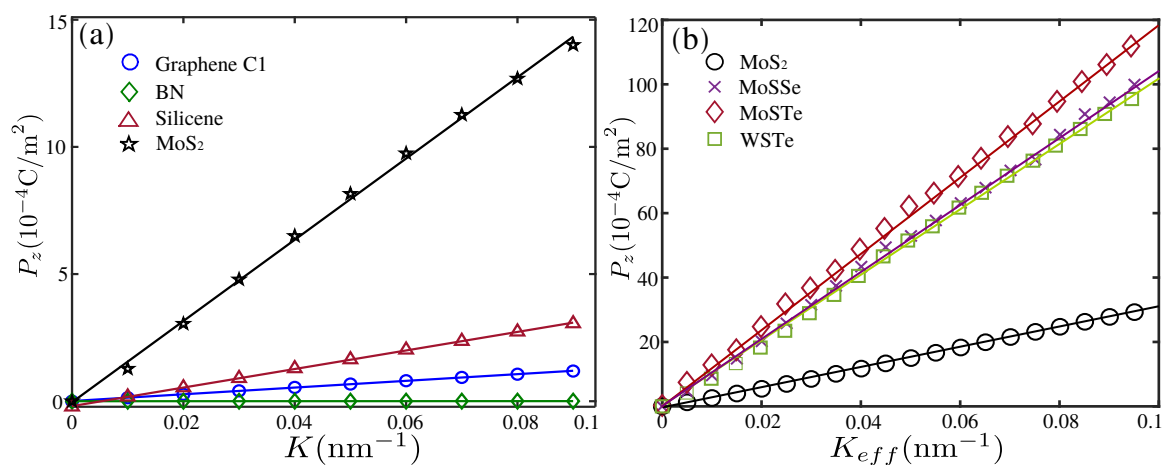


**Figure 3.6.** (a) Polarization  $P_z$  vs inverse of curvature  $K$  for graphene, BN, Silicene and MoS<sub>2</sub>. Markers indicate the simulation data, and solid lines indicate the linear fitting. (b) Polarization  $P_z$  vs effective strain gradient  $K_{eff}$  for Janus TMDCs. Markers indicate the simulation data, and solid lines indicate the linear fitting.

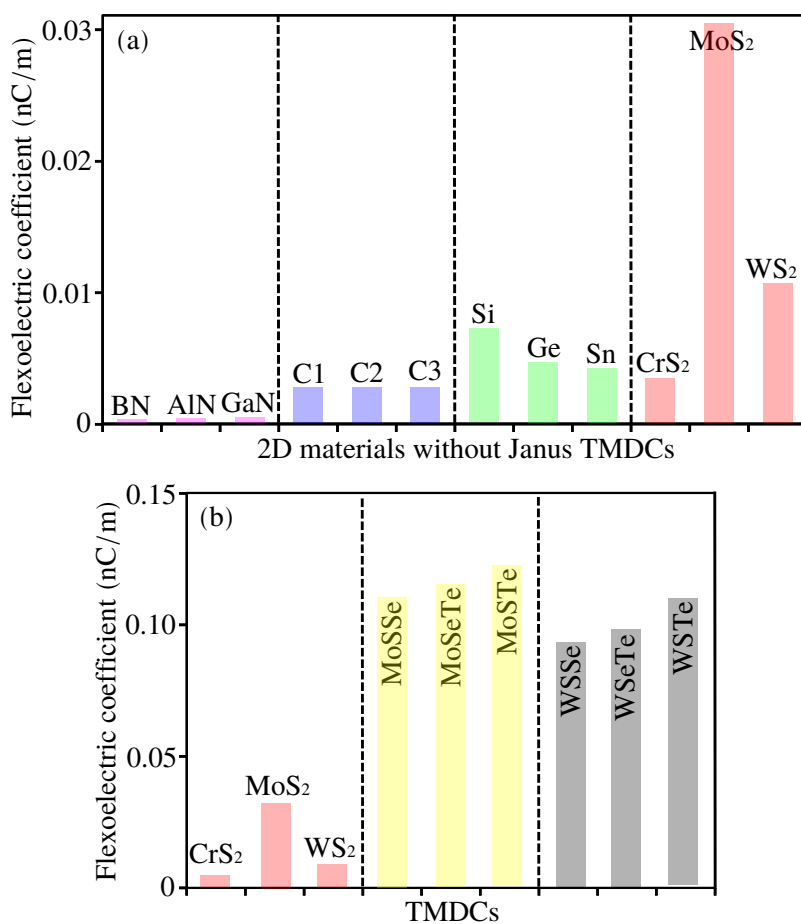


**Figure 3.7.** Bending flexoelectric coefficients of the studied 2D materials.

presence of a local electric field, which consists of three parts: the electric field at position  $\mathbf{r}_i$  due to neighboring (i) dipoles  $\mathbf{p}_j$ ; (ii) charges  $q_j$  and (iii) from the externally applied electric fields  $\mathbf{E}^{\text{ext}}$ . Because the only external stimulus is the prescribed bending deformation thus  $\mathbf{E}^{\text{ext}} = 0$  and the governing equation for the dipole moments (equation (3.13)) becomes

$$\mathbf{T}_{ii}^{\text{p-p}} \mathbf{p}_i - \sum_{j, i \neq j}^N \mathbf{T}_{ij}^{\text{p-p}} \mathbf{p}_j = \sum_{j, i \neq j}^N \mathbf{T}_{ij}^{\text{q-p}} q_j. \quad (3.23)$$

where  $\mathbf{T}_{ij}^{\text{p-p}}$  and  $\mathbf{T}_{ij}^{\text{q-p}}$  are the polarizability tensors. These two tensors represent dipole-dipole and charge-dipole interactions, respectively, which can also be interpreted as accounting for  $\sigma-\sigma$  and  $\sigma-\pi$  electron interactions, respectively, see MAYER (2007, 2005); ROBERT & DANNEAU (2014), and can be written as in MAYER (2005):

$$\mathbf{T}_{ij}^{\text{q-p}} = \frac{1}{4\pi\epsilon_0} \frac{\mathbf{r}_{ij}}{r_{ij}^3} \approx \frac{1}{4\pi\epsilon_0} \frac{\mathbf{r}_{ij}}{r_{ij}^3} \left[ \text{erf} \left( \frac{r_{ij}}{\sqrt{2}R} \right) - \sqrt{\frac{2}{\pi}} \frac{r_{ij}}{R} \exp \left( -\frac{r_{ij}^2}{2R^2} \right) \right], \quad (3.24)$$

$$\begin{aligned} \mathbf{T}_{ij}^{\text{p-p}} &= \frac{1}{4\pi\epsilon_0} \frac{3\mathbf{r}_{ij} \otimes \mathbf{r}_{ij} - r_{ij}^2 \mathbf{I}}{r_{ij}^5} \left[ \text{erf} \left( \frac{r_{ij}}{\sqrt{2}R} \right) - \sqrt{\frac{2}{\pi}} \frac{r_{ij}}{R} \exp \left( -\frac{r_{ij}^2}{2R^2} \right) \right] \\ &\quad - \frac{1}{4\pi\epsilon_0} \sqrt{\frac{2}{\pi}} \frac{\mathbf{r}_{ij} \otimes \mathbf{r}_{ij}}{r_{ij}^2} \frac{1}{R^3} \exp \left( -\frac{r_{ij}^2}{2R^2} \right). \end{aligned} \quad (3.25)$$

From equations (3.24) and (3.25), the inter-atomic distance ( $r_{ij}$ ) and parameter  $R$  (factor related to polarizability as shown in the section 3.1.2) are identified as the important factors in defining the dipole moment of atoms via the polarizability tensors. The following sections 3.3.2 to 3.3.5 adopt this analysis scheme.

### 3.3.2 Flat 2D Monolayers

Here considers the simplest 2D structures, flat graphene and BN mono-layer. To aid the analysis, the equation (3.23) is rewritten including only the  $p_{i,z}$  component (as in the equation (3.21)), which is

$$T_{ii,zz}^{\text{p-p}} p_{i,z} = E_{i,z}^{\text{p}} + E_{i,z}^{\text{q}}, \quad (3.26)$$

where  $E_{i,z}^{\text{p}} = \sum_{j, i \neq j}^N \{T_{ij,xz}^{\text{p-p}} p_{j,x} + T_{ij,yz}^{\text{p-p}} p_{j,y} + T_{ij,zz}^{\text{p-p}} p_{j,z}\}$  and  $E_{i,z}^{\text{q}} = \sum_{j, i \neq j}^N T_{ij}^{\text{q-p},z} q_j$  are the electric fields on atom  $i$  due to neighboring dipoles, charges and associated polarizability components.

For the undeformed graphene sheet, the out of plane dipole moment  $p_{i,z}$  is zero due to the monolayer's flat nature. However, once graphene is bent, the  $\pi-\sigma$  interactions increase, leading to a non-zero  $p_{i,z}$ . Specifically, for deformed graphene with bending curvature  $K = 0.02 \text{ nm}^{-1}$ , the measured contributions of  $E_{i,z}^{\text{p}}$  and  $E_{i,z}^{\text{q}}$  to the total electric field on atom  $i$  are 93.45% and 6.55%, respectively. As graphene is bent further, these contributions change to 93.27% and 6.73%, respectively, when  $K = 0.1 \text{ nm}^{-1}$ . The increased importance of  $E_{i,z}^{\text{q}}$  with increasing bending implies rising importance of  $\pi-\sigma$  interactions on the total electric field induced dipole moment on the atom  $i$ . It can also be interpreted through pyramidalization see, SURYA ET AL. (2012); DUMITRICĂ ET AL. (2002); NIKIFOROV ET AL.

(2014), in which  $sp^2$  bonding converts to  $sp^3$  bonding. In this process, each carbon atom's valence electrons develop bonding interactions with neighboring atoms due to the bond bending involved symmetry reduction, which allows mixing between  $\pi$  and  $\sigma$  electrons, leading to  $\pi - \sigma$  interactions, see GLEITER (1987). This interaction modifies the charge state of the carbon atom and the locally generated electric fields, which is captured by the CD model in the form of the charge-induced electric fields  $E_z^q$ . Overall, these increased  $\pi - \sigma$  interactions result in the flexoelectric coefficient for graphene being found as  $\mu_{gr} = 0.00286$  nC/m, which is found from the linear fitting of the polarization as a function of the bending curvature in the figure 3.6.

In the case of BN, the contribution of  $E_z^q$  also increases from 1.86% to 1.99% when bending curvature  $K$  increases from 0.02 to 0.1  $\text{nm}^{-1}$ , though the overall contribution of  $E_z^q$  to the total electric field is smaller than for graphene. This suggests that the  $\pi - \sigma$  interactions in BN are weaker than in graphene, which may be related to the difference in the tendency of pyramidalization between B and N atoms. Specifically, B atoms prefer the  $sp^2$  hybridization while N atoms are more likely to achieve  $sp^3$  hybridization or pyramidalization, see HERNÁNDEZ ET AL. (1998, 1999). Thus, even though the polarizability of BN is similar to graphene (see  $\alpha_{total}^{CAL}$  values in table 3.1), the flexoelectric constant of BN of 0.00026 nC/m is ten times smaller than graphene due to the smaller  $E_z^q$  contribution in BN.

The graphene allotropes C2 and C3 show similar flexoelectric coefficients to defect-free monolayer graphene (C1), as shown in the figure 3.7. Though C2 and C3 contain different arrangements of defects, the  $sp^2$  hybridization is unchanged, which induces nearly equal charges and dipole moments for atoms in C2 and C3 under deformation. As a result, the flexoelectric coefficients are nearly constant for this material group. In the nitride group, AlN and GaN are found to have larger flexoelectric constants than BN as shown in figure 3.7, though still significantly smaller than graphene. This is due to a corresponding increase in the contribution of  $E_z^q$ , from 1.99% for BN to 2.25% for AlN to 6.85% for GaN for a curvature of 0.1  $\text{nm}^{-1}$ .

### 3.3.3 Buckled 2D Monolayers

Figure 3.6(a) shows that the induced polarization for flat 2D materials is much smaller than is seen in silicene. From a structural point of view, silicene and graphene differ in that the atomic polarizability of silicene is larger and exists in a buckled configuration compared to graphene (see  $h$  values in table 3.1). Therefore, additional simulations are performed to examine both of these factors' effects on the induced polarization in silicene. Initially, a bending test is conducted for silicene in which the buckling height remains zero to understand the effect of buckling on the polarization. To do so, the simulation imposed the bending deformation on silicene without allowing any subsequent relaxation of the atomic positions. The variation of polarization for flat silicene and silicene is plotted in figure 3.8. From the numerical fitting, the flexoelectric coefficients for flat silicene  $\mu_{si-flat}$  and silicene  $\mu_{si}$  are identified as 0.00634 and 0.00728 nC/m, respectively. Noting that the graphene flexoelectric coefficient is  $\mu_{gr} = 0.00286$  nC/m, the ratio of  $\mu_{si-flat}/\mu_{gr}$  is 2.217, which is close to the ratio of their atomic polarizability parameters ( $R_{si}/R_{gr} = 2.141$  from the table 3.1). From this, it is clear that the atomic polarizability increases the induced polarization and thus flexoelectric

constants. The ratio of  $\mu_{\text{si}}/\mu_{\text{gr}}$  is 2.545, which is about 15% higher than 2.217. Therefore, this increase in polarization of about 15% between silicene and flat silicene can be ascribed to the buckled structure of silicene.

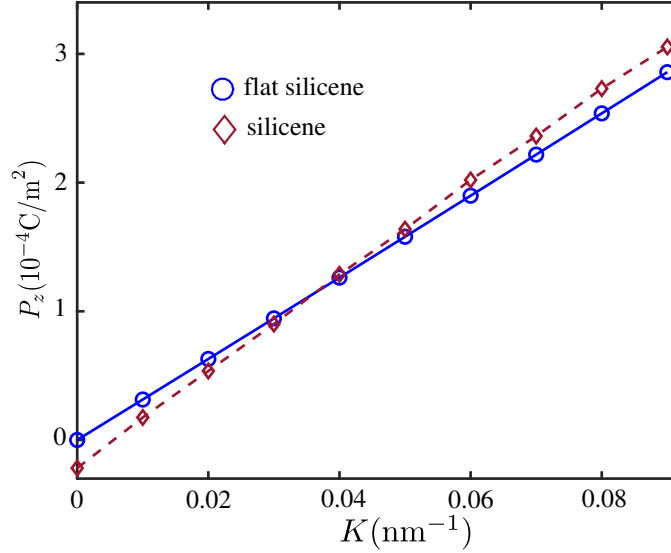


**Figure 3.8.** Polarization  $P_z$  versus applied inverse of curvature  $K$  for silicene and flat silicene.

Further understanding is drawn from the contributions of the electric fields from dipole-dipole and charge-dipole interactions. The contributions from  $E_i^{\text{p},z}$  and  $E_i^{\text{q},z}$  to the total electric field are estimated for flat silicene and silicene when the bending curvature is  $0.008 \text{ \AA}^{-1}$ . The numerical values for flat silicene are 91.89 and 8.10%, respectively, similar to that of graphene. Therefore, the increased dipole moment and flexoelectric coefficient for the flat silicene is primarily due to its larger atomic polarizability ( $R_{\text{si}}/R_{\text{gr}} = 2.141$ ) compared to graphene.

For buckled silicene, the contributions from  $E_{i,z}^{\text{p}}$  and  $E_{i,z}^{\text{q}}$  to the total electric field are 76.89 and 23.10%, respectively. Comparing to flat silicene, there is an increase in  $E_{i,z}^{\text{q}}$  and decrease in  $E_{i,z}^{\text{p}}$  for silicene. Thus, the CD model predicts that  $\pi - \sigma$  interactions are dramatically enhanced in buckled silicene as compared to flat silicene, which is in agreement with recent DFT studies, see PODSIADŁY-PASZKOWSKA & KRAWIEC (2017), who found that it is easier to achieve  $\text{sp}^3$  bonding in buckled silicene. Such changes in hybridization (pyramidalization) lead to significant charge modulations and induce large dipole moments. The difference in the numerical contribution of  $E_z^{\text{q}}$  to the total electric field in flat vs. buckled silicene of 15% is identical to the observed difference in magnitude of the flexoelectric coefficients. It demonstrates that buckling in the atomic structure of 2D materials can induce increased polarization, and thus flexoelectric constants.

Germanene and stanene also have flexoelectric constants larger than graphene and BN as shown in figure 3.7, though lower than silicene. This is due to a combination of lower polarizability of these materials as compared to silicene (see  $\alpha_{\text{total}}^{\text{CAL}}$  values in table 3.1), and due to reduced  $E_z^{\text{q}}$  contributions of 20.91% and 18.45%, respectively, indicating weaker  $\pi - \sigma$



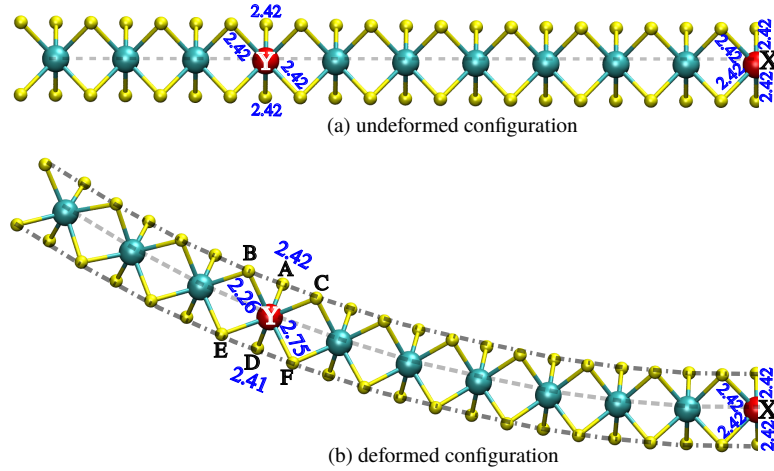


**Figure 3.9.** (a) Undeformed, and (b) Deformed atomic configuration of MoS<sub>2</sub> sheet. Red-colored atoms are used to explain the changes in bond length. Dashed lines represent the Mo layer and dash-dotted lines indicate the S layers. Atoms X and Y in (a) possess bond lengths of 2.42 Å with neighbor sulfur atoms. The bond length between atoms Y-A and Y-D is 2.42 Å and 2.41 Å, respectively. Atom Y has bond length of 2.26 Å with atoms B and C. The bond length between atoms Y-E and Y-F is 2.76 Å. Only left portion of the atomic system was shown here.

interactions in these buckled structures as compared to silicene.

### 3.3.4 Transition metal dichalcogenide monolayers

As shown in figure 3.6, the polarization under bending is significantly higher in MoS<sub>2</sub> than the other 2D materials. It found, for MoS<sub>2</sub>, the contributions from the dipole and charge-induced electric fields in the  $z$ -direction are 15.23% and 84.76%, respectively, where the contribution of  $E_z^q$  is significantly higher than for the previously discussed 2D materials.

Here elaborates that the mechanism enabling the large polarization and large flexoelectric constant in MoS<sub>2</sub>, is different from the other 2D materials. As shown in figure 3.9(a), MoS<sub>2</sub> is a tri-layer 2D material in which each central Mo atom bonds with the S atoms in the layers above and below. The thickness of this sheet defines as the sum of the vertical separation between these layers. The imposed bending deformation causes the top and bottom S layers to deform differently with respect to the central Mo atom. For the initial (flat) configuration in the figure 3.9(a), the central Mo atoms, labeled as X and Y, are located 2.42 Å away from both the neighboring top and bottom layer S atoms. This initial atomic configuration also induces non-zero dipole moments to each atom since the  $z$ -component of  $\mathbf{r}_{ij}$  is non-zero. An equal and opposite dipole moment is observed for the top and bottom S atoms due to the equidistant separation with the central Mo atoms, whereas no dipole moment is found on the Mo atoms due to symmetry.

However, after bending, there are significant bond length changes, as shown in the figure 3.9(b). The bond lengths between atom X and its nearest S atom neighbors are unchanged even after deformation; the bond lengths Y-A and Y-D are measured as 2.42 and 2.41 Å. In contrast, significant changes in bond length result for other nearest S neighbors,

where a compression in the Y-B and Y-C bond lengths is identified (2.42 to 2.26 Å) in figure 3.9(b), and where elongation of the Y-E and Y-F bond lengths (2.42 to 2.75 Å) is seen. The identified differences in bond lengths break the symmetry seen in the undeformed MoS<sub>2</sub> in figure 3.9(a), which leads to non-zero dipole moments, and increases the  $E_z^q$  contribution to the total electric field as compared to buckled silicene.

Interestingly, the polarizability of silicene is significantly larger than MoS<sub>2</sub>, i.e.  $R_{\text{MoS}_2}/R_{\text{si}}$  is about 0.5, according to the table 3.1. This indicates that MoS<sub>2</sub> has a significantly higher polarization and flexoelectric constant than buckled silicene for other reasons, starting with the enhanced  $\pi - \sigma$  interactions. Furthermore, a recent DFT study on the bonding characteristics and charge transfer in MoS<sub>2</sub> found that the S atoms share their electrons with the Mo atoms, which results in the transfer of electrons back to the Mo atoms, see PIKE ET AL. (2017). This charge transfer, coupled with the bond length asymmetry due to bending, results in a large  $E_z^q$  and large dipole moments.

The flexoelectric coefficients for other TMDC group members are smaller than MoS<sub>2</sub> as shown in figure 3.7, where the flexoelectric coefficient of WS<sub>2</sub> is 3 times smaller than MoS<sub>2</sub>, and where CrS<sub>2</sub> has an even smaller value. It's found that the bond length asymmetry between the layers after bending is highest for MoS<sub>2</sub> and decreases for WS<sub>2</sub> and CrS<sub>2</sub>, and also that the local difference in radius of curvature for MoS<sub>2</sub>, WS<sub>2</sub> and CrS<sub>2</sub> materials is 49%, 40%, and 26%, respectively, both of which lead to a decreasing contribution of  $E_z^q$  for WS<sub>2</sub> and CrS<sub>2</sub>. A DFT study also found a smaller Born effective charge for WS<sub>2</sub> compared to MoS<sub>2</sub>, which supports the observation of lower  $E_z^q$  for WS<sub>2</sub> compared to MoS<sub>2</sub>, see PIKE ET AL. (2017).

An interesting observation from figure 3.7 is that the flexoelectric constants of graphene (C1) and CrS<sub>2</sub> are nearly equal. Though CrS<sub>2</sub> exhibits higher atomic polarizability and bond length asymmetry, the final dipolar polarization is similar to graphene. This is because there is a relatively low asymmetry in dipole moment between S atoms in the top and bottom layers in CrS<sub>2</sub>, which results in the cancellation of the induced polarization, leading to a flexoelectric constant that is similar to graphene. However, for WS<sub>2</sub> and MoS<sub>2</sub>, the increased asymmetry between layers avoids the dipole moment cancellation to achieve larger flexoelectric coefficients.

As observed that MoS<sub>2</sub> has an intrinsic bending flexoelectric constant of 0.032 nC/m. This value is about ten times larger than found in graphene and about 3-5 times larger than seen in the buckled monolayers. Here compares flexoelectric constant of MoS<sub>2</sub> with the result extracted from the recent experimental study on the electromechanical properties of MoS<sub>2</sub> reported in BRENNAN ET AL. (2017). In that work, the out-of-plane piezoelectric coefficient ( $d$ ) of MoS<sub>2</sub> using piezoresponse force microscopy was measured to be 1.03 pm/V. That work also established a relationship between the flexoelectric constant ( $\mu$ ) and piezoelectric ( $d$ ) coefficient under the assumption of small length scales and linear electric field as

$$\mu = d E_{els} \frac{h}{2}, \quad (3.27)$$

where  $E_{els}$  is the elastic modulus of MoS<sub>2</sub> and  $h$  is the monolayer thickness of MoS<sub>2</sub>. With  $E_{els} = 270$  GPa and  $h = 0.65$  nm,  $\mu$  is about 0.091 nC/m, which is significantly higher than our calculated value of 0.032 nC/m. This difference is due to the usage of elastic modulus in the equation (3.27), where the bending modulus usage is more appropriate. The bending

**Table 3.4.** In-plane piezoelectric coefficients  $d_{yyy}$  ( $\times 10^{-10}$  C/m) for Janus TMDCs using proposed CD model in comparison to previous DFT results ( $d_{yyy}^{\text{DFT}}$ ).  $\mu_{zyzy}$  (nC/m) are the bending flexoelectric constants while  $l_2 - l_1$  ( $\text{\AA}$ ) is the initial asymmetry for Janus TMDCs.

Material	$d_{yyy}$	$d_{yyy}^{\text{DFT}}$	$l_2 - l_1$	$\mu_{zyzy}$
MoS <sub>2</sub>	3.95	3.56	0.0	0.032
MoSSe	4.099	3.74 <sup>a</sup>	0.114	0.117
MoSeTe	4.676	4.35 <sup>a</sup>	0.165	0.120
MoSTe	4.733	4.53 <sup>a</sup>	0.283	0.125
WSSe	3.144	2.57 <sup>a</sup>	0.117	0.089
WSeTe	3.209	3.34 <sup>a</sup>	0.163	0.092
WSTe	3.327	3.48 <sup>a</sup>	0.282	0.114

modulus of MoS<sub>2</sub> was previously found to be about 9.61 eV or 65.01 GPa, see JIANG ET AL. (2013b). Using this bending modulus, the flexoelectric coefficient from the equation (3.27) with bending modulus gives a value of 0.021 nC/m. This value is close compared to the calculated value of 0.032 nC/m from this work and demonstrates that the flexoelectric constant for MoS<sub>2</sub> estimated using the atomistic CD model is in good agreement with experimental measurement.

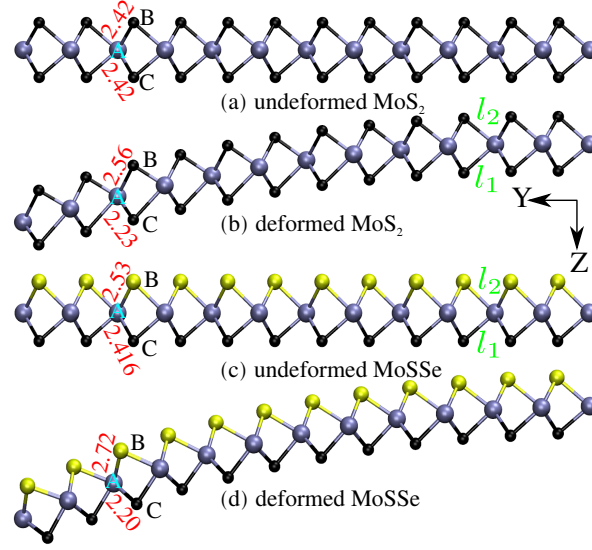
### 3.3.5 Janus transition metal dichalcogenide monolayers

Figure 3.7(b) indicates that the flexoelectric coefficients of Janus TMDCs are significant higher (up to 5 times) than the traditional TMDCs. This subsection first investigates the enhancement of the flexoelectric coefficients of Janus TMDCs comparing to the traditional TMDCs. For the comparison, MoS<sub>2</sub> and MoSSe are chosen from the TMDCs and Janus TMDCs group, respectively. Later, the difference among the Janus TMDCs in terms of the flexoelectric coefficient is studied.

#### Flexoelectric effect in MoS<sub>2</sub> and MoSSe

The major difference between TMDCs and Janus TMDCs is the structure configuration (symmetry versus asymmetry). Here investigates the impact of the structural configuration on the flexoelectric effect. MoS<sub>2</sub> is chosen as a representative TMDC that does not have structural asymmetry (MXX), while MoSSe is chosen as a representative Janus TMDC which does have structural asymmetry (MXY). To aid in the analysis of the resulting flexoelectric constants, it notes from previous section 3.3.1 that the dipole moment  $\mathbf{p}$  of an atom depends primarily on three factors: the effective atomic polarizability ( $R$ ), the charge induced electric field ( $E_z^q$ ), and the dipole induced electric field ( $E_z^p$ ). And the focus is, as shown previously in the equation (2.4), on the the out-of-plane ( $Z$ -direction) dipole moment  $p_z$  and associated polarization  $P_z$ .

The bond length between atoms A-B and A-C in figure 3.10(a) is equal to 2.42  $\text{\AA}$  ( $l_{Mo-S}$ ) for unibent MoS<sub>2</sub>. Because the A-B and A-C bond lengths are the same, there is no initial structural asymmetry for MoS<sub>2</sub>, and the bonds induce equal and opposite electric fields, which



**Figure 3.10.** Atomic configurations of (a) undeformed  $\text{MoS}_2$ , (b) deformed  $\text{MoS}_2$  at  $K_{eff} = 0.05 \text{ nm}^{-1}$ , (c) undeformed  $\text{MoSSe}$  and (d) deformed  $\text{MoSSe}$  at  $K_{eff} = 0.05 \text{ nm}^{-1}$ .

cause the total dipole moment, and thus total polarization of each  $\text{MoS}_2$  unit cell to be zero. However, significant changes in the bond lengths are observed in the deformed state (figure 3.10(b)) for a curvature of  $K_{eff} = 0.05 \text{ nm}^{-1}$ . Bond A-B is stretched from 2.42 to 2.56 Å while bond A-C is compressed from 2.42 to 2.23 Å. This difference in bond lengths breaks the electric field symmetry and increases the total dipole moment. At  $K_{eff} = 0.05 \text{ nm}^{-1}$ , the total electric field difference  $\Delta(E_z^p + E_z^q)$  with respect to the initial (undeformed) configuration is 53.06 V/Å, which increases the total polarization from 0 to 0.0016 C/m<sup>2</sup>. The changes to  $E_z^q$  and  $E_z^p$  at  $K_{eff} = 0.05 \text{ nm}^{-1}$  are 45.6 and 7.4 V/Å, respectively. The significant contribution of  $E_z^q$  implies the increasing importance of  $\pi - \sigma$  interactions in generating the dipole moment  $p_z$ . The  $\pi - \sigma$  interactions originate from the coupling between valence electrons and bonding electrons, see GLEITER (1987), which are also interpreted as pyramidalization, see SURYA ET AL. (2012); DUMITRICĂ ET AL. (2002); NIKIFOROV ET AL. (2014). Furthermore, a recent DFT study reported that electron transfer from the  $p$  orbitals of S atoms to the  $d_{z^2}$  orbital of Mo atoms, see PIKE ET AL. (2017). This electron transfer modifies the charges on the Mo and S atoms, which generates local charge induced electric fields, which are captured through  $E_z^q$  within the current CD model. Further changes in the bond length between Mo and S atoms enhance the  $\pi - \sigma$  coupling, see HUANG ET AL. (2018), resulting in large  $E_z^q$  and  $P_z$ . The variation of total polarization with the effective strain gradient for  $\text{MoS}_2$  is given in figure 3.6(b), where the slope represents the flexoelectric constant for  $\text{MoS}_2$  ( $\mu_{\text{MoS}_2}$ ), which is found to be 0.032 nC/m.

In contrast to  $\text{MoS}_2$ , the Janus TMDC  $\text{MoSSe}$  has a structural asymmetry in the undeformed configuration between the Mo-S and Mo-Se atomic layers. Specifically, the A-B ( $l_{\text{Mo-Se}}$ ) bond length in figure 3.10(c) is equal to 2.53 Å, while the A-C bond length ( $l_{\text{Mo-S}}$ ) is 2.416 Å. The bending deformation of  $\text{MoSSe}$  to a curvature of  $K_{eff} = 0.05 \text{ nm}^{-1}$  stretches  $l_{\text{Mo-Se}}$  ( $l_2$ ) from 2.53 to 2.72 Å and shrinks  $l_{\text{Mo-S}}$  ( $l_1$ ) from 2.416 to 2.20 Å. The initial bond

length asymmetry in MoSSe is further increased due to the given deformation and helps to produce larger dipole moments  $p_z$ , compared to MoS<sub>2</sub>. The dipole moment  $p_z$  is also related to the polarizability of the atomic system, where the polarizability of MoSSe ( $\alpha_{\text{MoSSe}}$ ) is 1.09 times larger than that of MoS<sub>2</sub> ( $\alpha_{\text{MoS}_2}$ ) as shown in the table 3.2, which shows the important effect of structural asymmetry for the Janus TMDCs.

Besides, the initial bond length asymmetry in unbent MoSSe induces an intrinsic electric field, which is not present in MoS<sub>2</sub>, as shown in recent DFT simulations, see JIN ET AL. (2018). That work also reported the non-overlapping of out-of-plane wavefunctions for electrons and holes due to this electric field, which implies a weak bonding between the electron-hole pair, and which reduces the bandgap by pushing the  $d$  orbitals of the metal atom closer to the Fermi level, see ER ET AL. (2018). The  $d$  orbital shifting may enhance the charge transfer process through  $\pi - \sigma$  coupling, which represents an easy transfer of charges from the S or Se atom to the Mo atom. This phenomenon is reflected in our CD model as the calculated charge on Mo (atom A in figure 3.10(d)) in MoSSe is  $0.733e$ , which is significantly larger than for Mo in MoS<sub>2</sub> (atom A in figure 3.10(b)), which is  $0.282e$ , and as such the charge acquired by the Mo atom in MoSSe is 2.6 times higher than in MoS<sub>2</sub>.

For a curvature of  $K_{eff}=0.05 \text{ nm}^{-1}$ , the charge transfer-induced change of  $E_z^q$  in MoSSe is  $117.6 \text{ V/\AA}$ , which is exactly 2.6 times higher than the field induced in MoS<sub>2</sub>, and which reflects stronger  $\pi - \sigma$  coupling in MoSSe. Furthermore, the value of  $E_z^p$  is higher in MoSSe ( $38.4 \text{ V/\AA}$ ) than in MoS<sub>2</sub> ( $7.4 \text{ V/\AA}$ ), which represents a stronger dipole interaction ( $\sigma - \sigma$  coupling) in MoSSe than MoS<sub>2</sub>. Recent studies on the electronic properties of strained Janus TMDCs suggest an increased coupling between the  $p$  orbitals of S/Se atoms with the in-plane bonding orbitals  $d_{x^2-y^2}$  and  $d_{xy}$  of Mo atom as a function of changes in bond angle, see HUANG ET AL. (2018). In MoSSe, the angle B-A-C in figure 3.10 varies from  $81.1^\circ$  to  $74.2^\circ$  between the initial and deformed states ( $K_{eff} = 0.05 \text{ nm}^{-1}$ ), while for MoS<sub>2</sub>, angle variations are  $81.93^\circ$  to  $78.66^\circ$  for the initial and deformed states. The reduction in bond angles between MoSSe and MoS<sub>2</sub> may increase the contribution of  $E_z^p$  in MoSSe.

Overall,  $E_z^q$  is higher than  $E_z^p$  in MoSSe, which represents that  $\pi - \sigma$  coupling is dominant over  $\sigma - \sigma$  coupling. DFT simulations have shown that coupling between  $d_{z^2}$  and  $p$  orbitals ( $\pi - \sigma$  coupling) is stronger than the coupling between  $p$  and  $d_{x^2-y^2}$  and  $d_{xy}$  ( $\sigma - \sigma$  coupling) orbitals in Janus TMDCs, see HUANG ET AL. (2018); ER ET AL. (2018). The total electric field increment  $\Delta(E^{p-z} + E^{q-z})$  in MoSSe is  $156.07 \text{ V/\AA}$  at a curvature of  $K_{eff} = 0.05 \text{ nm}^{-1}$ , which is 2.94 times higher than in MoS<sub>2</sub> at the same curvature. The increased polarizability and electric field increases the total dipole moment of MoSSe to 3.24 times higher than in MoS<sub>2</sub>. The flexoelectric constant for MoSSe ( $\mu_{\text{MoSSe}}$ ) is found to be  $0.117 \text{ nC/m}$ , which is 3.6 times higher than flexoelectric coefficient of MoS<sub>2</sub>, which is consistent with the larger polarizability of MoSSe. The polarizability is directly related to the dielectric constant ( $\epsilon$ ) of the material, see PAN ET AL. (2016). For instance,  $\alpha$  of MoSSe and MoS<sub>2</sub> are  $13.45$  and  $12.35 \text{ \AA}^3$ , respectively, as shown in the table 3.2. The DFT calculated values for  $\epsilon$  for these materials are  $8.67$  and  $8.05$ , see JIN ET AL. (2018). Thus, the increased flexoelectric constant for MoSSe over MoS<sub>2</sub> is in agreement with the fact that flexoelectric effect scales with the material dielectric constant, see YUDIN & TAGANTSEV (2013b); ZUBKO ET AL. (2013b).

As previously shown in table 3.4, the in-plane piezoelectric coefficient for MoSSe is comparable with that of MoS<sub>2</sub>. However, the out-of-plane flexoelectric coefficient is 3.6 times

higher than  $\text{MoS}_2$  (Table 3.4), which implies that there are relative benefits to bending flexoelectricity as compared to the in-plane piezoelectricity when comparing Janus TMDCs to standard TMDCs. In order to understand this further, here also compares the change in total electric field and asymmetry in bond length between in-plane tensile deformation and out-of-plane bending deformation for MoSSe for the same strain energy density, which is defined as the sum of atomic stress times the atomic strain over the volume of the deformed system. The change in  $E_z^q$  and  $E_z^p$  for bending deformation were previously noted as 117.6 and 38.4 V/Å for a curvature of  $K_{eff} = 0.05 \text{ nm}^{-1}$ , while for tensile deformation the values are 11.9 and 18.7 V/Å, respectively. This shows that the induced electric fields are higher in bending than in tension, which generates high dipole moments. It is also observed that the difference in bond length ( $l_2 - l_1$ ) for bending is higher than in tension for the same unit cell compared in tension and bending. This reflects the larger bond length asymmetry induced in bending, which supports the charge transfer and enhanced  $\pi - \sigma$  coupling based electric fields.

To further compare the resulting electromechanical coupling between standard TMDCs and Janus TMDCs, the author computed the electrical energy density for atomic configurations at the same strain energy density for MoSSe and  $\text{MoS}_2$ . The electrical energy density is defined as the sum of the dot product between the induced polarization and the electric field over the volume. The atomic configuration of MoSSe at  $K_{eff}=0.05 \text{ nm}^{-1}$  gives an electrical energy density of  $2.6 \times 10^9 \text{ J/m}^3$  and a strain energy density of  $1.13 \times 10^9 \text{ J/m}^3$ . By selecting an atomic configuration for  $\text{MoS}_2$  under bending deformation with the same strain energy density results in an electrical energy density that is about 39% of the MoSSe electrical energy density. The electrical energy density under the tensile deformation of MoSSe is about 84% of the electrical energy density for MoSSe under bending. These results show that the higher values of electric fields and large dipole moments under bending deformation point to the advantage of bending as compared to stretching in generating strong electromechanical coupling in Janus TMDCs.

### Flexoelectric effect among Janus TMDCs

From the previous subsection 3.3.5, it is clear that the asymmetry in bond lengths between layers of MXY induce large dipole moments through the increase in induced electric fields. Table 3.4 lists the out-of-plane bending flexoelectric coefficients of the Janus TMDCs along with the initial bond length difference  $l_2 - l_1$  in figure 3.10, from which a positive correlation is identified for both the MoXY and WXY Janus TMDCs. It's noted that the out-of-plane piezoelectric coefficients also show a similar dependence on bond length asymmetry, see DONG ET AL. (2017). Here mechanistically examines this correlation further using the electric fields due to charge-dipole ( $E_z^q$ ) and dipole-dipole ( $E_z^p$ ) interactions from the CD model. Under the prescribed bending scheme, the increase in the total electric field  $E_z^q + E_z^p$  increases with strain gradient  $K_{eff}$  for every Janus TMDC. However, the relative contribution from  $E_z^q$  or  $E_z^p$  to  $E_z^q + E_z^p$  varies between elements of the Janus TMDCs group. In the MoXY group for a strain gradient of  $K_{eff} = 0.1 \text{ nm}^{-1}$ , the contribution from the charge-dipole interaction induced electric field  $E_z^q$  in  $\text{MoS}_2$ , MoSSe, MoSeTe, and MoSTe to the increase in the total electric field ( $E_z^q + E_z^p$ ) is 84.76%, 75.48%, 70.33% and 56.29%, respectively. The contribution from the dipole-dipole interaction induced electric field  $E_z^p$  to the increase in the total electric field ( $E_z^q + E_z^p$ ) is then 15.24%, 24.52%, 29.67% and 43.71% in  $\text{MoS}_2$ , MoSSe,

MoSeTe, and MoSTe, respectively.

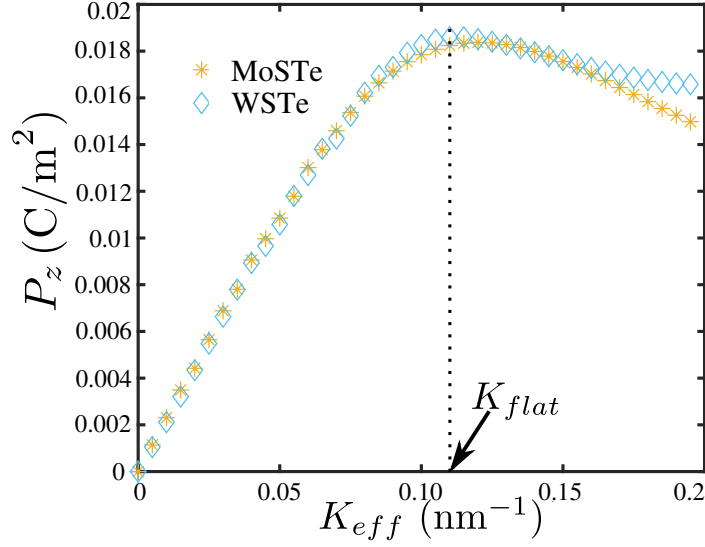
The bending deformation further develops a coupling among the induced dipole moments via the  $\sigma - \sigma$  interactions, which raises the contribution of  $E_z^p$ . For example in MoSTe, at  $K_{eff} = 0.01 \text{ nm}^{-1}$ ,  $E_z^q$  and  $E_z^p$  are  $56.82 \text{ (V/\AA)}$  and  $33.99 \text{ (V/\AA)}$ , respectively. When  $K_{eff}$  is increased to  $0.05 \text{ nm}^{-1}$ , these values increase to  $280.5 \text{ (V/\AA)}$  and  $216.99 \text{ (V/\AA)}$ . The enhanced dipole-dipole interaction  $E_z^p$  is due to the reduction in bond angle via the increased bond length asymmetry due to bending. The decrease in bond angle (B-A-C in figure 3.10) between initial and deformed states ( $K_{eff} = 0.05 \text{ nm}^{-1}$ ) is  $6.9^\circ$  for MoSSe and  $7.4^\circ$  for MoSTe. The difference in  $E_z^p$  for atom A in MoSSe is  $0.38 \text{ V/\AA}$  and for atom A in MoSTe is  $0.53 \text{ V/\AA}$  (not shown in figure 3.10). This further confirms that the increased reduction in the bond angle helps in increasing the dipolar interactions ( $\sigma - \sigma$  coupling), which are measured in the form of  $E_z^p$ . Note that atoms A, B, and C are selected at exactly the same unit cell locations in MoSSe and MoSTe. The cumulative effect of bond angle reduction within the unit cell and across the unit cell in the given atomic system makes the contribution of  $E_z^p$  significant. The total effect of increased electric fields and polarizability helps in inducing high polarization and thus high flexoelectric coefficient for MoSTe over other Janus TMDCs. A similar trend is found in the WXY group in table 3.4, where high charge transfer and higher bond angle reduction in WSTe compared to other elements in WXY group. This makes the flexoelectric coefficient of WSTe higher than WSSe and WSeTe.

Table. 3.4 also shows that the MoXY group exhibits higher out-of-plane bending flexoelectric coefficients than the WXY group. For example, MoSTe and WSTe have the highest flexoelectric coefficients in their groups, where the flexoelectric coefficient of MoSTe is about 1.09 times larger than WSTe. At  $K_{eff} = 0.05 \text{ nm}^{-1}$ , the total electric field change in MoSTe is 1.4 times larger than that of WSTe while the polarizability of MoSTe is 0.79 times that of WSTe. Though the polarizability of MoSTe is lower than WSTe, the larger induced electric fields result in the flexoelectric constant of MoSTe being slightly larger than that of WSTe.

### Bending against the initial spontaneous curvature

In the previous section 3.3.5, the bending-induced flexoelectric responses of MXY materials are obtained while applying the out-of-plane bending toward their initial curling direction (towards S in the case of MoSTe). Here the bending deformation is applied against the initial curling direction (towards Te in the case of MoSTe) to study the effect of bending direction on the induced polarization. A identical simulation procedure described in section 3.2 is adopted except for inserting a minus sign in the equation (3.19) to indicate that the applied deformation is opposite to the initial curling direction.

Figure 3.11 shows the variation of  $P_z$  with  $K_{eff}$ . The dashed line at  $K_{eff} = K_{flat}$  represents the MoSTe sheet's flattening from the initial spontaneously curved state. The notable feature of figure 3.11 is that the total polarization  $P_z$  increases up to  $K_{flat}$  and decreases afterwards. This is due to an increase in bond length between Mo and S atoms, which reduces the charge transfer when  $K_{eff}$  is larger than  $K_{flat}$ , which is seen in the form of decreasing  $E_z^q$ . Specifically, the charge on an Mo atom at  $K_{flat}$  and  $1.4 \times K_{flat}$  are  $0.55e$  and  $0.43e$ , respectively, which leads to a reduction in  $E_z^q$ . A simultaneous decrease in  $E_z^p$  is also observed due to an increase in the angle B-A-C, which increases from about  $3.96^\circ$  from  $K_{flat}$  to  $1.4 \times K_{flat}$ . While the slope of the polarization  $P_z$  variation with  $K_{eff}$  is similar to the flexoelectric co-



**Figure 3.11.** Polarization  $P_z$  versus the effective strain gradient  $K_{eff}$  for MoSTe and WSTe when bending against their initial spontaneous curvature.

efficient obtained in the case of bending towards the spontaneous curling direction, more energy is required to deform towards the Te layer in MoSTe as compared to the S layer in MoSTe. As a result, bending towards the S layer in MoSTe is a better choice for energy conversion. A similar observation is found in the case of WSTe.

### 3.3.6 In-plane flexoelectric polarization

The applied deformation in section 3.2.1 yields out-of-plane polarization  $P_z$  and in-plane polarizations ( $P_x$  and  $P_y$ ). The previous section 3.3.2 to 3.3.5 focus on the out-of-plane polarization  $P_z$  accordingly the out-of-plane flexoelectric coefficients of 2D materials. Here investigates the in-plane flexoelectric polarization of the 2D materials (Graphene, BN, Silicene and MoS<sub>2</sub>). The variation of in-plane polarization  $P_x$  and  $P_y$  show a quadratic dependence with bending curvature  $K$  as shown in figure 3.12, which is similar to earlier reports for BN, see MELE & KRÁL (2002); SAI & MELE (2003); NAKHMANSON ET AL. (2003). The fitting lines for the quadratic dependence between bending curvature  $K$  and the in-plane polarization  $P_x$  and  $P_y$  are governed by

$$P_y = d_{yzx}\varepsilon_{zx} + \mu_{yxzx} \frac{\partial \varepsilon_{zx}}{\partial x} = a_{0,y} + \frac{1}{2}a_{1,y}K + \frac{1}{4}a_{2,y}K^2, \quad (3.28)$$

$$P_x = d_{xzx}\varepsilon_{zx} + \mu_{xxzx} \frac{\partial \varepsilon_{zx}}{\partial x} = a_{0,x} + \frac{1}{2}a_{1,x}K + \frac{1}{4}a_{2,x}K^2, \quad (3.29)$$

where  $a_{1,x}$  and  $a_{1,y}$  have units of C/m, which are those of flexoelectric constants, while  $a_0$  and  $a_2$  have units of C/m<sup>2</sup> and C, respectively. Taking  $a_1$  as the flexoelectric coefficient, the numerical values for Graphene, BN, Silicene, and MoS<sub>2</sub> are tabulated in table 3.5 along with the bending flexoelectric coefficients. It's noted that because the imposed mechanical bending generates the out-of-plane flexoelectric constants only generate a constant strain in



**Table 3.5.** Flexoelectric coefficients ( $\mu_{zxzx}, \mu_{yxzx}(a_{1,y}), \mu_{xxzx}(a_{1,x})$ ) given in nC/m.  $a_0$  has unit of C/m<sup>2</sup>, while  $a_2$  has unit of C.

Material	$\mu_{zxzx}$	$a_{1,y}(\mu_{yxzx})$	$a_{1,x}(\mu_{xxzx})$	$a_{0,y}$	$a_{0,x}$	$a_{2,y}$	$a_{2,x}$
Graphene	0.00286	1.53E-7	5.18E-6	-7.40E-7	-1.61E-8	-1.72E-4	1.97E-4
Silicene-flat	0.00634	1.04E-5	1.91E-5	1.69E-5	5.35E-8	-0.00180	0.00072
BN	0.00026	0.00146	3.06E-5	-5.76E-6	3.04E-7	0.26296	-1.96E-4
Silicene	0.00728	0.0027	2.94E-5	-6.43E-5	8.03E-7	-0.0164	0.00152
MoS <sub>2</sub>	0.03194	0.00962	0.00164	-0.00039	0.00060	-4.5484	-0.0512

the X-direction from applied deformation in the Z-direction, the in-plane polarization that is generated also results in contributions to the in-plane piezoelectricity.

The in-plane flexoelectric constants for the 2D materials are calculated and summarized in table 3.5. Here focus on the in-plane flexoelectric constant for MoS<sub>2</sub> as they are larger than the out-of-plane constants for the other 2D materials. From the figure 3.12 and figure 3.6, it's observed that the polarization  $P_y$  is about an order of magnitude higher than  $P_z$  for MoS<sub>2</sub>, whereas the electric field  $E_y^q$  is less than  $E_z^q$  for MoS<sub>2</sub> ( $E_z^q/E_y^q = 7$ ). This is because of cancellations in the induced dipole moments in calculating the polarization. Specifically, the dipole moments  $p_y$  have the same sign for all S atoms, whereas  $p_z$  has a different sign for the top and bottom planes of S atoms, which induces cancellation of polarization in the Z-direction making  $P_z$  smaller than  $P_y$ . Thus, while  $P_y$  is higher than  $P_z$ , the flexoelectric coefficient  $\mu_{yxzx}$  is less than  $\mu_{zxzx}$  due to its correlation with  $E_q$ . Overall, the enhanced  $\pi-\sigma$  interactions and bond length asymmetry also leads to strong in-plane electromechanical coupling and an in-plane flexoelectric constant of  $\mu_{yxzx} = 0.00962$  nC/m.

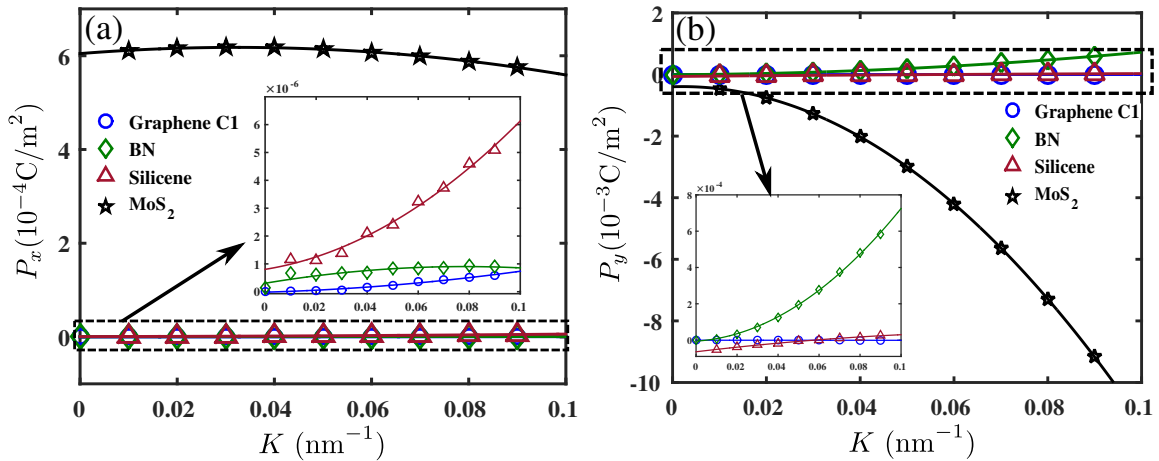


**Figure 3.12.** The variation of polarization (a)  $P_x$  and (b)  $P_y$  with bending curvature ( $K$ ) for Graphene, BN, Silicene and MoS<sub>2</sub>. The inset in (a) and (b) represent the polarization variation for materials other than MoS<sub>2</sub>.

From table 3.5, the in-plane flexoelectric coefficients ( $\mu_{yxzx}$  and  $\mu_{xxzx}$ ) are significantly

smaller than the out-of-plane coefficient ( $\mu_{zxx}$ ) of graphene under bending deformation. The corresponding in-plane polarizations  $P_x$  and  $P_y$  are also lower than the out of plane polarization  $P_z$ . This implies that the in-plane  $\pi - \sigma$  interactions for graphene generate relatively small in-plane dipole moments. A symmetry analysis can be used to show that  $\mu_{yxz}$  and  $\mu_{xzx}$  are zero, see SHU ET AL. (2011b), which implies that the graphene system is isotropic, see AHMADPOOR & SHARMA (2015b). Similarly, lower in-plane flexoelectric coefficients are observed for flat silicene (see table 3.5).

In the case of anisotropic BN, the in-plane coefficient ( $\mu_{yxz}$ ) is nearly 5 times larger than the out-of-plane coefficient ( $\mu_{zxx}$ ), as shown in table 3.5, while figure 3.12(b) and figure 3.6 show that the polarization  $P_y$  is higher than  $P_z$ . Besides, the charge-dipole coupling induced electric field  $E_y^q$  is greater than  $E_z^q$ , and that the ratio of  $E_y^q/E_z^q$  is about 4.6, which is similar to the ratio between the in-plane and out-of-plane flexoelectric coefficients. First-principles calculations for a corrugated BN sheet provide significant in-plane polarization, see NAUMOV ET AL. (2009), which is related to  $\pi$  and  $\sigma$  chemical bond shifts due to the out-of-plane atomic displacements. The minimal difference in out-of-plane displacements of the B and N atoms leads to relatively small out-of-plane dipole moments and also suggests that in-plane  $\pi - \sigma$  interactions are stronger, which makes  $\mu_{yxz}$  is higher than  $\mu_{zxx}$ , see WIRTZ ET AL. (2003); MOON & HWANG (2004).

The flexoelectric coefficient  $\mu_{zxx}$  is higher than  $\mu_{yxz}$  for the buckled silicene. The corresponding polarization  $P_z$  is greater than  $P_y$ , as observed from the figure 3.6 and 3.12(b), and the out-of-plane electric field is larger than the in-plane electric fields, which implies that the out-of-plane  $\pi - \sigma$  coupling is stronger than in-plane. It is also noted that the atomic buckling in silicene significantly enhances the in-plane flexoelectric coefficient compared to flat silicene (see values of  $\mu_{yxz}$  for silicene and silicene-flat materials in the table 3.5). Because the buckling height of silicene is significantly larger than seen in BN, larger dipole moments and larger in-plane and out-of-plane flexoelectric constants are predicted for buckled silicene as compared to BN.

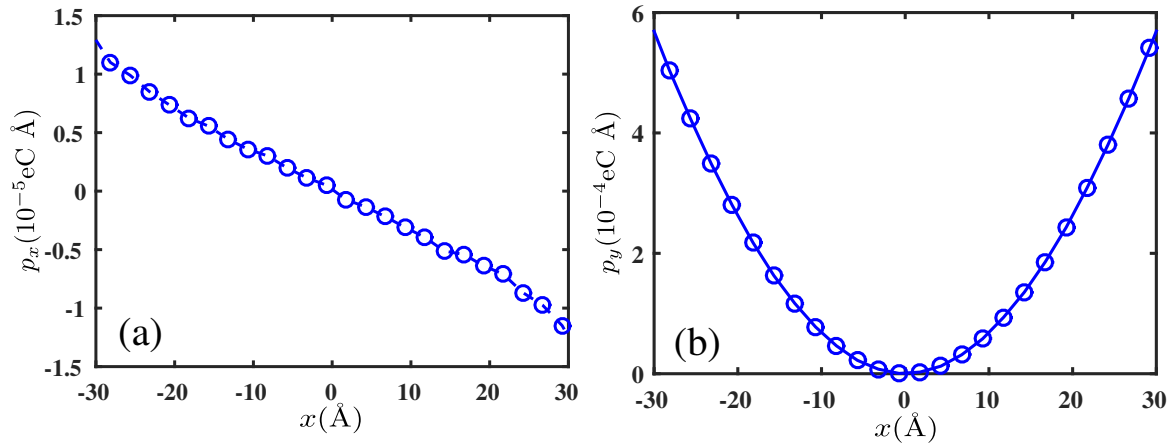


**Figure 3.13.** Bin-wise distribution of dipole (a)  $p_x$  and (b)  $p_y$  along X axis for BN at a curvature of  $K = 0.08 \text{ nm}^{-1}$ .

In BN, silicene and  $\text{MoS}_2$ , it is observed from the figure 3.12 for BN that the in-plane polar-

ization  $P_y$  is higher than the in-plane polarization  $P_x$ . In the present study, the X-direction is considered the armchair configuration. At the same time, the Y-direction represents the zigzag configuration, which means that polarization in the zigzag direction is higher than in the armchair direction, which was previously observed for BN, see NAUMOV ET AL. (2009). To further confirm this, the atomic system is rotated to change the X-direction to zigzag and the Y-direction to the armchair and repeated the bending test. There is no change in polarization of  $P_z$  and the corresponding flexoelectric coefficients. When coming to in-plane dipole, it's found  $p_x$  (zigzag) is higher than  $p_y$  (armchair) shown in figure 3.13. It's also observed that  $p_x$  is linear and  $p_y$  is parabolic, which is also the same form for the strain fields that were observed in the armchair and zigzag directions. This implies that the local atomic configuration strongly impacts the deformation, and thus the induced polarization, which was also observed in silicene and  $\text{MoS}_2$ . The observation of anisotropic in-plane polarization due to bending is similar to the earlier findings reviewed in AHMADPOOR & SHARMA (2015b). It's found that monatomic unit cells, such as graphene and flat silicene, do not exhibit spatial variations in the out-of-plane displacements due to bending, whereas  $\text{MoS}_2$ , buckled silicene, and BN do exhibit, to varying degrees, spatial variations in the out-of-plane displacements due to bending. As a result, the in-plane charge-dipole interactions are weak for graphene and flat silicene, resulting in low in-plane flexoelectric constants. In contrast,  $\text{MoS}_2$  exhibits significant structural asymmetry under bending, which enhances the in-plane  $\pi - \sigma$  coupling, with a similar effect seen in buckled silicene. While BN does not show some spatial variation in the out-of-plane displacements, the out-of-plane displacements are relatively small, and as such, the in-plane flexoelectric constants are smaller than buckled silicene and  $\text{MoS}_2$ .

### 3.4 Conclusion

This chapter presented a charge-dipole molecular dynamics model to study flexoelectricity in newly emerged 2D materials including graphene allotropes (C1, C2, C3), nitrides (BN, AlN, GaN), graphene analogues of group-IV elements (Si, Ge, Sn), transition metal dichalcogenides (TMDCs) ( $\text{MoS}_2$ ,  $\text{WS}_2$ ,  $\text{CrS}_2$ ) and Janus TMDCs ( $\text{MoSSe}$ ,  $\text{MoSTe}$ ,  $\text{MoSeTe}$ ,  $\text{WSSe}$ ,  $\text{WSTe}$ ,  $\text{WSeTe}$ ). A specially designed bending deformation applies to the 2D materials nanosheets to extract their bending flexoelectric coefficients while eliminating the interference from piezoelectricity. In doing so, the charge-dipole model analyzed the mechanisms underpinning the calculated flexoelectric coefficients by interpreting them through the electric fields generated from the dipole-dipole ( $\sigma - \sigma$  bonding) and the charge-dipole ( $\pi - \sigma$  bonding) interactions. While the charge-dipole interactions increase with bending curvature, their relative weakness in the flat monolayers (graphene, h-BN) leads to lower flexoelectric coefficients for these materials. In contrast, it is found that buckling height, which occurs in the monolayer group-IV elements, leads to more than 10% increases in flexoelectric coefficients. Additionally, due to significantly enhanced charge transfer coupled with structural asymmetry, the TMDCs have the largest flexoelectric coefficients, including the flexoelectric coefficient of  $\text{MoS}_2$  ten times larger than that of graphene. Furthermore, a particular group of TMDCs called Janus TMDCs to have flexoelectric coefficients that are several times larger than traditional TMDCs, such as  $\text{MoS}_2$ . The mechanism underlying this was the bond length asymmetry for the Janus TMDCs between the M-X and M-Y

atoms. This bond length asymmetry leads to stronger  $\sigma - \sigma$  interactions with increasing initial asymmetry, along with stronger  $\pi - \sigma$  interactions due to increased charge transfer, which combine to result in increased polarization for Janus TMDCs. So far in this work, flexoelectricity has been studied using discrete models. In the following chapter, continuum models are developed for the design guidance of flexoelectric composites.



## Chapter 4

# Continuum Modeling of Flexoelectric Composites

Continuum models for flexoelectricity need to fulfill the high-order continuity requirement ( $C^1$  continuity) due to the strain gradient coupling term in the governing equation of flexoelectricity. Two continuum approaches are capable of accommodating this  $C^1$  continuity. The first approach uses global higher order shape functions, as in the Meshless method or Isogeometric analysis (IGA). For instance, a Meshless model is developed to investigate the flexoelectric responses of a dielectric cantilever beam and truncated pyramid, see ABDOLLAHI ET AL. (2014, 2015). Later, the effect of material nonlinearity on flexoelectricity is also studied by another Meshless model and an IGA model, see ZHUANG ET AL. (2019b); THAI ET AL. (2018). The second approach to account for  $C^1$  continuity by introducing additional degrees of freedom. For example, a 2D mixed finite element model includes the Lagrange multiplier to achieve  $C^1$  continuity, and the model is used to characterize the electromechanical behavior of flexoelectric devices., see MAO ET AL. (2016). Later, researchers extended this model to 3D and developed a topology optimization scheme for flexoelectricity within its framework, see DENG ET AL. (2017); NANTHAKUMAR ET AL. (2017). So far, the existing continuum models for flexoelectricity in the literature mainly focus on the behavior of single-phase flexoelectric materials, while the behavior of multiphase flexoelectric materials (e.g., flexoelectric composites) remains unexplored.

Composite materials have demonstrated their advantages against single-phase materials in various applications, such as electrical and thermal devices, see GIBSON (2010); KONG ET AL. (2013); KALAMKAROV ET AL. (2009), sensors, see LI ET AL. (2008); GIBSON ET AL. (2007); RATNA & KARGER-KOCSIS (2008), energy harvesters, see PARK ET AL. (2008); SODANO ET AL. (2004); COOK-CHENNAULT ET AL. (2008), and electromagnetic devices, see CHUNG (2001); GEETHA ET AL. (2009); WANG & JING (2005). Meanwhile, several studies have shown that flexoelectric composites can induce a stronger electromechanical response than that of a single-phase flexoelectric material, see ZHANG ET AL. (2016); WAN ET AL. (2017); RAY (2018). To further investigate this enhancement and the underlying mechanism of flexoelectricity in composites. This chapter developed two

---

The content of this chapter is partially published in author's paper (DOI: 10.3390/en12020271)

continuum models to investigate flexoelectricity in composite structures. First, a 2D linear Meshless model couples with the level-set technique to characterize linear flexoelectricity in composite structures in section 4.1, followed by section 4.2 presenting a 3D nonlinear mixed finite element model (NMFEM) for 3D flexoelectric composites with the consideration of static and dynamic loading conditions.

## 4.1 Meshless model for flexoelectric composites

### 4.1.1 Theory of linear flexoelectricity

Based on the derivation in MAJDOUB ET AL. (2008, 2009), the enthalpy density  $\mathcal{H}$  of a dielectric solid including piezoelectric and flexoelectric effect follows

$$\mathcal{H}(\varepsilon_{ij}, E_i, \varepsilon_{jk,l}, E_{i,j}) = \frac{1}{2} \mathbb{C}_{ijkl} \varepsilon_{ij} \varepsilon_{kl} - d_{ikl} E_i \varepsilon_{kl} + (\bar{d}_{ijkl} E_{i,j} \varepsilon_{kl} + \bar{f}_{ijkl} E_i \varepsilon_{jk,l}) - \frac{1}{2} \kappa_{ij} E_i E_j, \quad (4.1)$$

where  $E_i = -\theta_{,i}$  is the electric field;  $\theta$  being the electric potential;  $\varepsilon$  is the mechanical strain;  $\mathbb{C}$  is the fourth-order elastic moduli;  $\mathbf{d}$  is the third-order tensor of piezoelectricity;  $\bar{\mathbf{f}}$  and  $\bar{\mathbf{d}}$  are the fourth-order direct and converse flexoelectric tensor, respectively;  $\mathbf{k}$  is the second-order dielectric tensor. Study shows that one material tensor  $\mu_{ijkl} = \bar{d}_{iljk} - \bar{f}_{ijkl}$  is sufficient to describe the overall flexoelectric coefficient, see SHARMA ET AL. (2010). The equation (4.1) rewrites as

$$\mathcal{H}(\varepsilon_{ij}, E_i, \varepsilon_{jk,l}, E_{i,j}) = \frac{1}{2} \mathbb{C}_{ijkl} \varepsilon_{ij} \varepsilon_{kl} - d_{ikl} E_i \varepsilon_{kl} - \mu_{ijkl} E_i \varepsilon_{jk,l} - \frac{1}{2} \kappa_{ij} E_i E_j. \quad (4.2)$$

The strain and electric displacement from piezoelectricity are

$$\hat{\sigma}_{ij} = \frac{\partial \mathcal{H}}{\partial \varepsilon_{ij}}; \quad \hat{D}_i = -\frac{\partial \mathcal{H}}{\partial E_i}. \quad (4.3)$$

Due to the presence of flexoelectricity, the higher-order stress and electric displacement read

$$\bar{\sigma}_{ijk} = \frac{\partial \mathcal{H}}{\partial \varepsilon_{ij,k}}; \quad \bar{D}_{ij} = -\frac{\partial \mathcal{H}}{\partial E_{i,j}}. \quad (4.4)$$

The physical stress and electric displacement are

$$\begin{aligned} \sigma_{ij} &= \hat{\sigma}_{ij} - \bar{\sigma}_{ijk,k} = \mathbb{C}_{ijkl} \varepsilon_{kl} - d_{kij} E_k + \mu_{lij} E_{l,k}; \\ D_i &= \hat{D}_i - \bar{D}_{ij,j} = d_{ikl} \varepsilon_{kl} + \kappa_{ij} E_j + \mu_{ijkl} \varepsilon_{jk,l}. \end{aligned} \quad (4.5)$$

The essential and natural electric boundary conditions are

$$\begin{aligned} \theta &= \bar{\theta} \quad \text{on} \quad \Gamma_\theta; \\ D_i n_i &= -w \quad \text{on} \quad \Gamma_D; \\ \Gamma_\theta \cup \Gamma_D &= \partial\Omega \quad \text{and} \quad \Gamma_\theta \cap \Gamma_D = \emptyset, \end{aligned} \quad (4.6)$$

where  $\bar{\theta}$  and  $w$  are the applied electric potential and surface charge density,  $\partial\Omega$  represents the boundary of the domain,  $n_i$  is the unit normal to the boundary  $\partial\Omega$ . The mechanical boundary conditions are given as

$$\begin{aligned} u &= \bar{u} & \text{on } \Gamma_u ; \\ t_k &= \bar{t}_k & \text{on } \Gamma_t ; \\ \Gamma_u \cup \Gamma_t &= \partial\Omega & \text{and } \Gamma_u \cap \Gamma_t = \emptyset , \end{aligned} \quad (4.7)$$

where  $\bar{u}$  and  $\bar{t}_k$  represent mechanical displacement and traction. The remain boundary conditions (normal derivation of displacement and higher-order tractions) resulted from strain gradient have been set to zero under the assumptions of homogeneous natural boundary conditions.

Rewrite the equation (4.3) and (4.4) as

$$\begin{aligned} \partial\mathcal{H} &= \hat{\sigma}_{ij}\partial\varepsilon_{ij} ; \\ \partial\mathcal{H} &= \bar{\sigma}_{ijk}\partial\varepsilon_{ij,k} ; \\ \partial\mathcal{H} &= -\hat{D}_i\partial E_i , \end{aligned} \quad (4.8)$$

and integrate them over the domain  $\Omega$  gives

$$\mathbf{H} = \frac{1}{2} \int_{\Omega} \left( \hat{\sigma}_{ij}\varepsilon_{ij} + \bar{\sigma}_{ijk}\varepsilon_{ij,k} - \hat{D}_i E_i \right) d\Omega , \quad (4.9)$$

where  $\mathbf{H}$  is the total electrical enthalpy.

The external work done by the mechanical and electrical forces on the surface is

$$\mathbf{W}_{ext} = \int_{\Gamma_t} \bar{t}_i u_i dS - \int_{\Gamma_D} w \theta dS . \quad (4.10)$$

Finally, the weak form of mechanical and electrical equilibrium derived from the Hamilton principle for static problem yields

$$0 = \int_{\Omega} \left( \hat{\sigma}_{ij}\delta\varepsilon_{ij} + \bar{\sigma}_{ijk}\delta\varepsilon_{ij,k} - \hat{D}_i\delta E_i \right) d\Omega - \int_{\Gamma_t} \bar{t}_i \delta u_i dS - \int_{\Gamma_D} w \delta\theta dS . \quad (4.11)$$

Substitute the equations (4.3), (4.4) and (4.5) into the equation (4.11) yields the final weak form of the governing equation of linear flexoelectricity:

$$\begin{aligned} & \int_{\Omega} \left( \mathbb{C}_{ijkl}\delta\varepsilon_{ij}\varepsilon_{kl} - d_{kij}E_k\delta\varepsilon_{ij} - \mu_{lij}E_l\delta\varepsilon_{ij,k} - \kappa_{ij}\delta E_i E_j - d_{ikl}\delta E_i \varepsilon_{kl} - \mu_{ijkl}\delta E_i \varepsilon_{jk,l} \right) d\Omega \\ & - \int_{\Gamma_t} \bar{t}_i \delta u_i dS - \int_{\Gamma_D} w \delta\theta dS = 0 . \end{aligned} \quad (4.12)$$

The unknowns (e.g. displacement and electric potential) in the equation (4.12) are approximated by the Moving Least Square approximation (MLS). The details of MLS are given in the following section 4.1.2.



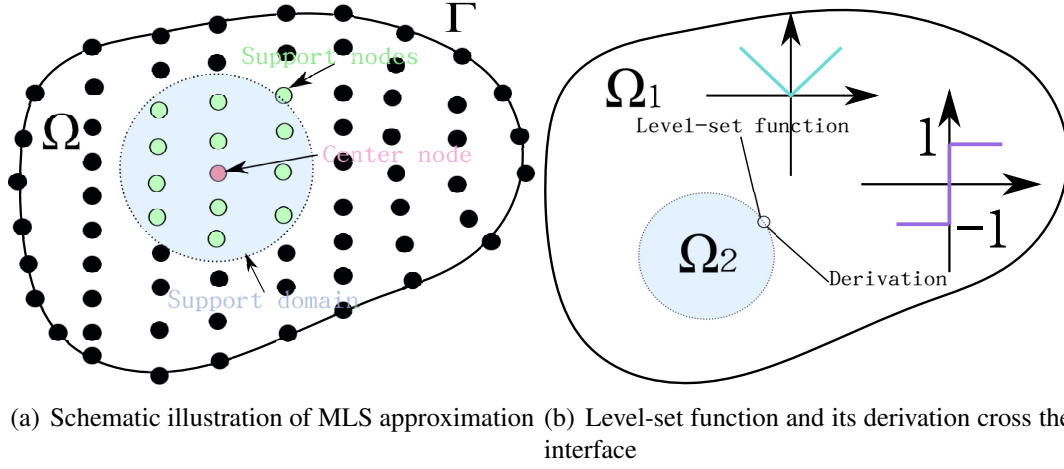


**Figure 4.1.** (a) Schematic illustration of the MLS approximation, and (b) Level-set function and its derivation cross the interface.

### 4.1.2 Moving least square approximation

The MLS approximation within the Element-Free Galerkin scheme is first introduced in BELYTSCHKO ET AL. (1994, 1995). It approximates the unknowns by the neighboring nodes in its support domain (figure 4.1(a)). To study the flexoelectricity in composite materials, the level-set technique is integrated into the standard MLS scheme to describe the weak discontinuity between the inclusions and matrix of composite materials. The level-set technique adds extra enrichments to the nodes, which locate on both sides of the interfaces between the inclusions and matrix. The extra enrichments are modeled by a level-set function based on the absolute sign distance function  $\bar{\Psi}(x)$ . The schematic illustration of the level-set function and its derivation cross the interface is shown in the figure 4.1(b). The local approximation of the displacement  $\mathbf{u}$  and electric potential  $\theta$  considering the enrichments are

$$\begin{aligned} \mathbf{u}(x) &= \sum_{i=1}^N N_i(x) \mathbf{u}_i + \sum_{i=j}^M N_j(x) \bar{\Psi}(x) \mathbf{u}_j ; \\ \theta(x) &= \sum_{i=1}^N N_i(x) \theta_i + \sum_{i=j}^M N_j(x) \bar{\Psi}(x) \theta_j , \end{aligned} \quad (4.13)$$

where  $N(x)$  are the shape functions at position  $x$ ,  $\mathbf{u}$  and  $\theta$  are the nodal displacements and electric potential,  $N$  and  $M$  are the number of support and enriched nodes, respectively. The shape function  $N_i(x)$  associates with node  $i$  and a point  $x$  reads

$$N_i(x) = \bar{\mathbf{p}}^T(x) [\mathbf{A}(x)]^{-1} \bar{w}(x - x_i) \bar{\mathbf{p}}(x_i) , \quad (4.14)$$

where  $\bar{\mathbf{p}}(x)$  is the complete polynomial order:

$$\bar{\mathbf{p}}^T(x) = [1 \ x \ y \ x^2 \ xy \ y^2] . \quad (4.15)$$

The quartic spline weight function  $\bar{w}$  ensures a second-order continuity inside an element, and achieves  $C^1$  continuity between elements, see NGUYEN ET AL. (2008).

$$\bar{w}(r) = \begin{cases} 1 - 6r^2 + 8r^3 - 3r^4 & \text{if } r \leq 1 \\ 0 & \text{if } r > 1 \end{cases}, \quad (4.16)$$

with

$$r = \frac{\|x_i - x\|}{d_s}, \quad (4.17)$$

$d_s$  is the predefined search radius of the support domain and  $d_s$  sets to 3 times of the nodal spacing to avoid a singular moment matrix  $\mathbf{A}(x)$ . The moment matrix  $\mathbf{A}(x)$  has the form

$$\mathbf{A}(x) = \sum_{i=1}^N \bar{w}(x - x_i) \bar{\mathbf{p}}(x_i) \bar{\mathbf{p}}^T(x_i). \quad (4.18)$$

The enrichment function  $\bar{\Psi}(x)$  has the form, see SUKUMAR ET AL. (2001):

$$\bar{\Psi}(x) = \text{abs}(\bar{\psi}(x)); \quad \bar{\psi}(x) = \min_{i=1,2,\dots,n_c} \{ \|x - x_c^i\| - r_c^i \}, \quad (4.19)$$

where  $n_c$  is the total number of inclusions inside the domain,  $x_c^i$  is the center coordinate of the  $i$ -th circular inclusion,  $r_c^i$  is the radius of the  $i$ -th circular inclusion. For simplicity, the approximations are written in a simplified form (e.g  $\mathbf{u}^h = \mathbf{N}_u \mathbf{u}^{std} + \mathbf{N}_u \bar{\Psi} \mathbf{u}^{enr}$ ). The derivatives of the unknowns  $\mathbf{u}$  and  $\theta$  (in equation (4.13)) contain the standard derivation for non-enriched nodes ( $\mathbf{u}^{std}$ ,  $\theta^{std}$ ) and the derivation for enriched nodes ( $\mathbf{u}^{enr}$ ,  $\theta^{enr}$ ):

$$\begin{aligned} \partial \mathbf{u}^h &= \partial \mathbf{N}_u \mathbf{u}^{std} + \partial \mathbf{N}_u \bar{\Psi} \mathbf{u}^{enr} + \mathbf{N}_u \partial \bar{\Psi} \mathbf{u}^{enr}; \\ \partial \partial \mathbf{u}^h &= \partial \partial \mathbf{N}_u \mathbf{u}^{std} + \partial \partial \mathbf{N}_u \bar{\Psi} \mathbf{u}^{enr} + \mathbf{N}_u \partial \partial \bar{\Psi} \mathbf{u}^{enr} + 2 \partial \mathbf{N}_u \partial \bar{\Psi} \mathbf{u}^{enr}; \\ \partial \theta^h &= \partial \mathbf{N}_\theta \theta^{std} + \partial \mathbf{N}_\theta \bar{\Psi} \theta^{enr} + \mathbf{N}_\theta \partial \bar{\Psi} \theta^{enr}, \end{aligned} \quad (4.20)$$

with

$$\mathbf{B}_u = \partial \mathbf{N}_u = \begin{bmatrix} \frac{\partial}{\partial x} & 0 & \frac{\partial}{\partial y} \\ 0 & \frac{\partial}{\partial y} & \frac{\partial}{\partial x} \end{bmatrix}; \quad (4.21)$$

$$\mathbf{B}_\theta = \partial \mathbf{N}_\theta = \begin{bmatrix} \frac{\partial}{\partial x} & \frac{\partial}{\partial y} \end{bmatrix}; \quad (4.22)$$

$$\mathbf{H}_u = \partial \partial \mathbf{N}_u = \begin{bmatrix} \frac{\partial^2}{\partial x^2} & 0 & \frac{\partial^2}{\partial x \partial y} & \frac{\partial^2}{\partial x \partial y} & 0 & \frac{\partial^2}{\partial y^2} \\ 0 & \frac{\partial^2}{\partial x \partial y} & \frac{\partial^2}{\partial x^2} & 0 & \frac{\partial^2}{\partial y^2} & \frac{\partial^2}{\partial x \partial y} \end{bmatrix}; \quad (4.23)$$

$$\mathbf{B}_u^{enr} = \partial \mathbf{N}_u \bar{\Psi} + \mathbf{N}_u \partial \bar{\Psi}; \quad (4.24)$$

$$\mathbf{B}_\theta^{enr} = \partial \mathbf{N}_\theta \bar{\Psi} + \mathbf{N}_\theta \partial \bar{\Psi}; \quad (4.25)$$

$$\mathbf{H}_u^{enr} = \partial \partial \mathbf{N}_u \bar{\Psi} + \mathbf{N}_u \partial \partial \bar{\Psi} + 2 \partial \mathbf{N}_u \partial \bar{\Psi}. \quad (4.26)$$

The details of  $\mathbf{B}_u^{enr}$ ,  $\mathbf{B}_\theta^{enr}$ ,  $\mathbf{H}_u^{enr}$  are listed in the Appendix B. Substitute the equations (4.20) ~ (4.26) into the equation (4.12), the matrix form of the equilibrium yields

$$\begin{bmatrix} \mathbf{K}_{uu} & \mathbf{K}_{u\theta} \\ \mathbf{K}_{u\theta}^T & \mathbf{K}_{\theta\theta} \end{bmatrix} \cdot \begin{bmatrix} \mathbf{u} \\ \boldsymbol{\theta} \end{bmatrix} = \begin{bmatrix} \mathbf{f}_u \\ \mathbf{f}_\theta \end{bmatrix}, \quad (4.27)$$

with

$$\mathbf{K}_{uu} = \sum_i \int_{\Omega_e} (\mathbf{B}_u + \mathbf{B}_u^{enr}) \mathbb{C} (\mathbf{B}_u + \mathbf{B}_u^{enr})^T d\Omega_e; \quad (4.28)$$

$$\mathbf{K}_{u\theta} = \sum_i \int_{\Omega_e} ((\mathbf{B}_u + \mathbf{B}_u^{enr}) \mathbf{e} (\mathbf{B}_\theta + \mathbf{B}_\theta^{enr})^T + (\mathbf{H}_u + \mathbf{H}_u^{enr}) \boldsymbol{\mu}^T (\mathbf{B}_\theta + \mathbf{B}_\theta^{enr})^T) d\Omega_e; \quad (4.29)$$

$$\mathbf{K}_{\theta\theta} = - \sum_i \int_{\Omega_e} (\mathbf{B}_\theta + \mathbf{B}_\theta^{enr}) \boldsymbol{\kappa} (\mathbf{B}_\theta + \mathbf{B}_\theta^{enr})^T d\Omega_e; \quad (4.30)$$

$$\mathbf{f}_u = \sum_i \int_{\Gamma_{te}} \mathbf{N}_u^T \mathbf{t}_\Gamma d\Gamma_{te}; \quad (4.31)$$

$$\mathbf{f}_\theta = - \sum_i \int_{\Gamma_{De}} \mathbf{N}_\theta^T \mathbf{w} d\Gamma_{De}. \quad (4.32)$$

The employed shape function does not preserve the Kronecker-Delta property, the developed model uses the Lagrange multiplier method to impose mechanical and electrical boundary conditions. The material property matrices (in Voigt notation)  $\mathbb{C}$ ,  $\boldsymbol{\kappa}$ ,  $\mathbf{e}$ ,  $\boldsymbol{\mu}$  have the form

$$\mathbb{C} = \frac{E_{els}}{(1+\nu)(1-2\nu)} \begin{bmatrix} 1-\nu & \nu & 0 \\ \nu & 1-\nu & 0 \\ 0 & 0 & (\frac{1}{2}-\nu) \end{bmatrix}; \quad (4.33)$$

$$\boldsymbol{\kappa} = \begin{bmatrix} k_{11} & 0 \\ 0 & k_{33} \end{bmatrix}; \quad (4.34)$$

$$\mathbf{d}^T = \begin{bmatrix} 0 & 0 & d_{15} \\ d_{31} & d_{33} & 0 \end{bmatrix}; \quad (4.35)$$

$$\boldsymbol{\mu} = \begin{bmatrix} \mu_{11} & \mu_{12} & 0 & 0 & 0 & \mu_{44} \\ 0 & 0 & \mu_{44} & \mu_{12} & \mu_{11} & 0 \end{bmatrix}. \quad (4.36)$$

### 4.1.3 Numerical results and discussion

In this section, the developed model validates with benchmark problems: (a) the flexoelectric response of a cantilever beam under mechanical and electrical loading conditions and (b) flexoelectric response in a mechanically-compressed truncated pyramid. Note that these problems are free from material discontinuity. The obtained results are validated with an existing study, see ABDOLLAHI ET AL. (2014). Subsequently, the model coupled with material discontinuity and local enrichments investigates the flexoelectric response in the composite structures.

**Table 4.1.** Material parameters.

Name	Symbol	Value
Poisson ratio	$\nu$	0.37
Young's modulus	$E_{els}$	100 GPa
Piezoelectric constant	$d_{31}$	-4.4 nC/m <sup>2</sup>
flexoelectric constant	$\mu_{12}$	1 $\mu$ C/m
dielectric constant	$\kappa_{11}; \kappa_{33}$	11 nC/Vm; 12.48 nC/Vm
electric susceptibility	$\bar{\chi}$	1408

### Cantilever beam

Figure 4.2(a) and 4.2(b) show the simulation setups for an open circuit cantilever beam under mechanical loading condition and a close circuit cantilever beam under electrical loading condition, respectively. The length to thickness ratio  $L/h$  of the cantilever beam is 20. Table 4.1 reports the material parameters, see GHASEMI ET AL. (2017).

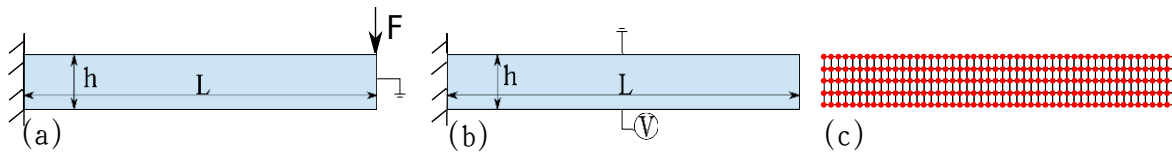


**Figure 4.2.** Schematic illustration of the cantilever beam under (a) mechanical load, (b) electrical load, and (c) MLS discretization with the red solid points representing the nodes.

**Mechanical loading** For the case of a cantilever beam under mechanical loading condition, a point load  $F = 100\mu N$  applies to the upper-right edge of the cantilever beam (figure 4.2(a)). Zero electric potential applies on the right edge. Electromechanical coupling generates the electrical energy under point-load deformation. The conversion ratio from mechanical to electrical energy ( $\bar{k}_{eff}^2$ ) is

$$\bar{k}_{eff}^2 = \frac{W_{elec}}{W_{mech}} = \frac{\int \mathbf{E} \cdot \boldsymbol{\kappa} \cdot \mathbf{E}}{\int \boldsymbol{\varepsilon} : \mathbb{C} : \boldsymbol{\varepsilon}}. \quad (4.37)$$

The present model assumes that the transversal piezoelectric ( $d = d_{31}$ ) and flexoelectric ( $\mu = \mu_{12}$ ) components are the only non-zero terms in the equations (4.35) and (4.36) for simplicity. The Poisson effect is also ignored. The results of this simplified model will be validated with the analytical solution derived in MAJDOUB ET AL. (2008). The analytical solution for  $k_{eff}$  is

$$\bar{k}_{eff} = \frac{\bar{\chi}}{1 + \bar{\chi}} \sqrt{\frac{\kappa}{E_{els}} \left( d^2 + 12 \left( \frac{\mu}{h} \right)^2 \right)}, \quad (4.38)$$

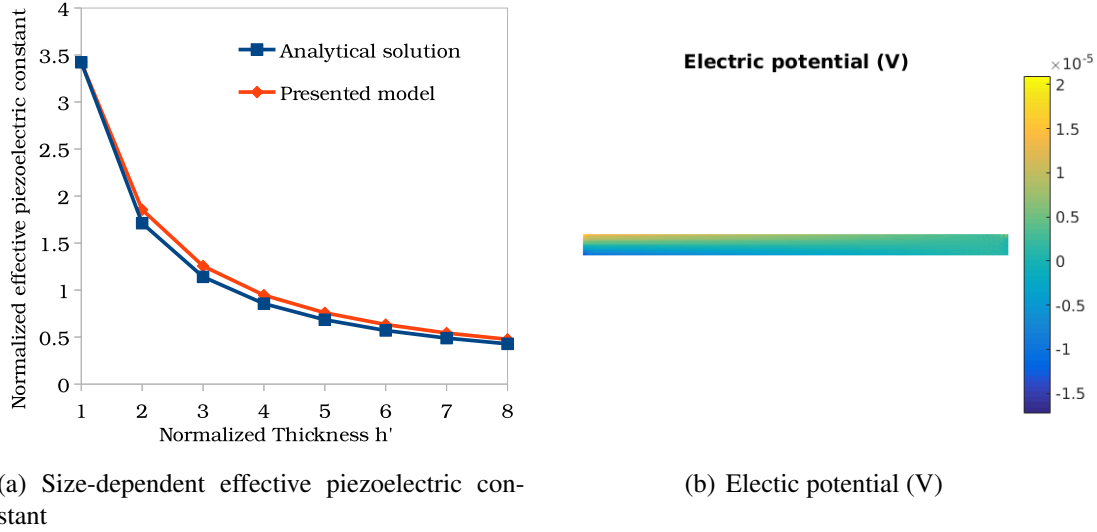


**Figure 4.3.** Calculation result: (a) size dependent effective piezoelectric constant, and (b) electric potential profile for the 2D fully coupled cantilever beam.

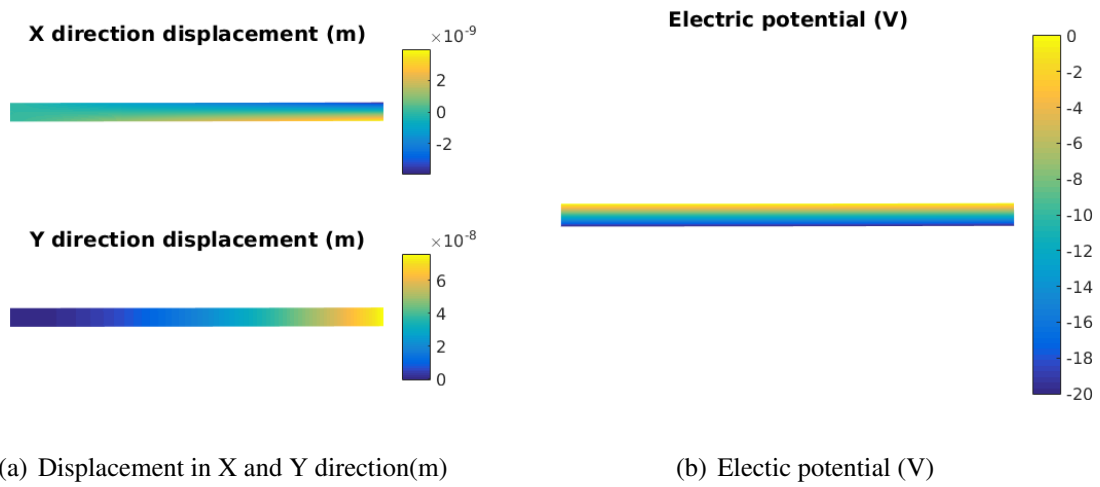
where the normalized piezoelectric constant is

$$d' = \frac{\bar{k}_{eff}}{\bar{k}_{piezo}}, \quad (4.39)$$

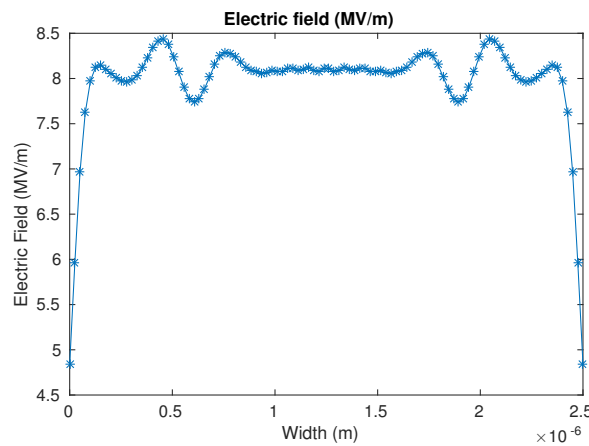
with  $\bar{k}_{piezo}$  obtained by neglecting flexoelectric effect in the equation (4.37).

Figure 4.3(a) plots the comparison between the present model and the analytical solution, where  $h' = -dh/\mu$  is the normalized beam thickness in the open circuit mechanical loading case. The variation between the normalized piezoelectric constant  $d'$  and the normalized thickness  $h'$  from the present model agrees with the analytical solution from the equation (4.39). It proves that the present model correctly estimates the electromechanical coupling behavior in a non-piezoelectric beam under bending deformation. The flexoelectricity dominates the conversion between the mechanical and electric energy due to the low piezoelectric constant of the material (refer to table 4.1). Figure 4.3(b) shows the generated electric potential profile of the open circuit cantilever beam.

**Electrical loading** Here investigates the electromechanical coupling of a cantilever beam (figure 4.2(b)) under pure electric loading condition, serving as an actuator. The setup enforces an electrical loading of  $-20$ V on the bottom edge of the cantilever beam (figure 4.2(b)), and grounds the top edge. There is no external mechanical loading on the cantilever beam. The left side of the cantilever beam is mechanically fixed. Figure 4.4 displays the induced displacement and electric potential profiles. The electric field across the beam in the Y-direction is shown in figure 4.5. Figure 4.5 indicates opposite electric field gradients near the top and bottom of the cantilever beam due to converse flexoelectricity, resulting in deformation of the cantilever beam. The displacement and electric potential profiles of the



**Figure 4.4.** Calculation result of a cantilever beam under electric loading condition: (a) beam displacement, and (b) electric potential profile.



**Figure 4.5.** The electric field profile cross the beam in the Y-direction at mid-length of the beam.

cantilever beam are in good agreement with an existing study based on an IGA analysis, see GHASEMI ET AL. (2017).

### Compressed truncated pyramid

This section further investigates the flexoelectric response of a mechanically compressed truncated pyramid (figure 4.6). The top edge of the pyramid is grounded, and a uniform force of  $-6 \mu\text{N}$  applies to it. The bottom edge length of the pyramid is  $2250 \mu\text{m}$ , and the top edge length is  $750 \mu\text{m}$ . The height  $h$  of the pyramid is  $750 \mu\text{m}$ . The remaining material parameters are listed in the table 4.1. Due to the difference in the top ( $a_1$ ) and bottom ( $a_2$ ) edge lengths of the truncated pyramid, the applied uniform force  $F$  leads to different strains at the top and bottom edges of the truncated pyramid, which results in a strain gradient in the vertical direction (Y-direction). Figure 4.7 shows the resulted strain in the YY-direction

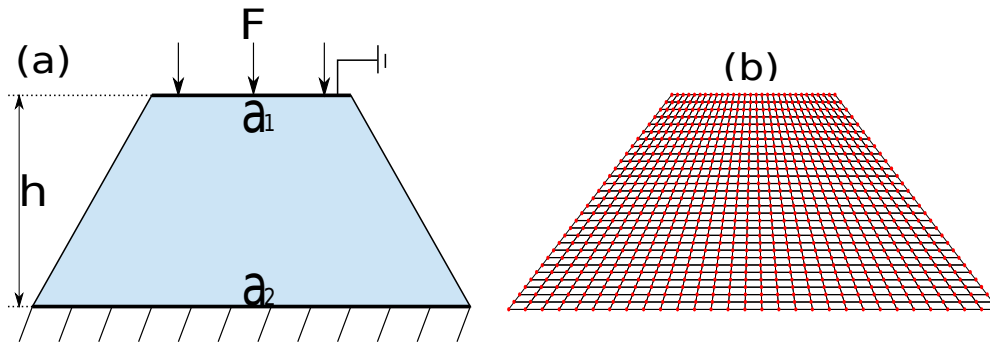


**Figure 4.6.** Schematic illustration of (a) truncated pyramid and its boundary conditions, and (b) MLS discretization with the red solid points representing the nodes.

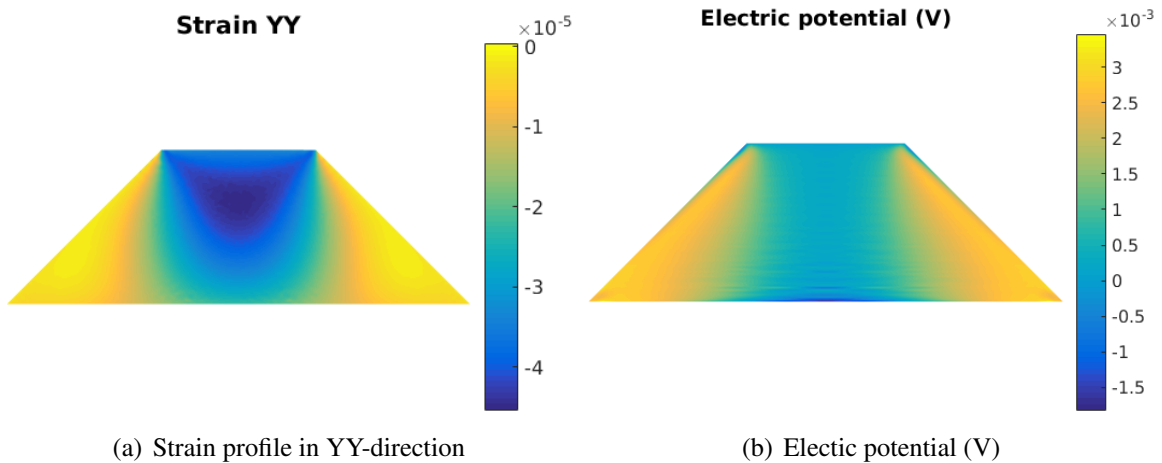


**Figure 4.7.** Calculation result of the compressed truncated pyramid: (a) strain profile in the Y-direction, and (b) electric field profile.

and the induced electric potential profiles. The resulting strain and electric potential agree well with a previous report in terms of numerical value and contour, see GHASEMI ET AL. (2017).

### Flexoelectricity in composite

This section demonstrates the possibility of inducing electric polarization in composite systems without the piezoelectric effect. A non-piezoelectric composite system consists of an embedding matrix (square shape) and an inclusion (circular shape) is shown in the figure 4.8. The edge length of the square domain is  $L = 10 \mu\text{m}$  with the center inclusion has a radius  $r_1 = 1.5 \mu\text{m}$ . The bottom edge of the matrix is grounded and a compressive force applies to its top edge. The dielectric constant of the inclusion is 10% as that of the matrix. It assumes that Young's modulus of the matrix material ( $E_{mat}$ ) is lower than that of the inclusion material ( $E_{inc}$ ). Three different Young's modulus ratios ( $\frac{E_{inc}}{E_{mat}} = 10, 100, 1000$ ) are used to

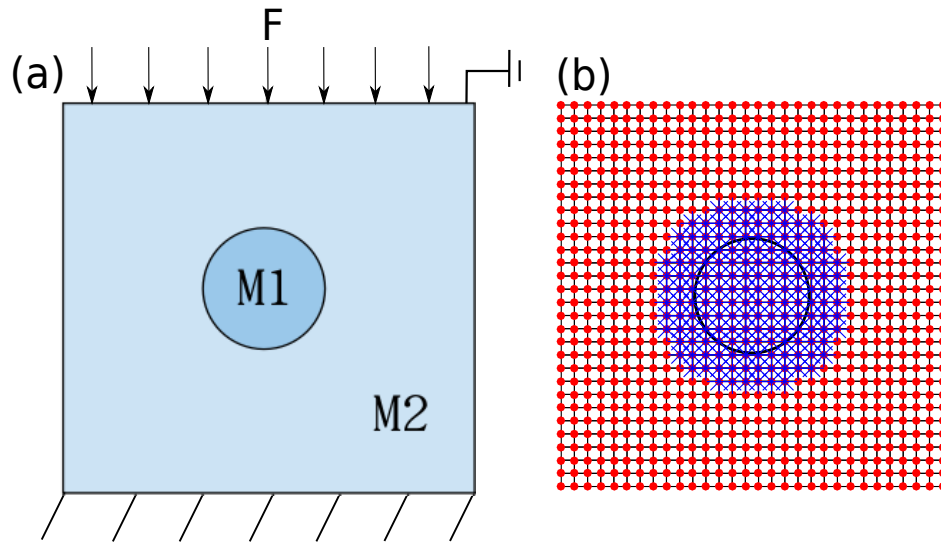


**Figure 4.8.** Schematic illustration of (a) square domain with center inclusion and the boundary conditions, and (b) MLS discretization with the red solid points representing the nodes and blue asterisks representing the enriched nodes.

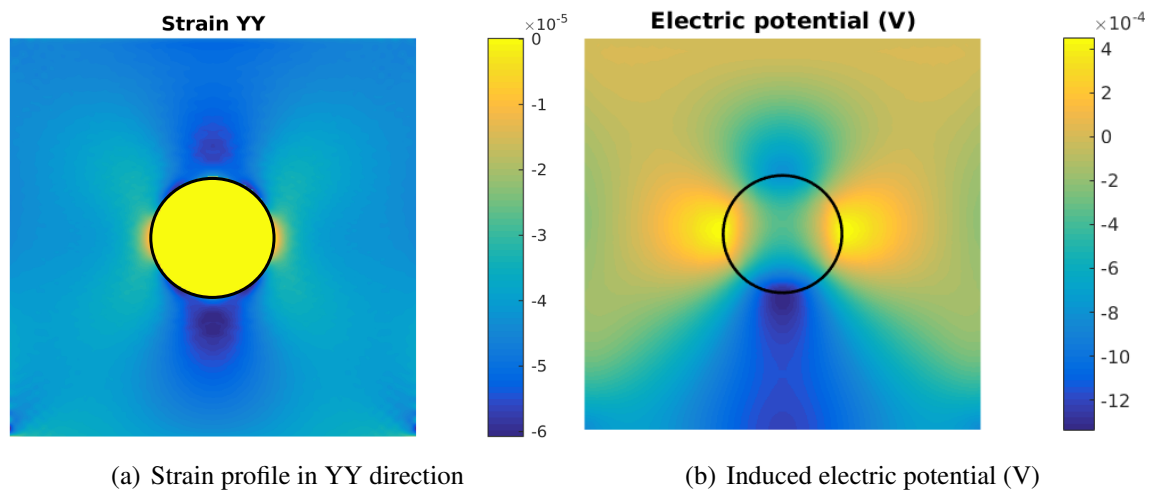
investigate its influence on the energy transfer ratio between mechanical energy and electrical energy. The remaining parameters (table 4.1) for both components are identical. Here assumes that under a mechanical load, electrical polarization will arise in the composite from flexoelectricity due to the local strain gradients near the inclusion boundary.

Figure 4.9 presents the strain and electric potential profile of the mechanically compressed composite. As assumed, the non-uniform strain field near the inclusion boundary generates a strong strain gradient field. Figure 4.10 plots the strain gradient profiles  $\varepsilon_{yy,y}$  and  $\varepsilon_{xx,x}$  along the horizontal and vertical centerlines of the square domain. In both directions, a high strain gradient is seen near the inclusion boundary due to the different material toughness (Young's modulus) of the matrix and the inclusion. Since the piezoelectric coefficients of the matrix and the inclusion are set to zero, the induced electrical potential rises only from flexoelectricity. More specifically, the linear relationship between the electrical potential and the strain gradient described by flexoelectricity is responsible for the strong electrical potential near the inclusion boundary, where strong strain gradient fields locate, as seen from figure 4.9(b).

Studies on composites indicated that the volume ratio of the inclusions has a significant impact on the overall properties of the composites, see HE ET AL. (2016); ZHANG ET AL. (2016); WAN ET AL. (2017); RAY (2018). To further investigate the effect of the varying volume ratio on the flexoelectric response in composites, here conducts simulations with different inclusion area ratios (in 2D) under the same loading condition. The area ratio of the inclusions varies from 0.5 ~ 2.5%. The area ratio is defined as the total area of the inclusions divides the area of square domain. For each area ratio, simulations with varying location of inclusions are conducted to avoid uncertainty, hereafter, the averaged result (energy conversion ratio calculated from equation (4.37)) from all simulations is taken for further analysis.



Note that, to insert multiple inclusions, the radius of the inclusion decreases to  $0.4 \mu\text{m}$ . Figure 4.11(a) shows the electric potential of a domain with 10 randomly-distributed inclusions. It shows that the non-uniform strain fields near the inclusion boundary induce high electric potential. Furthermore, enhanced electric potentials are noted in the region between nearby inclusions. It corresponds to the interaction of the non-uniform strain fields around the neighboring inclusions. Figure 4.11(b) plots the energy conversion ratio versus the inclusion area ratio. It shows that the energy conversion ratio increases with the inclusion area ratio. It is explained by the rising strain irregularity (higher strain gradient) inside the composite with the increasing inclusion area ratio, thus a stronger flexoelectric response. Figure 4.11(b) also indicates that composites with an identical inclusion area ratio but a higher  $\frac{E_{inc}}{E_{mat}}$  induce a stronger mechanical to electrical energy conversion. It suggests that a softer matrix material enhances the electromechanical response of flexoelectric composites.



**Figure 4.9.** Calculation result of the square composite under compression: (a) strain profile in the YY direction, and (b) induced electric potential.

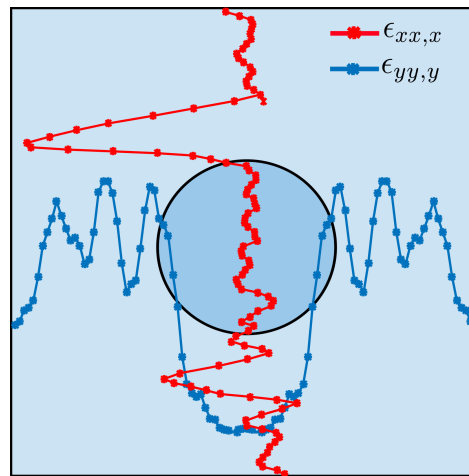
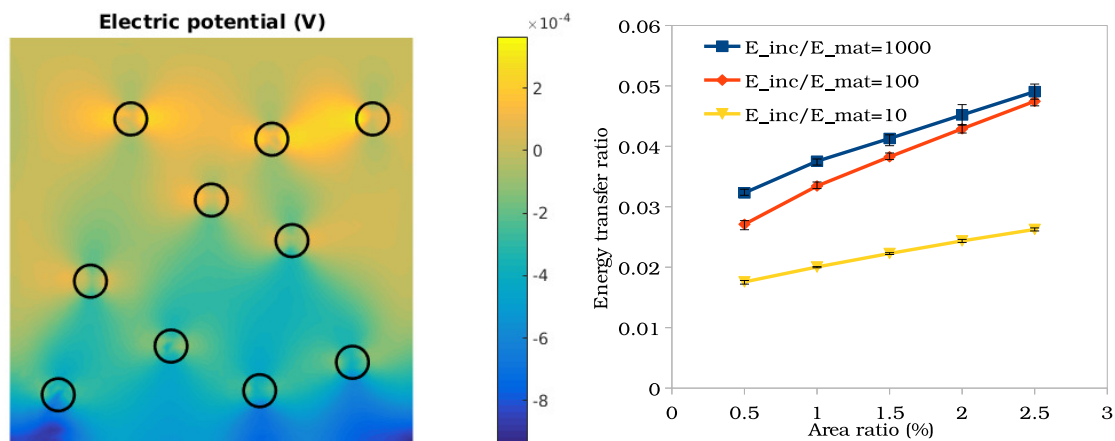


**Figure 4.10.** Strain gradient profiles along the horizontal center line ( $\epsilon_{yy,y}$ ) and vertical center line ( $\epsilon_{xx,x}$ ).



(a) Electric potential profile with ten inclusions (area ratio = 5.0%) (b) Energy conversion ratio calculated by equation (4.37) vs inclusion area ratio

**Figure 4.11.** Calculation result of a compressed square composite with randomly distributed inclusions: (a) electric potential profile, and (b) energy conversion ratio.

## 4.2 Mixed finite element model for flexoelectric composites

In the previous section 4.1, a Meshless model was developed to study flexoelectricity in 2D structures assuming small strains and static loading conditions. In this section, a 3D nonlinear mixed finite element model (NMFEM) considering geometric nonlinearity, strain gradient elasticity, static and dynamic loading conditions is developed to study flexoelectricity in 3D structures.

### 4.2.1 Mixed finite element formulation for the nonlinear flexoelectricity

This section presents the mixed finite element formulation considering geometric nonlinearity of flexoelectricity. The formulation adopts the Saint Venant–Kirchhoff material model. Hence the internal strain energy density of a flexoelectric structure follows, see SHEN & HU (2010),

$$U_{flexo} = \frac{1}{2} \mathbf{S} : \mathbf{G} + \frac{1}{2} \tilde{\boldsymbol{\tau}} : \tilde{\boldsymbol{\eta}} - \frac{1}{2} \mathbf{D} \cdot \mathbf{E}, \quad (4.40)$$

where  $\mathbf{S}$  is the second Piola-Kirchhoff stress tensor,  $\mathbf{G}$  is the second-order Green-Lagrange strain tensor,  $\tilde{\boldsymbol{\tau}}$  is the third order double stress tensor and  $\tilde{\boldsymbol{\eta}}$  is the gradient of the Green-Lagrange strain tensor in terms of the displacement gradient  $\boldsymbol{\psi}$ , where the second-order tensor  $\boldsymbol{\psi} = \nabla \mathbf{u}$ .  $\mathbf{D}$  is the first order electric displacement vector,  $\mathbf{E}$  is the first order electric field vector. The total potential energy  $\Pi$  of a flexoelectric structure, including the boundary conditions and the Lagrange multipliers for ensuring  $C^1$  continuity is

$$\begin{aligned} \Pi = & \int_{\Omega} U_{flexo} d\Omega - \int_{\Gamma_u} \mathbf{u} \cdot \mathbf{t} d\Gamma_u - \int_{\Omega} \mathbf{u} \cdot \mathbf{b} d\Omega \\ & + \int_{\Gamma_\theta} \theta q d\Gamma_\theta + \int_{\Omega} \boldsymbol{\lambda} : (\boldsymbol{\psi} - \nabla \mathbf{u}) d\Omega \end{aligned}, \quad (4.41)$$

where  $\mathbf{u}$  and  $\theta$  are mechanical displacement and electric potential, respectively.  $\mathbf{t}$  is the surface traction,  $\mathbf{b}$  is the body force and  $q$  is the surface charge density.  $\boldsymbol{\lambda}$  is the Lagrange multiplier to enforce the kinematic constraint between gradient of displacement and  $\boldsymbol{\psi}$ . The Neumann boundary for the mechanical displacement and electric potential denote as  $\Gamma_u$  and  $\Gamma_\theta$ , respectively. The first variation of the total potential energy  $\Pi$  gives

$$\begin{aligned} \delta \Pi = & \int_{\Omega} \mathbf{S} : \delta \mathbf{G} d\Omega + \int_{\Omega} \tilde{\boldsymbol{\tau}} : \delta \tilde{\boldsymbol{\eta}} d\Omega - \int_{\Omega} \mathbf{D} \cdot \delta \mathbf{E} d\Omega \\ & - \int_{\Gamma_u} \delta \mathbf{u} \cdot \mathbf{t} d\Gamma_u - \int_{\Omega} \delta \mathbf{u} \cdot \mathbf{b} d\Omega + \int_{\Gamma_\theta} \delta \theta q d\Gamma_\theta \\ & + \int_{\Omega} \boldsymbol{\lambda} : (\delta \boldsymbol{\psi} - \nabla \delta \mathbf{u}) d\Omega + \int_{\Omega} (\boldsymbol{\psi} - \nabla \mathbf{u}) : \delta \boldsymbol{\lambda} d\Omega = 0 \end{aligned}. \quad (4.42)$$

All components in the equation (4.42) are linearized as follows

$$\begin{aligned} L[\delta \Pi] = & \delta \bar{\Pi} + \mathbb{D} \delta \Pi \cdot \Delta \mathbf{u} \\ = & \delta \bar{\Pi} + \Delta(\delta \Pi), \end{aligned} \quad (4.43)$$

where  $L$  is the linearization operator. Here presents the details of the linearization procedure of the components in the equation (4.42):

$$L \left[ \int_{\Omega} \mathbf{S} : \delta \mathbf{G} d\Omega \right] = \int_{\Omega} \bar{\mathbf{S}} : \delta \bar{\mathbf{G}} d\Omega + \int_{\Omega} \Delta(\mathbf{S} : \delta \mathbf{G}) d\Omega, \quad (4.44)$$

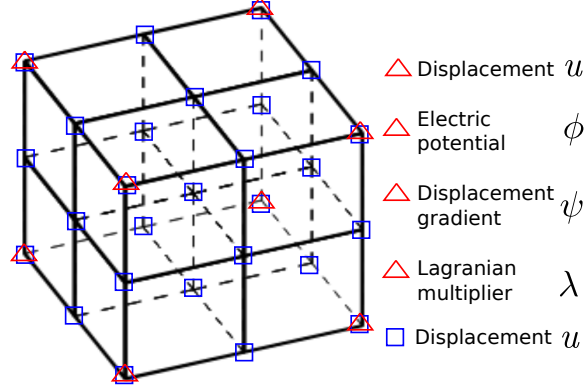


**Figure 4.12.** Schematic illustration of the H27 element, this element has 27 nodes includes 8 corner nodes equipped with displacement  $\mathbf{u}$  (blue rectangles), electric potential  $\theta$  (red triangles), displacement gradient  $\psi$  (red triangles) and Lagrange multiplier  $\lambda$  (red triangles) DOFs; the remain 19 nodes (blue rectangles) only hold displacement  $\mathbf{u}$  DOFs.

$$\begin{aligned}
\int_{\Omega} \Delta(\mathbf{S} : \delta \mathbf{G}) d\Omega &= \int_{\Omega} \mathbf{S} : \Delta(\delta \mathbf{G}) d\Omega + \int_{\Omega} \delta \mathbf{G} : \Delta \mathbf{S} d\Omega \\
&= \int_{\Omega} \mathbf{S} : \Delta(\delta \mathbf{G}) d\Omega + \int_{\Omega} \delta \mathbf{G} : \mathbb{C} : \Delta \mathbf{G} d\Omega - \int_{\Omega} \delta \mathbf{G} : \mathbf{d} \cdot \Delta \mathbf{E} d\Omega \\
&= \int_{\Omega} \mathbf{S} : [(\nabla_0 \delta \mathbf{u})^T (\nabla_0 (\Delta \mathbf{u}))] d\Omega + \int_{\Omega} \delta \mathbf{G} : \mathbb{C} : \Delta \mathbf{G} d\Omega \\
&\quad - \int_{\Omega} \delta \mathbf{G} : \mathbf{d} \cdot \Delta \mathbf{E} d\Omega
\end{aligned} \tag{4.45}$$

where,

$$\begin{aligned}
\mathbf{G} &= \frac{1}{2} (u_{i,j} + u_{j,i} + u_{k,i} u_{k,j}), \\
\delta \mathbf{G} &= \frac{1}{2} (\delta u_{i,j} + \delta u_{j,i} + \delta u_{k,i} u_{k,j} + u_{k,i} \delta u_{k,j}), \\
\Delta \delta \mathbf{G} &= \frac{1}{2} (\delta u_{k,i} \Delta u_{k,j} + \Delta u_{k,i} \delta u_{k,j}), \\
\mathbf{S} &= \mathbb{C} : \mathbf{G} - \mathbf{d} \cdot \mathbf{E}, \\
\Delta \mathbf{S} &= \mathbb{C} : \Delta \mathbf{G} - \mathbf{d} \cdot \Delta \mathbf{E};
\end{aligned} \tag{4.46}$$

$$L \left[ \int_{\Omega} \bar{\boldsymbol{\tau}} : \delta \bar{\boldsymbol{\eta}} d\Omega \right] = \int_{\Omega} \bar{\boldsymbol{\tau}} : \delta \bar{\boldsymbol{\eta}} d\Omega + \int_{\Omega} \Delta(\bar{\boldsymbol{\tau}} : \delta \bar{\boldsymbol{\eta}}) d\Omega, \tag{4.47}$$

$$\begin{aligned}
\int_{\Omega} \Delta(\tilde{\boldsymbol{\tau}}:\delta\tilde{\boldsymbol{\eta}})d\Omega &= \int_{\Omega} \tilde{\boldsymbol{\tau}}:\Delta(\delta\tilde{\boldsymbol{\eta}})d\Omega + \int_{\Omega} \delta\tilde{\boldsymbol{\eta}}:\Delta\tilde{\boldsymbol{\tau}}d\Omega \\
&= \int_{\Omega} \tilde{\boldsymbol{\tau}}:\Delta(\delta\tilde{\boldsymbol{\eta}})d\Omega - \int_{\Omega} \delta\tilde{\boldsymbol{\eta}}:\boldsymbol{\mu} \cdot \Delta\mathbf{E}d\Omega + \delta\tilde{\boldsymbol{\eta}}:\mathbf{g}:\Delta\tilde{\boldsymbol{\eta}}d\Omega \\
&= \int_{\Omega} \tilde{\boldsymbol{\tau}}:[(\delta\boldsymbol{\psi})(\nabla_0\Delta\boldsymbol{\psi}) + (\Delta\boldsymbol{\psi})(\nabla_0\delta\boldsymbol{\psi})]d\Omega \\
&\quad - \int_{\Omega} \delta\tilde{\boldsymbol{\eta}}:\boldsymbol{\mu} \cdot \Delta\mathbf{E}d\Omega + \int_{\Omega} \delta\tilde{\boldsymbol{\eta}}:\mathbf{g}:\Delta\tilde{\boldsymbol{\eta}}d\Omega
\end{aligned} \tag{4.48}$$

where,

$$\begin{aligned}
\tilde{\boldsymbol{\eta}} &= \frac{1}{2}(\psi_{ij,k} + \psi_{ji,k} + \psi_{mj}\psi_{mi,k} + \psi_{mj,k}\psi_{mi}), \\
\delta\tilde{\boldsymbol{\eta}} &= \frac{1}{2}(\delta\psi_{ij,k} + \delta\psi_{ji,k} + \delta\psi_{mj}\psi_{mi,k} + \psi_{mj}\delta\psi_{mi,k} + \delta\psi_{mj,k}\psi_{mi} + \psi_{mj,k}\delta\psi_{mi}), \\
\Delta\delta\tilde{\boldsymbol{\eta}} &= \frac{1}{2}(\delta\psi_{mj}\Delta\psi_{mi,k} + \Delta\psi_{mj}\delta\psi_{mi,k} + \delta\psi_{mj,k}\Delta\psi_{mi} + \Delta\psi_{mj,k}\delta\psi_{mi}), \\
&= \delta\psi_{mj}\Delta\psi_{mi,k} + \Delta\psi_{mj}\delta\psi_{mi,k}, \\
\tilde{\boldsymbol{\tau}} &= -\boldsymbol{\mu} \cdot \mathbf{E} + \mathbf{g}:\tilde{\boldsymbol{\eta}};
\end{aligned} \tag{4.49}$$

$$L \left[ \int_{\Omega} \mathbf{D} \cdot \delta\mathbf{E}d\Omega \right] = \int_{\Omega} \bar{\mathbf{D}} \cdot \delta\bar{\mathbf{E}}d\Omega + \int_{\Omega} \Delta(\mathbf{D} \cdot \delta\mathbf{E})d\Omega, \tag{4.50}$$

$$\begin{aligned}
\int_{\Omega} \Delta(\mathbf{D} \cdot \delta\mathbf{E})d\Omega &= \int_{\Omega} \mathbf{D} \cdot \Delta\delta\mathbf{E}d\Omega + \int_{\Omega} \Delta\mathbf{D} \cdot \delta\mathbf{E}d\Omega \\
&= \int_{\Omega} \delta\mathbf{E} \cdot \mathbf{d} : \Delta\mathbf{G}d\Omega + \int_{\Omega} \delta\mathbf{E} \cdot \boldsymbol{\mu}:\Delta\tilde{\boldsymbol{\eta}}d\Omega + \int_{\Omega} \delta\mathbf{E} \cdot \boldsymbol{\kappa} \cdot \Delta\mathbf{E}d\Omega,
\end{aligned} \tag{4.51}$$

where,

$$\begin{aligned}
\mathbf{D} &= \mathbf{d} : \mathbf{G} + \boldsymbol{\mu}:\tilde{\boldsymbol{\eta}} + \boldsymbol{\kappa} \cdot \mathbf{E}, \\
\Delta\mathbf{D} &= \mathbf{d} : \Delta\mathbf{G} + \boldsymbol{\mu}:\Delta\tilde{\boldsymbol{\eta}} + \boldsymbol{\kappa} \cdot \Delta\mathbf{E}, \\
E_i &= -\theta_{,i}, \\
\delta E_i &= -\delta\theta_{,i}, \\
\Delta\delta E_i &= 0;
\end{aligned} \tag{4.52}$$

$$L \left[ \int_{\Omega} \boldsymbol{\lambda} : (\delta\boldsymbol{\psi} - \nabla\delta\mathbf{u})d\Omega \right] = \int_{\Omega} \bar{\boldsymbol{\lambda}} : (\delta\bar{\boldsymbol{\psi}} - \nabla\delta\bar{\mathbf{u}})d\Omega + \int_{\Omega} \Delta\boldsymbol{\lambda} : (\delta\boldsymbol{\psi} - \nabla\delta\mathbf{u})d\Omega; \tag{4.53}$$

$$L \left[ \int_{\Omega} (\boldsymbol{\psi} - \nabla\mathbf{u}) : \delta\boldsymbol{\lambda}d\Omega \right] = \int_{\Omega} (\bar{\boldsymbol{\psi}} - \nabla\bar{\mathbf{u}}) : \delta\bar{\boldsymbol{\lambda}}d\Omega + \int_{\Omega} (\Delta\boldsymbol{\psi} - \nabla\Delta\mathbf{u}) : \delta\boldsymbol{\lambda}dd\Omega. \tag{4.54}$$

The algebraic form of equations (4.44),(4.47),(4.50),(4.53) and (4.54) are written as follows

$$L \left[ \int_{\Omega} \mathbf{S} : \delta \mathbf{G} d\Omega \right] = \delta \mathbf{u} \left( \int_{\Omega} \mathbf{B}^T \hat{\mathbf{R}} d\Omega \right) + \delta \mathbf{u} \left( \int_{\Omega} \mathbf{H}_1^T \mathbf{R} \mathbf{H}_1 d\Omega \right) \Delta \mathbf{u} \\ + \delta \mathbf{u} \left( \int_{\Omega} \mathbf{B}^T \mathbf{C} \mathbf{B} d\Omega \right) \Delta \mathbf{u} + \delta \mathbf{u} \left( \int_{\Omega} \mathbf{B}^T \mathbf{d} \mathbf{B}_{\theta} d\Omega \right) \Delta \theta ; \quad (4.55)$$

$$L \left[ \int_{\Omega} \tilde{\boldsymbol{\tau}} : \delta \tilde{\boldsymbol{\eta}} d\Omega \right] = \delta \psi \left( \int_{\Omega} \mathbf{H}_D^T \hat{\mathbf{R}}_D d\Omega \right) + \delta \psi \left( \int_{\Omega} \mathbf{N}^{lT} \mathbf{R}_D^T \mathbf{H}_2 d\Omega \right) \Delta \psi \\ + \delta \psi \left( \int_{\Omega} \mathbf{H}_D^T \boldsymbol{\mu}^T \mathbf{B}_{\theta} d\Omega \right) \Delta \theta + \delta \psi \left( \int_{\Omega} \mathbf{H}_2^T \mathbf{R}_D \mathbf{N}^l d\Omega \right) \Delta \psi ; \quad (4.56) \\ + \delta \psi \left( \int_{\Omega} \mathbf{H}_D^T \mathbf{g} \mathbf{H}_D d\Omega \right) \Delta \psi$$

$$L \left[ \int_{\Omega} \mathbf{D} \cdot \delta \mathbf{E} d\Omega \right] = -\delta \theta \int_{\Omega} \mathbf{B}_{\theta}^T \hat{\mathbf{D}} d\Omega - \delta \theta \left( \int_{\Omega} \mathbf{B}_{\theta}^T \mathbf{d} \mathbf{B} d\Omega \right) \Delta \mathbf{u} \\ - \delta \theta \left( \int_{\Omega} \mathbf{B}_{\theta}^T \boldsymbol{\mu} \mathbf{H}_D d\Omega \right) \Delta \psi + \delta \theta \left( \int_{\Omega} \mathbf{B}_{\theta}^T \boldsymbol{\kappa} \mathbf{B}_{\theta} d\Omega \right) \Delta \theta ; \quad (4.57)$$

$$L \left[ \int_{\Omega} \boldsymbol{\lambda} : (\delta \psi - \nabla \delta \mathbf{u}) d\Omega \right] = \delta \psi \int_{\Omega} \mathbf{N}^{lT} \bar{\boldsymbol{\lambda}} d\Omega - \delta \mathbf{u} \int_{\Omega} \mathbf{B}_{\psi u}^T \bar{\boldsymbol{\lambda}} d\Omega + \\ \delta \psi \left( \int_{\Omega} \mathbf{N}^{lT} \mathbf{N}^l d\Omega \right) \Delta \boldsymbol{\lambda} - \delta \mathbf{u} \left( \int_{\Omega} \mathbf{B}_{\psi u}^T \mathbf{N}^l d\Omega \right) \Delta \boldsymbol{\lambda} ; \quad (4.58)$$

$$L \left[ \int_{\Omega} (\psi - \nabla \mathbf{u}) : \delta \boldsymbol{\lambda} d\Omega \right] = \delta \boldsymbol{\lambda} \int_{\Omega} \mathbf{N}^{lT} \bar{\psi} d\Omega - \delta \boldsymbol{\lambda} \int_{\Omega} \mathbf{N}^{lT} \nabla \bar{\mathbf{u}} d\Omega \\ + \delta \boldsymbol{\lambda} \left( \int_{\Omega} \mathbf{N}^{lT} \mathbf{N}^l d\Omega \right) \Delta \psi + \delta \boldsymbol{\lambda} \left( \int_{\Omega} \mathbf{N}^{lT} \mathbf{B}_{\psi u} d\Omega \right) \Delta \mathbf{u} ; \quad (4.59)$$

The final algebraic form of the equation (4.43) can be written in a matrix form as

$$\mathbf{K} \Delta \mathbf{U} = \mathbf{F}_{ext} - \mathbf{F}_{int} . \quad (4.60)$$

In the matrix form, only the mechanical Neumann boundary condition is imposed

$$\begin{bmatrix} \mathbf{K}_{uu} & 0 & \mathbf{K}_{u\theta} & \mathbf{K}_{u\lambda} \\ 0 & \mathbf{K}_{\psi\psi} & \mathbf{K}_{\psi\theta} & \mathbf{K}_{\psi\lambda} \\ \mathbf{K}_{\theta u} & \mathbf{K}_{\theta\psi} & \mathbf{K}_{\theta\theta} & 0 \\ \mathbf{K}_{\lambda u} & \mathbf{K}_{\lambda\psi} & 0 & 0 \end{bmatrix} \begin{bmatrix} \Delta \mathbf{u} \\ \Delta \psi \\ \Delta \theta \\ \Delta \boldsymbol{\lambda} \end{bmatrix} = \begin{bmatrix} \mathbf{F}_{ext}^u \\ 0 \\ 0 \\ 0 \end{bmatrix} - \begin{bmatrix} \mathbf{F}_{int}^u \\ \mathbf{F}_{int}^{\psi} \\ \mathbf{F}_{int}^{\theta} \\ \mathbf{F}_{int}^{\lambda} \end{bmatrix} , \quad (4.61)$$

where

$$\begin{aligned}
\mathbf{K}_{uu} &= \int_{\Omega} \mathbf{B}^T \mathbb{C} \mathbf{B} d\Omega + \int_{\Omega} \mathbf{H}_1^T \mathbf{R} \mathbf{H}_1 d\Omega, \\
\mathbf{K}_{\psi\psi} &= \int_{\Omega} \mathbf{N}^{lT} \mathbf{R}_D^T \mathbf{H}_2 d\Omega + \int_{\Omega} \mathbf{H}_2^T \mathbf{R}_D \mathbf{N}^l d\Omega + \int_{\Omega} \mathbf{H}_D^T \mathbf{g} \mathbf{H}_D d\Omega, \\
\mathbf{K}_{\theta\theta} &= - \int_{\Omega} \mathbf{B}_{\theta}^T \boldsymbol{\kappa} \mathbf{B}_{\theta} d\Omega, \\
\mathbf{K}_{\psi\theta} &= \int_{\Omega} \mathbf{H}_D^T \boldsymbol{\mu}^T \mathbf{B}_{\theta} d\Omega = \mathbf{K}_{\theta\psi}^T, \\
\mathbf{K}_{u\theta} &= \int_{\Omega} \mathbf{B}^T \mathbf{d} \mathbf{B}_{\theta} d\Omega = \mathbf{K}_{\theta u}^T, \\
\mathbf{K}_{u\lambda} &= \int_{\Omega} \mathbf{B}_{\psi u}^T \mathbf{N}^l d\Omega = \mathbf{K}_{\lambda u}^T, \\
\mathbf{K}_{\psi\lambda} &= \int_{\Omega} \mathbf{N}^{lT} \mathbf{N}^l d\Omega = \mathbf{K}_{\lambda\psi}^T, \\
\mathbf{F}_{ext}^u &= \int_{\Gamma} \mathbf{t} \mathbf{N} d\Gamma, \\
\mathbf{F}_{int}^u &= \int_{\Omega} \mathbf{B}^T \hat{\mathbf{R}} d\Omega + \int_{\Omega} \mathbf{B}_{\psi u}^T \bar{\lambda} d\Omega, \\
\mathbf{F}_{int}^{\psi} &= \int_{\Omega} \mathbf{H}_D^T \hat{\mathbf{R}}_D d\Omega + \int_{\Omega} \mathbf{N}^{lT} \bar{\lambda} d\Omega, \\
\mathbf{F}_{int}^{\theta} &= \int_{\Omega} \mathbf{N}^{lT} \bar{\lambda} d\Omega, \\
\mathbf{F}_{int}^{\lambda} &= \int_{\Omega} \mathbf{N}^{lT} \bar{\psi} d\Omega - \int_{\Omega} \mathbf{N}^{lT} \nabla \bar{u} d\Omega.
\end{aligned} \tag{4.62}$$

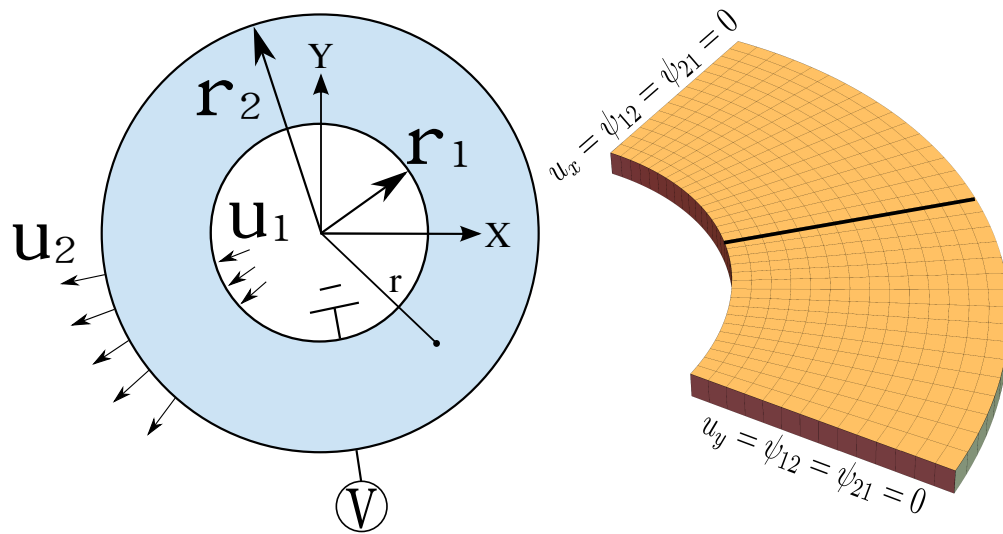
The details of the components in the equation (4.62) are presented in the Appendix C. The material matrices  $\mathbb{C}$ ,  $\mathbf{d}$ ,  $\boldsymbol{\kappa}$ ,  $\boldsymbol{\mu}$  and  $\mathbf{g}$  correspond to the elastic stiffness matrix, piezoelectric coupling matrix, dielectric permittivity matrix, flexoelectric coefficient matrix and tangent non-local elastic tensor, respectively. In this study, the NMFEM develops a H27 element (figure 4.12) for discretization. This element has in total 233 degrees-of-freedom (DOFs), including 3 displacement DOFs ( $\mathbf{u}$ ) in each node, 9 Lagrange multiplier DOFs ( $\boldsymbol{\lambda}$ ) per corner node (8 corner nodes), 9 displacement gradient DOFs ( $\boldsymbol{\psi}$ ) per corner node and 1 electric potential DOF ( $\theta$ ) per corner node. The developed NMFEM utilizes a quadratic shape function for interpolating the displacement DOFs. Linear shape function is employed to interpolate the Lagrange multiplier DOFs, displacement gradient DOFs, and electric potential DOF. For the numerical integration, 27 Gaussian points per element are used to obtain the stiffness matrix and residual vector.

## 4.2.2 Numerical results and discussion

In this section, the developed NMFEM first validates with an analytical model. Subsequently, the NMFEM investigates the influence of the geometric nonlinearity on flexoelectricity and

the underlying mechanism of flexoelectricity in composite structures under the influence of different material properties and structure configurations between the inclusions and matrix. The subsequent subsection proposes a cantilever flexoelectric composite beam for energy harvester application and the last subsection presents a topology optimization study for flexoelectricity in cylinder/cone-shaped devices.

### Model validation



(a) Schematic illustration of the analytical set-up (b) Mesh configuration of a quarter of the structure as in the analytical set-up

**Figure 4.13.** (a) Schematic illustration of the analytical set-up, the inner surface subjects to a displacement load  $u_1 = 0.045 \mu m$  and the displacement load  $u_2 = 0.05 \mu m$  is applied to the outer surface; The outer surface also subjects to electric potential equals to 1V whereas the inner surface is grounded. The inner radius  $r_1 = 10 \mu m$  and outer radius  $r_2 = 20 \mu m$ ; (b) The mesh configuration of a quarter of the structure as in the analytical set-up.

In this subsection, the developed NMFEM validates with an analytical solution presented in MAO ET AL. (2016). The analytical model's set-up is illustrated in figure 4.13(a). As shown in figure 4.13(a), a hollow cylinder subjects to a deformation load and a electric potential difference. The hollow cylinder's inner surface subjects to a radial displacement of  $u_1 = 0.045 \mu m$  and zero electric potential (grounded). The outer surface subjects to a radial displacement of  $u_2 = 0.05 \mu m$  and the electrical potential of 1V. The hollow cylinder has an inner radius  $r_1 = 10 \mu m$  and outer radius  $r_2 = 20 \mu m$ . Literature studies, see MAO ET AL. (2016); DENG ET AL. (2017), presented the analytical solution for the displacement and electric potential of this problem as follows

$$u_r(r) = C_1 r + \frac{C_2}{r} + C_3 I_1\left(\frac{r}{l_0}\right) + C_4 K_1\left(\frac{r}{l_0}\right), \quad (4.63)$$



and

$$\theta(r) = C_5 \ln r + C_6 + \frac{f}{\kappa} \left( \frac{\partial u_r(r)}{r} + \frac{u_r(r)}{r} \right), \quad (4.64)$$

where constants  $C_1$  to  $C_6$  are determined by the given boundary condition.  $f = \mu_{11} + 2\mu_{12}$ . The  $I_1$  and  $K_1$  are the first-order modified Bessel functions of the first and second kind. The  $r$  represents the location, where the displacement and electric potential are calculated. The length scale  $l_0$  of this problem derives from

$$l_0^2 = l^2 + \frac{f^2}{(\lambda + \mu)\kappa}, \quad (4.65)$$

where  $\lambda$  and  $\mu$  are the first and second Lamé-constant, respectively.

With the following boundary conditions:

$$\begin{aligned} u_r(r = r_1) &= u_1; & u_r(r = r_2) &= u_2; \\ \psi(r = r_1) &= 0 \text{ V}; & \psi(r = r_2) &= 1 \text{ V}; \\ \tilde{\tau}(r = r_1) &= \tilde{\tau}(r = r_2) = 0, \end{aligned} \quad (4.66)$$

and the material parameters in table 4.2, the constants  $C_1$  to  $C_6$  from the equation (4.63) and equation (4.64) are determined as 0.0018069, 0.28063  $\mu\text{m}^2$ ,  $-6.7032 \times 10^{-8} \mu\text{m}$ , -0.267117 $\mu\text{m}$ , 4.0166 V and 33.8698 V, respectively.

Due to the center-symmetrical set-up in the analytical model, it is sufficient to only construct a quarter of the hollow cylinder structure (the upper right quarter in figure 4.13(a)) with the NMFEM to replicate the analytical problem. This simplification imposes extra boundary conditions in the NMFEM on surfaces A and B, as shown in figure 4.13(b). The loading conditions and material constants are identical to the analytical setup.

**Table 4.2.** Material parameters.

Name	Symbol	Value
Poisson ratio	$\nu$	0.3
Young's modulus	E	139 GPa
Piezoelectric constant	$e_{31}$	0 nC/m <sup>2</sup>
flexoelectric constant	$\mu_{12}; \mu_{11}$	1 $\mu\text{C}/\text{m}$
dielectric constant	$\kappa_{11}; \kappa_{33}$	1 nC/Vm
electric susceptibility	$\chi$	1408
length scale	1	2 $\mu\text{m}$

Figure 4.14 shows the radial displacement profile and electric potential profile from the NMFEM. For validation, the values of radial displacement and electric potential along the marked line in the figure 4.13(b) are extracted and compared with the analytical solution (equation (4.63) and equation (4.64)). The comparison shown in the figure 4.15 demonstrates

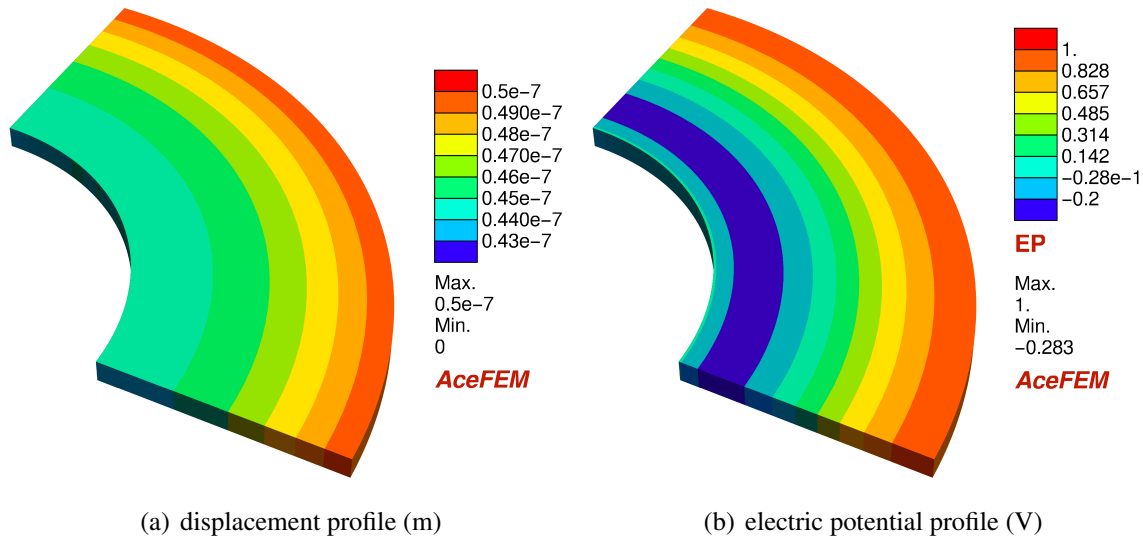
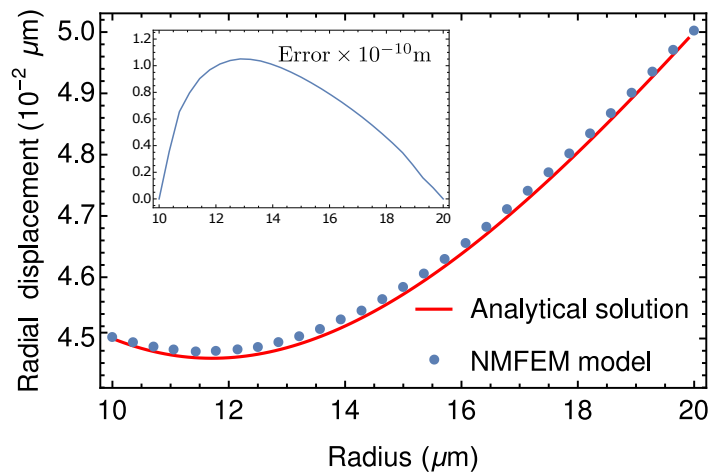


**Figure 4.14.** (a) radius displacement (m) distribution profile, and (b) electric potential (V) profile from the NMFEM model with strain gradient elasticity.

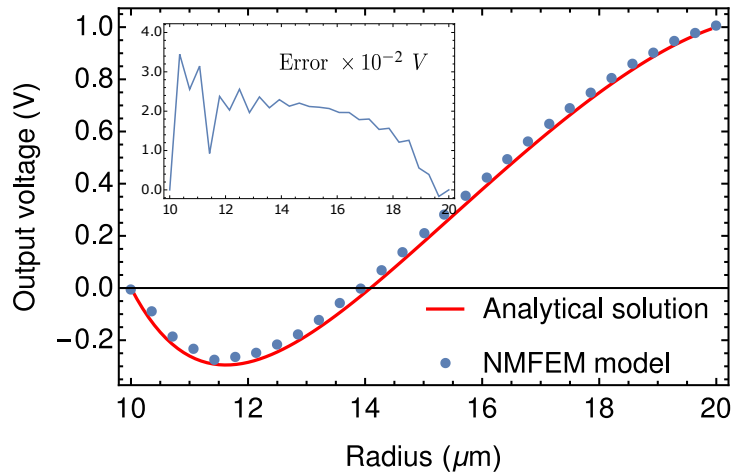
an excellent agreement between the NMFEM and the analytical solution, which validates the proposed NMFEM. It's also worth noting that the NMFEM captures the non-linear voltage profile (shown in figure 4.15(b)) caused by the consideration of the strain gradient elasticity in the equation (4.48). Existing study shows that the significance of the strain gradient elasticity on the behavior of an electromechanical structure at a small length scale, where the flexoelectric effect is predominant, see MAO ET AL. (2016). The NMFEM successfully predicts the electromechanical response of the analytical setup under the influence of strain gradient elasticity.

### Nonlinear flexoelectricity under static and dynamic loading conditions

**Nonlinear flexoelectricity under static loading condition** Here studies the influence of the geometric nonlinearity on flexoelectricity under static loading condition. The geometric nonlinearity is due to the consideration of higher-order terms in the Green-Lagrange strain tensor  $\mathbf{G}$  (equation (4.46)), which is ignored in the linear model. Here employs cantilever beams (figure 4.16) under bending load to investigate the influence of geometric nonlinearity on flexoelectricity. The cantilever beams subject to a line load at their free end. Their left-ends are mechanically fixed, and the right-ends are grounded to mimic an open circuit setup. And the beams have an aspect ratio of  $100 \times 10 \times 10$ . Two sets of beam depths ( $d = 10 \mu\text{m}$  and  $d = 5 \mu\text{m}$ ) are adopted for both linear and nonlinear cases. The applied material constants are listed in table 4.2. A ramp loading scheme for 30 loading steps with an incremental line load  $F = 30 \text{ N/m}$  is applied. The Newton-Raphson method obtains the converged solution by minimizing the residual in each loading step. The maximum output voltage and the beam displacement for each loading step are noted.



(a) Radial displacement comparison



(b) Electric potential comparison

**Figure 4.15.** Comparison between the analytical solution and NMFEM. (a) displacement comparison, the insertion is the relative error of displacement between the NMFEM result and analytical solution in the unit of  $10^{-10}$  m; (b) electric potential comparison, the insertion is the relative error of electric potential between the NMFEM result and analytical solution in the unit of  $10^{-2}$  Volt.

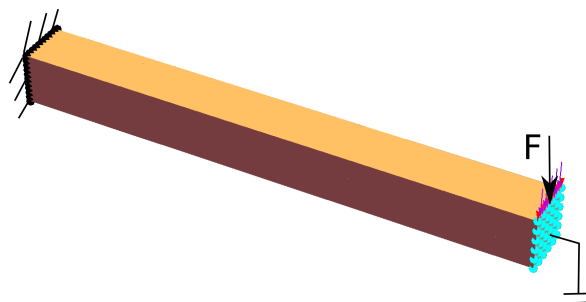


**Figure 4.16.** Schematic illustration of a cantilever beam and its boundary conditions.

The maximum output voltages and displacements of the cantilever beams at each load step are plotted in figure 4.17. The subplots in figure 4.17 indicate that the linear model agrees with the nonlinear model only for the first few loading steps. After that, the discrepancies between the linear and nonlinear models increase with the loading step. For instance, at step 30, the discrepancy between the linear model and nonlinear model in terms of the maximum displacement and output voltage of the beam with depth  $d = 5 \mu\text{m}$  reaches  $2.61 \times 10^{-5} / -1.1 \times 10^{-5} = 237\%$  and  $44.1/29.5 = 149\%$ , respectively, which suggests that the linear model severely overestimated the electromechanical response of the flexoelectric cantilever beam compared to the nonlinear model. A nonlinear Meshless model for flexoelectricity also reported the same discrepancy due to the geometric nonlinearity, see ZHUANG ET AL. (2020). Furthermore, figure 4.17 also observes a size-dependent effect. Namely, at each loading step, the discrepancy in terms of displacement and electrical potential between the linear and nonlinear models of the beam with height  $d = 5 \mu\text{m}$  is always larger than that of the beam with height  $d = 10 \mu\text{m}$ . For instance, at step 30, the maximum displacement discrepancy between the linear model and nonlinear model of the beam with depth  $d = 5 \mu\text{m}$  (figure 4.17(a)) is about  $2.37/1.66 = 1.5$  times higher than that of the  $10 \mu\text{m}$  deep beam (figure 4.17(c)). Similar trend (at step 30,  $1.49/1.27 = 1.16$ ) is also observed in the electric voltage output plot (figure 4.17(b) vs figure 4.17(d)). This size-dependent behavior suggests that the flexoelectric effect is more vulnerable to the geometric nonlinearity at a smaller length scale. Considering this behavior, it is necessary to employ the nonlinear model for analyzing any given flexoelectric structure at the nanoscale or even at the microscale.

Figure 4.18 shows the electric voltage distribution in the deformed beam with depth  $d = 5 \mu\text{m}$  at loading step 1, 15 and 30. It demonstrates that the proposed NMFEM captures the full nonlinear region with excellent stability.

**Nonlinear flexoelectricity under dynamic loading condition** Here further investigates the influence of the geometric nonlinearity on flexoelectricity under dynamic loading conditions. For this purpose, the mass and acceleration terms are included in the equation (4.60) to accommodate the dynamic behavior.

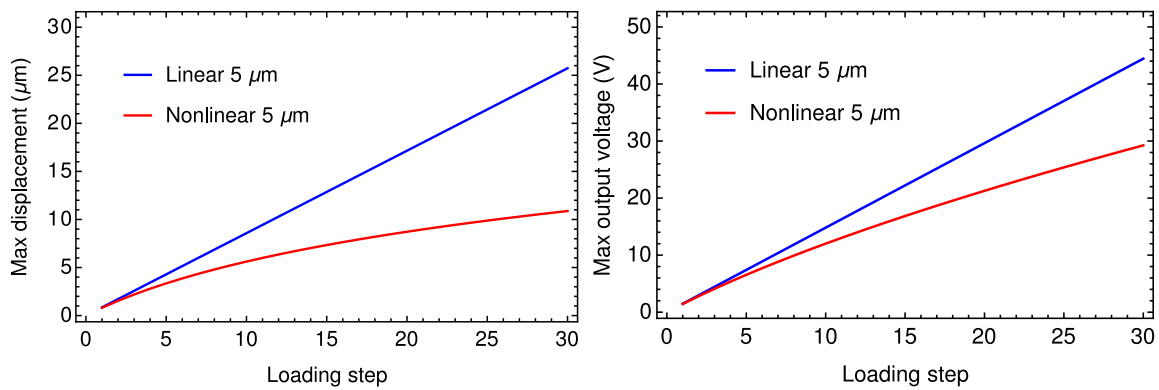
$$M\ddot{\mathbf{u}} + C\dot{\mathbf{u}} + \mathbf{K}\Delta U = \mathbf{F} - \mathbf{F}_{int}, \quad (4.67)$$

where the consistent mass matrix and matrix  $C$  have the form:

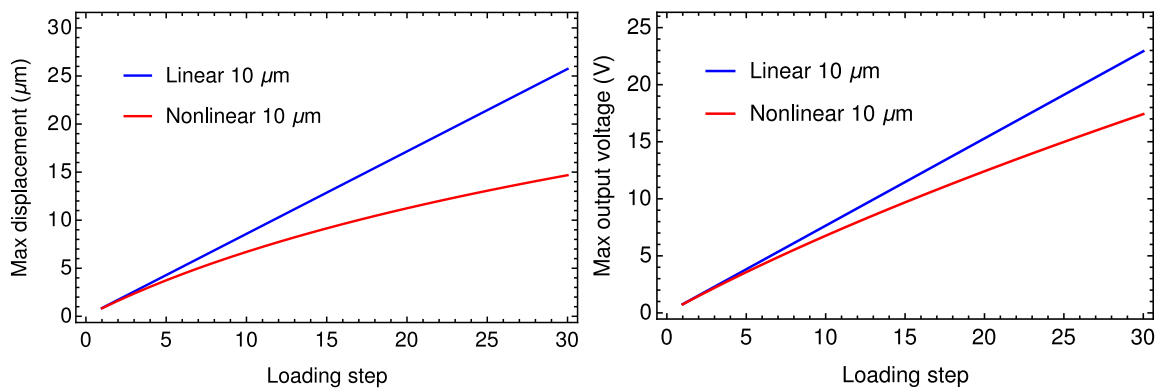
$$\mathbf{M} = \int_{\Omega} \mathbf{N}^t \rho \mathbf{N} d\Omega \quad \text{and} \quad \mathbf{C} = \alpha \mathbf{M} + \beta \mathbf{K}_{uu}, \quad (4.68)$$

and  $\rho = 6000 \text{ kg/m}^3$  is the material density,  $\alpha$  and  $\beta$  are constants of proportionality, which are as described in DENG ET AL. (2014); CLOUGH ET AL. (1977). The  $\ddot{\mathbf{u}}$  and  $\dot{\mathbf{u}}$  are nodal accelerations and velocities, respectively. The excitation force  $\mathbf{F} = \mathbf{f} \sin(\omega t)$ , and  $\mathbf{f}$  indicates nodal excitation amplitude and  $\omega$  is the excitation frequency. The time-dependent nonlinear equations are solved by the Newmark-Beta method, see NEWMARK (1959).

Here chooses a cantilever slab to study the influence of the geometric nonlinearity on flexoelectricity under dynamic loading condition. The insertion in figure 4.19 shows that the slab



(a) maximum displacement vs loading step (beam depth  $d = 5 \mu\text{m}$ ) (b) maximum output voltage vs loading step (beam depth  $d = 5 \mu\text{m}$ )



(c) maximum displacement vs loading step (beam depth  $d = 10 \mu\text{m}$ ) (d) maximum output voltage vs loading step (beam depth  $d = 10 \mu\text{m}$ )

**Figure 4.17.** Maximum displacement and output voltage of the cantilever beams from the linear and nonlinear model. (a) and (b) show the maximum displacement and output voltage of a cantilever beam with depth  $d = 5 \mu\text{m}$ , respectively; (c) and (d) show the maximum displacement and output voltage of a cantilever beam with depth  $d = 10 \mu\text{m}$ , respectively.

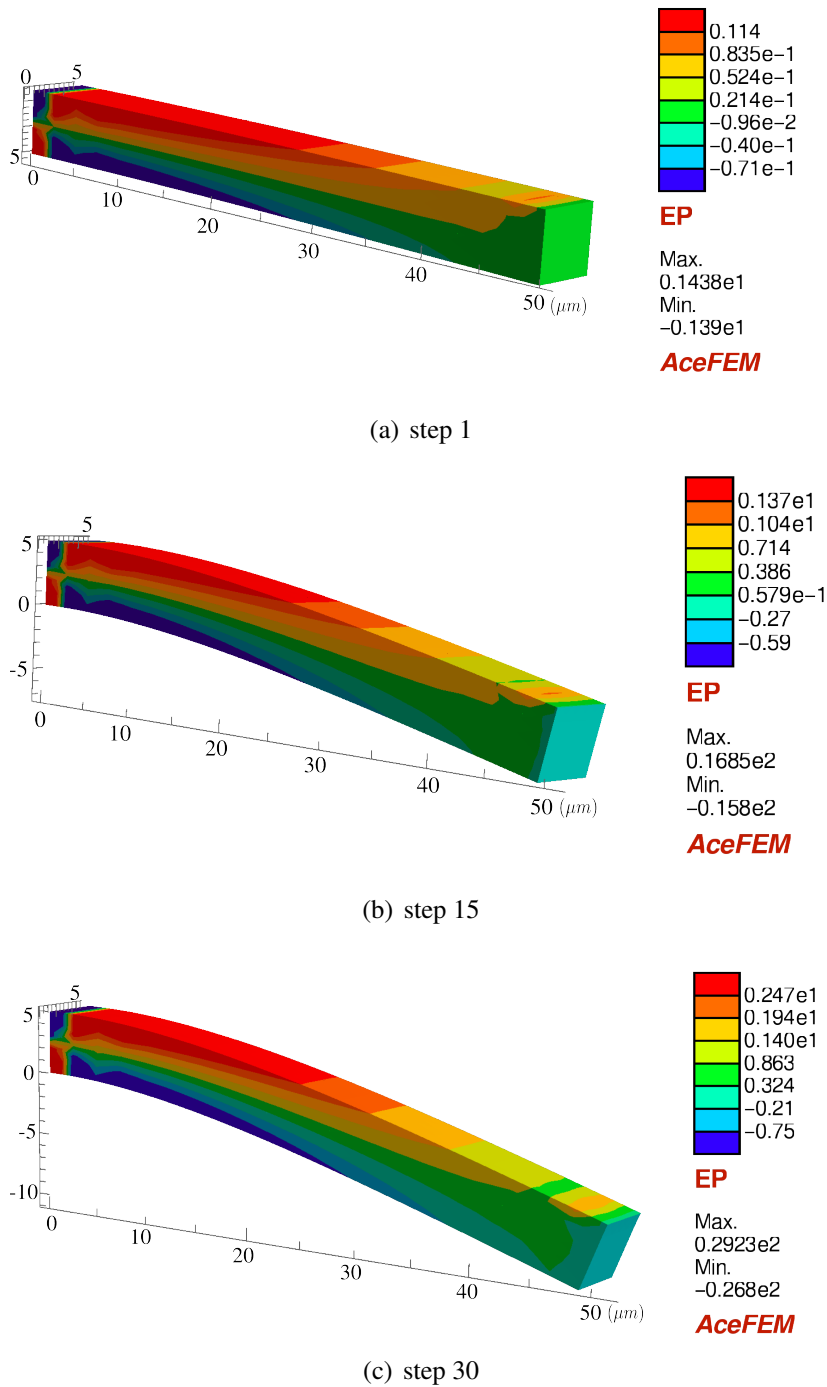


**Figure 4.18.** Electric potential profile of the deformed beam with depth  $d = 5 \mu\text{m}$  at (a) step 1; (b) step 15; (c) step 30.

is fixed at the left end, and a line load applies on the right end. The dimension of the slab is  $100 \times 10 \times 1$  with the depth of the slab equals  $1 \mu\text{m}$ . The material constants are the same as in table 4.2. A sinusoidal loading function imposes on the free edge of the slab, which has the form:  $F = f \sin(\omega t)$ , where  $f$  is the loading amplitude,  $\omega$  is the excitation frequency in the unit of rad/s and  $t$  is the time in s. The linear and nonlinear models' loading amplitude ranges from 0.002 N/m to 0.01 N/m and from 0.002 N/m to 0.05 N/m, respectively. The slab subjects to 30 loading cycles, which has loading amplitude equals to each cycle's maximum or minimum and the excitation frequencies range between 250000 Hz and 600000 Hz.

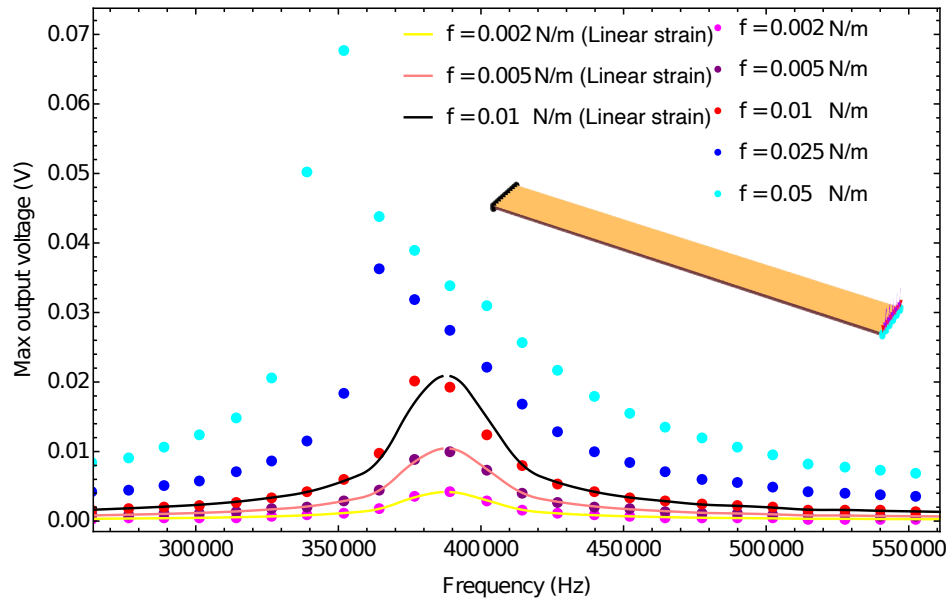
Figure 4.19 presents the maximum output voltage versus the given loading frequency under different loading amplitudes for both linear and nonlinear models. As shown by the solid lines in the figure 4.19, the linear model determines the maximum output voltage response to be localized and symmetric to the natural frequency and reaches its maximum when the loading frequency equals the nature resonant frequency of the slab. Figure 4.19 also shows that the symmetric voltage response is independent of the excitation amplitudes ( $f = 0.002 \text{ N/m}$ ,  $f = 0.005 \text{ N/m}$  and  $f = 0.01 \text{ N/m}$ ). Another linear analytical model proposed in DENG ET AL. (2014) studies flexoelectric effect under dynamic loading condition also reported that the voltage response remains symmetric regardless of the excitation amplitude. In contrast to the linear model, the maximum output voltage response from the nonlinear model tends to behave more asymmetrically as the excitation amplitude increases. The nonlinear effect is negligible for small excitation amplitudes ( $f = 0.002 \text{ N/m}$  and  $f = 0.005 \text{ N/m}$ ), which yields the same voltage response profile as the linear model. As the excitation amplitude increases (from  $f = 0.005 \text{ N/m}$  to  $f = 0.05 \text{ N/m}$ ), the asymmetrical behavior of the voltage response rises. The asymmetric voltage response of the nonlinear model indicates the structural softening of the cantilever slab via the consideration of higher-order terms in the equation (4.46). It indicates that the profile of the output voltage versus excitation frequency depends on the force amplitude. Besides, if the flexoelectric structure subjects to higher force amplitudes such that the structure is geometrically nonlinear, then the response bandwidth is broader than it at lower force amplitudes.

Figure 4.20 shows the maximum voltage response of the cantilever slab with different damping ratios  $\xi = 0.01, 0.15,$  and  $0.3$  under the same sinusoidal loading condition, which has a force amplitude  $f = 0.05 \text{ N/m}$ . The voltage output decreases with the increase of damping ratio, which is expected since the damping effect diminishes the dynamic response of the structure.

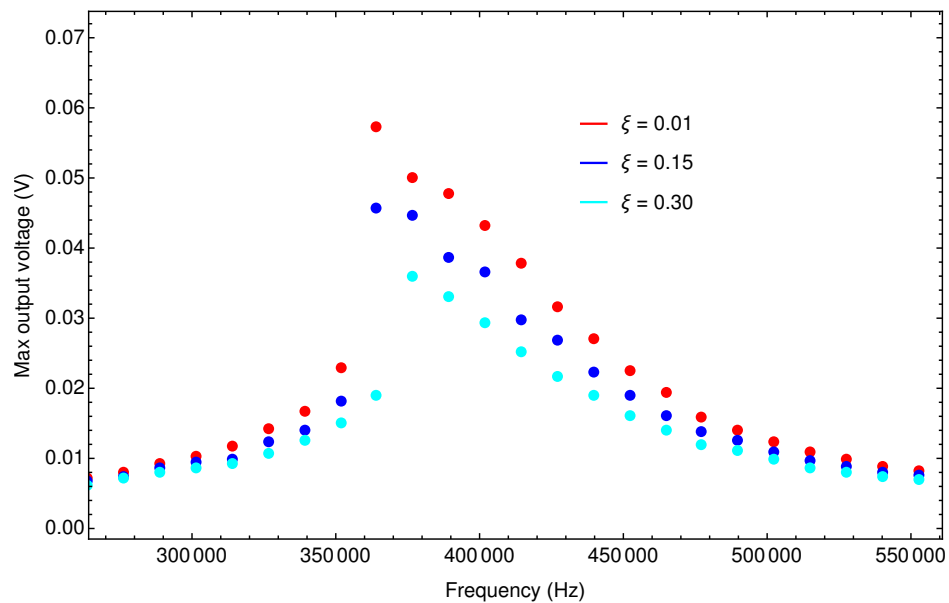
### Flexoelectricity in composite material

This subsection first explores the mechanism of flexoelectricity in a composite with a single inclusion inside the matrix (shown in figure 4.21(a)). Follows by the investigation of flexoelectricity in composites with different setups in terms of varying volume ratios and material parameters of the inclusions.

**Mechanism of flexoelectricity in composite material** Figure 4.21(a) shows the setup for studying the mechanism of flexoelectricity in a composite, consisting of a square matrix



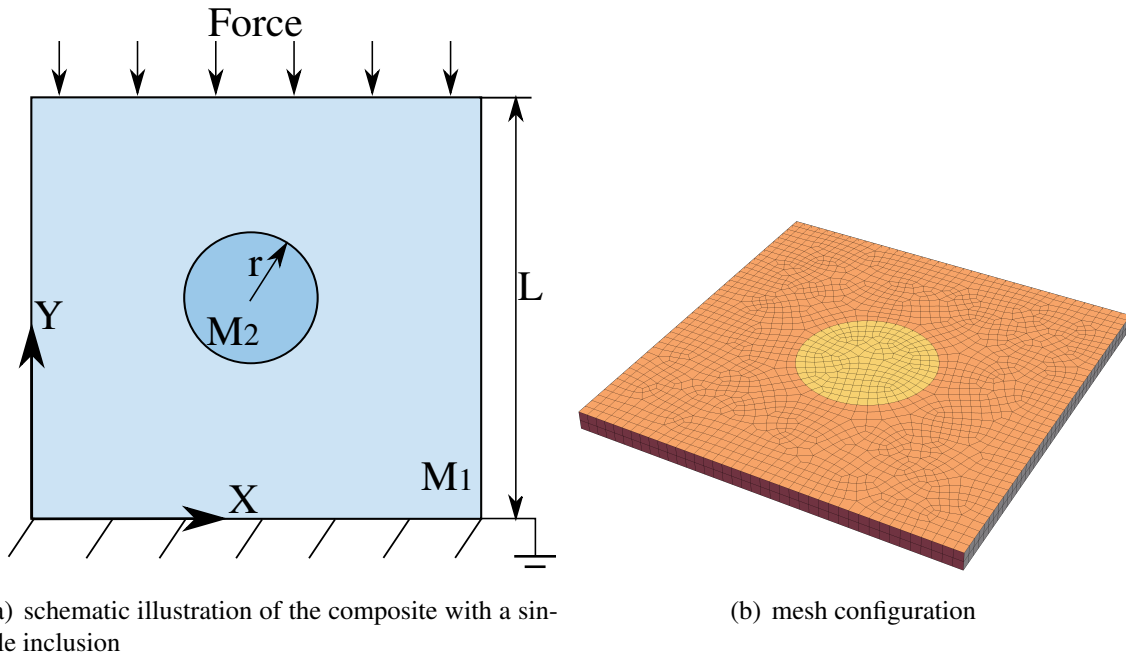
**Figure 4.19.** Maximum output voltage versus loading frequency under different loading amplitudes, ranging from  $f = 0.002$  N/m to  $f = 0.01$  N/m and from  $f = 0.002$  N/m to  $f = 0.05$  N/m for linear and nonlinear model, respectively. The dot plots present the results from the nonlinear model. The solid lines present the results from the linear model. The schematic illustration of the cantilever slab with its boundary conditions are also presented.



**Figure 4.20.** Maximum output voltage versus loading frequency under loading amplitude  $f = 0.05$  N/m for nonlinear model with different structural damping ratios:  $\xi = 0.01$ ,  $\xi = 0.15$  and  $\xi = 0.30$ .

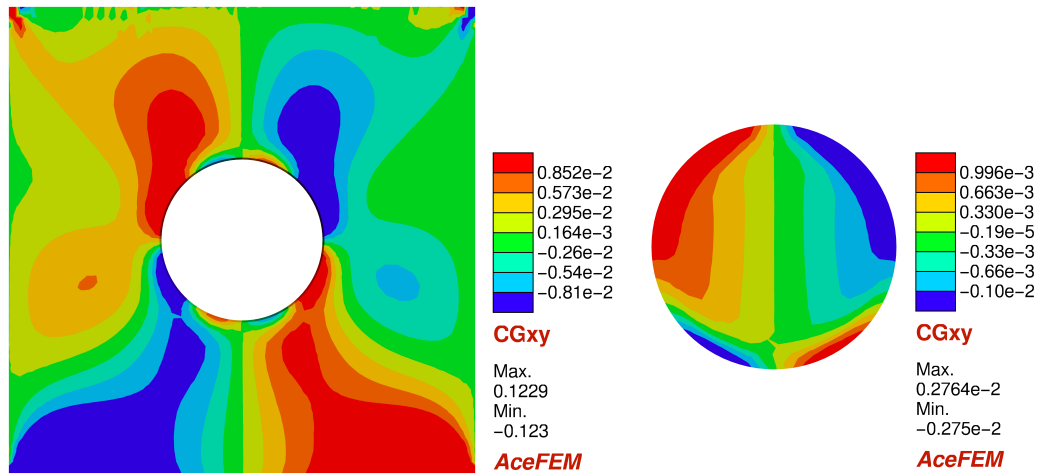
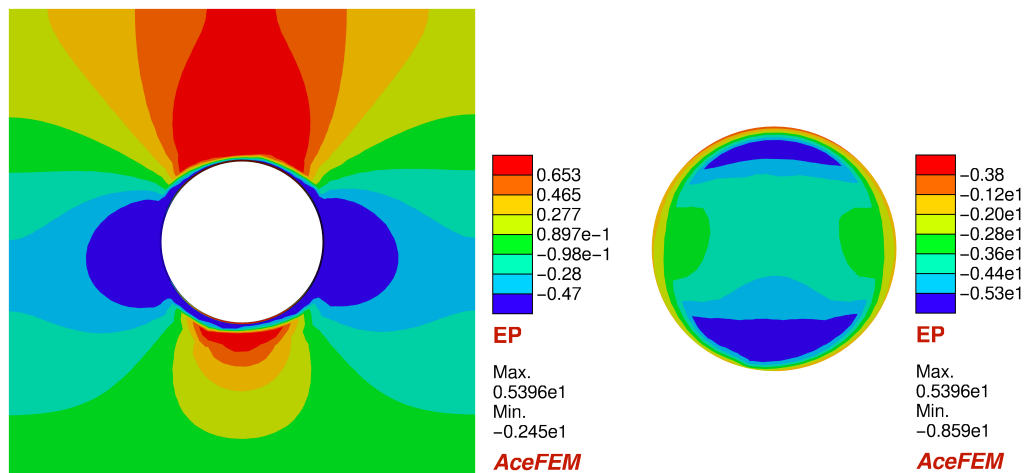


material M1 and an inclusion M2 located at the center. The height of the matrix is  $10 \mu\text{m}$ , and the inclusion radius is  $2 \mu\text{m}$ . The upper surface of the matrix M1 subjects to a compression force with a magnitude of  $1 \mu\text{N}$ , whereas its lower surface is fixed and grounded (zero electric potential). The material constants of M1 are taken from table 4.2 with the flexoelectric coefficients set to zero serving as a conductive material, which is the standard procedure in practice for composite energy harvester, see CIOFANI & MENCIASSI (2012); GULLAPALLI ET AL. (2010). The Young's modulus of M2 is four times higher than that of M1, and other material constants of M2 are taken from the table 4.2. Figure 4.21(b) shows the composite material's mesh configuration with a total of 3644 H27 elements, including 428 H27 elements for the inclusion M2.



**Figure 4.21.** (a) Schematic illustration of the composite with a single inclusion located in the center of the matrix. The matrix denotes as M1 and the inclusion as M2, and (b) Mesh configuration of the composite material.

As shown in figure 4.22(a), under compression, the difference in Young's modulus between the matrix M1 and inclusion M2 results an non-uniform strain ( $\varepsilon_{xy}$ ) profile inside the composite material, especially near the interface region between the matrix and inclusion. Due to a significant range difference in strain and electric potential value, figure 4.22 presents the contour plots for inclusion and matrix separately for a clear representation. The non-uniform strain distribution (figure 4.22(a)) of the inclusion indicates the existence of strain gradient in the X and Y-direction, which induces electric potential through flexoelectricity. The electric potential distribution in the figure 4.22(b) confirms the existence of flexoelectric response in the composite. To further investigate the composite's flexoelectric response, the electric potential along the centerline in the Y-direction is presented in the figure 4.23. It shows a

(a) strain  $\varepsilon_{xy}$  distribution of the matrix M1 (left) and inclusion M2 (right)

(b) electric potential distribution of the matrix M1 (left) and inclusion M2 (right)

**Figure 4.22.** (a) strain  $\varepsilon_{xy}$  distribution of the matrix M1 and inclusion M2, and (b) electric potential (V) of the matrix M1 and inclusion M2

significant difference between the matrix and inclusion in terms of electric potential distribution, as the matrix sets to be non-flexoelectric. The flexoelectric inclusion produces electric potential due to the non-uniform strain field, while the matrix serves only as a conductive material. Figure 4.23 shows that the highest electric potential locates near the interface region, where the strain gradient is maximum. It also indicates that the electric potential generated by the inclusion permeates into the matrix domain with a significant decrease in magnitude. The non-symmetric electric potential distribution in the Y-direction across the domain shown in figure 4.23 is due to the applied electric boundary condition (zero electric potential on the lower surface as shown in figure 4.21(a)).

The presented composite model with a single inclusion demonstrates the underlying mechanism of flexoelectricity in composite material. The magnitude of the generated electric

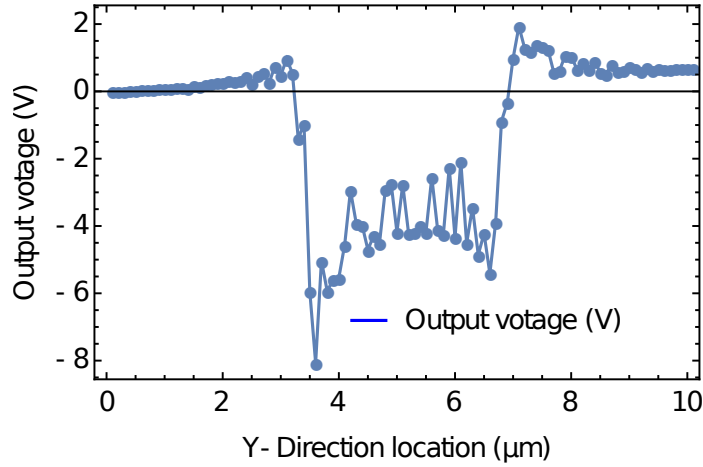


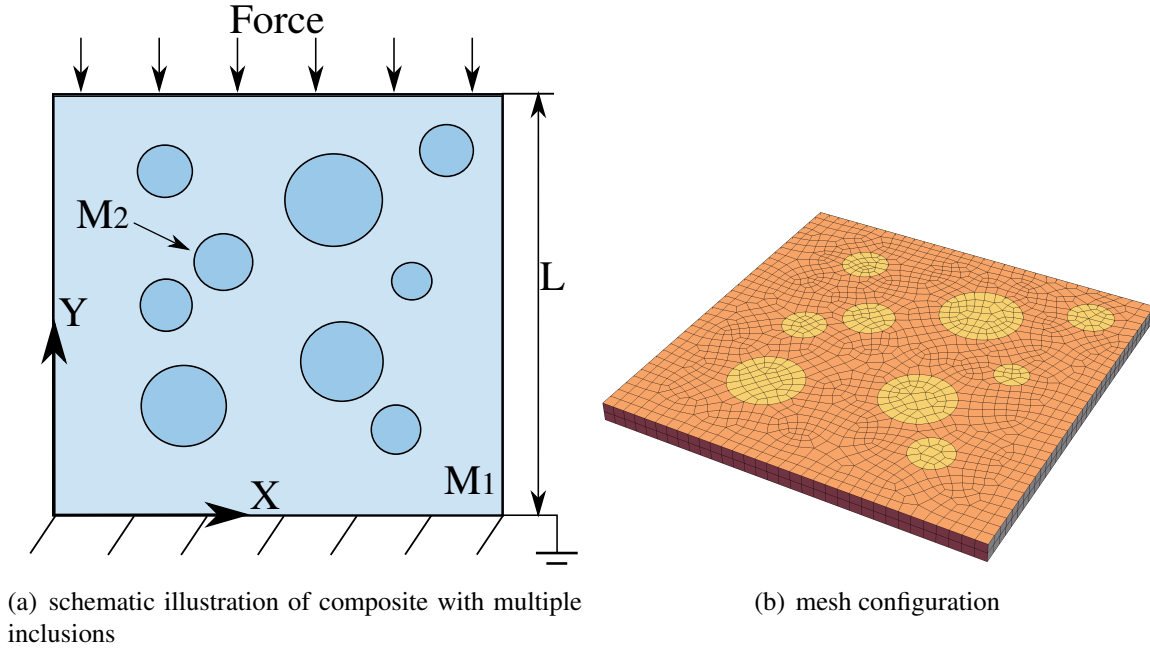
**Figure 4.23.** Electric potential profile along the centerline of the composite in the Y-direction.

potential decreases rapidly in the matrix as the distance from the inclusion increases, suggesting that the inclusion needs to be placed close to the electrode (generally located on the surface) in an energy harvester device for obtaining the maximum electric potential.

**Flexoelectricity in composite with multiple inclusions** This subsection further explores the influence of the setups of composite in terms of inclusion volume ratio  $V_{ratio}$  and relative Young's modulus  $E_{rel}$  on the overall electromechanical behavior of the composites.  $V_{ratio}$  equals the volume of inclusions  $V_{inc}$  over the total volume  $V_{tot}$ .  $E_{rel}$  is the ratio between the Young's modulus of inclusion  $E_{inc}$  and the matrix  $E_{mat}$ . For this purpose, here constructs composites with  $V_{inc}$  and  $E_{rel}$  ranging from 1%, 3%, 5%, 7%, 10% to 15% and from 2, 3 to 4, respectively. The remaining material parameters and the boundary conditions are identical to the model in the previous subsection. The schematic illustration of a setup is shown in figure 4.24(a). It indicates that the geometrical configuration of a setup with a fixed  $V_{ratio}$  and  $E_{rel}$  can vary with the size and location of each individual inclusion since only the total volume of inclusions is controlled with  $V_{ratio}$ , this imposes an uncertainty in the setup. To further investigate this topological uncertainty, here constructs ten examples with the same setup of  $V_{ratio} = 5\%$  and  $E_{rel} = 3$  but different inclusion locations and dimensions (radius). All ten examples subject to the same boundary conditions as shown in the figure 4.24(a) with force  $F = 1 \mu\text{N}$ . To quantify this topological uncertainty, here employs the well known effective electromechanical coupling factor  $\bar{k}_{eff}$  as the reference measurement, see MAJDOUB ET AL. (2008). The definition of  $\bar{k}_{eff}$  is

$$\bar{k}_{eff}^2 = \frac{\int \mathbf{E} \cdot \boldsymbol{\kappa} \cdot \mathbf{E} d\Omega}{\int \boldsymbol{\varepsilon} : \mathbb{C} : \boldsymbol{\varepsilon} d\Omega}, \quad (4.69)$$

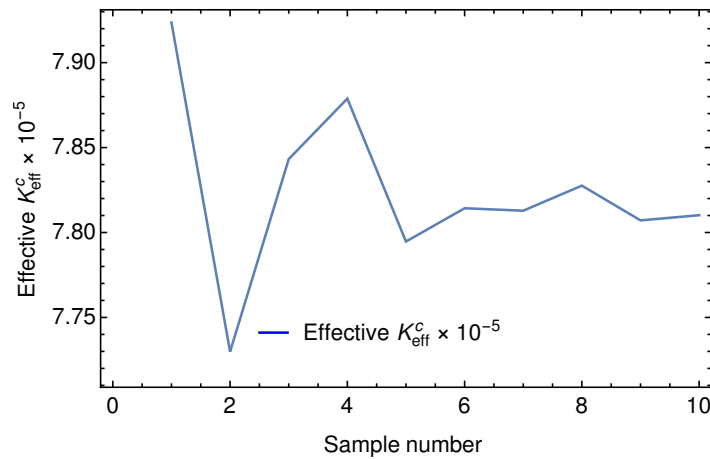
where  $\mathbf{E}$  is the electric field vector,  $\boldsymbol{\kappa}$  is the second order dielectric tensor,  $\boldsymbol{\varepsilon}$  is the strain tensor and  $\mathbb{C}$  is the elastic constant matrix.



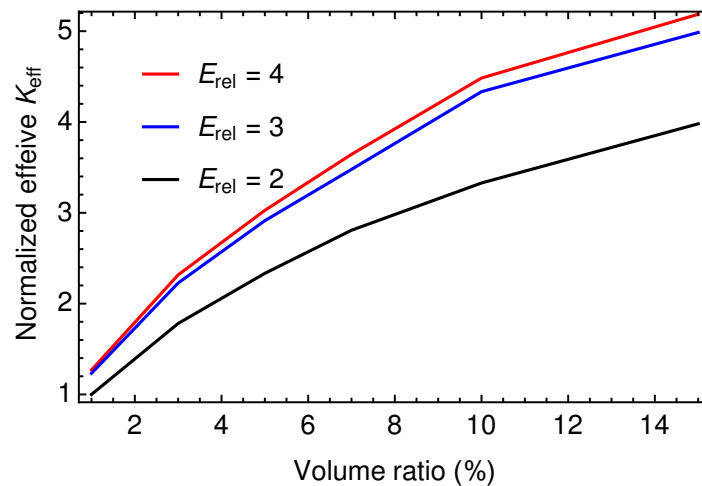
**Figure 4.24.** (a) Schematic illustration of a composite with multiple inclusions. The matrix denotes as M1 (light blue) and the inclusions as M2 (dark blue), and (b) Mesh configuration of the composite.

Figure 4.25 shows the convergence study of the ten samples in terms of the effective electromechanical coupling factor  $\bar{k}_{eff}^{ci}$  (the superscript c denotes convergence). The converged value of  $K_{eff}^{ci}$  of the  $i$ -th sample is  $\bar{k}_{eff}^{c1} = \bar{k}_{eff}^1$ ;  $\bar{k}_{eff}^{c2} = (\bar{k}_{eff}^{c1} + \bar{k}_{eff}^2) / 2$ ;  $\dots$ ;  $\bar{k}_{eff}^{ci} = (\bar{k}_{eff}^{c1} + \bar{k}_{eff}^{c2} + \dots + \bar{k}_{eff}^i) / i$ , where  $\bar{k}_{eff}^i$  is the calculated effective electromechanical coupling factor from the equation (4.69) of the  $i$ -th sample. Figure 4.25 demonstrates that minimum five samples are required to achieve convergence for the given setup  $V_{ratio} = 5\%$  and  $E_{rel} = 3$ . Considering this, at least five samples are constructed for each setup to ensure convergence, and the averaged value of the effective electromechanical coupling factors  $\bar{k}_{eff}$  of each setup is taken for further analysis. Figure 4.26 shows the normalized effective electromechanical coupling factor  $K_{eff}^n$  (the superscript n denotes normalized) of each setup. The values  $K_{eff}^n$ s derive from an normalization procedure against the effective electromechanical coupling factor  $\bar{k}_{eff}$  of a reference setup  $V_{ratio} = 1\%$  and  $E_{rel} = 2$ . Figure 4.26 reveals two trends: (a) the increase of inclusion volume ratio results in higher electromechanical coupling of the flexoelectric composites. It is explained by the increase of non-uniform strain fields due to the randomly located inclusions, enabling a stronger flexoelectric effect. Figure 4.27(a) demonstrates the highly irregular strain field due to the inclusions, especially near the interface regions. Additionally, it observes a linkage effect, which represents an enhancement of the electric potential between an inclusion and its neighboring inclusions; (b) softer matrix material generates a stronger electromechanical coupling. It is clear that for a fixed inclusion volume ratio, the setup with a higher  $E_{rel}$  results in a higher normalized effective electromechanical coupling factor  $\bar{k}_{eff}$ . For instance, at 15% inclusion volume ratio, the setup with  $E_{rel} = 4$  shows 30% enhancement in the normalized effective electromechanical coupling factor  $\bar{k}_{eff}$  compared to the setup with  $E_{rel} = 2$ . Under the identical loading

condition, the larger structural deformation of a softer matrix contributes to the enhancement of strain gradient, thus leads to a stronger electromechanical coupling from flexoelectricity.



**Figure 4.25.** Convergence study of a setup  $V_{ratio} = 5\%$  and  $E_{rel} = 3$  with ten samples.



**Figure 4.26.** The normalized effective electromechanical coupling factor  $K_{eff}^n$  for different setup of  $V_{ratio}$  and  $E_{rel}$  values.

### A composite flexoelectric device

The previous subsection reveals two essential phenomena of flexoelectricity in composite structure: (1) high electric potential generated near the interface between the inclusions and matrix; (2) softer matrix material results in a stronger flexoelectric coupling. Here utilizes these phenomena to design a new composite flexoelectric device, as shown in the figure

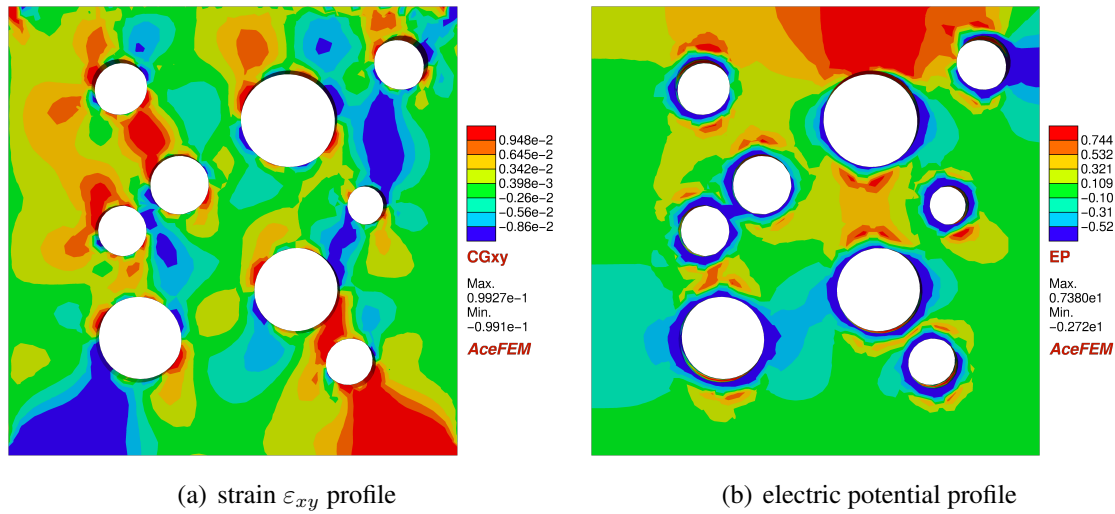


**Figure 4.27.** (a) strain  $\varepsilon_{xy}$  plot of a composite with multiple inclusions, and (b) the induced electrical potential distribution of a composite with multiple inclusions.

4.28(a). It is well established that a cantilever beam under bending serves perfectly as a flexoelectric device thanks to the bending induced non-linear distributed strain field. Thus the linear strain gradient for flexoelectric coupling across the beam in the bending direction, see ABDOLLAHI ET AL. (2014); GHASEMI ET AL. (2017). Under an identical bending load, a cantilever beam constructed by a softer material, such as a polymer, undergoes a larger deformation and induces a higher strain gradient field than a cantilever beam been built from a stiffer material, such as Barium titanate oxide (BTO) or Barium strontium titanate (BST), see CHU & SALEM (2012); MA & CROSS (2006, 2002). However, the electromechanical coupling via the flexoelectric effect in the polymer cantilever beam is minimal due to the low flexoelectric coefficient of the polymer, see CHU & SALEM (2012); LIU ET AL. (2017). On the other hand, materials such as BTO and BST have extremely high flexoelectric coefficients (almost 1000 times higher than that of polymer) but also more than 100 times stiffer than polymer, see MA & CROSS (2006, 2002); HE ET AL. (2018). Furthermore, a study shows that the BTO / BST material is susceptible to brittle fracture under large deformation, limiting its application in flexible flexoelectric devices, see WANG ET AL. (2004). To utilize the flexibility of the polymer and high flexoelectric coefficients of the BTO / BST, the proposed composite device in figure 4.28(a) combines the polymer material with BTO / BST to serve as a flexible flexoelectric energy harvester. The main structure of the composite beam constructs with the polymer to ensure structural flexibility. Besides, the last subsection demonstrated that a softer matrix material leads to a more substantial flexoelectric effect. The BTO/BST inclusions serve as generators inducing strong flexoelectric response thanks to their high flexoelectric coefficients. Due to the short distance between the electrodes and inclusions in the proposed flexoelectric composite device, the high electric potential generated near the inclusion (proved in the previous subsection 4.2.2) can be directly harvested by the electrodes.

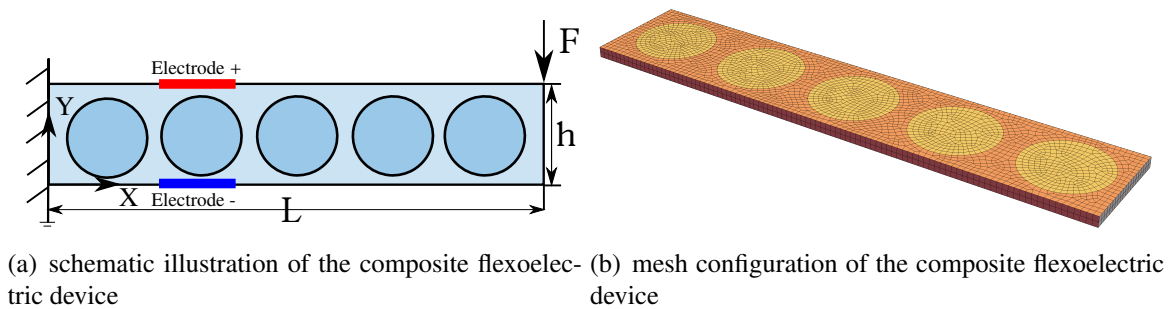


**Figure 4.28.** (a) Schematic illustration of the composite flexoelectric device, the device subjects to a line load  $F$  at its free end. The darker blue circles represent the inclusions. The red bar represents the positive electrode, and the blue bar is the negative electrode, and (b) Mesh configuration of the composite flexoelectric device.

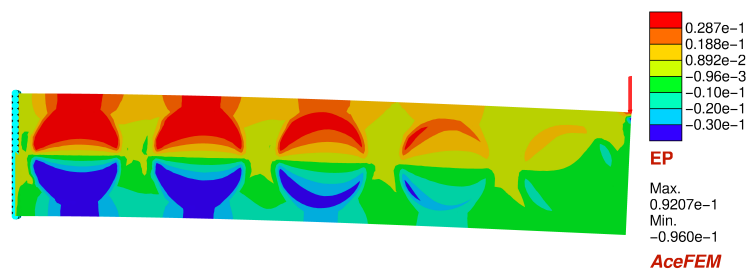
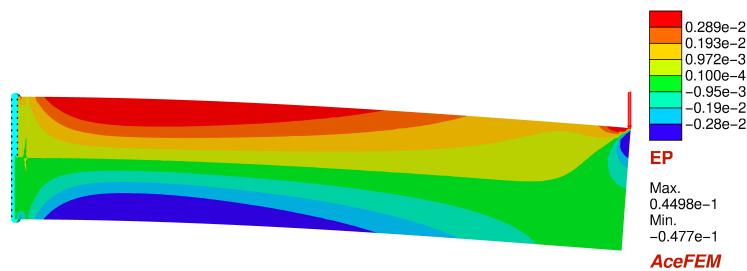


**Figure 4.29.** (a) Electric potential distribution from the pure polymer beam, and (b) Electric potential distribution from the proposed composite flexoelectric device.

To validate the effectiveness of the proposed flexoelectric device, here compares the generated electric potential of the proposed flexoelectric device to a flexoelectric cantilever beam constructed purely from polymer. For the proposed flexoelectric device, the inclusions' properties are listed in table 4.2 and the polymer matrix is 100 times softer than the inclusion and has a flexoelectric coefficient equals 1/1000 as that of the inclusion. The remaining material

parameters are identical to the inclusions. Both structures have a dimension of  $50 \mu\text{m} \times 10 \mu\text{m} \times 1 \mu\text{m}$  and subject to a line load  $F = 0.01 \text{ N/m}$ . The mesh configuration of the flexoelectric device is shown in figure 4.28(b). Figure 4.29 shows the generated electric potential from the pure polymer beam and the proposed composite flexoelectric device. It reveals that the pure polymer beam has a uniform distributed electric potential field with a maximum magnitude of  $0.44 \text{ V}$ , whereas the composite beam yields a maximum electric potential of  $0.92 \text{ V}$ , which is more than twice that of the polymer beam. This significant enhancement of the electric potential in the composite beam originates from the inclusions, as shown in figure 4.29(b). It also shows that the composite beam's flexibility decreases by about  $20 \%$  due to BTO / BST inclusions strengthening the structure. Nevertheless, the proposed composite device is more efficient than the device constructed by the pure polymer material and offers a relative high flexibility.

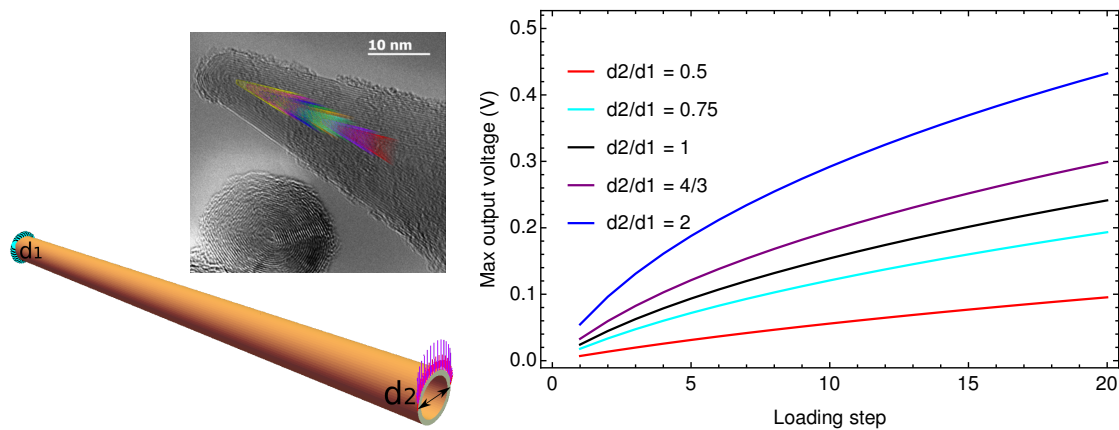


**Figure 4.30.** (a) Schematic illustration of a cone structure and its boundary conditions, its left side (outer diameter is  $d_1$ ) is fixed and connected to the ground; on the right side, a line load applies to the top edge of the outer circle (outer diameter  $d_2$ ). The insertion is an image of BN cone, see KVASHNIN ET AL. (2018), and (b) Maximum output voltage versus loading step for cone structures with different diameter ratios under identical incremental load for 20 steps.

### Truncated cone shaped flexoelectric device

Truncated cone structures exhibit intrinsic flexoelectric coupling effect under both bending and axial loading condition thanks to their varying cross-sections, see DENG (2017); LU ET AL. (2016). Furthermore, experimental studies discovered that truncated cone nanostructures (such as carbon nanocone or Boron nitride (BN) nanocone shown in figure 4.30(a)) exist in nature, which can serve directly as a flexoelectric device, see KVASHNIN ET AL. (2018); NAESS ET AL. (2009). This subsection studies the flexoelectric effect in truncated cone structures under bending. For this purpose, here constructs cone structures as shown in figure 4.30(a), and they are mechanically fixed and grounded on the left side. A ramp loading scheme for 20 loading steps with an incremental semi-circle line load  $F = 10 \text{ N/m}$  is applied



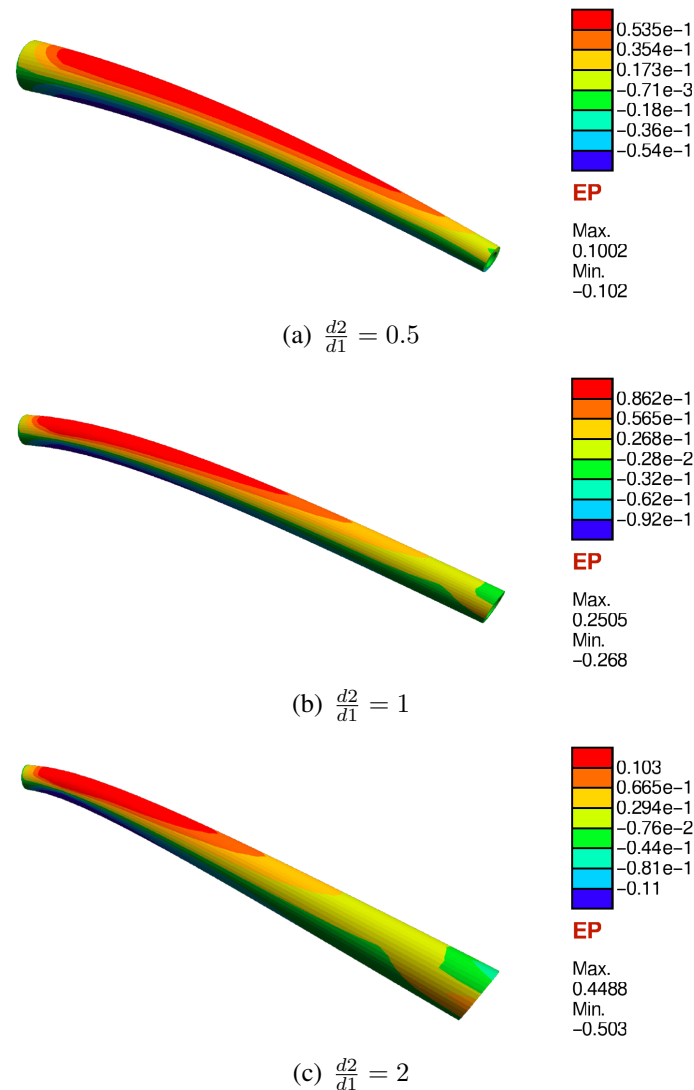


**Figure 4.31.** Electric potential distribution of the deformed cone structures with  $\frac{d_2}{d_1} = 0.5, 1$  and  $2$  at step 20.

on the right side. The length of the cones is  $100 \mu\text{m}$ , and their thickness is  $1 \mu\text{m}$ . Their material parameters are listed in table 4.2. Here also explores the influence of the diameter ratio ( $D_r = \frac{d_2}{d_1}$ ) between the left end outer diameter  $d_1$  and right end the outer diameter  $d_2$  on the maximum output voltage of cone structures under identical bending load. For each diameter ratio, the cone structure's volume remains  $1650 \mu\text{m}^3$ . Figure 4.30(b) shows the maximum output voltage versus loading step for cone structures with diameter ratio ranging from  $D_r = 0.5$  to  $D_r = 2$ . It demonstrates that the maximum output voltage increases with decreasing diameter ratio of cone structures. This behavior is understood through the geometrical configuration. As the diameter ratio  $D_r < 1$ , the cross-section near the fixed end (left end) is larger than the cross-section on the right end, which stiffens the cone structure. In contrast, as the diameter ratio  $D_r > 1$ , the cross-section near the fixed end is smaller than the cross-section on the right end, making the cone structure more flexible. For instance, as

the diameter ratio  $D_r = 0.5$ , the cone structure's displacement is low, and the resulted strain remains in the linear range throughout the 20 loading steps (indicated by the straight line of the output voltage). However, cone structure with the diameter ratio  $D_r = 2$ , the displacement is higher, such that the cone structure enters the nonlinear range after a few loading steps. The observed ratio-dependent behavior suggests that one should utilize a truncated cone with a larger diameter ratio of  $D_r$  to induce a stronger flexoelectric coupling effect. Figure 4.31 shows the electric potential distribution of the deformed cone structures with different diameter ratios  $D_r = 0.5, 1$ , and 2 at load step 20.

### 4.3 Conclusion

This chapter presented two continuum models to investigate flexoelectricity in composite structures. The first model is a 2D Meshless model coupled with the level-set technique studies flexoelectricity in composites under the assumption of small strain. The higher-order shape function of the Meshless model fulfills the requirement of  $C^1$  continuity imposed by the strain gradient term in the governing equation of flexoelectricity, and the level-set technique supervises the material discontinuity between the inclusion and matrix of the composites. The Meshless model is validated with several benchmark problems of flexoelectricity in single-phase material. Hereafter, the model studies flexoelectricity in two-phase composites. The results show that the non-uniform strain fields near the inclusion boundary induce electric potential through flexoelectricity, and the intensity of the flexoelectric effect mainly depends on the area ratio between the inclusions and the matrix. Namely, the higher the inclusion area ratio, the stronger the flexoelectric effect. The Meshless model also found that a softer matrix material leads to a stronger flexoelectric effect in composites. The second model is a 3D nonlinear mixed finite element model (NMFEM) studies flexoelectricity in composite structures under large deformation conditions. The NMFEM includes displacement gradients and Lagrange multipliers as additional degrees of freedom to accommodate the  $C^1$  continuity required by the governing equation of flexoelectricity. The geometric nonlinearity and strain gradient elasticity are also incorporated into the model to accurately capture the electromechanical behavior of flexoelectric structures. The results show that geometric nonlinearity and strain gradient elasticity significantly influence the overall electromechanical response of flexoelectric structures under static and dynamic loading conditions. Specifically, the NMFEM with geometric nonlinearity significantly overestimates the intensity of the flexoelectric effect under static loading conditions and predicts an incomplete electromechanical response under dynamic loading conditions. Regarding the flexoelectricity in composites, the NMFEM arrived at the same conclusions as the Meshless model, i.e., a higher volume ratio of inclusions and a softer matrix material lead to a stronger flexoelectric effect in composites.



## Chapter 5

# Conclusions and Future Perspectives

This work developed molecular dynamics models to investigate the underlying mechanism of flexoelectricity in various 2D and 3D nanomaterials. Additionally, continuum models were established to characterize flexoelectricity in solid continuum structures, such as flexoelectric composites. The conclusions of this work can be summarized as follows.

- A core-shell molecular dynamics model studies the size-dependent flexoelectric coefficient of  $\text{BaTiO}_3$  nanostructures. The core-shell model is validated with experimental studies as it accurately reproduces the phase transition process of  $\text{BaTiO}_3$ . The longitudinal and shear flexoelectric coefficients of  $\text{BaTiO}_3$  nanostructures are evaluated using the core-shell model with specially designed deformation schemes. The results show that the surface effect significantly influences the longitudinal and shear flexoelectric coefficients of the  $\text{BaTiO}_3$  nanostructures. Namely, the longitudinal flexoelectric coefficients decrease with the surface atom ratios of the  $\text{BaTiO}_3$  nanostructures, while the shear flexoelectric coefficients show an opposite trend.
- A charge-dipole molecular dynamics model studies the bending flexoelectric coefficients of five groups of 2D materials: graphene allotropes (C1, C2, C3), nitrides (BN, AlN, GaN), graphene analogues of group-IV elements (Si, Ge, Sn), transition metal dichalcogenides (TMDCs) ( $\text{MoS}_2$ ,  $\text{WS}_2$ ,  $\text{CrS}_2$ ) and Janus TMDCs ( $\text{MoSSe}$ ,  $\text{MoSTe}$ ,  $\text{MoSeTe}$ ,  $\text{WSSe}$ ,  $\text{WSTe}$ ,  $\text{WSeTe}$ ). A proposed bending deformation scheme enables direct estimation of the flexoelectric coefficients of the 2D materials by eliminating the piezoelectric contribution to the polarization. In doing so, the charge-dipole model analyzed the mechanisms underpinning the calculated flexoelectric coefficients by interpreting them through the electric fields generated from the dipole-dipole ( $\sigma - \sigma$  bonding) and charge-dipole ( $\pi - \sigma$  bonding) interactions. While the charge-dipole interactions increase with bending curvature, their relative weakness in the flat monolayers (graphene, BN) leads to lower flexoelectric coefficients for these materials. In contrast, it is found that buckling height, which occurs in the monolayer group-IV elements, leads to more than 10% increases in flexoelectric coefficients. Additionally, due to the significantly enhanced charge transfer coupled with structural asymmetry, the TMDCs have the largest flexoelectric coefficients, including the flexoelectric coefficient of  $\text{MoS}_2$  ten times larger than that of graphene. Furthermore, a particular group of TMDCs called Janus TMDCs to have flexoelectric coefficients that are several times

larger than that of the traditional TMDCs, such as  $\text{MoS}_2$ . The mechanism underlying this was the bond length asymmetry of the Janus TMDCs between the M-X and M-Y atoms. This bond length asymmetry leads to stronger  $\sigma-\sigma$  interactions with increasing initial asymmetry, along with stronger  $\pi-\sigma$  interactions due to the increased charge transfer, which combine to result in increased polarization for Janus TMDCs.

- Two continuum models explore flexoelectricity in composite structures. The first model is a 2D Meshless model coupled with the level-set technique studies flexoelectricity in composites under the assumption of small strain. The higher-order shape function of the Meshless model fulfills the requirement of  $C^1$  continuity imposed by the strain gradient term in the governing equation of flexoelectricity, and the level-set technique supervises the material discontinuity between the inclusion and matrix of the composites. The Meshless model is validated with several benchmark problems of flexoelectricity in single-phase material. Hereafter, the model studies flexoelectricity in two-phase composites. The results show that the non-uniform strain fields near the inclusion boundary induce electric potential through flexoelectricity, and the intensity of the flexoelectric effect mainly depends on the area ratio between the inclusions and the matrix. Namely, the higher the inclusion area ratio, the stronger the flexoelectric effect. The Meshless model also found that a softer matrix material leads to a stronger flexoelectric effect in composites. The second model is a 3D nonlinear mixed finite element model (NMFEM) studies flexoelectricity in continuum structures under large deformation conditions. The NMFEM includes displacement gradients and Lagrange multipliers as additional degrees of freedom to accommodate the  $C^1$  continuity required by the governing equation of flexoelectricity. The geometric nonlinearity and strain gradient elasticity are also incorporated into the model to accurately capture the electromechanical behavior of flexoelectric structures. The results show that geometric nonlinearity and strain gradient elasticity significantly influence the overall electromechanical response of flexoelectric structures under static and dynamic loading conditions. Specifically, the NMFEM with geometric nonlinearity significantly overestimates the intensity of the flexoelectric effect under static loading conditions and predicts an incomplete electromechanical response under dynamic loading conditions. Regarding the flexoelectricity in composites, the NMFEM arrived at the same conclusions as the Meshless model, i.e., a higher volume ratio of inclusions and a softer matrix material lead to a stronger flexoelectric effect in composites.

Flexoelectricity is in its early stages for engineering applications. There are many potential areas to explore, for instance,

- To continue the search for 2D materials with high flexoelectric coefficients by the presented charge-dipole molecular dynamics model;
- To develop a topology optimization scheme for flexoelectric structures within the framework of the presented nonlinear mixed finite element model;
- To develop a fully homogenized MD-FEM model for flexoelectricity.

# Appendix A

## Derivatives of potential function

The first order derivative of  $E^{q-q}$  with respect to  $\alpha^{\text{th}}$  component of position vector  $\mathbf{r}_i$  is ( $r_{i,\alpha}$ ) is

$$\frac{\partial E^{q-q}}{\partial r_{i,\alpha}} = \sum_{j=1, i \neq j}^N \frac{q_i q_j}{4\pi\epsilon_0} \left\{ \frac{\partial}{\partial r_{i,\alpha}} \left( \frac{1}{r_{ij}} \right) \operatorname{erf} \left( \frac{r_{ij}}{\sqrt{2}R} \right) + \frac{1}{r_{ij}} \frac{\partial}{\partial r_{i,\alpha}} \left( \operatorname{erf} \left( \frac{r_{ij}}{\sqrt{2}R} \right) \right) \right\}. \quad (\text{A.1})$$

The term  $\frac{\partial}{\partial r_{i,\alpha}}$  in equation (A.1) is further split, based on chain rule of the derivatives as shown below

$$\frac{\partial f}{\partial r_{i,\alpha}} = \frac{\partial f}{\partial r_{ij}} \frac{\partial r_{ij}}{\partial r_{i,\alpha}} = \frac{\partial f}{\partial r_{ij}} \frac{r_{ij,\alpha}}{r_{ij}}, \quad (\text{A.2})$$

where  $f$  is any function that depends on  $r$ . The derivative of error function is given as

$$\frac{\partial}{\partial r_{i,\alpha}} (\operatorname{erf}(ax)) = \frac{2a}{\sqrt{\pi}} \exp(-a^2 x^2), \quad (\text{A.3})$$

where  $a$  is any numerical constant. Using equation (A.2) and (A.3), equation (A.1) becomes

$$\frac{\partial E^{q-q}}{\partial r_{i,\alpha}} = \sum_{j=1, i \neq j}^N \frac{q_i q_j}{4\pi\epsilon_0} \left\{ \sqrt{\frac{2}{\pi}} \frac{1}{R r_{ij}} \exp \left( -\frac{r_{ij}^2}{2R^2} \right) - \frac{1}{r_{ij}^2} \operatorname{erf} \left( \frac{r_{ij}}{\sqrt{2}R} \right) \right\} \frac{r_{ij,\alpha}}{r_{ij}}. \quad (\text{A.4})$$

The first derivative of  $E^{q-p}$  with respect to  $\alpha^{\text{th}}$  component of position vector  $\mathbf{r}_i$  is ( $r_{i,\alpha}$ ) is

$$\frac{\partial E^{q-p}}{\partial r_{i,\alpha}} = - \sum_{j=1, i \neq j}^N \frac{q_i}{4\pi\epsilon_0} \left\{ \frac{1}{r_{ij}^3} \frac{\partial \mathbf{r}_{ij}}{\partial r_{i,\alpha}} \zeta + \mathbf{r}_{ij} \zeta \frac{\partial}{\partial r_{i,\alpha}} \left( \frac{1}{r_{ij}^3} \right) + \frac{\mathbf{r}_{ij}}{r_{ij}^3} \frac{\partial \zeta}{\partial r_{i,\alpha}} \right\} \cdot \mathbf{p}_j, \quad (\text{A.5})$$

where

$$\zeta = \operatorname{erf} \left( \frac{r_{ij}}{\sqrt{2}R} \right) - \sqrt{\frac{2}{\pi}} \frac{r_{ij}}{R} \exp \left( -\frac{r_{ij}^2}{2R^2} \right). \quad (\text{A.6})$$

The derivative of  $\zeta$  using equation (A.2) and (A.3) is

$$\begin{aligned} \frac{\partial \zeta}{\partial r_{i,\alpha}} &= \frac{\partial}{\partial r_{i,\alpha}} \left( \operatorname{erf} \left( \frac{r_{ij}}{\sqrt{2}R} \right) \right) - \sqrt{\frac{2}{\pi}} \frac{1}{R} \frac{\partial r_{ij}}{\partial r_{i,\alpha}} \exp \left( -\frac{r_{ij}^2}{2R^2} \right) \\ &- \sqrt{\frac{2}{\pi}} \frac{r_{ij}}{R} \frac{\partial}{\partial r_{i,\alpha}} \left( \exp \left( -\frac{r_{ij}^2}{2R^2} \right) \right) = \sqrt{\frac{2}{\pi}} \frac{r_{ij}^2}{R^3} \exp \left( -\frac{r_{ij}^2}{2R^2} \right) \frac{r_{ij,\alpha}}{r_{ij}}, \end{aligned} \quad (\text{A.7})$$

Substituting equation (A.7), equation (A.5) is written as

$$\frac{\partial E^{q-p}}{\partial r_{i,\alpha}} = - \sum_{j=1, i \neq j}^N \sum_{\beta=1}^3 \frac{q_i p_{j,\beta}}{4\pi\epsilon_0} \left\{ -\frac{\zeta}{r_{ij}^3} \delta_{\alpha\beta} - \frac{3\zeta}{r_{ij}^4} \frac{r_{ij,\alpha} r_{ij,\beta}}{r_{ij}} + \frac{r_{ij,\beta}}{r_{ij}^3} \sqrt{\frac{2}{\pi}} \frac{r_{ij}^2}{R^3} \exp\left(-\frac{r_{ij}^2}{2R^2}\right) \frac{r_{ij,\alpha}}{r_{ij}} \right\}. \quad (\text{A.8})$$

The first derivative of  $E^{p-p}$  with respect to  $\alpha^{\text{th}}$  component of position vector  $\mathbf{r}_i$  is ( $r_{i,\alpha}$ ) is

$$\begin{aligned} \frac{\partial E^{p-p}}{\partial r_{i,\alpha}} = & - \sum_{j=1, i \neq j}^N \frac{\mathbf{p}_i}{4\pi\epsilon_0} \cdot \left\{ \left[ \frac{3}{r_{ij}^5} \frac{\partial}{\partial r_{i,\alpha}} (\mathbf{r}_{ij} \otimes \mathbf{r}_{ij}) - 3 (\mathbf{r}_{ij} \otimes \mathbf{r}_{ij}) \frac{\partial}{\partial r_{i,\alpha}} \left( \frac{1}{r_{ij}^5} \right) - \mathbf{I} \frac{\partial}{\partial r_{i,\alpha}} \left( \frac{1}{r_{ij}^2} \right) \right] \zeta \right. \\ & + \left( \frac{3 (\mathbf{r}_{ij} \otimes \mathbf{r}_{ij}) - \mathbf{I} r_{ij}^2}{r_{ij}^5} \right) \frac{\partial \zeta}{\partial r_{i,\alpha}} \\ & - \sqrt{\frac{2}{\pi}} \frac{1}{R^3} \left[ \left( \frac{\partial}{\partial r_{i,\alpha}} (\mathbf{r}_{ij} \otimes \mathbf{r}_{ij}) + (\mathbf{r}_{ij} \otimes \mathbf{r}_{ij}) \frac{\partial}{\partial r_{i,\alpha}} \left( \frac{1}{r_{ij}^2} \right) \right) \exp\left(-\frac{r_{ij}^2}{2R^2}\right) \right] \\ & \left. + \frac{(\mathbf{r}_{ij} \otimes \mathbf{r}_{ij})}{r_{ij}^2} \frac{\partial}{\partial r_{i,\alpha}} \left( \exp\left(-\frac{r_{ij}^2}{2R^2}\right) \right) \right\} \cdot \mathbf{p}_j. \end{aligned} \quad (\text{A.9})$$

The derivative of the dyadic product between position vectors in equation (A.9) can be written as

$$\frac{\partial (\mathbf{r}_{ij} \otimes \mathbf{r}_{ij})}{\partial r_{i,\alpha}} = \frac{\partial (r_{ij,\alpha} r_{ij,\beta})}{\partial r_{i,\alpha}} = -r_{ij,\beta} - \delta_{\alpha\beta} r_{ij,\alpha}. \quad (\text{A.10})$$

Substituting the equation (A.10) in equation (A.9) results into

$$\begin{aligned} \frac{\partial E^{p-p}}{\partial r_{i,\alpha}} = & - \sum_{j=1, i \neq j}^N \frac{p_{i,\alpha} p_{j,\beta}}{4\pi\epsilon_0} \left\{ \left[ -\frac{3}{r_{ij}^5} (r_{ij,\beta} + \delta_{\alpha\beta} r_{ij,\alpha}) + \frac{15 r_{ij,\alpha} r_{ij,\beta} r_{ij,\alpha}}{r_{ij}^6} + \delta_{\alpha,\beta} \frac{3}{r_{ij}^4} \frac{r_{ij,\alpha}}{r_{ij}} \right] \zeta \right. \\ & + \frac{3 (r_{ij,\alpha} r_{ij,\beta} - r_{ij}^2 \delta_{\alpha\beta})}{r_{ij}^5} \sqrt{\frac{2}{\pi}} \frac{r_{ij}^2}{R^3} \exp\left(-\frac{r_{ij}^2}{2R^2}\right) \frac{r_{ij,\alpha}}{r_{ij}} \\ & - \sqrt{\frac{2}{\pi}} \frac{1}{R^3} \left[ \left( (-r_{ij,\beta} - \delta_{\alpha\beta} r_{ij,\alpha}) - \frac{2 r_{ij,\alpha} r_{ij,\beta} r_{ij,\alpha}}{r_{ij}^3} \right) \exp\left(-\frac{r_{ij}^2}{2R^2}\right) \right. \\ & \left. \left. - \frac{r_{ij,\alpha} r_{ij,\beta} r_{ij}}{r_{ij}^2} \exp\left(-\frac{r_{ij}^2}{2R^2}\right) \frac{r_{ij,\alpha}}{r_{ij}} \right] \right\}. \end{aligned} \quad (\text{A.11})$$

# Appendix B

## Mathematical expression for the elements in equation (4.27)

$$\mathbf{B}_u^{enr} = \begin{bmatrix} \frac{\partial}{\partial x} \psi(x) + \text{sign}(\psi(x)) \frac{(x-x_c)}{d} & 0 \\ 0 & \frac{\partial}{\partial x} \psi(x) + \text{sign}(\psi(x)) \frac{(y-y_c)}{d} \\ \frac{\partial}{\partial x} \psi(x) + \text{sign}(\psi(x)) \frac{(y-y_c)}{d} & \frac{\partial}{\partial x} \psi(x) + \text{sign}(\psi(x)) \frac{(x-x_c)}{d} \end{bmatrix}^T ; \quad (\text{B.1})$$

$$\mathbf{B}_\phi^{enr} = \begin{bmatrix} \frac{\partial}{\partial x} \psi(x) + \text{sign}(\psi(x)) \frac{(x-x_c)}{d} \\ \frac{\partial}{\partial x} \psi(x) + \text{sign}(\psi(x)) \frac{(y-y_c)}{d} \end{bmatrix}^T ; \quad (\text{B.2})$$

$$\mathbf{H}_u^{enr} = \begin{bmatrix} \frac{\partial^2}{\partial x^2} \psi(x) + 2 \frac{\partial}{\partial x} \text{sign}(\psi(x)) \frac{(x-x_c)}{d} + \text{sign}(\psi(x)) \frac{(x-x_c)^2}{d^3} & 0 & \frac{\partial^2}{\partial y \partial x} \psi(x) + \frac{\partial}{\partial y} \text{sign}(\psi(x)) \frac{(x-x_c)}{d} + \frac{\partial}{\partial x} \text{sign}(\psi(x)) \frac{(x-x_c)}{d} + \text{sign}(\psi(x)) \frac{(x-x_c)(y-y_c)}{d^2} \\ \frac{\partial^2}{\partial y \partial x} \psi(x) + \frac{\partial}{\partial y} \text{sign}(\psi(x)) \frac{(x-x_c)}{d} + \frac{\partial}{\partial x} \text{sign}(\psi(x)) \frac{(y-y_c)}{d} + \text{sign}(\psi(x)) \frac{(x-x_c)(y-y_c)}{d^2} & \frac{\partial^2}{\partial x^2} \psi(x) + 2 \frac{\partial}{\partial x} \text{sign}(\psi(x)) \frac{(x-x_c)}{d} + \text{sign}(\psi(x)) \frac{(x-x_c)^2}{d^3} & \frac{\partial^2}{\partial x^2} \psi(x) + \frac{\partial}{\partial x} \text{sign}(\psi(x)) \frac{(x-x_c)}{d} + \text{sign}(\psi(x)) \frac{(x-x_c)(y-y_c)}{d^2} \\ \frac{\partial^2}{\partial y \partial x} \psi(x) + \frac{\partial}{\partial y} \text{sign}(\psi(x)) \frac{(x-x_c)}{d} + \frac{\partial}{\partial x} \text{sign}(\psi(x)) \frac{(y-y_c)}{d} + \text{sign}(\psi(x)) \frac{(x-x_c)(y-y_c)}{d^2} & 0 & \frac{\partial^2}{\partial y^2} \psi(x) + 2 \frac{\partial}{\partial y} \text{sign}(\psi(x)) \frac{(y-y_c)}{d} + \text{sign}(\psi(x)) \frac{(y-y_c)^2}{d^3} \\ \frac{\partial^2}{\partial y^2} \psi(x) + 2 \frac{\partial}{\partial y} \text{sign}(\psi(x)) \frac{(y-y_c)}{d} + \text{sign}(\psi(x)) \frac{(y-y_c)^2}{d^3} & \frac{\partial^2}{\partial y \partial x} \psi(x) + \frac{\partial}{\partial y} \text{sign}(\psi(x)) \frac{(x-x_c)}{d} + \frac{\partial}{\partial x} \text{sign}(\psi(x)) \frac{(x-x_c)(y-y_c)}{d^2} & \frac{\partial^2}{\partial y^2} \psi(x) + \frac{\partial}{\partial y} \text{sign}(\psi(x)) \frac{(y-y_c)}{d} + \text{sign}(\psi(x)) \frac{(y-y_c)(x-x_c)}{d^2} \end{bmatrix}^T . \quad (\text{B.3})$$





## Appendix C

### Matrix form of the components in equation (4.62)

$$\mathbf{B} = \begin{bmatrix} N_{I,x} & 0 & 0 \\ 0 & N_{I,y} & 0 \\ 0 & 0 & N_{I,z} \\ N_{I,y} & N_{I,x} & 0 \\ 0 & N_{I,z} & N_{I,y} \\ N_{I,z} & 0 & N_{I,x} \end{bmatrix} + \mathbf{A} \mathbf{H}_1; \quad (\text{C.1})$$

$$\mathbf{A} = \begin{bmatrix} \frac{\partial u_{Ix}}{\partial x} & 0 & 0 & \frac{\partial u_{Iy}}{\partial x} & 0 & 0 & \frac{\partial u_{Iz}}{\partial x} & 0 & 0 \\ 0 & \frac{\partial u_{Ix}}{\partial y} & 0 & 0 & \frac{\partial u_{Iy}}{\partial y} & 0 & 0 & \frac{\partial u_{Iz}}{\partial y} & 0 \\ 0 & 0 & \frac{\partial u_{Ix}}{\partial z} & 0 & 0 & \frac{\partial u_{Iy}}{\partial z} & 0 & 0 & \frac{\partial u_{Iz}}{\partial z} \\ \frac{\partial u_{Ix}}{\partial y} & \frac{\partial u_{Ix}}{\partial x} & 0 & \frac{\partial u_{Iy}}{\partial y} & \frac{\partial u_{Iy}}{\partial x} & 0 & \frac{\partial u_{Iz}}{\partial y} & \frac{\partial u_{Iz}}{\partial x} & 0 \\ 0 & \frac{\partial u_{Ix}}{\partial z} & \frac{\partial u_{Ix}}{\partial y} & 0 & \frac{\partial u_{Iy}}{\partial z} & \frac{\partial u_{Iy}}{\partial y} & 0 & \frac{\partial u_{Iz}}{\partial z} & \frac{\partial u_{Iz}}{\partial y} \\ \frac{\partial u_{Ix}}{\partial z} & 0 & \frac{\partial u_{Ix}}{\partial x} & \frac{\partial u_{Iy}}{\partial z} & 0 & \frac{\partial u_{Iy}}{\partial x} & \frac{\partial u_{Iz}}{\partial z} & 0 & \frac{\partial u_{Iz}}{\partial x} \end{bmatrix}; \quad (\text{C.2})$$

$$\mathbf{H}_1 = \begin{bmatrix} N_{I,x} & 0 & 0 \\ N_{I,y} & 0 & 0 \\ N_{I,z} & 0 & 0 \\ 0 & N_{I,x} & 0 \\ 0 & N_{I,y} & 0 \\ 0 & N_{I,z} & 0 \\ 0 & 0 & N_{I,x} \\ 0 & 0 & N_{I,y} \\ 0 & 0 & N_{I,z} \end{bmatrix}; \quad (\text{C.3})$$

$$\mathbf{H}_D = \mathbf{H}_u + \mathbf{A}_D \mathbf{H}_2; \quad (\text{C.4})$$



$$\mathbf{H}_2 = \begin{bmatrix}
N_{I,x} & 0 & 0 & 0 & 0 & 0 & 0 & 0 & 0 \\
N_{I,y} & 0 & 0 & 0 & 0 & 0 & 0 & 0 & 0 \\
N_{I,z} & 0 & 0 & 0 & 0 & 0 & 0 & 0 & 0 \\
0 & 0 & 0 & N_{I,x} & 0 & 0 & 0 & 0 & 0 \\
0 & 0 & 0 & N_{I,y} & 0 & 0 & 0 & 0 & 0 \\
0 & 0 & 0 & N_{I,z} & 0 & 0 & 0 & 0 & 0 \\
0 & 0 & 0 & 0 & 0 & 0 & N_{I,x} & 0 & 0 \\
0 & 0 & 0 & 0 & 0 & 0 & N_{I,y} & 0 & 0 \\
0 & 0 & 0 & 0 & 0 & 0 & N_{I,z} & 0 & 0 \\
0 & N_{I,x} & 0 & 0 & 0 & 0 & 0 & 0 & 0 \\
0 & N_{I,y} & 0 & 0 & 0 & 0 & 0 & 0 & 0 \\
0 & N_{I,z} & 0 & 0 & 0 & 0 & 0 & 0 & 0 \\
0 & 0 & 0 & 0 & N_{I,x} & 0 & 0 & 0 & 0 \\
0 & 0 & 0 & 0 & N_{I,y} & 0 & 0 & 0 & 0 \\
0 & 0 & 0 & 0 & N_{I,z} & 0 & 0 & 0 & 0 \\
0 & 0 & 0 & 0 & 0 & 0 & 0 & N_{I,x} & 0 \\
0 & 0 & 0 & 0 & 0 & 0 & 0 & N_{I,y} & 0 \\
0 & 0 & 0 & 0 & 0 & 0 & 0 & N_{I,z} & 0 \\
0 & 0 & N_{I,x} & 0 & 0 & 0 & 0 & 0 & 0 \\
0 & 0 & N_{I,y} & 0 & 0 & 0 & 0 & 0 & 0 \\
0 & 0 & N_{I,z} & 0 & 0 & 0 & 0 & 0 & 0 \\
0 & 0 & 0 & 0 & 0 & N_{I,x} & 0 & 0 & 0 \\
0 & 0 & 0 & 0 & 0 & N_{I,y} & 0 & 0 & 0 \\
0 & 0 & 0 & 0 & 0 & N_{I,z} & 0 & 0 & 0 \\
0 & 0 & 0 & 0 & 0 & 0 & 0 & 0 & N_{I,x} \\
0 & 0 & 0 & 0 & 0 & 0 & 0 & 0 & N_{I,y} \\
0 & 0 & 0 & 0 & 0 & 0 & 0 & 0 & N_{I,z}
\end{bmatrix}; \quad (\text{C.7})$$

$$\mathbf{R} = \begin{bmatrix}
S_{11} & S_{12} & S_{13} & 0 & 0 & 0 & 0 & 0 & 0 \\
S_{12} & S_{22} & S_{23} & 0 & 0 & 0 & 0 & 0 & 0 \\
S_{13} & S_{32} & S_{33} & 0 & 0 & 0 & 0 & 0 & 0 \\
0 & 0 & 0 & S_{11} & S_{12} & S_{13} & 0 & 0 & 0 \\
0 & 0 & 0 & S_{12} & S_{22} & S_{23} & 0 & 0 & 0 \\
0 & 0 & 0 & S_{11} & S_{23} & S_{33} & 0 & 0 & 0 \\
0 & 0 & 0 & 0 & 0 & 0 & S_{11} & S_{12} & S_{13} \\
0 & 0 & 0 & 0 & 0 & 0 & S_{21} & S_{22} & S_{23} \\
0 & 0 & 0 & 0 & 0 & 0 & S_{13} & S_{23} & S_{33}
\end{bmatrix}; \quad (\text{C.8})$$

$$\hat{\mathbf{R}} = [ S_{11} \ S_{22} \ S_{33} \ S_{12} \ S_{23} \ S_{13} ]^T; \quad (\text{C.9})$$

$$\mathbf{R}_D = \begin{bmatrix}
\tilde{\tau}_{111} & 0 & 0 & \tilde{\tau}_{211} & 0 & 0 & \tilde{\tau}_{311} & 0 & 0 \\
\tilde{\tau}_{112} & 0 & 0 & \tilde{\tau}_{212} & 0 & 0 & \tilde{\tau}_{312} & 0 & 0 \\
\tilde{\tau}_{113} & 0 & 0 & \tilde{\tau}_{213} & 0 & 0 & \tilde{\tau}_{313} & 0 & 0 \\
\tilde{\tau}_{211} & 0 & 0 & \tilde{\tau}_{221} & 0 & 0 & \tilde{\tau}_{321} & 0 & 0 \\
\tilde{\tau}_{212} & 0 & 0 & \tilde{\tau}_{222} & 0 & 0 & \tilde{\tau}_{322} & 0 & 0 \\
\tilde{\tau}_{213} & 0 & 0 & \tilde{\tau}_{223} & 0 & 0 & \tilde{\tau}_{323} & 0 & 0 \\
\tilde{\tau}_{311} & 0 & 0 & \tilde{\tau}_{321} & 0 & 0 & \tilde{\tau}_{331} & 0 & 0 \\
\tilde{\tau}_{312} & 0 & 0 & \tilde{\tau}_{322} & 0 & 0 & \tilde{\tau}_{332} & 0 & 0 \\
\tilde{\tau}_{313} & 0 & 0 & \tilde{\tau}_{323} & 0 & 0 & \tilde{\tau}_{333} & 0 & 0 \\
0 & \tilde{\tau}_{111} & 0 & 0 & \tilde{\tau}_{211} & 0 & 0 & \tilde{\tau}_{311} & 0 \\
0 & \tilde{\tau}_{112} & 0 & 0 & \tilde{\tau}_{212} & 0 & 0 & \tilde{\tau}_{312} & 0 \\
0 & \tilde{\tau}_{113} & 0 & 0 & \tilde{\tau}_{213} & 0 & 0 & \tilde{\tau}_{313} & 0 \\
0 & \tilde{\tau}_{211} & 0 & 0 & \tilde{\tau}_{221} & 0 & 0 & \tilde{\tau}_{321} & 0 \\
0 & \tilde{\tau}_{212} & 0 & 0 & \tilde{\tau}_{222} & 0 & 0 & \tilde{\tau}_{322} & 0 \\
0 & \tilde{\tau}_{213} & 0 & 0 & \tilde{\tau}_{223} & 0 & 0 & \tilde{\tau}_{323} & 0 \\
0 & \tilde{\tau}_{311} & 0 & 0 & \tilde{\tau}_{321} & 0 & 0 & \tilde{\tau}_{331} & 0 \\
0 & \tilde{\tau}_{312} & 0 & 0 & \tilde{\tau}_{322} & 0 & 0 & \tilde{\tau}_{332} & 0 \\
0 & \tilde{\tau}_{313} & 0 & 0 & \tilde{\tau}_{323} & 0 & 0 & \tilde{\tau}_{333} & 0 \\
0 & 0 & \tilde{\tau}_{111} & 0 & 0 & \tilde{\tau}_{211} & 0 & 0 & \tilde{\tau}_{311} \\
0 & 0 & \tilde{\tau}_{112} & 0 & 0 & \tilde{\tau}_{212} & 0 & 0 & \tilde{\tau}_{312} \\
0 & 0 & \tilde{\tau}_{113} & 0 & 0 & \tilde{\tau}_{213} & 0 & 0 & \tilde{\tau}_{313} \\
0 & 0 & \tilde{\tau}_{211} & 0 & 0 & \tilde{\tau}_{221} & 0 & 0 & \tilde{\tau}_{321} \\
0 & 0 & \tilde{\tau}_{212} & 0 & 0 & \tilde{\tau}_{222} & 0 & 0 & \tilde{\tau}_{322} \\
0 & 0 & \tilde{\tau}_{213} & 0 & 0 & \tilde{\tau}_{223} & 0 & 0 & \tilde{\tau}_{323} \\
0 & 0 & \tilde{\tau}_{311} & 0 & 0 & \tilde{\tau}_{321} & 0 & 0 & \tilde{\tau}_{331} \\
0 & 0 & \tilde{\tau}_{312} & 0 & 0 & \tilde{\tau}_{322} & 0 & 0 & \tilde{\tau}_{332} \\
0 & 0 & \tilde{\tau}_{313} & 0 & 0 & \tilde{\tau}_{323} & 0 & 0 & \tilde{\tau}_{333}
\end{bmatrix} ; \quad (\text{C.10})$$

$$\hat{\mathbf{R}}_D = \begin{bmatrix}
\tilde{\tau}_{111} & \tilde{\tau}_{112} & \tilde{\tau}_{113} & \tilde{\tau}_{221} & \tilde{\tau}_{222} & \tilde{\tau}_{223} & \tilde{\tau}_{331} & \tilde{\tau}_{332} & \tilde{\tau}_{333} \\
\tilde{\tau}_{211} & \tilde{\tau}_{212} & \tilde{\tau}_{213} & \tilde{\tau}_{311} & \tilde{\tau}_{312} & \tilde{\tau}_{313} & \tilde{\tau}_{321} & \tilde{\tau}_{322} & \tilde{\tau}_{323}
\end{bmatrix}^T ; \quad (\text{C.11})$$

$$\hat{\mathbf{D}} = \begin{bmatrix} D_1 \\ D_2 \\ D_3 \end{bmatrix} ; \quad (\text{C.12})$$

$$\mathbf{B}_\phi = [N_{I,x}, N_{I,y}, N_{I,y}]^T ; \quad (\text{C.13})$$

$$\mathbf{B}_{\psi u} = \begin{bmatrix} N_{I,x} & 0 & 0 \\ 0 & N_{I,x} & 0 \\ 0 & 0 & N_{I,x} \\ N_{I,y} & 0 & 0 \\ 0 & N_{I,y} & 0 \\ 0 & 0 & N_{I,y} \\ N_{I,z} & 0 & 0 \\ 0 & N_{I,z} & 0 \\ 0 & 0 & N_{I,z} \end{bmatrix} . \quad (\text{C.14})$$

Material constants:

$$\mathbb{C} = \frac{E}{(1+\nu)(1-2\nu)} \begin{bmatrix} 1-\nu & \nu & \nu & 0 & 0 & 0 \\ \nu & 1-\nu & \nu & 0 & 0 & 0 \\ \nu & \nu & 1-\nu & 0 & 0 & 0 \\ 0 & 0 & 0 & 1-2\nu & 0 & 0 \\ 0 & 0 & 0 & 0 & 1-2\nu & 0 \\ 0 & 0 & 0 & 0 & 0 & 1-2\nu \end{bmatrix}, \quad (\text{C.15})$$

$$\boldsymbol{\kappa} = \begin{bmatrix} \kappa_{11} & 0 & 0 \\ 0 & \kappa_{11} & 0 \\ 0 & 0 & \kappa_{33} \end{bmatrix}, \quad (\text{C.16})$$

$$\boldsymbol{e} = \begin{bmatrix} 0 & 0 & e_{31} \\ 0 & 0 & e_{31} \\ 0 & 0 & e_{33} \\ 0 & e_{15} & 0 \\ e_{15} & 0 & 0 \\ 0 & 0 & 0 \end{bmatrix}, \quad (\text{C.17})$$

$$\boldsymbol{\mu} = \begin{bmatrix} \mu_{11} & \mu_{12} & \mu_{12} & 0 & 0 & 0 & 0 & 0 & 0 & 0 & 0 & \mu_{44} & 0 & 0 & 0 & 0 & \mu_{44} & 0 \\ 0 & 0 & 0 & 0 & 0 & \mu_{44} & \mu_{12} & \mu_{11} & \mu_{12} & 0 & 0 & 0 & 0 & 0 & 0 & \mu_{44} & 0 & 0 \\ 0 & 0 & 0 & 0 & \mu_{44} & 0 & 0 & 0 & 0 & \mu_{44} & 0 & 0 & \mu_{12} & \mu_{12} & \mu_{11} & 0 & 0 & 0 \end{bmatrix}, \quad (\text{C.18})$$

$$\boldsymbol{g} = l^2 \begin{bmatrix} \mathbb{C} & \mathbf{0} & \mathbf{0} \\ \mathbf{0} & \mathbb{C} & \mathbf{0} \\ \mathbf{0} & \mathbf{0} & \mathbb{C} \end{bmatrix}. \quad (\text{C.19})$$



# Bibliography

- ABADI R., SHIRAZI A.H.N., IZADIFAR M., SEPAHI M. ET AL. Fabrication of nanopores in polycrystalline boron-nitride nanosheet by using si, sic and diamond clusters bombardment. *Computational Materials Science*, 145 (2018): 280–290.
- ABDOLLAHI A., DOMINGO N., ARIAS I. & CATALAN G. Converse flexoelectricity yields large piezoresponse force microscopy signals in non-piezoelectric materials. *Nature communications*, 10 (2019) (1): 1–6.
- ABDOLLAHI A., MILLÁN D., PECO C., ARROYO M. ET AL. Revisiting pyramid compression to quantify flexoelectricity: A three-dimensional simulation study. *Physical Review B*, 91 (2015) (10): 104103.
- ABDOLLAHI A., PECO C., MILLÁN D., ARROYO M. ET AL. Computational evaluation of the flexoelectric effect in dielectric solids. *Journal of Applied Physics*, 116 (2014) (9): 093502.
- AHMADPOOR F. & SHARMA P. Flexoelectricity in two-dimensional crystalline and biological membranes. *Nanoscale*, 7 (2015a) (40): 16555–16570.
- AHMADPOOR F. & SHARMA P. Flexoelectricity in two-dimensional crystalline and biological membranes. *Nanoscale*, 7 (2015b) (40): 16555–16570.
- ANDREW R.C., MAPASHA R.E., UKPONG A.M. & CHETTY N. Mechanical properties of graphene and boronitrene. *Physical review B*, 85 (2012) (12): 125428.
- AZIMI S., GOLABCHI A., NEKOOKAR A., RABBANI S. ET AL. Self-powered cardiac pacemaker by piezoelectric polymer nanogenerator implant. *Nano Energy*, 83 (2021): 105781.
- BELYTSCHKO T., LIU W.K., MORAN B. & ELKHODARY K. *Nonlinear finite elements for continua and structures*. John wiley & sons, 2013.
- BELYTSCHKO T., LU Y., GU L. & TABBARA M. Element-free galerkin methods for static and dynamic fracture. *International Journal of Solids and Structures*, 32 (1995) (17-18): 2547–2570.
- BELYTSCHKO T., LU Y.Y. & GU L. Element-free galerkin methods. *International journal for numerical methods in engineering*, 37 (1994) (2): 229–256.



- BERLINCOURT D. & JAFFE H. Elastic and piezoelectric coefficients of single-crystal barium titanate. *Physical Review*, 111 (1958) (1): 143.
- BLONSKY M.N., ZHUANG H.L., SINGH A.K. & HENNIG R.G. Ab initio prediction of piezoelectricity in two-dimensional materials. *ACS nano*, 9 (2015) (10): 9885–9891.
- BRENNAN C.J., GHOSH R., KOUL K., BANERJEE S.K. ET AL. Out-of-Plane Electromechanical Response of Monolayer Molybdenum Disulfide Measured by Piezoresponse Force Microscopy. *Nano Lett.*, 17 (2017): 5464–5471.
- BRENNER D.W., SHENDEROVA O.A., HARRISON J.A., STUART S.J. ET AL. A second-generation reactive empirical bond order (rebo) potential energy expression for hydrocarbons. *J. Phys.: Condens. Matter*, 14 (2002) (4): 783.
- BRISCOE J., JALALI N., WOOLLIAMS P., STEWART M. ET AL. Measurement techniques for piezoelectric nanogenerators. *Energy & Environmental Science*, 6 (2013) (10): 3035–3045.
- CHANDRATRE S. & SHARMA P. Coaxing graphene to be piezoelectric. *Applied Physics Letters*, 100 (2012) (2): 023 114.
- CHATZOPOULOS A., BECK P., ROTH J. & TREBIN H.R. Atomistic modeling of flexoelectricity in periclase. *Physical Review B*, 93 (2016) (2): 024 105.
- CHEN H. & CALLAWAY J. Lattice dielectric functions based on the shell model. *Physical Review B*, 45 (1992) (5): 2085.
- CHEN X., MENG R., JIANG J., LIANG Q. ET AL. Electronic structure and optical properties of graphene/stanene heterobilayer. *Phys. Chem. Chem. Phys.*, 18 (2016) (24): 16 302–16 309.
- CHEN Y., LIU B., MA Y. & ZHOU Y. Modification of a shell model for the study of the radiation effects in batio 3. *Nuclear Instruments and Methods in Physics Research Section B: Beam Interactions with Materials and Atoms*, 267 (2009) (18): 3090–3093.
- CHENG B., GABBAY M., DUFFY W. & FANTOZZI G. Mechanical loss and young's modulus associated with phase transitions in barium titanate based ceramics. *Journal of materials science*, 31 (1996) (18): 4951–4955.
- CHU B. & SALEM D. Flexoelectricity in several thermoplastic and thermosetting polymers. *Applied Physics Letters*, 101 (2012) (10): 103 905.
- CHUNG D. Electromagnetic interference shielding effectiveness of carbon materials. *carbon*, 39 (2001) (2): 279–285.
- CIOFANI G. & MENCIASSI A. *Piezoelectric nanomaterials for biomedical applications*. Springer, 2012.

- CLOUGH R.W., PENZIEN J. & GRIFFIN D. Dynamics of structures. *Journal of Applied Mechanics*, 44 (1977): 366.
- COHEN R.E. & KRAKAUER H. Electronic structure studies of the differences in ferroelectric behavior of batio<sub>3</sub> and pbtio<sub>3</sub>. *Ferroelectrics*, 136 (1992) (1): 65–83.
- COMPANO R., MOLENKAMP L. & PAUL D. Roadmap for nanoelectronics. *European Commission IST programme, Future and Emerging Technologies*, (2000).
- COOK-CHENNAULT K.A., THAMBI N. & SASTRY A.M. Powering mems portable devices a review of non-regenerative and regenerative power supply systems with special emphasis on piezoelectric energy harvesting systems. *Smart materials and structures*, 17 (2008) (4): 043 001.
- DÁVILA M.E. & LE LAY G. Few layer epitaxial germanene: a novel two-dimensional dirac material. *Sci. Rep.*, 6 (2016): 20714.
- DE JONG M., CHEN W., GEERLINGS H., ASTA M. ET AL. A database to enable discovery and design of piezoelectric materials. *Sci. Data*, 2 (2015): 150 053.
- DENG F., DENG Q., YU W. & SHEN S. Mixed finite elements for flexoelectric solids. *Journal of Applied Mechanics*, 84 (2017) (8): 081 004.
- DENG Q. Size-dependent flexoelectric response of a truncated cone and the consequent ramifications for the experimental measurement of flexoelectric properties. *Journal of Applied Mechanics*, 84 (2017) (10): 101 007.
- DENG Q., KAMMOUN M., ERTURK A. & SHARMA P. Nanoscale flexoelectric energy harvesting. *International Journal of Solids and Structures*, 51 (2014) (18): 3218–3225.
- DIMOULAS A. Silicene and germanene: Silicon and germanium in the flatland. *Microelectronic engineering*, 131 (2015): 68–78.
- DONG L., LOU J. & SHENOY V.B. Large in-plane and vertical piezoelectricity in janus transition metal dichalcogenides. *ACS nano*, 11 (2017) (8): 8242–8248.
- DOU K.P., HU H.H., WANG X., WANG X. ET AL. Asymmetrically flexoelectric gating effect of janus transition-metal dichalcogenides and their sensor applications. *Journal of Materials Chemistry C*, 8 (2020) (33): 11 457–11 467.
- DROTH M., BURKARD G. & PEREIRA V.M. Piezoelectricity in planar boron nitride via a geometric phase. *Phys. Rev. B*, 94 (2016): 075 404.
- DUERLOO K.A.N., ONG M.T. & REED E.J. Intrinsic piezoelectricity in two-dimensional materials. *J. Phys. Chem. Lett.*, 3 (2012) (19): 2871–2876.
- DUERLOO K.A.N. & REED E.J. Flexural electromechanical coupling: a nanoscale emergent property of boron nitride bilayers. *Nano letters*, 13 (2013) (4): 1681–1686.

- DUMITRICĂ T., LANDIS C.M. & YAKOBSON B.I. Curvature-induced polarization in carbon nanoshells. *Chemical physics letters*, 360 (2002) (1-2): 182–188.
- ENYASHIN A.N. & IVANOVSKII A.L. Graphene allotropes. *Phys. Stat. Solidi (b)*, 248 (2011) (8): 1879–1883.
- ER D., YE H., FREY N.C., KUMAR H. ET AL. Prediction of Enhanced Catalytic Activity for Hydrogen Evolution Reaction in Janus Transition Metal Dichalcogenides. *Nano Letters*, 18 (2018) (6): 3943–3949.
- FEI R. & YANG L. Strain-engineering the anisotropic electrical conductance of few-layer black phosphorus. *Nano letters*, 14 (2014) (5): 2884–2889.
- FINCHAM D., MACKRODT W. & MITCHELL P. Mgo at high temperatures and pressures: shell-model lattice dynamics and molecular dynamics. *Journal of Physics: Condensed Matter*, 6 (1994) (2): 393.
- FRISCH M.J., TRUCKS G.W., SCHLEGEL H.B., SCUSERIA G.E. ET AL. Gaussian 16 Revision B.01 (2016). Gaussian Inc. Wallingford CT.
- FU J.Y., ZHU W., LI N. & CROSS L.E. Experimental studies of the converse flexoelectric effect induced by inhomogeneous electric field in a barium strontium titanate composition. *Journal of Applied Physics*, 100 (2006) (2): 024 112.
- GEETHA S., SATHEESH KUMAR K., RAO C.R., VIJAYAN M. ET AL. EMI shielding: Methods and materials a review. *Journal of applied polymer science*, 112 (2009) (4): 2073–2086.
- GHASEMI H., PARK H.S. & RABCZUK T. A level-set based IGA formulation for topology optimization of flexoelectric materials. *Computer Methods in Applied Mechanics and Engineering*, 313 (2017): 239–258.
- GHOSH S., BAO W., NIKA D.L., SUBRINA S. ET AL. Dimensional crossover of thermal transport in few-layer graphene. *Nature materials*, 9 (2010) (7): 555.
- GIBSON R.F. A review of recent research on mechanics of multifunctional composite materials and structures. *Composite structures*, 92 (2010) (12): 2793–2810.
- GIBSON R.F., AYORINDE E.O. & WEN Y.F. Vibrations of carbon nanotubes and their composites: a review. *Composites science and technology*, 67 (2007) (1): 1–28.
- GLEITER R. Pi-sigma interactions: Experimental evidence and its consequences for the chemical reactivity of organic compounds. *Pure & Appl. Chem.*, 59 (1987) (594): 1585–1594.
- GODDARD III W.A., ZHANG Q., ULUDOGAN M., STRACHAN A. ET AL. The reaxff polarizable reactive force fields for molecular dynamics simulation of ferroelectrics. In *AIP Conference Proceedings*, volume 626, pages 45–55. AIP, 2002.

- GULLAPALLI H., VEMURU V.S., KUMAR A., BOTELLO-MENDEZ A. ET AL. Flexible piezoelectric zno–paper nanocomposite strain sensor. *small*, 6 (2010) (15): 1641–1646.
- HANAKATA P.Z., CARVALHO A., CAMPBELL D.K. & PARK H.S. Polarization and valley switching in monolayer group-iv monochalcogenides. *Physical Review B*, 94 (2016) (3): 035 304.
- HE B., JAVVAJI B. & ZHUANG X. Size dependent flexoelectric and mechanical properties of barium titanate nanobelt: A molecular dynamics study. *Physica B: Condensed Matter*, (2018).
- HE B., MORTAZAVI B., ZHUANG X. & RABCZUK T. Modeling kapitza resistance of two-phase composite material. *Composite Structures*, 152 (2016): 939–946.
- HERNÁNDEZ E., GOZE C., BERNIER P. & RUBIO A. Elastic Properties of C and B<sub>x</sub> C<sub>y</sub> N<sub>z</sub> Composite Nanotubes. *Phys. Rev. Lett.*, 80 (1998) (20): 4502–4505.
- HERNÁNDEZ E., GOZE C., BERNIER P. & RUBIO A. Elastic properties of single-wall nanotubes. *Applied Physics A*, 68 (1999) (3): 287–292.
- HONG J., CATALAN G., SCOTT J. & ARTACHO E. The flexoelectricity of barium and strontium titanates from first principles. *Journal of Physics: Condensed Matter*, 22 (2010) (11): 112 201.
- HU C.J., LIN Y.H., TANG C.W., TSAI M.Y. ET AL. Zno-coated carbon nanotubes: flexible piezoelectric generators. *Advanced Materials*, 23 (2011) (26): 2941–2945.
- HU S., LI H. & TZOU H. Comparison of flexoelectric and piezoelectric dynamic signal responses on flexible rings. *Journal of Intelligent Material Systems and Structures*, 25 (2014) (7): 832–844.
- HU T., JIA F., ZHAO G., WU J. ET AL. Intrinsic and anisotropic rashba spin splitting in janus transition-metal dichalcogenide monolayers. *Physical Review B*, 97 (2018) (23): 235 404.
- HUANG C.T., SHEN C.L., TANG C.F. & CHANG S.H. A wearable yarn-based piezoresistive sensor. *Sensors and Actuators A: Physical*, 141 (2008) (2): 396–403.
- HUANG S., KIM T., HOU D., CANN D. ET AL. Flexoelectric characterization of batio<sub>3</sub>-0.08 bi (zn<sub>1/2</sub>ti<sub>1/2</sub>) o<sub>3</sub>. *Applied Physics Letters*, 110 (2017) (22): 222 904.
- HUANG W., KIM K., ZHANG S., YUAN F.G. ET AL. Scaling effect of flexoelectric (ba, sr) tio<sub>3</sub> microcantilevers. *physica status solidi (RRL)–Rapid Research Letters*, 5 (2011) (9): 350–352.
- HUANG Z., ZHONG J., LIU H., WU Y. ET AL. Strain engineering the structures and electronic properties of Janus monolayer transition-metal dichalcogenides. *Journal of Applied Physics*, 125 (2018) (8): 082 516.

- IHN J.B. & CHANG F.K. Detection and monitoring of hidden fatigue crack growth using a built-in piezoelectric sensor/actuator network: I. diagnostics. *Smart materials and structures*, 13 (2004) (3): 609.
- IKEDA T. *Fundamentals of piezoelectricity*. Oxford university press, 1996.
- ISHIGAMI M., CHEN J.H., CULLEN W.G., FUHRER M.S. ET AL. Atomic Structure of Graphene on SiO<sub>2</sub>. *Nano. Lett.*, 7 (2007): 1643–1648.
- JAVVAJI B., BUDARAPU P., SUTRAKAR V., MAHAPATRA D.R. ET AL. Mechanical properties of Graphene: Molecular dynamics simulations correlated to continuum based scaling laws. *Computational Materials Science*, 125 (2016): 319–327.
- JAVVAJI B., HE B. & ZHUANG X. The generation of piezoelectricity and flexoelectricity in graphene by breaking the materials symmetries. *Nanotechnology*, 29 (2018) (22): 225 702.
- JIANG H.L., JIA S.H., ZHOU D.W., PU C.Y. ET AL. First-principles calculations of the mechanical and elastic properties of 2hc-and 2ha-ws2/crs2 under pressure. *Zeitschrift für Naturforschung A*, 71 (2016) (6): 517–524.
- JIANG J.W. Misfit strain-induced buckling for transition-metal dichalcogenide lateral heterostructures: A molecular dynamics study. *Acta Mechanica Sinica*, 32 (2019) (1): 17–28.
- JIANG J.W., PARK H.S. & RABCZUK T. Molecular dynamics simulations of single-layer molybdenum disulphide (mos2): Stillinger-weber parametrization, mechanical properties, and thermal conductivity. *J. Appl. Phys.*, 114 (2013a) (6): 064 307.
- JIANG J.W., QI Z., PARK H.S. & RABCZUK T. Elastic bending modulus of single-layer molybdenum disulfide (MoS 2): Finite thickness effect. *Nanotechnology*, 24 (2013b) (43): 435 705.
- JIANG J.W. & ZHOU Y.P. Parameterization of stillinger-weber potential for two- dimensional atomic crystals. In JIANG J.W. & ZHOU Y.P., eds., *Handbook of Stillinger-Weber Potential Parameters for Two-Dimensional Atomic Crystals*, chapter 1. IntechOpen, Rijeka, 2017.
- JIANG X., HUANG W. & ZHANG S. Flexoelectric nano-generator: Materials, structures and devices. *Nano Energy*, 2 (2013c) (6): 1079–1092.
- JIN H., WANG T., GONG Z.R., LONG C. ET AL. Prediction of an extremely long exciton lifetime in a Janus-MoSTe monolayer. *Nanoscale*, 10 (2018) (41): 19 310–19 315.
- JIN Y., ZHANG F., ZHOU K., SUEN C.H. ET AL. Oxygen vacancy and photoelectron enhanced flexoelectricity in perovskite srtio3 crystal. *Applied Physics Letters*, 118 (2021) (16): 164 101.
- KALAMKAROV A.L., ANDRIANOV I.V. & DANISHEVS KYV V.V. Asymptotic homogenization of composite materials and structures. *Applied Mechanics Reviews*, 62 (2009) (3).

- KALININ S.V. & MEUNIER V. Electronic flexoelectricity in low-dimensional systems. *Phys. Rev. B*, 77 (2008) (3): 033 403.
- KARTHIK J., MANGALAM R., AGAR J. & MARTIN L. Large built-in electric fields due to flexoelectricity in compositionally graded ferroelectric thin films. *Physical Review B*, 87 (2013) (2): 024 111.
- KIM S.J., CHOI K., LEE B., KIM Y. ET AL. Materials for flexible, stretchable electronics: graphene and 2d materials. *Annual Review of Materials Research*, 45 (2015): 63–84.
- KONG L., LI Z., LIU L., HUANG R. ET AL. Recent progress in some composite materials and structures for specific electromagnetic applications. *International Materials Reviews*, 58 (2013) (4): 203–259.
- KUNDALWAL S.I., MEGUID S.A. & WENG G.J. Strain gradient polarization in graphene. *Carbon*, 117 (2017): 462–472.
- KVASHNIN A.G., SOROKIN P.B. & YAKOBSON B.I. Flexoelectricity in carbon nanostructures: nanotubes, fullerenes, and nanocones. *J. Phys. Chem. Lett.*, 6 (2015) (14): 2740–2744.
- KVASHNIN D.G., MATVEEV A.T., LEBEDEV O.I., YAKOBSON B.I. ET AL. Ultrasharp h-bn nanocones and the origin of their high mechanical stiffness and large dipole moment. *The journal of physical chemistry letters*, 9 (2018) (17): 5086–5091.
- KWEI G., LAWSON A., BILLINGE S. & CHEONG S. Structures of the ferroelectric phases of barium titanate. *The Journal of Physical Chemistry*, 97 (1993) (10): 2368–2377.
- KWON S.R., HUANG W., SHU L., YUAN F.G. ET AL. Flexoelectricity in barium strontium titanate thin film. *Applied Physics Letters*, 105 (2014) (14): 142 904.
- LEMANOV V., SMIRNOVA E., SYRNIKOV P. & TARAKANOV E. Phase transitions and glasslike behavior in sr 1- x ba x tio 3. *Physical Review B*, 54 (1996) (5): 3151.
- LI C., THOSTENSON E.T. & CHOU T.W. Sensors and actuators based on carbon nanotubes and their composites: a review. *Composites Science and Technology*, 68 (2008) (6): 1227–1249.
- LI Y., SHU L., HUANG W., JIANG X. ET AL. Giant flexoelectricity in ba<sub>0.6</sub>sr<sub>0.4</sub>tio<sub>3</sub>/ni<sub>0.8</sub>zn<sub>0.2</sub>fe<sub>2</sub>o<sub>4</sub> composite. *Applied Physics Letters*, 105 (2014) (16): 162 906.
- LI Z., ZHU G., YANG R., WANG A.C. ET AL. Muscle-driven in vivo nanogenerator. *Advanced materials*, 22 (2010) (23): 2534–2537.
- LIN Y.F., SONG J., DING Y., LU S.Y. ET AL. Piezoelectric nanogenerator using cds nanowires. *Applied Physics Letters*, 92 (2008) (2): 022 105.
- LINDAN P. & GILLAN M. Shell-model molecular dynamics simulation of superionic conduction in caf<sub>2</sub>. *Journal of Physics: Condensed Matter*, 5 (1993) (8): 1019.

- LIU K., ZHANG S., XU M., WU T. ET AL. The research of effective flexoelectric coefficient along 1123 direction in polyvinylidene fluoride. *Journal of Applied Physics*, 121 (2017) (17): 174 104.
- LU H., BARK C.W., DE LOS OJOS D.E., ALCALA J. ET AL. Mechanical writing of ferroelectric polarization. *Science*, 336 (2012) (6077): 59–61.
- LU J., LV J., LIANG X., XU M. ET AL. Improved approach to measure the direct flexoelectric coefficient of bulk polyvinylidene fluoride. *Journal of Applied Physics*, 119 (2016) (9): 094 104.
- LU W. & LIEBER C.M. Nanoelectronics from the bottom up. *Nanoscience And Technology: A Collection of Reviews from Nature Journals*, (2010): 137–146.
- MA W. & CROSS L.E. Observation of the flexoelectric effect in relaxor pb (mg 1/3 nb 2/3) o 3 ceramics. *Applied Physics Letters*, 78 (2001) (19): 2920–2921.
- MA W. & CROSS L.E. Flexoelectric polarization of barium strontium titanate in the paraelectric state. *Applied Physics Letters*, 81 (2002) (18): 3440–3442.
- MA W. & CROSS L.E. Flexoelectricity of barium titanate. *Applied Physics Letters*, 88 (2006) (23): 232 902.
- MACHADO R., SEPLIARSKY M. & STACHIOTTI M. Phase transitions and piezoelectric properties of srbi2ta2o9 by molecular dynamics simulations. *Journal of materials science*, 45 (2010) (18): 4912–4918.
- MAHDIZADEH S.J. & AKHLAMADI G. Optimized tersoff empirical potential for germanene. *Journal of Molecular Graphics and Modelling*, 72 (2017): 1–5.
- MAJDOUB M., SHARMA P. & CAGIN T. Enhanced size-dependent piezoelectricity and elasticity in nanostructures due to the flexoelectric effect. *Phys. Rev. B*, 77 (2008) (12): 125 424.
- MAJDOUB M.S., SHARMA P. & ÇAĞIN T. Erratum: Enhanced size-dependent piezoelectricity and elasticity in nanostructures due to the flexoelectric effect [phys. rev. b 77, 125424 (2008)]. *Phys. Rev. B*, 79 (2009): 119 904.
- MALLOUK T.E. & SEN A. Powering nanorobots. *Scientific American*, 300 (2009) (5): 72–77.
- MAO S., PUROHIT P.K. & ARAVAS N. Mixed finite-element formulations in piezoelectricity and flexoelectricity. *Proc. R. Soc. A*, 472 (2016) (2190): 20150 879.
- MARANGANTI R. & SHARMA P. Atomistic determination of flexoelectric properties of crystalline dielectrics. *Physical Review B*, 80 (2009) (5): 054 109.
- MAS-BALLESTÉ R., GÓMEZ-NAVARRO C., GÓMEZ-HERRERO J. & ZAMORA F. 2d materials: to graphene and beyond. *Nanoscale*, 3 (2011) (1): 20–30.

- MATSUI M. Breathing shell model in molecular dynamics simulation: Application to mgo and cao. *The Journal of chemical physics*, 108 (1998) (8): 3304–3309.
- MAYER A. Polarization of metallic carbon nanotubes from a model that includes both net charges and dipoles. *Phys. Rev. B*, 71 (2005) (23): 235 333.
- MAYER A. Formulation in terms of normalized propagators of a charge-dipole model enabling the calculation of the polarization properties of fullerenes and carbon nanotubes. *Phys. Rev. B*, 75 (2007) (4): 045 407.
- MBARKI R., HASKINS J., KINACI A. & CAGIN T. Temperature dependence of flexoelectricity in batio 3 and srtio 3 perovskite nanostructures. *Physics Letters A*, 378 (2014) (30): 2181–2183.
- MEGRICHE A., LEBRUN L. & TROCCAZ M. Materials of bi4ti3o12 type for high temperature acoustic piezo-sensors. *Sensors and Actuators A: Physical*, 78 (1999) (2-3): 88–91.
- MELE E.J. & KRÁL P. Electric polarization of heteropolar nanotubes as a geometric phase. *Phys. Rev. Lett.*, 88 (2002) (5): 568 031–568 034.
- MITCHELL P. & FINCHAM D. Shell model simulations by adiabatic dynamics. *Journal of Physics: Condensed Matter*, 5 (1993) (8): 1031.
- MOMENI K., ODEGARD G.M. & YASSAR R.S. Finite size effect on the piezoelectric properties of zno nanobelts: A molecular dynamics approach. *Acta materialia*, 60 (2012) (13-14): 5117–5124.
- MOON W.H. & HWANG H.J. Molecular mechanics of structural properties of boron nitride nanotubes. *Physica E*, 23 (2004) (1-2): 26–30.
- NAESS S.N., ELGSAETER A., HELGESEN G. & KNUDSEN K.D. Carbon nanocones: wall structure and morphology. *Science and technology of advanced materials*, 10 (2009) (6): 065 002.
- NAKHMANSO S.M., CALZOLARI A., MEUNIER V., BERNHOLC J. ET AL. Spontaneous polarization and piezoelectricity in boron nitride nanotubes. *Phys. Rev. B*, 67 (2003): 235 406.
- NANTHAKUMAR S., ZHUANG X., PARK H.S. & RABCZUK T. Topology optimization of flexoelectric structures. *Journal of the Mechanics and Physics of Solids*, 105 (2017): 217–234.
- NAUMOV I., BRATKOVSKY A.M. & RANJAN V. Unusual Flexoelectric Effect in Two-Dimensional Noncentrosymmetric sp<sup>2</sup>-Bonded Crystals. *Phys. Rev. Lett.*, 102 (2009): 217 601.
- NEWMARK N.M. A method of computation for structural dynamics. *Journal of the engineering mechanics division*, 85 (1959) (3): 67–94.



- NGUYEN V.P., RABCZUK T., BORDAS S. & DUFLOT M. Meshless methods: a review and computer implementation aspects. *Mathematics and computers in simulation*, 79 (2008) (3): 763–813.
- NIKIFOROV I., DONTSOVA E., JAMES R.D. & DUMITRICĂ T. Tight-binding theory of graphene bending. *Phys. Rev. B*, 89 (2014) (15): 155 437.
- NORD J., ALBE K., ERHART P. & NORDLUND K. Modelling of compound semiconductors: analytical bond-order potential for gallium, nitrogen and gallium nitride. *J Phys: Condens. Matter*, 15 (2003) (32): 5649.
- OLSEN J. & JØRGENSEN P. Linear and nonlinear response functions for an exact state and for an MCSCF state. *J. Chem. Phys.*, 82 (1985) (7): 3235–3264.
- OLSON M.L. & SUNDBERG K.R. An atom monopole–dipole interaction model with charge transfer for the treatment of polarizabilities of  $\pi$ -bonded molecules. *J. Chem. Phys.*, 69 (1978) (12): 5400–5404.
- ONEN A., KECIK D., DURGUN E. & CIRACI S. Gan: From three-to two-dimensional single-layer crystal and its multilayer van der waals solids. *Phy. Rev. B*, 93 (2016) (8): 085 431.
- PADILHA J.E. & PONTES R.B. Free-standing bilayer silicene: The effect of stacking order on the structural, electronic, and transport properties. *J. Phys. Chem. C*, 119 (2015) (7): 3818–3825.
- PAN L., ZOU B. & SHI L.J. Electric field modulation of the band gap, dielectric constant and polarizability in SnS atomically thin layers. *Physics Letters, Section A: General, Atomic and Solid State Physics*, 380 (2016) (27-28): 2227–2232.
- PARK G., ROSING T., TODD M.D., FARRAR C.R. ET AL. Energy harvesting for structural health monitoring sensor networks. *Journal of Infrastructure Systems*, 14 (2008) (1): 64–79.
- PARK K.I., SON J.H., HWANG G.T., JEONG C.K. ET AL. Highly-efficient, flexible piezoelectric pzt thin film nanogenerator on plastic substrates. *Advanced materials*, 26 (2014) (16): 2514–2520.
- PIKE N.A., VAN TROEYE B., DEWANDRE A., PETRETTO G. ET AL. Origin of the counterintuitive dynamic charge in the transition metal dichalcogenides. *Phys. Rev. B*, 95 (2017) (20): 201 106(R).
- PILANIA G. & RAMPRASAD R. Complex polarization ordering in pbtio 3 nanowires: A first-principles computational study. *Physical Review B*, 82 (2010) (15): 155 442.
- PLIMPTON S. Fast parallel algorithms for short-range molecular dynamics. *Journal of computational physics*, 117 (1995a) (1): 1–19.

- PLIMPTON S. Fast Parallel Algorithms for Short-Range Molecular Dynamics. *J. Comp. Phys.*, 117 (1995b): 1–19.
- PODSIADŁY-PASZKOWSKA A. & KRAWIEC M. Rehybridization-induced charge density oscillations in the long-range corrugated silicene. *Phys. Chem. Chem. Phys.*, 19 (2017) (22): 14 269–14 275.
- POP E., VARSHNEY V. & ROY A.K. Thermal properties of graphene: Fundamentals and applications. *MRS bulletin*, 37 (2012) (12): 1273–1281.
- RATNA D. & KARGER-KOCSIS J. Recent advances in shape memory polymers and composites: a review. *Journal of Materials Science*, 43 (2008) (1): 254–269.
- RAY M. Enhanced magnetoelectric effect in multiferroic composite beams due to flexoelectricity and transverse deformations. *International Journal of Mechanics and Materials in Design*, 14 (2018) (4): 461–472.
- REQUICHA A.A. Nanorobots, nems, and nanoassembly. *Proceedings of the IEEE*, 91 (2003) (11): 1922–1933.
- ROBERT P.T. & DANNEAU R. Charge distribution of metallic single walled carbon nanotube-graphene junctions. *New J. Phys.*, 16 (2014): 013 019.
- ROY R., NEČAS D. & ZAJÍČKOVÁ L. Evidence of flexoelectricity in graphene nanobubbles created by tip induced electric field. *Carbon*, (2021).
- SAI N. & MELE E.J. Microscopic theory for nanotube piezoelectricity. *Phys. Rev. B*, 68 (2003): 241 405.
- SANCHEZ S. & PUMERA M. Nanorobots: the ultimate wireless self-propelled sensing and actuating devices. *Chemistry—An Asian Journal*, 4 (2009) (9): 1402–1410.
- SANG Y., LIU B. & FANG D. The size and strain effects on the electric-field-induced domain evolution and hysteresis loop in ferroelectric batio 3 nanofilms. *Computational Materials Science*, 44 (2008) (2): 404–410.
- SAXENA S., CHAUDHARY R.P. & SHUKLA S. Stanene: atomically thick free-standing layer of 2d hexagonal tin. *Sci. Rep.*, 6 (2016): 31 073.
- SEKINO H. & BARTLETT R.J. Frequency dependent nonlinear optical properties of molecules. *J. Chem. Phys.*, 85 (1986) (2): 976–989.
- SEPLIARSKY M., ASTHAGIRI A., PHILLPOT S., STACHIOTTI M. ET AL. Atomic-level simulation of ferroelectricity in oxide materials. *Current Opinion in Solid State and Materials Science*, 9 (2005) (3): 107–113.
- SETTER N., DAMJANOVIC D., ENG L., FOX G. ET AL. Ferroelectric thin films: Review of materials, properties, and applications. *Journal of Applied Physics*, 100 (2006) (5): 051 606.

- SHAHRAKI M.G., GHORBANALI S. & SAVALONI H. Influence of crystallographic orientation and diameter on piezoelectric constant and youngs modulus of batio 3 nanobelts. *Solid State Communications*, 196 (2014): 40–45.
- SHARMA N., LANDIS C. & SHARMA P. Piezoelectric thin-film superlattices without using piezoelectric materials. *Journal of Applied Physics*, 108 (2010) (2): 024 304.
- SHEN S. & HU S. A theory of flexoelectricity with surface effect for elastic dielectrics. *Journal of the Mechanics and Physics of Solids*, 58 (2010) (5): 665–677.
- SHIRANE G. & TAKEDA A. Transition energy and volume change at three transitions in barium titanate. *Journal of the Physical Society of Japan*, 7 (1952) (1): 1–4.
- SHU L., WAN M., JIANG X., LI F. ET AL. Frequency dispersion of flexoelectricity in pmn-pt single crystal. *AIP Advances*, 7 (2017a) (1): 015 010.
- SHU L., WAN M., WANG Z., WANG L. ET AL. Large flexoelectricity in al<sub>2</sub>o<sub>3</sub>-doped ba (ti<sub>0.85</sub>sn<sub>0.15</sub>) o<sub>3</sub> ceramics. *Applied Physics Letters*, 110 (2017b) (19): 192 903.
- SHU L., WEI X., PANG T., YAO X. ET AL. Symmetry of flexoelectric coefficients in crystalline medium. *Journal of Applied Physics*, 110 (2011a) (10): 104 106.
- SHU L., WEI X., PANG T., YAO X. ET AL. Symmetry of flexoelectric coefficients in crystalline medium. *J. Appl. Phys.*, 110 (2011b) (10): 104 106.
- SILBERSTEIN L. L. molecular refractivity and atomic interaction. ii. *The London, Edinburgh, and Dublin Philosophical Magazine and Journal of Science*, 33 (1917) (198): 521–533.
- SODANO H.A., INMAN D.J. & PARK G. A review of power harvesting from vibration using piezoelectric materials. *Shock and Vibration Digest*, 36 (2004) (3): 197–206.
- SONG X., HUI F., KNOBLOCH T., WANG B. ET AL. Piezoelectricity in two dimensions: Graphene vs. molybdenum disulfide. *Appl. Phys. Lett*, 111 (2017): 083 107.
- STEWART J.A. & SPEAROT D. Atomistic simulations of nanoindentation on the basal plane of crystalline molybdenum disulfide (mos<sub>2</sub>). *Modell. Simul. Mater. Sci. Eng.*, 21 (2013) (4): 045 003.
- STILLINGER F.H. & WEBER T.A. Computer simulation of local order in condensed phases of silicon. *Phys. Rev. B*, 31 (1985) (8): 5262.
- SUKUMAR N., CHOPP D.L., MOËS N. & BELYTSCHKO T. Modeling holes and inclusions by level sets in the extended finite-element method. *Computer methods in applied mechanics and engineering*, 190 (2001) (46-47): 6183–6200.
- SUN Z., MARTINEZ A. & WANG F. Optical modulators with 2d layered materials. *Nature Photonics*, 10 (2016) (4): 227.

- SURYA V.J., IYAKUTTI K., MIZUSEKI H. & KAWAZOE Y. Modification of graphene as active hydrogen storage medium by strain engineering. *Computational Materials Science*, 65 (2012): 144–148.
- SWOPE W.C., ANDERSEN H.C., BERENS P.H., WILSON K.R. ET AL. A computer simulation method for the calculation of equilibrium constants for the formation of physical clusters of molecules : Application to small water clusters. *J. Chem. Phys*, 76 (1982): 637–649.
- THAI T.Q., RABCZUK T. & ZHUANG X. A large deformation isogeometric approach for flexoelectricity and soft materials. *Computer Methods in Applied Mechanics and Engineering*, (2018).
- THOLE B.T. Molecular polarizabilities calculated with a modified dipole interaction. *Chem. Phys.*, 59 (1981) (3): 341–350.
- TILOCCA A., DE LEEUW N.H. & CORMACK A.N. Shell-model molecular dynamics calculations of modified silicate glasses. *Physical Review B*, 73 (2006) (10): 104 209.
- TINTE S. & STACHIOTTI M. Surface effects and ferroelectric phase transitions in batio 3 ultrathin films. *Physical Review B*, 64 (2001) (23): 235 403.
- TINTE S., STACHIOTTI M., PHILLPOT S., SEPLIARSKY M. ET AL. Ferroelectric properties of baxsr1- xtio3 solid solutions obtained by molecular dynamics simulation. *Journal of Physics: Condensed Matter*, 16 (2004) (20): 3495.
- TINTE S., STACHIOTTI M., SEPLIARSKY M., MIGONI R. ET AL. Atomistic modelling of batio3 based on first-principles calculations. *Journal of Physics: Condensed Matter*, 11 (1999) (48): 9679.
- VERMA V., JINDAL V. & DHARAMVIR K. Elastic moduli of a boron nitride nanotube. *Nanotechnology*, 18 (2007) (43): 435 711.
- VIELMA J.M. & SCHNEIDER G. Shell model of batio3 derived from ab-initio total energy calculations. *Journal of Applied Physics*, 114 (2013) (17): 174 108.
- WAN M., YONG Z., HUANG W., ZHANG S. ET AL. Design of a flexure composite with large flexoelectricity. *Journal of Materials Science: Materials in Electronics*, 28 (2017) (9): 6505–6511.
- WANG B., YANG S. & SHARMA P. Flexoelectricity as a universal mechanism for energy harvesting from crumpling of thin sheets. *Physical Review B*, 100 (2019) (3): 035 438.
- WANG J., SHU H., ZHAO T., LIANG P. ET AL. Intriguing electronic and optical properties of two-dimensional Janus transition metal dichalcogenides. *Physical Chemistry Chemical Physics*, 20 (2018a) (27): 18 571–18 578.

- WANG Q.H., KALANTAR-ZADEH K., KIS A., COLEMAN J.N. ET AL. Electronics and optoelectronics of two-dimensional transition metal dichalcogenides. *Nature nanotechnology*, 7 (2012) (11): 699.
- WANG R., CHU W., GAO K., SU W. ET AL. Stress corrosion cracking of a batio<sub>3</sub> ferroelectric ceramics. *Materials Letters*, 58 (2004) (11): 1811–1814.
- WANG W., BAI L., YANG C., FAN K. ET AL. The electronic properties of o-doped pure and sulfur vacancy-defect monolayer ws<sub>2</sub>: A first-principles study. *Materials*, 11 (2018b) (2): 218.
- WANG X., SONG J., LIU J. & WANG Z.L. Direct-current nanogenerator driven by ultrasonic waves. *Science*, 316 (2007) (5821): 102–105.
- WANG X., TIAN H., XIE W., SHU Y. ET AL. Observation of a giant two-dimensional band-piezoelectric effect on biaxial-strained graphene. *NPG Asia Materials*, 7 (2015): e154.
- WANG X., WATANABE H., FUJI M. & TAKAHASHI M. Molecular dynamics simulation of nacl at the air/water interface with shell model. *Chemical Physics Letters*, 458 (2008) (1-3): 235–238.
- WANG Y. & JING X. Intrinsically conducting polymers for electromagnetic interference shielding. *Polymers for advanced technologies*, 16 (2005) (4): 344–351.
- WANG Z.L. & SONG J. Piezoelectric nanogenerators based on zinc oxide nanowire arrays. *Science*, 312 (2006) (5771): 242–246.
- WASER R. ET AL. *Nanoelectronics and information technology*. Wiley Online Library, 2003.
- WIRTZ L., RUBIO A., DE LA CONCHA R.A. & LOISEAU A. *Ab initio* calculations of the lattice dynamics of boron nitride nanotubes. *Phys. Rev. B*, 68 (2003) (4): 045 425.
- WU W., WANG L., LI Y., ZHANG F. ET AL. Piezoelectricity of single-atomic-layer mos<sub>2</sub> for energy conversion and piezotronics. *Nature*, 514 (2014a) (7523): 470–474.
- WU Z., ZHANG Y., BAI G., TANG W. ET AL. Effect of biaxial strain induced by piezoelectric PMN-PT on the upconversion photoluminescence of BaTiO<sub>3</sub>:Yb/Er thin films. *Opt. Express*, 22 (2014b) (23): 29 014–29 019.
- XIONG Q.L., ZHOU J., ZHANG J., KITAMURA T. ET AL. Spontaneous curling of free-standing janus monolayer transition-metal dichalcogenides. *Physical Chemistry Chemical Physics*, 20 (2018) (32): 20 988–20 995.
- XU T., WANG J., SHIMADA T. & KITAMURA T. Direct approach for flexoelectricity from first-principles calculations: cases for srtio<sub>3</sub> and batio<sub>3</sub>. *Journal of Physics: Condensed Matter*, 25 (2013) (41): 415 901.

- YU S., WU X., WANG Y., GUO X. ET AL. 2d materials for optical modulation: challenges and opportunities. *Advanced Materials*, 29 (2017) (14): 1606–128.
- YUDIN P. & TAGANTSEV A. Fundamentals of flexoelectricity in solids. *Nanotechnology*, 24 (2013a) (43): 432–001.
- YUDIN P.V. & TAGANTSEV A.K. Fundamentals of flexoelectricity in solids. *Nanotechnology*, 24 (2013b) (43): 432–001.
- ZELISKO M., HANLUMYUANG Y., YANG S., LIU Y. ET AL. Anomalous piezoelectricity in two-dimensional graphene nitride nanosheets. *Nat. Comm.*, 5 (2014): 4284.
- ZHANG C., ZHANG L., SHEN X. & CHEN W. Enhancing magnetoelectric effect in multiferroic composite bilayers via flexoelectricity. *Journal of Applied Physics*, 119 (2016) (13): 134–102.
- ZHANG D., YANG Z., LI P., PANG M. ET AL. Flexible self-powered high-performance ammonia sensor based on au-decorated mos<sub>2</sub> nanoflowers driven by single layer mos<sub>2</sub>-flake piezoelectric nanogenerator. *Nano Energy*, 65 (2019): 103–974.
- ZHANG J. Boron nitride honeycombs with superb and tunable piezopotential properties. *Nano Energy*, 41 (2017): 460–468.
- ZHANG J., XU R., DAMODARAN A., CHEN Z.H. ET AL. Understanding order in compositionally graded ferroelectrics: flexoelectricity, gradient, and depolarization field effects. *Physical Review B*, 89 (2014) (22): 224–101.
- ZHAO L., XU S., WANG M. & LIN S. Probing the thermodynamic stability and phonon transport in two-dimensional hexagonal aluminum nitride monolayer. *J. Phys. Chem. C*, 120 (2016) (48): 27–675–27–681.
- ZHENG X.Q., LEE J. & FENG P.X.L. Hexagonal boron nitride nanomechanical resonators with spatially visualized motion. *Microsystems & Nanoengineering*, 3 (2017): 17–038.
- ZHONG W., KING-SMITH R. & VANDERBILT D. Giant lo-to splittings in perovskite ferroelectrics. *Physical review letters*, 72 (1994) (22): 3618.
- ZHOU M. A new look at the atomic level virial stress: on continuum-molecular system equivalence. In *Proceedings of the Royal Society of London A: Mathematical, Physical and Engineering Sciences*, volume 459, pages 2347–2392. The Royal Society, 2003.
- ZHOU Y., LIU W., HUANG X., ZHANG A. ET AL. Theoretical study on two-dimensional mos<sub>2</sub> piezoelectric nanogenerators. *Nano Research*, 9 (2016) (3): 800–807.
- ZHUANG X., HE B., JAVVAJI B. & PARK H.S. Intrinsic bending flexoelectric constants in two-dimensional materials. *Physical Review B*, 99 (2019a) (5): 054–105.
- ZHUANG X., NANTHAKUMAR S. & RABCZUK T. A meshfree formulation for large deformation analysis of flexoelectric structures accounting for the surface effects. *arXiv preprint arXiv:1911.06553*, (2019b).

- ZHUANG X., NANTHAKUMAR S. & RABCZUK T. A meshfree formulation for large deformation analysis of flexoelectric structures accounting for the surface effects. *Engineering Analysis with Boundary Elements*, 120 (2020): 153–165.
- ZUBKO P., CATALAN G., BUCKLEY A., WELCHE P. ET AL. Strain-gradient-induced polarization in strontium 3 single crystals. *Physical Review Letters*, 99 (2007) (16): 167 601.
- ZUBKO P., CATALAN G. & TAGANTSEV A.K. Flexoelectric effect in solids. *Annual Review of Materials Research*, 43 (2013a): 387–421.
- ZUBKO P., CATALAN G. & TAGANTSEV A.K. Flexoelectric Effect in Solids. *Annual Review of Materials Research*, 43 (2013b) (1): 387 –421.

# List of Figures

2.1	Schematic illustration of the interactions between particles. . . . .	13
2.2	Temperature versus lattice parameters ( $\text{\AA}$ ) of different size $\text{BaTiO}_3$ systems.	15
2.3	Size-dependent phase transition temperatures (K) of $\text{BaTiO}_3$ systems. . . . .	16
2.4	Temperature versus averaged absolute spontaneous polarization ( $C/m^2$ ) of different size $\text{BaTiO}_3$ systems. . . . .	17
2.5	Schematic illustration of (a) deformed supercell structure according to the equation (2.6); (b) Deformation (equation (2.6)), strain and strain gradient (equation (2.7)) profile, $h/4$ position indicated by the dash line; (c) deformed supercell structure according to the equation (2.9); (d) Deformation (equation (2.9)), strain and strain gradient (equation (2.10)) profile, $h/2$ position indicated by the dash line. . . . .	20
2.6	Plot of (a) polarization vs applied maximum strain $\varepsilon_{max}$ (b) size-dependent longitudinal flexoelectric coefficient. The bulk flexoelectric coefficients are from systems with total atom number equals 30000, the yellow and green triangle shows the DFT calculation result of MARANGANTI & SHARMA (2009) (0.15 nC/m) and HONG ET AL. (2010) (0.36 nC/m), respectively. The MD calculated bulk longitudinal flexoelectric coefficient is 0.201 nC/m.	20
2.7	Cell by cell (at $z = h/4$ section) polarization (calculated by the equation (2.8)) of different system sizes demonstrate the surface cells have higher polarization compare to the inner cells due to the higher mobility of surface atoms. . . . .	21
2.8	Plot of (a) polarization vs applied strain $\varepsilon_{max}$ (b) size-dependent shear flexoelectric coefficient. The bulk flexoelectric coefficient indicated by the light green triangle shows the DFT calculation result (1.5 nC/m) of XU ET AL. (2013). . . . .	22
2.9	Schematic illustration of (a) $\text{BaTiO}_3$ nanostructure and (b) loading procedure for extracting Young's modulus of $\text{BaTiO}_3$ nanostructure. . . . .	23
2.10	Illustration of (a) size-dependent stress-strain diagram and (b) influence of the surface effect on Young's modulus of $\text{BaTiO}_3$ nanostructures. . . . .	23



3.1	Top and side view of the studied materials: (a) Graphene allotropes AB, A = B = Carbon; (b) Nitrides AB, A = Nitrogen, B = Boron, Aluminium or Gallium; (c) graphene analogues of group-IV elements AB, A = B = Silicon, Germanium, Tin; (d) transition metal dichalcogenides AB <sub>2</sub> , A = Molybdenum, Tungsten or Chromium, B = Sulfur; (e) Janus transition metal dichalcogenides MXY, M = Molybdenum or Tungsten; X= Sulfur or Selenium, Y = Selenium or Tellurium. For (a)-(c), $h$ refers to the buckling height, while in (d)-(e) $h_1$ and $h_2$ refer to intralayer distances. . . . .	26
3.2	Loading scheme for estimating piezoelectric coefficient. . . . .	33
3.3	Polarization $P_x$ vs strain $\epsilon_{xx}$ for BN and MoS <sub>2</sub> and Janus TMDCs material systems. . . . .	33
3.4	Schematic illustration of the geometry and loading condition for 2D material system. (a) flat system (graphene allotropes, nitrides, graphene analogues of group-IV elements and TMDC monolayers); (b) curled system (Janus TMDCs). . . . .	34
3.5	(a) Atomic configuration colored with strain $\epsilon_{xz}$ in X-direction for MoS <sub>2</sub> sheet when strain gradient $K = 0.01 \text{ \AA}^{-1}$ ; the large spheres represent Mo atoms and small spheres represent S atoms. (b) Bin-wise distribution of strain $\epsilon_{xz}$ along X axis, circles represent the calculated average strain $\epsilon_{xz}$ at location $x$ and the solid line is linear fitting to the calculated data. . . . .	36
3.6	(a) Polarization $P_z$ vs inverse of curvature $K$ for graphene, BN, Silicene and MoS <sub>2</sub> . Markers indicate the simulation data, and solid lines indicate the linear fitting. (b) Polarization $P_z$ vs effective strain gradient $K_{eff}$ for Janus TMDCs. Markers indicate the simulation data, and solid lines indicate the linear fitting. . . . .	38
3.7	Bending flexoelectric coefficients of the studied 2D materials. . . . .	38
3.8	Polarization $P_z$ versus applied inverse of curvature $K$ for silicene and flat silicene. . . . .	41
3.9	(a) Undeformed, and (b) Deformed atomic configuration of MoS <sub>2</sub> sheet. Red-colored atoms are used to explain the changes in bond length. Dashed lines represent the Mo layer and dash-dotted lines indicate the S layers. Atoms X and Y in (a) possess bond lengths of 2.42 Å with neighbor sulfur atoms. The bond length between atoms Y-A and Y-D is 2.42 Å and 2.41 Å, respectively. Atom Y has bond length of 2.26 Å with atoms B and C. The bond length between atoms Y-E and Y-F is 2.76 Å. Only left portion of the atomic system was shown here. . . . .	42
3.10	Atomic configurations of (a) undeformed MoS <sub>2</sub> , (b) deformed MoS <sub>2</sub> at $K_{eff} = 0.05 \text{ nm}^{-1}$ , (c) undeformed MoSSe and (d) deformed MoSSe at $K_{eff} = 0.05 \text{ nm}^{-1}$ . . . . .	45
3.11	Polarization $P_z$ versus the effective strain gradient $K_{eff}$ for MoSTe and WSTe when bending against their initial spontaneous curvature. . . . .	49
3.12	The variation of polarization (a) $P_x$ and (b) $P_y$ with bending curvature ( $K$ ) for Graphene, BN, Silicene and MoS <sub>2</sub> . The inset in (a) and (b) represent the polarization variation for materials other than MoS <sub>2</sub> . . . . .	50

3.13	Bin-wise distribution of dipole (a) $p_x$ and (b) $p_y$ along X axis for BN at a curvature of $K = 0.08 \text{ nm}^{-1}$ . . . . .	51
4.1	(a) Schematic illustration of the MLS approximation, and (b) Level-set function and its derivation cross the interface. . . . .	58
4.2	Schematic illustration of the cantilever beam under (a) mechanical load, (b) electrical load, and (c) MLS discretization with the red solid points representing the nodes. . . . .	61
4.3	Calculation result: (a) size dependent effective piezoelectric constant, and (b) electric potential profile for the 2D fully coupled cantilever beam. . . . .	62
4.4	Calculation result of a cantilever beam under electric loading condition: (a) beam displacement, and (b) electric potential profile. . . . .	63
4.5	The electric field profile cross the beam in the Y-direction at mid-length of the beam. . . . .	63
4.6	Schematic illustration of (a) truncated pyramid and its boundary conditions, and (b) MLS discretization with the red solid points representing the nodes. . . . .	64
4.7	Calculation result of the compressed truncated pyramid: (a) strain profile in the Y-direction, and (b) electric field profile. . . . .	64
4.8	Schematic illustration of (a) square domain with center inclusion and the boundary conditions, and (b) MLS discretization with the red solid points representing the nodes and blue asterisks representing the enriched nodes. . . . .	65
4.9	Calculation result of the square composite under compression: (a) strain profile in the YY direction, and (b) induced electric potential. . . . .	66
4.10	Strain gradient profiles along the horizontal center line ( $\varepsilon_{yy,y}$ ) and vertical center line ( $\varepsilon_{xx,x}$ ). . . . .	67
4.11	Calculation result of a compressed square composite with randomly distributed inclusions: (a) electric potential profile, and (b) energy conversion ratio. . . . .	67
4.12	Schematic illustration of the H27 element, this element has 27 nodes includes 8 corner nodes equipped with displacement $\mathbf{u}$ (blue rectangles), electric potential $\theta$ (red triangles), displacement gradient $\psi$ (red triangles) and Lagrange multiplier $\lambda$ (red triangles) DOFs; the remain 19 nodes (blue rectangles) only hold displacement $\mathbf{u}$ DOFs. . . . .	69
4.13	(a) Schematic illustration of the analytical set-up, the inner surface subjects to a displacement load $u_1 = 0.045 \mu\text{m}$ and the displacement load $u_2 = 0.05 \mu\text{m}$ is applied to the outer surface; The outer surface also subjects to electric potential equals to 1V whereas the inner surface is grounded. The inner radius $r_1 = 10\mu\text{m}$ and outer radius $r_2 = 20\mu\text{m}$ ; (b) The mesh configuration of a quarter of the structure as in the analytical set-up. . . . .	73
4.14	(a) radius displacement (m) distribution profile, and (b) electric potential (V) profile from the NMFEM model with strain gradient elasticity. . . . .	75

4.15	Comparison between the analytical solution and NMFEM. (a) displacement comparison, the insertion is the relative error of displacement between the NMFEM result and analytical solution in the unit of $10^{-10}$ m; (b) electric potential comparison, the insertion is the relative error of electric potential between the NMFEM result and analytical solution in the unit of $10^{-2}$ Volt.	76
4.16	Schematic illustration of a cantilever beam and its boundary conditions. . . . .	76
4.17	Maximum displacement and output voltage of the cantilever beams from the linear and nonlinear model. (a) and (b) show the maximum displacement and output voltage of a cantilever beam with depth $d = 5 \mu\text{m}$ , respectively; (c) and (d) show the maximum displacement and output voltage of a cantilever beam with depth $d = 10 \mu\text{m}$ , respectively. . . . .	78
4.18	Electric potential profile of the deformed beam with depth $d = 5 \mu\text{m}$ at (a) step 1; (b) step 15; (c) step 30. . . . .	79
4.19	Maximum output voltage versus loading frequency under different loading amplitudes, ranging from $f = 0.002$ N/m to $f = 0.01$ N/m and from $f = 0.002$ N/m to $f = 0.05$ N/m for linear and nonlinear model, respectively. The dot plots present the results from the nonlinear model. The solid lines present the results from the linear model. The schematic illustration of the cantilever slab with its boundary conditions are also presented. . . . .	81
4.20	Maximum output voltage versus loading frequency under loading amplitude $f = 0.05$ N/m for nonlinear model with different structural damping ratios: $\xi = 0.01$ , $\xi = 0.15$ and $\xi = 0.30$ . . . . .	81
4.21	(a) Schematic illustration of the composite with a single inclusion located in the center of the matrix. The matrix denotes as M1 and the inclusion as M2, and (b) Mesh configuration of the composite material. . . . .	82
4.22	(a) strain $\varepsilon_{xy}$ distribution of the matrix M1 and inclusion M2, and (b) electric potential (V) of the matrix M1 and inclusion M2 . . . . .	83
4.23	Electric potential profile along the centerline of the composite in the Y-direction. . . . .	84
4.24	(a) Schematic illustration of a composite with multiple inclusions. The matrix denotes as M1 (light blue) and the inclusions as M2 (dark blue), and (b) Mesh configuration of the composite. . . . .	85
4.25	Convergence study of a setup $V_{ratio} = 5\%$ and $E_{rel} = 3$ with ten samples. . . . .	86
4.26	The normalized effective electromechanical coupling factor $K_{eff}^n$ for different setup of $V_{ratio}$ and $E_{rel}$ values. . . . .	86
4.27	(a) strain $\varepsilon_{xy}$ plot of a composite with multiple inclusions, and (b) the induced electrical potential distribution of a composite with multiple inclusions. . . . .	87
4.28	(a) Schematic illustration of the composite flexoelectric device, the device subjects to a line load F at its free end. The darker blue circles represent the inclusions. The red bar represents the positive electrode, and the blue bar is the negative electrode, and (b) Mesh configuration of the composite flexoelectric device. . . . .	88
4.29	(a) Electric potential distribution from the pure polymer beam, and (b) Electric potential distribution from the proposed composite flexoelectric device. . . . .	88

- 
- 4.30 (a) Schematic illustration of a cone structure and its boundary conditions, its left side (outer diameter is  $d_1$ ) is fixed and connected to the ground; on the right side, a line load applies to the top edge of the outer circle (outer diameter  $d_2$ ). The insertion is an image of BN cone, see KVASHNIN ET AL. (2018), and (b) Maximum output voltage versus loading step for cone structures with different diameter ratios under identical incremental load for 20 steps. . . . . 89
- 4.31 Electric potential distribution of the deformed cone structures with  $\frac{d_2}{d_1} = 0.5, 1$  and  $2$  at step 20. . . . . 90



# List of Tables

2.1	Core-Shell model parameters from VIELMA & SCHNEIDER (2013). Charges are in unit of electrons, energies in unit of eV, and length in unit of Å. . . .	14
2.2	BaTiO <sub>3</sub> transition temperature (K) comparison by different methods. Rhombohedral (R) → Orthorhombic (O) → Tetragonal (T) → Cubic (C). . . . .	16
3.1	Calculation details for each material. The unit cell dimensions $a, b, c$ and $h$ are given in Å. The bonding interactions are modeled using different types of 'short-range potentials'. $\alpha_{\text{total}}^{\text{DFT}}$ is the polarizability estimates from DFT and $\alpha_{\text{total}}^{\text{CAL}}$ is calculated using the equation (3.18) in Å <sup>3</sup> . The $R_A$ and $R_B$ (in Å units) are the CD potential parameters for atom types $A$ and $B$ in the given unit cell. . . . .	31
3.2	Total polarizability estimated by DFT ( $\alpha_{\text{DFT}}$ in Å <sup>3</sup> ) and the estimation from the present CD model ( $\alpha_{\text{Cal}}$ in Å <sup>3</sup> ), see ZHUANG ET AL. (2019a). Atomic polarizability ( $R_i$ in Å) and lattice parameters ( $a, b$ are the lattice constants, $l_1$ and $l_2$ are the bond lengths for M-X and M-Y in Å, respectively) for the Janus TMDCs. For simplicity, in this study the Janus TMDCs are denoted as MXY with M = Mo and W; X, Y = S, Se and Te; X represents the chalcogenide atom with a smaller atomic number while Y represents the chalcogenide atom with a larger atomic number. . . . .	32
3.3	Piezoelectric coefficients ( $\times 10^{-10}$ C/m) from the CD model estimation and literature. . . . .	32
3.4	In-plane piezoelectric coefficients $d_{yyy}$ ( $\times 10^{-10}$ C/m) for Janus TMDCs using proposed CD model in comparison to previous DFT results ( $d_{yyy}^{\text{DFT}}$ ). $\mu_{zyzy}$ (nC/m) are the bending flexoelectric constants while $l_2 - l_1$ (Å) is the initial asymmetry for Janus TMDCs. . . . .	44
3.5	Flexoelectric coefficients ( $\mu_{zxxz}, \mu_{yxzx}(a_{1,y}), \mu_{xxzx}(a_{1,x})$ ) given in nC/m. $a_0$ has unit of C/m <sup>2</sup> , while $a_2$ has unit of C. . . . .	50
4.1	Material parameters. . . . .	61
4.2	Material parameters. . . . .	74

## Curriculum vitae

Bo He

born September 20, 1990 in Hubei, China

### Professional Experience

since 06.2020

Calculation and Simulation Engineer at SAMSON AG,  
Frankfurt am Main

03.2016 - 05.2020

Research Associate at the Institute of Continuum Mechanics,  
Leibniz Universität Hannover

### Education

since 02.2022

Leibniz Universität Hannover  
Institute of Photonics  
Doctoral candidate

03.2016 - 05.2020

Leibniz Universität Hannover  
Institute of Continuum Mechanics  
Doctoral candidate

10.2013 - 12.2015

Bauhaus-Universität Weimar  
Civil Engineering  
Focus: Structural Engineering  
Degree: M. Sc.

10.2009 - 09.2013

Zivilluftfahrt Universität von China  
Civil Engineering  
Degree: B. Sc.

## Publications

1. Bo He, Brahmanandam Javvaji, and Xiaoying Zhuang. Size dependent flexoelectric and mechanical properties of barium titanate nanobelt: A molecular dynamics study. *Physica B: Condensed Matter*, 545:527-535, 2018.
2. Brahmanandam Javvaji, Bo He, and Xiaoying Zhuang. The generation of piezoelectricity and flexoelectricity in graphene by breaking the materials symmetries. *Nanotechnology*, 29(22):225702, 2018.
3. Bo He, Brahmanandam Javvaji, and Xiaoying Zhuang. Characterizing flexoelectricity in composite material using the element-free galerkin method. *Energies*, 12(2):271, 2019.
4. Xiaoying Zhuang, Bo He, Brahmanandam Javvaji, and Harold S Park. Intrinsic bending flexoelectric constants in two-dimensional materials. *Physical Review B*, 99(5):054105, 2019.
5. Brahmanandam Javvaji, Bo He, Xiaoying Zhuang, and Harold S Park. High flexoelectric constants in janus transition-metal dichalcogenides. *Physical Review Materials*, 3(12):125402, 2019.
6. Bo He. Hydromechanical model for hydraulic fractures using xfem. *Frontiers of Structural and Civil Engineering*, 13(1):240-249, 2019.
7. Yangyang Long, Bo He, Weizhe Cui, Yuhang Ji, Xiaoying Zhuang, and Jens Twiefel. Investigations on the mechanism of microweld changes during ultrasonic wire bonding by molecular dynamics simulation. *Materials & Design*, page 108718, 2020.







